

Computational Uncertainty Quantification of Thermal Radiation in Supersonic Combustion Chambers

by

Andrew Joseph Crow

A dissertation submitted in partial fulfillment
of the requirements for the degree of
Doctor of Philosophy
(Aerospace Engineering)
in The University of Michigan
2013

Doctoral Committee:

Professor Iain D. Boyd, Chair
Assistant Professor Krzysztof J. Fidkowski
Associate Professor Xianglei Huang
Professor Ken Powell

Why do engineers never volunteer to be test pilots?
Is it because they only care about the technical challenges?

No,
we just know everything
that can go wrong.



Image Courtesy of Andrew Joseph Crow: <http://www.mildlymiffed.com> [19].

© Andrew Joseph Crow 2013

All Rights Reserved

Despite the paradox that is a work undertaken for its own sake being dedicated to another, the journey was given meaning not by itself but by far too many people for this singular sentence to contain and in ways that, if enumerated, would dwarf the text to which they pertain.

ACKNOWLEDGEMENTS

First, Iain D. Boyd deserves much credit for taking in a lost student and keeping him on track. I know that all students offer unique challenges, and I thank you for putting up with mine.

Also, I would like to thank my committee: Krzysztof J. Fidkowski, Xianglei Huang, and Ken Powell for reviewing this document and providing useful information and guidance along the way. Each one of you taught me many things that made this work what it is.

I would like to thank the Stanford Predictive Sciences Academic Alliance Program (PSAAP) team for fostering an environment in which I could complete this work. I, specifically, am very grateful to Ivan Bermejo-Moreno and Vincent Terrapon for providing me with a great amount of information and allowing me to use their work as a starting point of my own.

I am, also, grateful to the staff at the Air Force Research Laboratory, particularly Michael Brown for providing experimental data and hosting while I took my own measurements. Additionally, I would like to thank Jiwen Liu for the use of his code “GRASP,” saving me an unmeasurable amount of time. This project would not have been what it is without your help.

I would like to thank Professor Mark J. Kushner for lending me computer time when I needed it the most.

I am very grateful to the staff at Lawrence Livermore National Laboratory, especially David Larson for giving me an opportunities to explore unique lines of research.

My fellow students, especially my fellow lab-mates in NGPDL, allowed me to make it through the rigors of this process. Thank you for tolerating any questions or problems I had and for always being willing to offer time and support. I would specifically like to thank Adam Irvine for allowing me to take his work and morph it for my own purposes.

Thank you to my study group: Roland Florenz, Cyril Galitzine, and Paul Giuliano, for challenging me, keeping me on track, and making these years much more colorful than expected. Finally, I am giving a big thank you to the Aerospace Broomball team for many late-night spills and celebrations. “There’s no love... Like Strangelove.”

Denise Phelps, you have been thanked in more dissertations than anyone else in this department, and you have earned every one. Thank you for making so many parts of this process absolutely seamless and for informing me whenever free food was available.

I would like to thank Katherine Swart for proof-reading the more intricate parts of this document. Your dedication saved a substantial amount of confusion.

I would like to thank all of my friends who provided sympathy, inspiration, relaxation, and challenges along the way. I embarked on this journey because you made it look like so much fun. Honestly, it was. So many of you kept me going and changed me along the way.

Thank you Dr. Stephen Matthew Crabtree for deepening my love of cinema. It is through your guidance that I have learned to see the wonder in the mundane that others would pass by. Thank you Dr. Alton James Benjamin Luder III for encouraging my love of visual art, making me a little more rounded in my endeavors. Also, thank you for making me much more appreciative of my technical skills. Thank you Dr. Torstens “The Mad Latvian Slammer” Skujins for always encouraging me to do things I would not regret, and for always being up for a sporting event. Jennifer Priebe, thank you, for always being willing to hear me out and offer an opposing

viewpoint on any subject, even when it was not requested. I am giving a big thank you to Abhilasha Anna for giving me reasons to get out of the office. Finally, thank you to the members of TNPK for making me feel like I belonged here right off the bat.

The men of the Nixon House for being great housemates and for putting up with my odd hours. Also, I have quite a few new favorite foods and cooking styles because of you.

Also, I would like to thank George and Mary Lindquist for opening up their home and kitchen to so many hungry graduate students every week.

Most importantly, I would like to thank my family. You were always willing to lend time and tolerated me working at all times, including holidays. Dad, you set the standard and, more than anyone else, you inspired me to start on this process. Without your advice, I might not have made it through. Mom, you kept me on track for what was really important during a very isolating time, and you were a sounding board when I needed honesty.

Finally, I would like to thank several organizations for supporting this work:

The experimental work was supported in part by Advanced Propulsion Test Technology and the Air Force Office of Scientific Research.

This material is based upon work supported by the Department of Energy [National Nuclear Security Administration] under Award Number NA28614.

TABLE OF CONTENTS

DEDICATION	ii
ACKNOWLEDGEMENTS	iii
LIST OF FIGURES	ix
LIST OF TABLES	xvii
LIST OF APPENDICES	xix
LIST OF ABBREVIATIONS	xx
LIST OF SYMBOLS	xxii
ABSTRACT	xxv
CHAPTER	
I. Introduction	1
1.1 Project Goals	2
1.1.1 Uncertainty Margin	3
1.1.2 Thesis Outline	5
1.2 The Scramjet	8
1.2.1 History and Current State	11
1.2.2 HyShot-II Experiment	12
1.2.3 HIFiRE-2 Experiment	14
1.2.4 Challenges	16
1.3 Thermal Radiation	17
1.3.1 Principles	18
1.3.2 Spectral Modeling	20
1.3.3 Computational Modeling	22
1.4 Prior Thermal Radiative Investigations	24
1.5 Introduction Summary	26

II. Methodology	28
2.1 Introduction	28
2.2 Thermal Radiation	29
2.2.1 Radiation Field Modeling	32
2.2.2 Spectral Resolution	34
2.2.3 Band Modeling	36
2.3 Sensitivities and Errors	39
2.3.1 Sensitivities	41
2.3.2 Uncertainty Estimation	43
2.3.3 Combined Errors	45
2.4 CFD Modeling	47
2.5 Experimental Setup	48
2.6 Conclusions	52
III. Parameter Sensitivity Studies	54
3.1 Introduction	54
3.1.1 HyShot-II	56
3.1.2 HIFiRE-2	60
3.2 Geometric Approximation	67
3.2.1 Simulation Dimensions	67
3.2.2 Size Approximations	72
3.3 Flowfield Parameters	75
3.3.1 Sensitivity Analysis	78
3.3.2 Property Selection	84
3.4 Boundary Conditions	87
3.5 Flowfield Temperature	92
3.6 Conclusions	95
IV. Model Uncertainty	98
4.1 Introduction	98
4.2 Spectral Accuracy	100
4.2.1 Model Comparison	102
4.2.2 Error Tables	111
4.2.3 Error Propagation	114
4.3 Numerical Accuracy	122
4.3.1 Grid Refinement	124
4.3.2 Numerical Method Comparison	136
4.4 Comparisons to Measurements	138
4.5 Conclusions	145
V. Flowfield Variation	148

5.1	Introduction	148
5.2	Flowfield Examination	149
5.2.1	Initial Large Eddy Simulation Examination	150
5.2.2	Large Eddy Simulation Radiative Heat Fluxes	155
5.3	Uncertainty Incorporation	160
5.3.1	Radiative Modeling Uncertainty	161
5.3.2	Boundary Condition Uncertainty	166
5.3.3	Sensor Prediction Uncertainty	178
5.4	Conclusions	183
VI. Conclusions and Looking Forward		187
6.1	Project Goals	187
6.2	Conclusions	189
6.3	Contributions	190
6.4	Looking Forward	193
6.4.1	Revisiting Issues	194
6.4.2	Future Work	196
6.5	Project Evaluation	198
APPENDICES		199
A.1	Methodology	201
A.1.1	Governing Equations	201
A.1.2	Procedure	203
A.2	Results	206
B.1	Spectral Model Statistics Error Tables	213
BIBLIOGRAPHY		219

LIST OF FIGURES

Figure

1.1	Diagram of the Stanford PSAAP project goals of predicting probabilistic uncertainty for different design criteria [50].	5
1.2	Diagram of shock jump properties for air over a range of Mach numbers. Pressure and temperature ratios are presented in (a), and entropy generation is presented in (b)	9
1.3	Diagram of a generic Scramjet. Hypersonic, free-stream air is compressed by the vehicle bow-shock, and funneled into the engine inlet. The air-stream is further compressed by a shock-train, and fuel is injected. The fuel is ignited in the combustion chamber, and thrust is generated at the exit nozzle. Flow is from left to right.	10
1.4	Diagram of efficiency in specific impulse vs. Mach number for various jet propulsion engines [99].	11
1.5	Diagram of the HyShot-II combustor [5]. Flow is from left to right.	13
1.6	Diagram of one half of the HyShot-II ramp and inlet [100]. Flow is from left to right.	14
1.7	Diagram of the HIFiRE-2 combustor as mounted on the flight experiment. The shrouded is in place during launch and is ejected before the combustion experiment [51]. Flow is from left to right.	15
1.8	HDCR domain: Illustration of the facility nozzle, flame holding cavity, injection ports, and outlet. Flow is from left to right.	16
1.9	Example spectrum of the linestrength variation in a narrow spectral band of carbon dioxide [91].	21
2.1	Angular Coordinate System	31

2.2	Schematic of flowpath: Flow is left to right. The isolator extends from station 1 to 2, the cavity flameholder extends from from 3 to 6. Primary and secondary fuel injection sites are denoted by P1 and S1, respectively. Emission measurements are made at the exit of the combustor, denoted as station 7. The CFD domain is denoted in gray.	48
2.3	Optical hardware mounted to the exit plane of the HDCR combustor. The 16 photodetectors used in the emission measurements are located in two housings as indicated. (Flow is right to left.) Photo courtesy of Michael Brown at the AFRL.	50
2.4	Location of the emission photodetectors with respect to the exit of the combustor shown in yellow. Flow is out of the page. Image courtesy of Michael Brown at the AFRL.	51
3.1	HyShot-II combustion chamber geometry. (a) Side, (b) bottom, (c) Orthographic. All dimensions in millimeters. Flow is from left to right.	57
3.2	HyShot-II combustion chamber RANS calculations (without radiation) for (a) Temperature and (b) Pressure. Flow is from left to right.	58
3.3	HyShot-II combustion chamber RANS calculations (without radiation) for (a) H ₂ O and (b) OH mole fraction. Flow is from left to right.	59
3.4	HDCR domain: Illustration of the facility nozzle, flame holding cavity, injection ports, and outlet. Flow is from right to left.	61
3.5	HDCR temperature (a), pressure (b), density (c), and Mach number (d) from the AFRL CFD simulation (without radiation). Flow is from right to left.	63
3.6	HDCR molar concentrations of water vapor (a) and carbon dioxide (b) from the AFRL CFD simulation (without radiation). Flow is from right to left.	64
3.7	HDCR molar concentrations of the hydroxyl radical (a), carbon monoxide (b), and methane (c) from the AFRL CFD simulation (without radiation). Flow is from right to left.	66
3.8	Spectral heat flux profiles for the using DOM (dashed) and RT method (solid) at the lower wall (y=0.0 mm) for various locations given in Table 3.1.	71

3.9	Spectral heat flux profiles using DOM for various conditions given in Table 3.2	74
3.10	DOM solutions to HIFiRE-2 for (a) volumetric radiative heat loss per cell, (b) radiative heat flux at the wall, (c) convective heat flux at the wall, and (d) the ratio of radiative to convective heat flux at the wall. Flow is from the right to left.	77
3.11	Relative contribution of an individual cell quantity to wall heat flux for (a) temperature, (b) pressure, (c) water vapor, and (d) carbon dioxide. Flow is from right to left.	81
3.12	Relative contribution of an individual cell quantity to wall heat flux for partial pressure of (a) hydroxyl radical, (b) carbon monoxide, and (c) methane. Flow is from right to left.	83
3.13	Net volumetric radiative heating for (a) absorbing non-emitting (cold), (b) blackbody, (c) half-emissive, and (d) completely reflective boundary conditions. Flow is from right to left.	89
3.14	Net heat flux for (a) absorbing non-emitting (cold), (b) blackbody, (c) half-emissive, and (d) completely reflective boundary conditions. Flow is from right to left.	91
3.15	Path traces of a highly entrained stream-trace (green), mildly entrained stream-trace (red), and un-entrained stream-trace (blue). Flow is from right to left.	93
3.16	Temperature loss ($-\Delta T$) vs. residence time (τ) along stream-traces for radiative outflow, blackbody, half-black half-reflective, and reflective conditions.	94
4.1	Spectrally resolved radiative heat flux of water vapor for the high-fidelity spectral ($\Delta\nu = 0.01 \text{ cm}^{-1}$) model (solid line) and a low-fidelity spectral ($\Delta\nu = 25 \text{ cm}^{-1}$) one-point c-k model (dashed line). Differences are displayed (dash-dot line). All simulations have a one-dimensional path of 0.10 m, at a partial pressure of 0.1 atm (10.133 kPa). Temperatures are at (a) 500 K, (b) 1000 K, (c) 1500 K, (d) 2000 K, (e) 2500 K, and (f) 3000 K.	104

4.2	Spectrally resolved radiative heat flux of water vapor for the high-fidelity spectral ($\Delta\nu = 0.01 \text{ cm}^{-1}$) model (solid line) and a low-fidelity spectral ($\Delta\nu = 25 \text{ cm}^{-1}$) two-point c-k model (dashed line). Differences are displayed (dash-dot line). All simulations have a one-dimensional path of 0.10 m, at a partial pressure of 0.1 atm (10.133 kPa). Temperatures are at (a) 500 K, (b) 1000 K, (c) 1500 K, (d) 2000 K, (e) 2500 K, and (f) 3000 K.	106
4.3	Spectrally resolved radiative heat flux of water vapor for the high-fidelity spectral ($\Delta\nu = 0.01 \text{ cm}^{-1}$) model (solid line) and a low-fidelity spectral ($\Delta\nu = 25 \text{ cm}^{-1}$) two-point model (dashed line) over four, 0.10 m layers with temperatures of 500, 1500, 2000, and 2500 K. The partial pressure is 0.1 atm (10.133 kPa) over the one-dimensional path. Radiative wall heat flux differences are given for each simulation (dash-dot line).	107
4.4	Spectrally resolved radiative heat flux for the high-fidelity spectral ($\Delta\nu = 0.01 \text{ cm}^{-1}$) model (solid line) and a low-fidelity spectral ($\Delta\nu = 25 \text{ cm}^{-1}$) two-point model (dashed line) over four 0.10 m layers with species of water vapor, carbon dioxide, carbon monoxide, and the hydroxyl radical, respectively. The partial pressure is 0.1 atm (10.133 kPa) over the entire one-dimensional path. Radiative wall heat flux differences are given for each simulation (dash-dot line). Temperatures are (a) 500 K, (b) 1000 K, (c) 1500 K, (d) 2000 K, (e) 2500 K, and (f) 3000 K	109
4.5	Radiative wall heat flux for a water vapor simulation of the HIFiRE-2 combustion chamber. Solutions from (a) the IMC method and (b) the DOM on identical grids. Flow is from right to left.	116
4.6	Relative error of a radiative simulation of the HIFiRE-2 combustion chamber for water vapor. (a) The relative change between the base level high-spectral-resolution IMC simulation and the low-spectral-resolution DOM simulation. (b) The error estimated with the low-spectral-resolution DOM error tables. (c) The ratio of the error estimated with DOM error tables to the actual error computed from the high-spectral-resolution IMC simulation. Flow is from right to left.	118
4.7	Locations of sample points in the HIFiRE-2 combustion chamber corresponding to Table 4.2. Sample points are denoted by red dots. Flow is from right to left	119

4.8	DOM solutions for fine spatial sampling with an S_8 angular quadrature scheme comparing the radiative wall heat fluxes for (a) the fine and (b) the coarse CFD sampling meshes. The relative difference between the simulations is given in (c), in which the difference between the two simulations is normalized by the values from the fine grid sampling. Flow is from right to left.	125
4.9	DOM solutions for fine grids and an S_8 angular quadrature scheme comparing the radiative wall heat fluxes for (a) the fine and (b) the coarse CFD sampling meshes. The relative difference between the simulations is given in (c) and is normalized by the fine grid sampling values. Flow is from right to left.	126
4.10	DOM solutions for coarse CFD sampling mesh and an S_8 quadrature scheme comparing the radiative wall heat fluxes for (a) the fine and (b) the coarse spatial radiative meshes. The relative difference between the simulations is given in (c) and is normalized by the fine grid sampling values. Flow is from right to left.	130
4.11	DOM solutions for coarse CFD sampling mesh and an S_8 quadrature scheme comparing the spectral error predictions for (a) the fine and (b) the coarse spatial radiative meshes. The relative difference between the simulations is given in (c) and is normalized by the fine grid sampling values. Flow is from right to left.	131
4.12	DOM solutions for a coarse grid comparing the radiative wall heat flux for (a) the S_8 quadrature scheme and (b) the S_6 quadrature scheme. The relative difference between the simulations is given in (c) with and is normalized by the S_8 quadrature scheme values. Flow is from right to left	134
4.13	DOM solutions for a coarse grid comparing the spectral error predictions for (a) the S_8 quadrature scheme and (b) the S_6 quadrature scheme. The relative difference between the simulations is given in (c) with and is normalized by the S_8 quadrature scheme values. Flow is from right to left	135
4.14	Location of the emission photodetectors with respect to the exit of the combustor shown in yellow. Flow is out of the page. Associated angular widths given for each detector in degrees. Image courtesy of Michael Brown at the AFRL.	139

4.15	Comparison of the net radiative heat flux to the wall at the experimental exhaust port. Experimental results presented with experimental measurement uncertainty. RT simulations presented with computational uncertainty predictions.	140
4.16	Exit plane profiles for a CFD RANS simulation of the HDCR experiments for (a) temperature and (b) water vapor mole fraction. Flow is out of the page.	143
4.17	Exit plane profiles measured from the HDCR experiments for (a) temperature and (b) water vapor mole fraction. Flow is out of the page. Images courtesy of Michael Brown at the AFRL [8].	144
5.1	Flow temperature, for LES flowfield snapshots of the HDCR (a and b) and time-averaged LES flowfield (c). Flow is from right to left. .	152
5.2	Flow temperature at the HDCR exit plane, for various LES flowfield snapshots (a - c) and time-averaged LES flowfield (d).	153
5.3	Flow water vapor mole fraction at the HDCR exit plane, for various LES flowfield snapshots (a - c) and time-averaged LES flowfield (d).	154
5.4	Radiative wall heat flux profiles for non-radiative outflow walls, for various LES flowfield snapshots (a-c) and time-averaged LES flowfield (d). Flow is from right to left.	156
5.5	Histograms of the spectrally integrated spatially averaged heat fluxes, for various LES flowfield snapshots. Locations are for (a) the back of the flame holding cavity, (b) the sidewall near flame holding cavity, (c) the sidewall near the flowfield exit, and (d) the top wall near the flowfield exit.	158
5.6	HIFiRE-2 wall areas used for spatial averaging of radiative heat flux in the histograms of Fig. 5.5	159
5.7	Probability of individual LES flowfield snapshots	160
5.8	Cumulative distribution function of the spectrally integrated spatially averaged heat fluxes, for various LES flowfield snapshots. Locations are for (a) the back of the flame holding cavity, (b) the sidewall near flame holding cavity, (c) the sidewall near the flowfield exit, and (d) the top wall near the flowfield exit. Wall boundary conditions are radiative outflows.	163

5.9	Combined epistemic uncertainties for radiative wall flux using strictly wall outflow boundary conditions. Uncertainties are for (a) upper uncertainty limit and (b) lower limit uncertainties relative to LES time-averaged nominal condition.	165
5.10	Cumulative distribution function of the spectrally integrated spatially averaged heat fluxes, for various LES flowfield snapshots. Locations are for (a) the back of the flame holding cavity, (b) the sidewall near flame holding cavity, (c) the sidewall near the flowfield exit, and (d) the top wall near the flowfield exit. Three boundary conditions are given along with a spectral perturbation comparison.	169
5.11	Radiative wall heat fluxes for a single LES flowfield snapshot with (a) radiative outflow, (b) time-resolved blackbody and (c) time-averaged blackbody radiative wall conditions.	171
5.12	Predicted radiative temperature loss versus residence time for various streamtraces with radiative outflow boundary conditions. The minimum, maximum, and mean values based on multiple flowfield snapshots are given.	172
5.13	Cumulative distribution functions over a range of flowfield snapshots for streamtraces with residence times of (a) 0.6, (b) 3.3, (c) 1.1, and (d) 17.7 ms. The ranges due to spectral modeling and numerical grid uncertainty are presented for simulations with various physical wall boundary conditions. Simulations corresponding to a time-averaged, steady-state flow are given with black vertical bars.	174
5.14	Normalized probability density functions over a range of flowfield snapshots for streamtraces with residence times of (a) 0.6, (b) 3.3, (c) 1.1, and (d) 17.7 ms. The combined epistemic and aleatory uncertainties are presented for all factors. Simulations corresponding to outflow boundary conditions.	176
5.15	Comparison of the net radiative heat flux to the wall at the experimental exhaust port. Nominal values of different CFD modeling predictions are given in (a), RT simulations presented with computational uncertainty predictions in (b) for time-averaged LES flowfield and averaged radiative heat flux of LES flowfield snapshots. Experimental results presented with experimental measurement uncertainty.	179
A.1	Optical path of laser beam to photodetector, passing through a collimating lens and neutral-density filter.	202

A.2	Layout of photodetector of radius r and laser beam or half-width w offset by distance x_0	205
A.3	Normalized incident power on a photodetectors vs. beam position for multiple beam widths for numerical data (black/thin) and experimental data (colored/thick). Numerical predictions correspond to a radius of a) 1.13 mm and b) 1.15 mm	211
A.4	Normalized incident power on a photodetectors vs. beam position. Experimental data for multiple detectors given by symbols. Numerical predictions for multiple beam widths given by curves for a photodetector radius of (a) 1.13 mm and (b) 1.15 mm	212

LIST OF TABLES

Table

2.1	Position and field of view of photodetectors at the exhaust port . . .	50
3.1	Comparison of convective and radiative heat fluxes using the 1D DOM and the 3D RT methods at the lower wall ($y=0.0$ mm)	69
3.2	Comparison of variation between data from Nelson [77]. and the HyShot-II test cases. The temperature, pressure, and mole fraction quantities for the HyShot simulation are averages. The quantities for the Nelson cases are uniform throughout the flow domain.	73
3.3	Comparison of variation between data from Nelson [77]. and current the one-dimensional approximations of the flowfields presented in this work.	73
3.4	Cell averaged contribution to wall averaged heat flux for each flow quantity	78
3.5	Comparison of the Planck Mean function of several major flow species at various temperature as calculated from the HITEMP 2010 Database [92]. CH_3 and C_2H_4 not present in the database.	86
4.1	Errors associated with simplified two-point c-k model vs LBL at various temperatures. All species partial pressures are 0.10 atm. All path lengths are 0.10 m.	108
4.2	Radiative heat flux evaluated at different wall locations for the HIFiRE-2 test case. The two methods employed are a high-fidelity spectral IMC model F_{IMC} and a RT method with a banded spectral model F_{RT1} . The spectral error is estimated using a perturbed banded spectral model F_{RT2} . The estimated error from the perturbed RT model and the actual error from the IMC are given.	120

4.3	Radiative heat flux evaluated at different wall locations for the HIFiRE-2 test case. The two methods employed are the RT method (F_{RT}) and the DOM with a banded spectral model (F_{DOM}). The fine and coarse spatial radiative meshes for the DOM are denoted by “1” and “2,” respectively. The relative difference in radiative wall heat flux is given and normalized by the radiative wall heat flux from the RT simulations.	138
A.1	Nominal and upper and lower bound of measured variables	207
A.2	Possible limits of known gain functions with raw signal responses for each sensor.	208
A.3	Radiative Power Values to the Photodetectors During the Experiment.	209
A.4	Radiative Heat Flux Predictions to the wall during experiments. . .	210
B.1	Statistics of error predictor $E_{\nu 2}$ for water vapor at a partial pressure 1 atm (101.325 kPa) for various path lengths and temperatures. . .	214
B.2	Statistics of error predictor $E_{\nu 2}$ for carbon dioxide at a partial pressure 1 atm (101.325 kPa) for various path lengths and temperatures.	215
B.3	Statistics of error predictor $E_{\nu 2}$ for the hydroxyl radical at a partial pressure 1 atm (101.325 kPa) for various path lengths and temperatures.	216
B.4	Statistics of error predictor $E_{\nu 2}$ for carbon monoxide at a partial pressure 1 atm (101.325 kPa) for various path lengths and temperatures.	217
B.5	Statistics of error predictor $E_{\nu 2}$ for methane at a partial pressure of 1 atm (101.325 kPa) for various path lengths and temperatures. . .	218

LIST OF APPENDICES

Appendix

A. Photodetector Calibration 200

B. Spectral Model Error Statistics 213

LIST OF ABBREVIATIONS

AFRL	Air Force Research Laboratory
AHSTF	Arc-Heated Scramjet Test Facility
CDF	Cumulative Distribution Function
CFD	Computational Fluid Dynamics
c-k	correlated-k
DOM	Discrete Ordinates Method
DLR	Deutsches Zentrum für Luft- und Raumfahrt
DTSO	Defense Science and Technology Organization
FSCK	Full Spectrum Correlated-k
IMC	Implicit Monte Carlo
IR	Infra-Red
LBL	Line By Line
LES	Large Eddy Simulation
GRASP	General Radiation Simulation Program
HIFiRE	Hypersonic International Flight Research Experimentation
HDCR	HIFiRE Direct Connect Rig
HEG	High Enthalpy Shock Tunnel Goettingen
NASA	National Aeronautics and Space Administration
PDF	Probability Density Function
POD	Proper Orthogonal Decomposition

RANS Reynolds Average Navier-Stokes

RMS Root Mean Square

ROM Reduced Order Model

RTE Radiative Transfer Equation

RT Ray Tracing

SNB Statistical Narrow Band

WSGG Weighted Sum of Gray Gas

LIST OF SYMBOLS

A	Radiative Transfer Equation Linear Operator Matrix	
a	Cell Face Area Vector	[m ²]
B_ν	Frequency Specific Blackbody Intensity	[W/(m ² Hz Sr)]
C	Cumulative Distribution Function	
c	Speed of Light	[m/s]
c_1	Tuning Parameter	
c_p	Constant Pressure Specific Heat	[J/(kg K)]
c_v	Constant Volume Specific Heat	[J/(kg K)]
E	Frequency Integrated Combined Uncertainty Estimation	
E_ν	Intensity Error Estimation	
$E_{\nu 1}$	Experimental Error Estimation	
$E_{\nu 2}$	Modeling Error Estimation	
F	Spectrally Integrated Heat Flux	[W/m ²]
F'	Secondary Spectrally Integrated Heat Flux	[W/m ²]
F_{max}	Maximum Spectrally Integrated Heat Flux	[W/m ²]
F_ν	Frequency Specific Heat Flux	[W/m ²]
f_ν	Scattering Redistribution Function	
g	Quadrature Weight	
g_E	Earth Surface Gravity	[m/s ²]
H	Volumetric Heating	[W/m ³]
h	Planck's Constant	[J/ Hz]
I	Intensity	[W/(m ² Sr)]
I_{sp}	Specific Impulse	[s]
I_ν	Frequency Specific Intensity	[W/(m ² Hz Sr)]
i	Location Index	
j	Ordinate Index	
k	Frequency Index	
k_b	Boltzmann's Constant	[J/K]
l	Quadrature Index	
Ma	Mach Number	
m	Cell Face Index	
n	Flow Quantitiy Index	
n'	Maximum Time-step Index	

N_{band}	Number of Frequency Bands	
N_{cell}	Number of Cells	
N_{face}	Number of Cell Faces	
N_{mod}	Number of Flowfield Snapshots	
N_{ord}	Number of Ordinates	
N_{quad}	Number of Quadrature Points	
N_{spec}	Number of Radiative Species	
P	Pressure	[Pa]
\dot{p}	Thrust	[N]
Q	Radiative Intensity Source Vector	[W/(m ² Hz Sr)]
R	Gas Constant	[J/(kg K)]
R_I	Residual Intensity Matrix	[W/(m ² Hz Sr)]
S	Entropy	[J/(kg K)]
S_ν	Frequency Specific Species Absorptivity	[1/m]
r_ν	Frequency Specific Reflectivity	
s	Path Location	[m]
s_{wall}	Wall Location	[m]
T	Temperature	[K]
t	Time-step Index	
t_n	Time-step Index for Specific Flow Quantity	
t'	Secondary Time-Step Index	
u	Cell Quantity	
\bar{u}	Normalized Cell Quantity	
u_{rms}	Root Mean Square Cell Quantity	
V	Cell Volume	[m ³]
\dot{w}	Mass Rate of Fuel	[kg/s]
X	Mole Fraction	
x	Location	[m]
y	Location	[m]
z	Location	[m]
Greek		
γ	Ratio of Specific Heats	
ϵ_ν	Frequency Specific Emissivity	
θ	Azimuthal Angle	[rad]
θ'	Secondary Azimuthal Angle	[rad]
κ_{abs}	Absorption Coefficient	[1/m]
$\bar{\kappa}_{abs}$	Frequency Averaged Absorption Coefficient	[1/m]
κ_{eff}	Effective Band Absorption Coefficient	[1/m]
κ_{high}	Maximum Band Absorption Coefficient	[1/m]
κ_{low}	Minimum Band Absorption Coefficient	[1/m]
κ_{sca}	Scattering Coefficient [1/m]	
μ	Ordinate Angle Factor Relative to Path	[(cos(ϕ))]
μ'	Secondary Ordinate Angle Factor Relative to Path	[(cos(ϕ'))]
ν	Frequency	[Hz]
ν_{max}	Maximum Band Frequency	[Hz]

ν_{min}	Minimum Band Frequency	[Hz]
ξ	Number Density	[mole/m ³]
ξ_n	Normalized Number Density	
π	Geometric Constant	
ρ	Density	[kg/m ³]
σ_ν	Frequency Specific Scattering Coefficient	[1/m]
τ	Time	[s]
Φ	Probability Density Function	
$\bar{\Phi}$	Normalized Probability Density Function	
ϕ	Vertical Angle	[rad]
ϕ'	Secondary Vertical Angle	[rad]
Ψ	Adjoint Matrix	[Sr Hz]

ABSTRACT

Computational Uncertainty Quantification of Thermal Radiation in Supersonic
Combustion Chambers

by

Andrew J. Crow

Chair: Iain D. Boyd

The scramjet engine is an air-breathing jet propulsion system for hypersonic vehicles. Currently, the scramjet exists at an experimental development stage, with numerous physical phenomena necessary for the prediction of flight behavior still uncharacterized. Thermal radiation is predicted to significantly affect the thermal management of scramjet engines, but it is difficult to completely characterize through measurements in experiments and, therefore, requires the use of computational modeling.

Two scramjet engines, the HyShot-II and HIFiRE-2 combustors, are simulated with radiative heat transfer approaches using the Ray Tracing and Discrete Ordinates Methods. The computational predictions characterize the thermal radiative heat transfer of the scramjet engines, and the numerical simulations are, themselves, characterized for the uncertainties in their predictions. Radiative wall heating and flow cooling are studied as the direct effects of thermal radiative heat transfer.

The realistic variation in the predictions of thermal radiation, known as computational uncertainty, is effected by a lack of numerical modeling convergence and numerical modeling truncations, as well as by a lack of knowledge of the scramjet

flowfield parameters, spectral modeling parameters, and radiative boundary conditions. The factors of uncertainty are quantified in individual as well as ensemble investigations of the radiative heat flux uncertainty.

Experimental measurements of thermal radiation within a scramjet allow for a direct comparison to the computational predictions. The measurements are conducted for the HIFiRE-2 scramjet using a series of photodetectors whose fields of view can be directly modeled with a Ray Tracing approach. The comparison between experimental measurement and computational predictions has a partial agreement, giving support to the validity of the computational predictions.

CHAPTER I

Introduction

“I’m afraid,” he said at last, “that the Question and the Answer are mutually exclusive. Knowledge of one logically precludes knowledge of the other. It is impossible that both can ever be known about the same Universe”...“if it happened, it seems that the Question and the Answer would just cancel each other out, and take the Universe with them, which would then be replaced by something even more bizarrely inexplicable. It is possible that this has already happened,” he added with a weak smile, “but there is a certain amount of uncertainty about it [1].”

The principle of the scramjet has been around since the 1940s and has been demonstrated in limited experiments to fill need for propulsion faster than today’s commercially available air-breathing engines and more efficient than any modern combustion based rocket [99]. However, with such a promising technology many hurdles of reliability and design remain to be overcome.

The particular challenge of the scramjet is that the operating principles require speeds far too great for any full-scale wind-tunnel test, and the associated cost of a single flight experiment greatly limits the ability to gather complete data [32, 99, 113]. Computational modeling allows for the simulations of any phenomenon at any flight conditions. The only limitations of the computational modeling is the fidelity of

the model techniques and the associated computational cost. However, the fidelity of many modeling techniques rely greatly on the particular test-cases and must be characterized for each flow regime under consideration. Even though a computational simulation gives a single, often deterministic, output for a particular quantity, the possible changes of outputs due to uncertain modeling fidelity and input parameters results in a finite range of realistic computational outputs. The characterization of this range of realistic outputs is known as “Uncertainty Quantification” [106].

The particular phenomenon of interest in the current study is the thermal radiative heat transfer in the combustion chamber of a scramjet engine. The sensitivity of the combustion processes to temperature changes, the sensitivity of the boundary layer to thermal wall changes, and the material heating limits are very high in scramjets with smaller margins of error than commercially available combustion engines. As such, the effects of radiative heat transfer, although considered small in comparison to other forms of heating, can still have a significant effect in the reliability of a scramjet engine. The main thrust of the current work is to model and characterize the limits of thermal radiation in two different scramjet combustion chambers and predict the realistic ranges of the overall radiative heating effects therein.

1.1 Project Goals

The computational analysis of a scramjet is intended by many researchers to not only optimize the design of a scramjet, but, also, predict scramjet-specific physics. Scramjet unstart is a significant issue which remains to be addressed and is being computationally investigated by a number of researchers at the Stanford PSAAP Center [113]. Unstart is the phenomenon in which the internal supersonic flow of a scramjet engine becomes stagnated and starves the engine of oxidizer, which is more rigorously described in Section 1.2.

Two major issues exist for unstart predictions. The first issue is the characteriza-

tion of the physical mechanisms that cause unstart. This issue requires a continued understanding of underlying physics within a supersonic channel, often resulting from rigorous experiment.

The second issue is that computational simulations used to predict the the unstart conditions of a Scramjet must be reliable enough to be useful as design tools. Even with the unstart conditions perfectly characterized, the uncertainty of the computational simulations still persists. The accuracy of any prediction depends on the characterization of a number of physical processes, including turbulent flow modeling, shockwave prediction, combustion modeling, and thermal management. The predictions of radiative heat transfer may play a significant role in the thermal management of a scramjet engine, which may affect turbulent physics through wall heating and combustion physics through flow cooling [20, 63, 35].

1.1.1 Uncertainty Margin

Computational reliability can be defined as the uncertainty of numerical predictions, wherein the combination of inherent modeling and convergence errors and unknown parameters produce a range of possible realistic results. Uncertainties stemming from a lack of knowledge of the system are classified as epistemic uncertainties. The uncertainties stemming from an unknowable randomness are classified as aleatory uncertainties [24, 106].

Examples of epistemic uncertainty sources are physical parameters that have exact values but rely on experimental measurements which can never be known exactly. Additionally, the modeling equations for any physical phenomena are often approximated or truncated making the exact physical model unknown. Also, the number of physical parameters and phenomena are limited through the logistics and scope of the investigation, thus limiting the accuracy of the physical models. Finally, the numerical solutions are never found to converge perfectly for a non-trivial domain,

resulting in a numerical error as well. These uncertainties must be estimated for the realistic range of errors that each parameter can produce in the simulation results. Ideally, further investigation and knowledge will drive these errors to a relative value of zero.

Examples of aleatory uncertainty sources are the unknown flow and flight conditions that may be experienced for the scramjet engine. Additionally, the domain and boundary conditions will never match nominal design criteria and may change throughout the lifetime of the engine or even over the course of a flight. These variations must be investigated to determine the limits of the effects of the possible conditions. Ideally, the range of effects can never be eliminated for a design condition, but it can be fully bounded.

The effects of these uncertainties are not always flat error bars and are often probabilistic in nature. Thus, whereas the nominal prediction may be most probable, all values are possible. The effects of all uncertainties can be combined into a total uncertainty curve. Provided that the acceptable boundaries for a phenomenon of interest are known, then the probability of a computational prediction lying on the correct side of these boundaries is known, as illustrated in Fig. 1.1 (originally published as Figure 1.5 in the thesis by Irvine) [50].

In Fig 1.1, an illustration of a nominal prediction is shown for a given set of conditions. This simulation may predict successful or unsuccessful performance of the engine, depending on where it lies within a pre-determined operation window. However, given the probabilistic nature of the computational uncertainty, there is always a possibility that the simulation has predicted that it is operating in the inaccurate regime. The goal of uncertainty quantification is to understand the overall system and to use numerical simulations to predict the operating and design points of the system that maximize the probability that the system will perform in the intended regime [113]. The current work looks specifically at the uncertainty quantification as

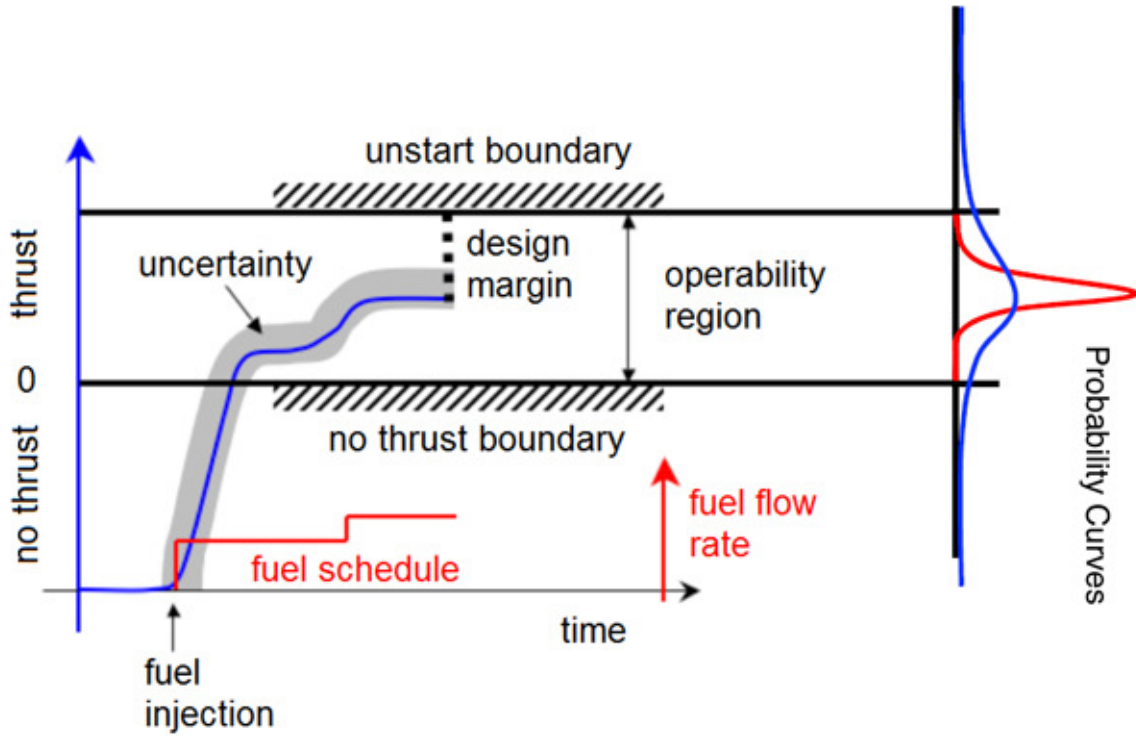


Figure 1.1: Diagram of the Stanford PSAAP project goals of predicting probabilistic uncertainty for different design criteria [50].

it pertains to the simulation of thermal radiation in scramjet combustion chambers.

1.1.2 Thesis Outline

The thesis is divided into six chapters. The goal of the project is to process a number of CFD simulations of scramjet combustors, then predict the radiative heat flux effects and the associated uncertainty of the simulations. In order to accomplish such a goal, the methodologies are laid out, the importance of different modeling parameters are established, the accuracy of the models is investigated, and the overall variation in the predictions is bounded through a rigorous series of simulations.

The remainder of Chapter I discusses the operating principles of the scramjet combustion engine and background of the test cases considered in the current work. Also, included is an overview of the principles used for thermal radiative modeling

and a history of radiative modeling as it has been applied to scramjet combustion chambers.

Chapter II covers the methodology of the project. The goal of the methodology is to establish a mathematical basis for the following topics: radiative modeling, spectral modeling, sensitivity analysis, probability analysis, computational fluid modeling, and experimental comparisons. The mathematical formula for radiative modeling is presented with the Radiative Transfer Equation. More specifically, the procedures for the Discrete Ordinates Method (DOM) and Ray Tracing (RT) methods are introduced. The methodology for spectral modeling is discussed within a mathematical framework, and the procedures are given for creating the band models employed. Additionally, methodologies are developed for predicting the sensitivity of radiative heat transfer to flowfield quantities through an adjoint sensitivity analysis. The means of estimating uncertainty is presented through the establishment of parameter variation and comparing Cumulative Distribution Function (CDF) curves. The methodology for establishing the initial scramjet flowfields, which are employed as inputs to all radiative analysis are discussed, and the procedure for validating the radiative predictions through experimental measurements is presented.

Chapter III establishes the importance of different parameters and sensitivities in the radiative simulations. The initial flowfields for the two test cases of interest are processed with radiative heat flux codes. Geometric approximations such as dimensionality and domain size are examined for their effects on physical simulation accuracy. A procedure for determining the absolute contribution of a flowfield quantity to radiative heat flux is established, and a selection is made as to which radiative species are included in the radiative model and which flow quantities are to be used as characteristic parameters of flowfield simulations. Finally, a methodology for estimating the flow cooling effects for thermal radiation is established, and the effects of boundary conditions on radiative wall heating and radiative flow cooling are

investigated.

Chapter IV establishes the accuracies and uncertainties of both the computational and numerical models employed in the current investigation. The exact parameters for the spectral model are established, and procedures of estimating their uncertainty in various radiative simulations is presented. The accuracy of radiative simulations with respect to refinement of the numerical domain is investigated. From the numerical investigation, decisions are made as to the size of the numerical domain required as well as estimations of the associated uncertainty parameters. Finally, predictions are compared to laboratory experiments to establish partial validation of the computational modeling procedures.

Chapter V investigates the combined effects of all the uncertainties and variations established in the preceding chapters. Additionally, new variations coming from the unsteady nature of the turbulent flows are considered. The combined uncertainties are investigated for radiative wall heating and flow cooling for the established spectral model and a variety of boundary conditions. The overall uncertainties are translated into probability functions for both the wall heating and flow cooling predicted by the radiative simulations. Finally, the experimental validation is revisited with a more rigorous investigation.

Chapter VI revisits the main points of the investigation. The main conclusions are summarized and placed into the context of a larger scientific investigation. Future lines of investigation are proposed to expand on the current work, and issues to be revisited at a later time are listed for the current work.

Finally, Appendix A gives the procedure for calibration of the experimental measurements employed in the current work. Appendix B gives tabulated numerical statistics on the spectral model employed.

1.2 The Scramjet

The main principle of the scramjet is based around the compressive shockwaves that form around a supersonic vehicle as given in Eq. 1.1 and illustrated for air in Fig. 1.2 (a) [3]. In Eq. 1.1, “ Ma_1 ” is the freestream Mach number, “ P_1 ” is the freestream density, “ P_2 ” is the internal density, and, “ γ ” is the ratio of specific heats. If a vehicle is moving at a high enough velocity, then a turbine powered compressor is not necessary to condition the incoming air-stream for combustion. If the compressive shock is strong enough to reduce the incoming airflow to a subsonic regime, then the system is known as a ramjet. These engines have been demonstrated to sustain velocities from Mach 3 through 5 [32].

$$\frac{P_2}{P_1} = 1 + \frac{2\gamma}{\gamma + 1}(Ma_1^2 - 1) \quad (1.1)$$

However, the introduction of a compressive shockwave introduces a large amount of entropy into the system, as given by Eq. 1.2 and illustrated for air in Fig. 1.2 (b) [12]. In Eq. 1.2, “ ΔS ” is the entropy generated across the shock for an idea gas, “ c_v ” is the constant volume specific heat, “ R ” is the gas constant, “ T_1 ” is the freestream temperature, and “ T_2 ” is the combustion chamber temperature. The ratio for temperatures across the shock is determined by Eq. 1.3 and is illustrated for air in Fig. 1.2 (a) [3]. As the freestream Mach number, “ Ma_1 ,” increases, the compression from the shockwaves increase, resulting in a larger amount of incoming flow energy being rendered unusable for propulsion. A means of decreasing the entropy generation is to decrease the compression inside of the combustion chamber, thus increasing the internal velocity to a supersonic state, producing a supersonic combustion ramjet, “Scramjet.”

$$\Delta S = c_p \ln \frac{T_2}{T_1} - R \ln \frac{P_2}{P_1} \quad (1.2)$$

$$\frac{T_2}{T_1} = \left[1 + \frac{2\gamma}{\gamma + 1}(Ma_1^2 - 1) \right] \frac{2 + (\gamma - 1)Ma_1^2}{(\gamma + 1)Ma_1^2} \quad (1.3)$$

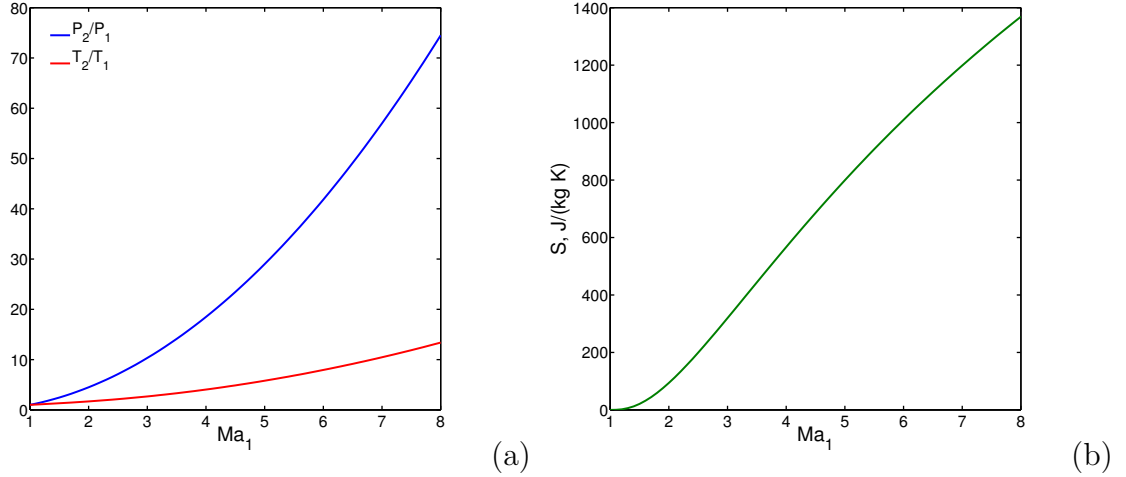


Figure 1.2: Diagram of shock jump properties for air over a range of Mach numbers. Pressure and temperature ratios are presented in (a), and entropy generation is presented in (b)

A diagram of a generic scramjet is given in Fig. 1.3. The scramjet functions over a range of freestream Mach numbers from 5 to 14 [32]. The principle relies on the vehicle itself working as part of the compressor as the initial bow-shock compresses the flow. The flow is further compressed at the inlet of the combustion chamber as the geometry creates an additional series of shockwaves. The series of shockwaves must be strong enough to compress the flow for combustion as given in Eq. 1.1 but not strong enough to generate an excess of entropy as given in Eq. 1.2. The compressed flow has fuel directly injected into the stream, and combustion takes place as the flow passes through the combustion chamber at supersonic velocities. The combustion is intended to be completed before the supersonic expansion nozzle, which accelerates the flow to a hypersonic velocity, providing a net thrust on the system.

The main advantage of the scramjet is that it is a hypersonic air-breathing engine. As shown in Fig. 1.4, the scramjet can produce thrust at a Mach number higher than

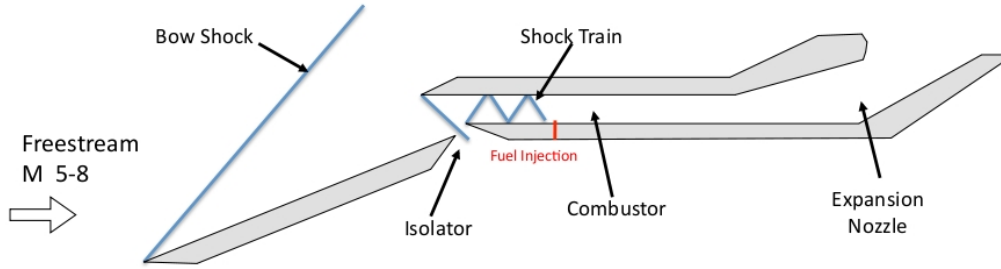


Figure 1.3: Diagram of a generic Scramjet. Hypersonic, free-stream air is compressed by the vehicle bow-shock, and funneled into the engine inlet. The air-stream is further compressed by a shock-train, and fuel is injected. The fuel is ignited in the combustion chamber, and thrust is generated at the exit nozzle. Flow is from left to right.

conventional turbo-machinery due to its lack of moving parts and ramjets due to its faster internal stream. Figure 1.4 is originally published as Fig. 2 in the paper by Smart [99]. The specific impulse, “ I_{sp} ,” of a scramjet is a measure of fuel efficiency, which is calculated as the amount of thrust, “ \dot{p} ,” garnered per unit mass fuel rate, “ \dot{w} ,” (often divided by Earth surface gravity, “ g_E ”) as given in equation 1.4.

$$I_{sp} = \frac{\dot{p}}{g_E \dot{w}} \quad (1.4)$$

The specific impulse is directly related to the amount of air passing through the engine [32]. As such, lower-speed, higher volumetric flow rate engines tend to have the highest efficiency. Rockets, are the least efficient jet propulsion system, as they take in no external air, and they must rely on the mass of the internal fuel and oxidizer as propellant. Rockets do have the advantage of a constant specific impulse as their Mach number does not affect their combustion processes, and they are able to operate over ranges of conditions that would starve an air-breathing engine of oxidizer.

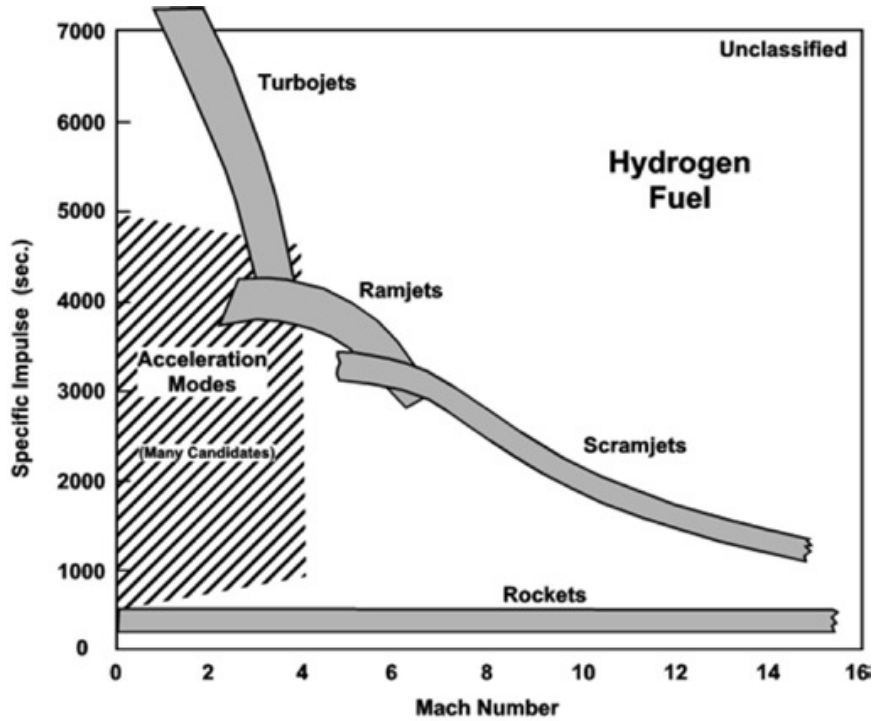


Figure 1.4: Diagram of efficiency in specific impulse vs. Mach number for various jet propulsion engines [99].

1.2.1 History and Current State

The scramjet was first theorized in the 1940s and first received combustion investigations in 1965 [99]. Since then, a significant number of wind-tunnel tests have been performed for scramjets, mostly at and on the behalf of NASA Langley Research Center [11, 99]. Although the D-21 probe and SR-71 had success as ramjet powered vehicles, no scramjet has been flown except as a scientific experiment [32]. In the modern era, a handful of experimental hypersonic scramjets have been flown for either sustained flight or sounding rocket experiments. Additionally, ongoing ground experiments and modeling support these tests. This section briefly discusses some of the free flight experiments. However, the main focus of this work is a pair of sounding rocket experiments and their associated support work. For a comprehensive overview of the scramjet, consult the works by Fry or Smart [32, 99].

Possibly, the most successful scramjet vehicle was developed in the NASA Hyper-X program, which is a self contained scramjet flight vehicle launched in 2004 [25, 32]. The vehicle flight tests demonstrated the performance ability of a scramjet to accelerate to and sustain flight speeds of Mach 7 and Mach 10, as powered by a hydrogen fueled scramjet combustor. However, not all flight tests have been as successful or sustainable. The X-51A was intended to demonstrate capability of a hydrocarbon-fueled hypersonic scramjet-power vehicle [40]. The X-51A was planned to have a self-propelled flight time of ten minutes, but it failed due to a loss of a control fin partially through flight testing [2]. With the large cost of sustainable flight experiments, such failures can cause substantial setbacks in research. As such, a series smaller scale characterization flights are more effective for fully understanding the operating conditions of a scramjet engine.

The two characterization flights discussed in this work are the HyShot-II flight experiment and the HIFiRE-2 flight experiment [6, 51]. Both experiments are scramjet engine combustors propelled to hypersonic velocities on sounding rockets. The combustors produced no net positive thrust, as they were strictly intended to gather data on the internal physics of supersonic combustion chamber during flight. Both flight tests have extensive ground experimental and computational simulation support.

1.2.2 HyShot-II Experiment

The HyShot-II combustor experiment was a hypersonic flight test of a scramjet performed by the University of Queensland in 2003 [99]. The experiment consisted of a combustor launched on the front of a sounding rocket in order to achieve a high-altitude hypersonic velocity flight. The engine burned a hydrogen fuel over a range of freestream Mach numbers from 6.6 to 7.4 over altitudes from 167 km to 23 km before returning to the ground.

A layout of the combustor is given in Fig. 1.5, and a diagram of the interior is

given in Fig 1.6. The cross-section of the combustion chamber is 75 mm wide and 9.8 mm high, making it a relatively small flight experiment, but it is able to be placed inside of wind tunnels. Further diagrams are provided in Section 3.1. The path of the air-stream is similar to that described in Section 1.2, in which the incoming air freestream is compressed by the bow-shock and a series of internal shockwaves. The hydrogen fuel is then injected perpendicular to the flow, and it is burned throughout the chamber before exiting through an expansion nozzle.

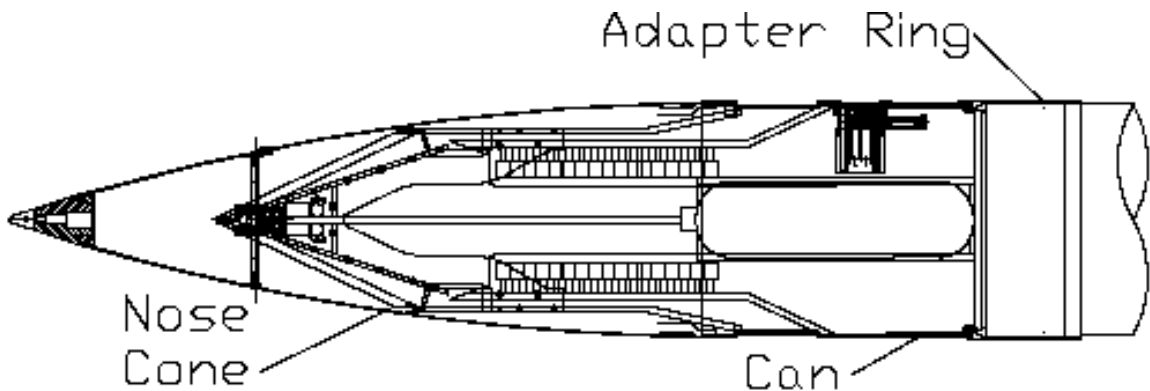


Figure 1.5: Diagram of the HyShot-II combustor [5]. Flow is from left to right.

The flight, although successful, was limited to a single experiment, and thus requires additionally modeling and support to fully understand. The researchers at the University of Queensland have performed numerical fluids modeling in support of the data analysis of the flight test to augment the understanding of the experiment [6, 5, 100]. Additionally, a number of ground experiments have been performed by the Deutsches Zentrum für Luft- und Raumfahrt (DLR) to duplicate the experiment. The particular tests are performed in the High Enthalpy Shock Tunnel Goettingen (HEG) facility at the DLR, which is a shock tube experimentation facility [33, 56, 96]. The short-run shock experiments allow for understanding of combustion physics and shockwave positioning within the combustor. In conjunction with the experiments, a number of researchers are attempting to predict phenomena within

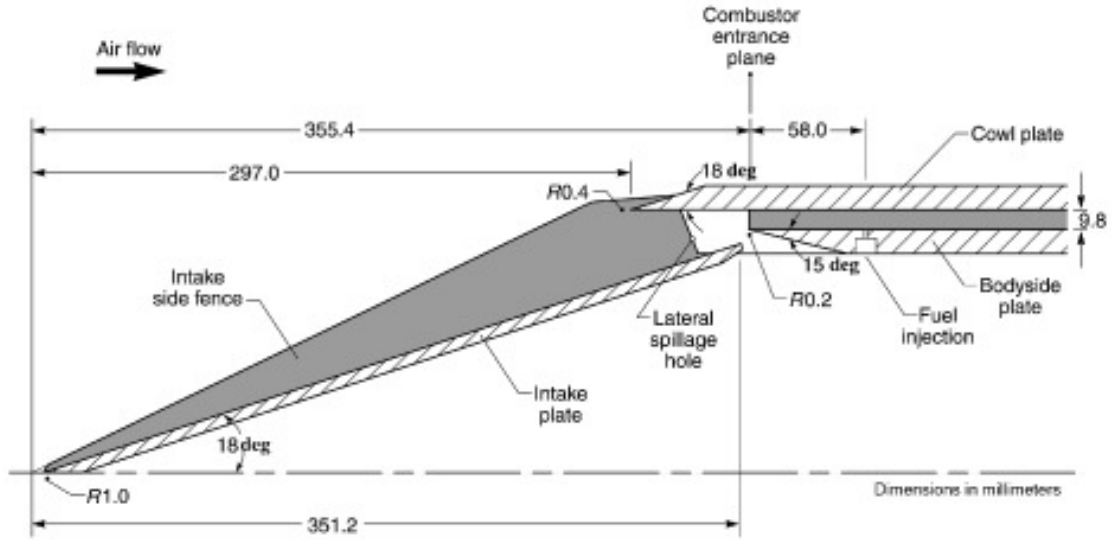


Figure 1.6: Diagram of one half of the HyShot-II ramp and inlet [100]. Flow is from left to right.

the scramjet using computational modeling as discussed in Section 2.2 [21, 49, 81]. As such, the use of the HyShot-II as an experimental testbed is lasting well beyond its initial flight test lifetime. The current work focuses briefly on the radiative aspects of the HyShot-II flight.

1.2.3 HIFiRE-2 Experiment

A substantially larger flight experiment was the Hypersonic International Flight Research Experimentation (HIFiRE)-2 flight, which is part of a series of HIFiRE flights run as a joint program among the Air Force Research Laboratory (AFRL) and the Defense Science and Technology Organization (DTSO) of Australia [51, 52]. The HIFiRE-2 is a flight test, initially intended to burn a hydrocarbon fuel in a supersonic combustion chamber at hypersonic flight conditions. Like the HyShot-II, the HIFiRE-2 experiment was launched by a sounding rocket with the intention of gathering flight data but not producing a net positive thrust. The trajectory of the experiment flown in 2012 intended to take the combustor to a velocity range from

Mach 5.5 to 8.5 over an altitude range of 60,000 to 100,000 ft for a duration of over 12 seconds [52]. A diagram of the combustion chamber is presented in Fig. 1.7, showing the flow-path, experimental hardware, and rocket mounting [51].

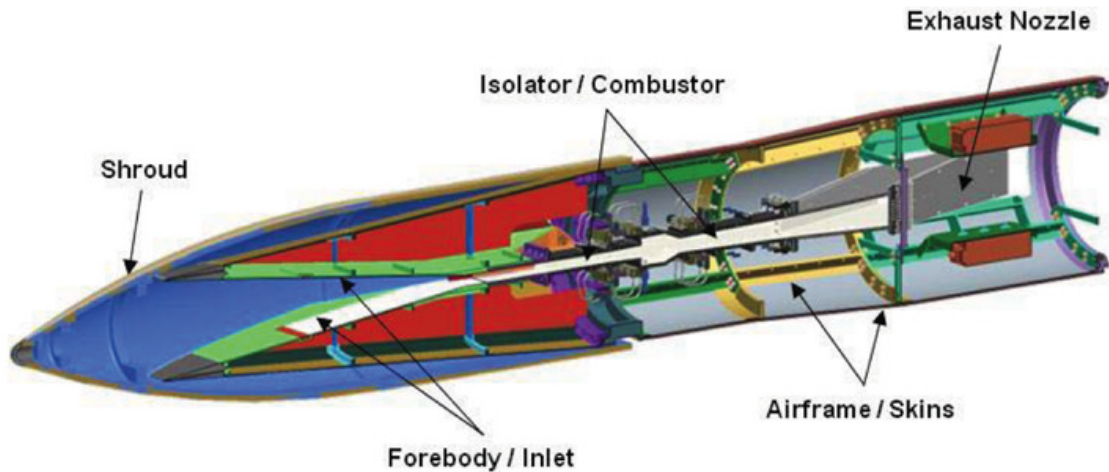


Figure 1.7: Diagram of the HIFiRE-2 combustor as mounted on the flight experiment. The shrouded is in place during launch and is ejected before the combustion experiment [51]. Flow is from left to right.

Support for the HIFiRE-2 combustor was performed in two facilities, the AFRL RC22 test facility and the NASA HIFiRE Direct Connect Rig (HDCR) [11, 39, 104]. Both facilities attempt to duplicate the HIFiRE-2 test flight for both internal Mach number and flow energy. However, the RC22 test facility has a circular cross-section, unlike the rectangular cross section of the HIFiRE-2 combustor as given in Fig 1.8.

The HDCR is an arc-heated facility, which allows for test runs of over 30 seconds, establishing steady-state test runs [11]. The arc-heated air-stream is accelerated through a facility nozzle before passing through an isolator to remove flow variation. The fuel is injected at several points in the main stream or in the flame holding cavity. The fuel under consideration is a mixture of ethylene and methane, intended to be a surrogate of cracked JP-7 [18, 80]. The flow is then ejected to an open-air exhaust port, where a series of radiative diagnostics are stationed. The HDCR has been computationally simulated at a variety of test conditions, including simulations

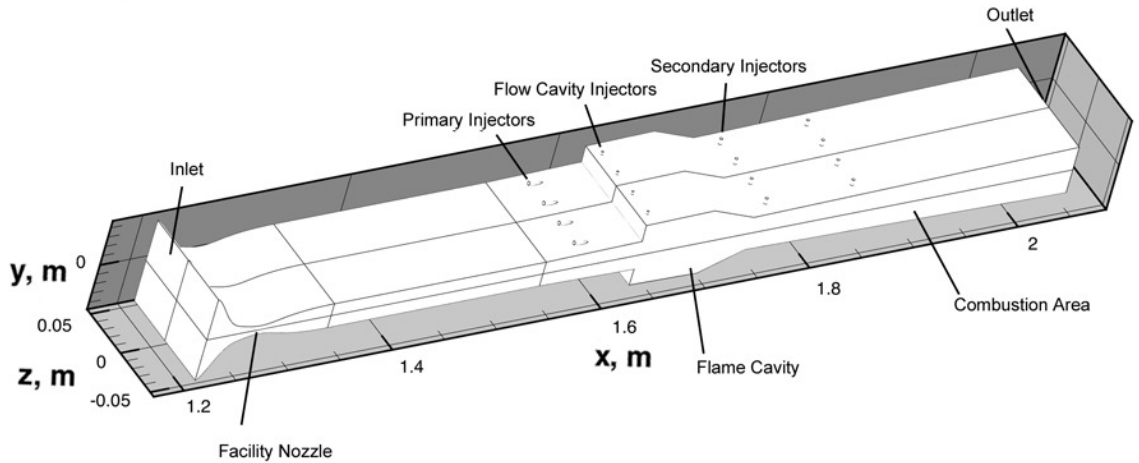


Figure 1.8: HDCR domain: Illustration of the facility nozzle, flame holding cavity, injection ports, and outlet. Flow is from left to right.

for radiative analysis [8, 20, 104]. One of the main goals of the current work is to characterize the radiative heat flux within the HDCR.

1.2.4 Challenges

Currently, one of the major challenges associated with scramjet performance is a phenomenon known as unstart, in which the inlet shock train collapses into a single, stronger shockwave [113]. This wave lowers the internal flow speed of the combustion chamber and diverts the air stream around the inlet. The resulting loss of incoming oxidizer causes the engine to stop combustion. Several phenomena in the system can cause unstart. The incoming fuel stream creates a significant choke point. Thus, excessive mass injection from the fuel stream has been demonstrated to cause unstart. Additionally, even if the fuel mass does not slow down the stream excessively, the resulting thermal injection can cause a reduction in effective internal flow area leading to unstart.

The exact causes and conditions behind unstart are under investigation by researchers for both the isolated physical phenomenon as well as for the ensemble effects

[113]. The effects of combustion completeness and heat release can cause changes in pressure rise and effective flow cross section, leading to a thermal unstart. The flow temperature plays a large role in the overall combustion rates, which can greatly affect the effective flow cross-section. The wall temperature may greatly affect boundary layer thickness, which in turn affects the shock boundary-layer interaction of the inlet shock train. Perturbations of the shock train are found to have a substantial effect on the shock train location which must be precisely metered in order to maintain a controlled scramjet environment [42].

Given the importance of thermal management in the scramjet combustor, all means of heat transfer require investigation. Radiative heat transfer has been historically left out of jet combustion chamber design considerations, as its effects are generally smaller than those of convective heat transfer [63]. As such, many of the mitigating factors applied to convective heat transfer, such as introduction of cooling air along the boundary layer, greatly outweigh the effects of radiative heat transfer. However, with scramjet performance being far more sensitive to thermal conditions and many means of thermal heat transfer mitigation being unusable in a supersonic boundary layer regime, radiative heat transfer can not be implicitly ignored. The current work looks to examine two particular test cases of scramjet combustion chambers in light of the effects of thermal radiation.

1.3 Thermal Radiation

Thermal radiation is the electromagnetic radiation coming from the local thermal energy of a material. The phenomenon was first quantified by Planck [84]. Electromagnetic energy can be modeled as either a directional electromagnetic wave or as a discrete set of photons [23, 31]. For the purpose of the current work, electromagnetic energy is described in wave terminology. The waves travel and propagate energy along all direction across the entire electromagnetic spectrum. The waves can,

additionally, interact with any medium or boundary which they contact leading to the need to model the wave with respect to all matter in the domain. The interaction of the medium with the wave greatly varies depending on the frequency of the wave, requiring extensive spectral modeling. Additionally, the spatial variation of the wave can require extensive numerical approximations in order to properly calculate.

1.3.1 Principles

Thermal radiative transfer is a specialized condition of electromagnetic energy transmission. The main principles are that the electromagnetic energy interacts with a medium based on the medium's thermal energy distribution. For this interaction to be defined, both the internal and electromagnetic energy distributions need to be defined along with a physical coupling mechanism. This coupling creates a net energy transfer out of a medium that can pass along electromagnetic waves to be absorbed elsewhere in the medium in a phenomenon known as radiative heat transfer.

For the purposes of the current work, the medium is assumed to be in local thermodynamic equilibrium adhering to an internal Boltzmann distribution [65, 84, 109]. The energy distribution relates directly to the electromagnetic spectrum through a quantization of the internal energy levels resulting in the Planck function [84]. The Planck function is strictly dependent on the temperature of the medium and is not directly affected by the electromagnetic energy distribution. For the purpose of the current investigations, the majority of the energy distribution lies within the infrared range of the electromagnetic spectrum.

The electromagnetic radiation is assumed to not necessarily be in an equilibrium state, as any location can have an intensity that varies dependent on direction and a frequency distribution not equal to that of the Planck function. The electromagnetic energy propagates as a wave through the medium, but it interacts with the medium as well.

For the purposes of thermal radiative heat transfer, the coupling of electromagnetic energy to the internal energy of the medium is made through the quantized physical structure of the medium [36]. The strength of the coupling for any one frequency is known as the linestrength, and the coupling varies based on the temperature, physical composition, motion, orientation, and phase of the medium [65]. Ongoing experiments are being performed to characterize different media for electromagnetic coupling [89, 91, 92]. The strength of the coupling determining the ability of the medium to absorb energy from the electromagnetic medium, “absorptivity,” dictates the spatial rate at which electromagnetic energy is attenuated through the medium. Additionally, the strength of the coupling determining the ability of the medium to transmit electromagnetic energy, “emissivity,” dictates the rate at which electromagnetic energy is emitted through the medium. For the purpose of the current work, the rates of absorptivity and emissivity are assumed to be identical, meaning that the net rate of energy transfer between the medium and the electromagnetic waves for any particular frequency is dependent on the linestrength multiplied by the difference between the internal and electromagnetic energy distributions. This balance is explored mathematically in Section 2.2 with the Radiative Transfer Equation (RTE). If the linestrength is infinite, then the two media are perfectly coupled resulting in the electromagnetic energy distribution being the local Planck function. This phenomenon is known as blackbody radiation. If the medium has absolutely no linestrength, then it is transparent with no interactions.

In addition to absorbing and emitting radiation, a medium can directionally redistribute electromagnetic waves through a processes known as scattering. Scattering has a variety of forms which happen above the subatomic level and do not depend on the quantum structure of the medium [65]. However, due to the nature of the media under consideration, scattering is not considered except as boundary conditions, as discussed in Section 2.2. The boundary conditions of any medium can be quite com-

plex. For the sake of the current investigation, boundary conditions are assumed to be a medium of infinite density, meaning they are assumed to have some combination of infinite absorptivity and reflectivity that allows no thermal radiation to transmit through them.

1.3.2 Spectral Modeling

The coupling of electromagnetic energy to internal thermal energy is frequency-dependent with the individual linestrengths only existing at quantized energy levels known as spectral lines [36, 65]. The individual energy levels differ for each atom, isotope, and molecule in the system, and they become active at different temperatures, leading to every particle type at every temperature (even when in thermal equilibrium) having a different spectral profile. These profiles can be very complicated, even for such simple molecules as water or carbon dioxide. As such, a means of modeling the profile is required. An example of the spectral line strength profile for carbon dioxide from the HITEMP database is given in Fig. 1.9. Figure 1.9 displays the linestrength variation through the transmissivity of carbon dioxide, as given by Figure 3 of the work by Rothman et al [91].

For a single molecule, the individual energy levels are delta functions along the electromagnetic spectrum domain. However, the effects of Doppler frequency shifting and molecular collisions serve to give each quantum energy level a range of frequencies over which it can absorb and emit electromagnetic energy. The profiles of these ranges are known as the Voigt and Doppler broadening profiles [65]. The resulting combination of billions of spectral lines, each with an associated profile, creates a very large modeling problem to determine the spectral linestrengths at any one frequency [92].

The most direct method for modeling a spectrum is the Line By Line (LBL) method, wherein the spectrum is sampled along a series of chosen frequencies, and the

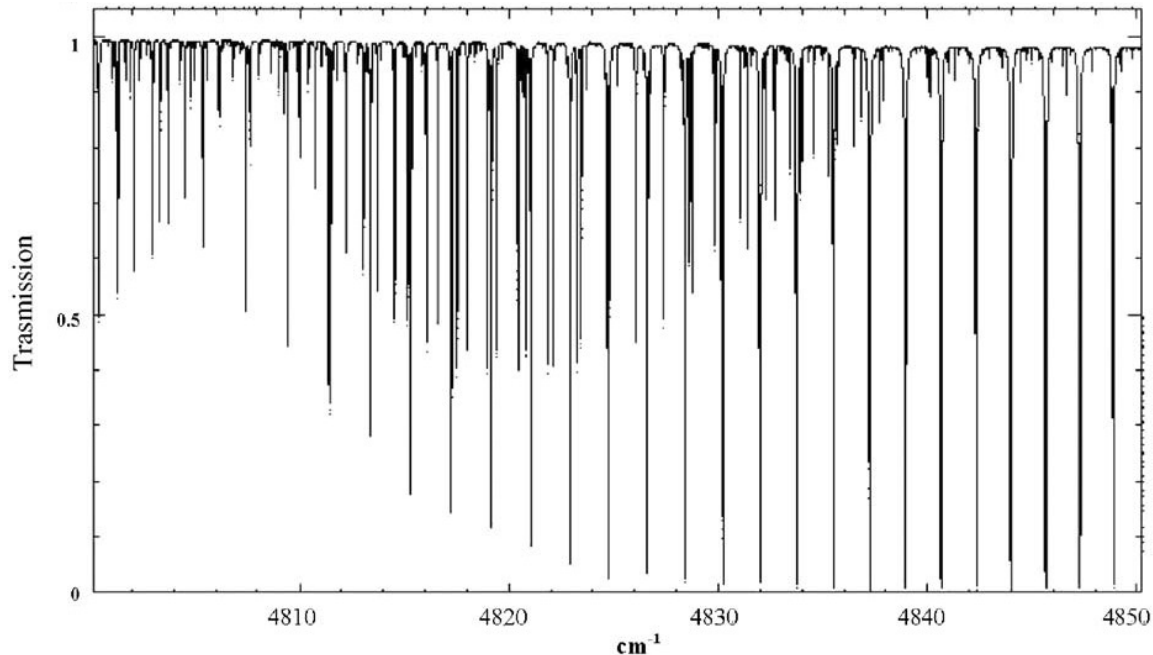


Figure 1.9: Example spectrum of the linestrength variation in a narrow spectral band of carbon dioxide [91].

spectral linestrength at each frequency is calculated as the summation of all spectral line profiles that overlap the frequency of interest (assuming Voigt and Doppler line profiles) [102, 111]. For very complicated molecules, the summation for a single point can include millions of lines and may require millions of points to properly resolve. However, an intelligent sampling of the profile can be used to generate a profile in a timely manner. These profiles can be simplified into a usable model.

Many methods of simplifying the spectrum have been proposed, ranging from highly simplistic to very complicated. The most simplistic model is a gray gas model, which assumes that the linestrength of the molecule is even across the spectrum of interest. The effects of multiple species are addressed by a linear addition of the two species linestrengths. Some improvement is made by repeating the gray gas model with multiple linestrengths and taking a weighted summation for the results. This method, known as the Weighted Sum of Gray Gas (WSGG) model, has been shown to still have errors of up to 35% in combustion simulations [83, 86, 101]. Addition-

ally, more complicated full-spectrum profiles, such as the Full Spectrum Correlated-k (FSCK) method, which apply the spectral variance linestrengths over the full spectrum, are shown to have errors of 5 to 20% in combustion simulations [79, 78, 112].

One of the issues of full-spectrum models is that the electromagnetic and internal energy distributions vary greatly over the range of frequencies of interest. An alternative is to employ a banded model. The ideal banded model divides the electromagnetic spectrum into segments of small enough ranges for which the Planck distribution and electromagnetic energy distribution are roughly invariant. The linestrength profiles, even over these small intervals, can still vary greatly and a model is required to properly account for the changes. The most promising method is the correlated-k (c-k), which uses an arbitrarily large number of quadrature-based samples to reconstruct the linestrength profile over the band of interest [76, 78, 103, 110]. For the majority of the current work, a variation on the c-k method is employed, as it is shown to have errors as low as 5% in combustion situations. A description of the procedure for calculating the spectrum is given in Section 2.2, and the results of the calculation for real gases are given in Section 4.2.

1.3.3 Computational Modeling

Even without considering the spectral modeling effects discussed in the previous section, thermal radiative modeling requires full three-dimensional accounting of all directional vectors of the thermal radiative propagation. With the consideration of a full three-dimensional domain, all methods must be discretized for both the spatial and directional components of the electromagnetic wave propagation. Numerous methods are employed for such modeling, many of which either discretize both the directional and spatial components of the electromagnetic wave, or they apply simplified models.

Given the complexity of the systems often employed, modeling simplifications can

lead to large errors in computations. As such, a varying degree of models fidelity is often employed depending on context. The Monte Carlo Ray Tracing method stochastically chooses a location and direction and propagates thermal radiation along the direction until the path reaches a point of termination [14, 30, 60, 71]. The spatial and angular fidelity of the system is considered arbitrarily high as the numerical accuracy strictly depends on the number of samples. However, due to the rigor of the method and the inherent difficulty in handling reflective surfaces, a more structured model is desired. The principle of tracing paths can be applied in a structured manner as is discussed in Section 2.2.

The Discrete Ordinates Method (DOM) was first proposed by Chandrasekhar [13]. Unlike Monte Carlo methods, the DOM relies on subdividing the spatial domain and solving the system deterministically. The physical domain is divided into a number of finite volume cells. The angular domain is then divided into a number of weighted quadrature directions. The individual radiative fluxes are propagated between cells along the discrete ordinate directions. The electromagnetic thermal energy coupling also occurs along the discrete directions. These finite number of directions and positions can be simulated numerically over the entire domain per the description given in Section 2.2. The DOM has been found to have errors ranging from 3 to 20% in combustion simulations [53, 57]. One similar model to the DOM is the finite volume method, which, unlike the DOM, subdivides the angular domain into known solid angles, and propagates thermal radiation along them and not an infinitely thin ordinate [87].

Additional methods, such as the Spherical Harmonics Method propagate radiation based on directional harmonics and not by subdividing the angular domain. However, these methods are more effective in cases with higher optical thickness than the optically thin scramjet environment [21, 86].

A combined strategy for computational and spectral modeling is implemented in

the current work. The strategy looks to verify models used, and understand the errors and limitations to the application.

1.4 Prior Thermal Radiative Investigations

Previous investigations into radiative quantification in scramjet combustion chambers date back to the 1970s, with various researchers investigating the problem since. The research, however, has been limited to a handful of experimental and numerical investigations over the decades. These investigations have looked individually at the radiative spectrum, the relative radiative heat transfer as compared to convective heat transfer, and the effects of radiative flow cooling.

The first investigations performed for the NASA Langley Research Center in 1976, employed a detonation tube with a hydrogen-air gas mixture, to duplicate the exhaust of a Mach 8 scramjet [45]. Instrumentation was placed on the tube, including a photodetector array. The array measured the thermal radiative spectrum of the exhaust plane for wavelengths ranging from 2.4 to 4.9 microns. The exhaust spectrum was also simulated with an infrared spectral band model. The simulated spectrum was predicted with a 4 to 10 % accuracy when compared to experiment. A further investigation was performed for the NASA Langley Research Center in 1980 investigating the exhaust emissions of a short-run (5-10 second) scramjet wind tunnel [88]. The experiments measured the spectral profile of the exhaust over a spectral range from 2.3 to 3.2 microns, with the intention of determining hydrogen combustion completion. To the knowledge of the author, these experiments are the only published spectra of a scramjet exhaust. The current work expands the series of measurements to further wavelengths and for hydrocarbon combustion products.

Later investigations have found that the radiative heat transfer of a scramjet system is very dependent on chamber size. An investigation of hypothetical hydrogen scramjet chambers employing hydrogen-air combustion for a variety of geometries and

flight conditions found that the thermal radiation of a system can vary widely with respect to the rate of convective heat transfer [77]. The radiative heat flux ranges were found to vary widely with a geometry change of only a few centimeters resulting in radiative heat fluxes from as low as less than 1 % of the convective heat fluxes to radiative heat fluxes at almost 10 % of the convective heat fluxes. Additional numerical investigations into a hypothetical supersonic hydrogen combustion nozzle have found that radiative heat flux can be both smaller and larger than the convective heating over an expanding flow-path [72, 108]. These investigations lead to the belief that a generalized radiative scheme for scramjets is not possible without knowledge of the system geometry, and these results warrant further investigation into the radiative properties of a physical system. The current work investigates a pair of physical geometries that have been built and flight tested and, thus, have definite geometries.

Investigations have been made into the effects of thermal radiation on hypothetical supersonic flows similar to those of scramjets [34]. The flows under consideration were supersonic channel flows of pure turbulent water vapor. The flows experienced temperature changes by as much as 50 K. Given the non-dimensionalization of the flow and the pure water vapor environment, a further investigation into flow cooling is warranted to properly examine the radiative effects in a physical combustion chamber. The scope of the current work includes the effects of a non-fully radiating flow with a physical residence time.

Two recent examples of thermal radiative analysis of a physical scramjet combustion chamber have been published. The first analysis is for the RC-22 test circular cross section test rig at the AFRL [69]. The rig, as described in section 1.2, is a supersonic hydrocarbon-air combustion chamber. The rig was simulated with an H₂O-CO₂ WSGG Discrete Ordinates/ Finite Volume Method radiative heat transfer code for a number of flow and radiative wall boundary conditions. Radiative wall heat flux is found to vary between 1 and 10 % of the convective wall heating for the combustion

chamber. Further investigation is warranted for an expansion of the spectral model and inclusion of addition of radiative species. The thrust of the current work examines these factors in the very similar HIFiRE Direct Connect Rig (HDCR) domain.

Finally, the second recent example is an investigation into the radiative properties of the HDCR [50]. The investigation examines the water vapor aspects of a supersonic hydrocarbon combustion chamber using an Implicit Monte Carlo (IMC) code with a LBL spectral model for water vapor. Both of these methods are considered the highest possible fidelity modeling techniques for radiative computations. The investigation found water vapor to contribute as much as 7% of the convective heat flux in some areas of the chamber. The investigation also found that the highest fidelity spectral modeling available has an inherent 20 to 25% uncertainty due to spectral database uncertainty. The work motivates an investigation into the accuracy of faster and lower fidelity models and the inclusion of multiple combustion species in the radiative heat transfer prediction of the HDCR. The current work includes an uncertainty investigation into faster methodology with expanded spectral databases, allowing for a greater number of flowfields to be processed.

1.5 Introduction Summary

The current chapter introduces a number of topics considered in the current investigations. The principles of uncertainty quantification and margin are introduced as a framework for predicting the probability of unstart characteristics of scramjet engines. The main goal of the current work is to determine the effects and associated numerical error and modeling induced uncertainty of thermal radiation in scramjet combustion chambers.

The principles of the scramjet engine, a supersonic internal flow engine, are introduced. Some examples of scramjet experiments are given, and the working tests on which this work is based are introduced. The sounding rocket-based scramjet

experiments, HyShot-II and HIFiRE-2, are described along with the support ground experiments performed for them.

The basic principles of thermal radiation are introduced. The methods of numerically modeling thermal radiation are briefly discussed for both spatial and spectral models. The main spatial and spectral models under consideration are the DOM and the c-k, method respectively.

Finally, the history of previous investigations into the thermal radiation of scramjets is briefly discussed. Additionally discussed is how the current work addresses and expands on previous works.

CHAPTER II

Methodology

2.1 Introduction

The current chapter addresses the basic principles behind thermal radiation and the modeling thereof, along with several directly supporting studies working as direct inputs to the analysis.

The main thrust of the current work focuses on the computational radiative analysis of the HyShot-II and HIFiRE-2 scramjet combustors. Thermal radiation is a form of heat transfer that is dependent on the spatial location within a medium, but thermal radiation also depends on direction considered at any location of concern [65]. Additionally, even at an identical location and direction, the radiative heat transfer varies based on the electromagnetic frequency of concern. Whereas many methods for the simulation of the radiation field exist, they all require that the spatial and directional differentiations of radiative intensity be resolved simultaneously. The two particular numerical methods addressed in this chapter are the RT Method and the DOM [13, 17]. The spectral integration can be modeled in a number of manners, many of which can be combined with a large number of spatial numerical solution schemes [75, 76, 65]. In this work, a series of spectrally-resolved band methods of varying resolution and complexity are applied to the cases considered.

Additionally, analysis of the numerical simulations are performed using a vari-

ety of methods. Adjoint methods are applied to both one-dimensional and three-dimensional cases in order to find the locations and sources of thermal radiation to the chamber walls. Uncertainty estimations are found using perturbation-based techniques. Uncertainties arising from the spectral models are treated as epistemic uncertainties and are calculated by applying a single perturbation to the system. The perturbations are based on unit problems and prior knowledge of the system. The computational uncertainties arising from uncertainties in the physical domain are treated as aleatory uncertainties and are calculated by a structured variation of input parameters over the entire domain.

The input domains for the thermal radiation simulations are the numerically converged outputs from Computational Fluid Dynamics (CFD) flowfield solutions of scramjet combustion chambers. The thermal radiations code post-processes these Computational Fluid Dynamics (CFD) solutions to estimate radiative effects. The particulars of the CFD methods are discussed in later sections, but they are only considered as data sources for the current work.

Finally, experimental measurements are compared to the computational radiative predictions. A brief description of the methodology is given in this chapter.

2.2 Thermal Radiation

As stated in the previous section, radiation is a spatially, spectrally, and directionally resolved phenomenon. The process of thermal radiation generation comes from internal energy distribution of the medium. The internal energy transfers to electromagnetic waves through physical quantum structures of the material comprising the medium. The transfer of energy is known as emission. Additionally, the electromagnetic waves can transfer energy back into the medium along the same quantum structures used in emission in a process is known as absorption. Also, the medium can redirect the electromagnetic waves without absorbing or emitting any radiation

in a process known as scattering [84].

The main equation for modeling radiative intensity is the Radiative Transfer Equation (RTE), which is given by Eq. 2.1, where the left-hand side of the equation represents the change in frequency-specific intensity, “ I_ν ,” over distance, “ s ,” and the terms on the right-hand side represent (from left to right) extinction due to absorption, extinction due to scattering, contribution due to scattering, and contribution due to emission. Extinction due to absorption is the phenomenon of radiative intensity being filtered out by passing through the medium. Extinction due to scattering is the portion of radiative intensity that, by interaction with the medium, is diverted away from the direction of interest into another direction. Contribution due to scattering is the portion of radiative intensity that by interaction with the medium is diverted into the angular of interest from another angular direction. Contribution due to emission is the portion of the radiative intensity that is added from the thermal radiative properties of the medium.

$$\frac{dI_\nu(s, \mu, \theta)}{ds} = -\frac{\kappa_{abs}(s)}{\mu} I_\nu(s, \mu, \theta) - \frac{\kappa_{sca}(s)}{\mu} I_\nu(s, \mu, \theta) + \frac{\kappa_{sca}(s)}{4\pi\mu} \int_0^{2\pi} d\theta' \int_{-1}^1 d\mu' f_\nu(s, \mu, \theta, \mu', \theta') I_\nu(s, \mu', \theta') + \frac{\kappa_{abs}(s)}{\mu} B_\nu(T(s)) \quad (2.1)$$

The intensity direction is given by the vertical and azimuthal angles, “ ϕ ” and “ θ ,” respectively. The vertical angle is best handled as the cosine of the angle with respect to the vertical axis ($\mu = \cos(\theta)$). The coordinate system is given in Fig. 2.1. The terms “ κ_{abs} ” and “ κ_{sca} ” are the absorption and scatter coefficients, respectively, which dictate the amount of intensity removed or added over a unit of path-length for the corresponding physical phenomena. The term “ f_ν ” refers to the scattering redistribution function, where the source angles (the secondary angles) are denoted by primes. The term “ B_ν ” denotes the frequency specific blackbody intensity as

determined by the Planck distribution function [84].

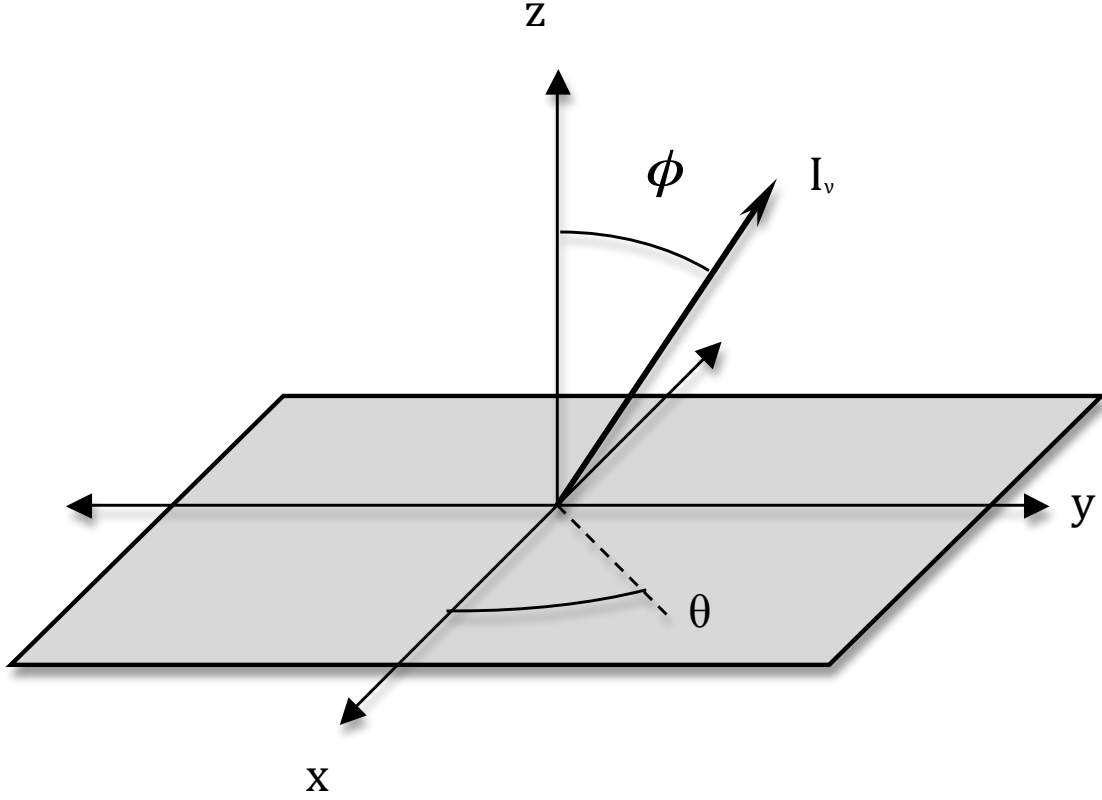


Figure 2.1: Angular Coordinate System

The boundary conditions at the walls are modeled as partially emissive and reflective walls as represented by Eq. 2.2, where “ ϵ_ν ” is the emissivity, and “ r_ν ” is the reflectivity.

$$I_\nu(s_{wall}, \mu, \theta) = \epsilon_\nu B_\nu(T(s_{wall})) + \frac{r_\nu}{2\pi} \int_0^{2\pi} d\theta' \int_0^1 d\mu' I_\nu(s_{wall}, \mu', \theta') f_\nu(s_{wall}, \mu, \theta, \mu', \theta') \quad (2.2)$$

2.2.1 Radiation Field Modeling

In order to solve the RTE, numerical spatial solution methods are employed. The main method in the current work is the DOM, which is chosen for its versatility over different radiative regimes and its spatial accuracy. Additionally, a RT method is employed as a high-accuracy spatial benchmark [55, 17, 65, 13].

The DOM is implemented in a three-dimensional computational code called General Radiation Simulation Program (GRASP), provided by Jewin Liu with significant modification for the purpose of this work [68]. A new band model is implemented, which increases spectral resolution and allows the simulations to be parallelized by assigning different spectral bands to different processors.

The DOM code provides a first-order spatial solution to the RTE and employs a simplified correlated-k narrow-band spectral model. These methods allow for both spatially and spectrally resolved solutions for radiation intensity, heat flux, and absorptivity.

The three-dimensional discretized Ray Tracing (RT) Method provides a second-order spatial solution with a narrow-band spectral model, and it provides arbitrarily accurate spatial and angular resolution, which is an improvement over the DOM [75, 17]. However, it only computes solutions for one location at a time. The DOM code can compute scattering and reflective boundary conditions, whereas the Ray Tracing (RT) method cannot account for such conditions [65]. The RT code employs an identical spectral model to that used by the DOM.

For the three-dimensional DOM, the properties of the medium are projected onto a structured grid for which the radiative intensity is solved for a series of discrete directions at each grid point [13]. Scattering will be ignored in all analysis ($\kappa_{sca} = 0$) even though the DOM code is robust enough to incorporate it [65]. The justification for ignoring scattering is given in the next section. With this simplification, the RTE is discretized by a flux-based finite-volume scheme for multi-dimensional solvers, such

as GRASP. The resulting formula is given by Eq. 2.3 where “ i ” is the spatial index, “ j ” is the directional index, “ m ” is the cell face index, “ V ” is the cell volume, “ a ” cell face area, and “ N_{face} ” is the number of cell faces [54, 68].

$$\sum_m^{N_{face}} I_\nu(m, j) \cdot a(m) = \kappa_{abs}(i)V(i)(B_\nu(i) - I_\nu(i, j)) \quad (2.3)$$

The total spectrally-resolved radiative energy flux, “ F_ν ,” to a cell face is found by integrating the total angular intensity contributions, “ I_ν ,” that are normal to the plane of the cell face. This expression is given in Eq. 2.4, where “ μ ” is the cosine of the angle, “ ϕ ,” between the ordinate and the vector normal to the incident plane. The coordinate system is illustrated in Fig. 2.1. Equation 2.4 can be numerically integrated based on an S_n weighting scheme, as given in Eq. 2.5, where “ w ” is the DOM quadrature weighting coefficient [28, 29].

$$F_\nu(s) = \int_0^{2\pi} \int_0^1 I_\nu(s, \mu, \theta) \mu d\mu d\theta \quad (2.4)$$

$$F_\nu(m, i) = \sum_j^{N_{ord}} w(j) I_\nu(i, j) \cdot a(m) \quad (2.5)$$

The boundary conditions, as based on Eq. 2.2, can be varied as desired with the emissivity and reflectivity both able to be set to any value between zero and one. Additionally, the reflection redistribution factor, “ f_ν ,” can be set to be specularly reflective as defined by Eq. 2.6, or diffusely reflective as defined by Eq. 2.7.

$$f_\nu(s_{wall}, \mu, \theta, \mu', \theta') = 2\pi \delta(\mu, -\mu') \delta(\theta, \theta') \quad (2.6)$$

$$f_\nu(s_{wall}, \mu, \theta, \mu', \theta') = 1 \quad (2.7)$$

For the purpose of verification, a second-order spatially discretized three-dimensional Ray Tracing method with a two-point narrow-band spectral method is employed [17]. Whereas the selection of paths for the RT method is often chosen with a Monte Carlo scheme, a pre-determined ray spacing is opted for in this application [75]. The RT method divides a solid angle hemisphere into a discrete series of angles and one-dimensionally integrates the radiative heat transfer along each path until it reaches a simulation boundary. The one-dimensional integration is given by Eq. 2.8. The individual intensities are then integrated angularly as in Eq. 2.4, which can then be performed numerically with Eq. 2.9, where “ N_{ord} ” is the number of directional ordinates [17].

$$\frac{3I_\nu(i, j) - 4I_\nu(i - 1, j) + I_\nu(i - 2, j)}{2\Delta s(i)} = \frac{\kappa_{abs}(i)}{\mu(j)}(B_\nu(i) - I_\nu(i, j)) \quad (2.8)$$

$$F_\nu = \sum_j^{N_{ord}} I_\nu(\theta(j), \phi(j)) \sin(\phi(j)) \cos(\phi(j)) \sin(\Delta\phi(j)) \Delta\theta(j) \quad (2.9)$$

2.2.2 Spectral Resolution

The radiative transfer equation and respective boundary condition equation are frequency-dependent. The frequency-dependent phenomena that must be taken into account are absorption in the medium, emission in the medium, scattering in the medium, absorption at the wall, emission from the wall, and reflection from the wall.

Both medium absorption and emission are dictated by the absorption coefficient. The absorption coefficient is a frequency-dependent quantity, which dictates the path-specific coupling of the thermodynamic energy in the medium and the electromagnetic energy passing through the medium [84]. The coefficient at any point in the medium is determined by the local temperature, pressure, and species concentration in the medium. The exact combination is very complicated and different for every combination of state variables [36, 76]. As such, a model must be employed to determine

the coefficient.

The scattering coefficient through the medium is the path-specific coupling of the effects of one intensity direction with other intensity directions. Several forms of scattering phenomena exist, such as Rayleigh, Mie, and Raman scattering [36]. In cases examined in this work, however, scattering can be neglected. The reason is that Mie scattering requires particulate in the medium, which in most cases would be water or fuel droplets. The high temperatures and pre-cracked state of the fuel in scramjet engines prevent water or fuel droplet formation. Additionally, particulate can result from sooting in the medium [75]. However, the experimental measurements found no evidence of soot particles are present in the medium [7]. Both sets of conditions show that scattering is not prevalent in the current setup. Additionally, Rayleigh scattering is highly dependent on wavelength and particle size. With the infrared wavelengths and particles no bigger than diatomic and triatomic atoms being considered, Rayleigh scattering is negligible [65]. Finally, the Raman scattering effects, which result in frequency changes in scattering, are negligible in heat transfer application [75].

The frequency-specific distribution of the radiative energy emission potential is determined by the factor “ B_ν ” from Eq. 2.1. When the system is in local thermodynamic equilibrium, the emission potential is a temperature and frequency-dependent phenomenon calculated by the Planck Equation, Eq. 2.10, where “ h ” is Planck’s constant, “ k_b ” is Boltzmann’s constant, “ c ” is the speed of light, “ ν ” is the frequency, and “ T ” is the local temperature. The emission ability, along with the coupling as dictated by the absorption coefficient in Eq. 2.1, determines the thermodynamic contribution of thermal radiation from the medium [84].

$$B_\nu = \frac{2h\nu^3}{c^2 \left(e^{\frac{h\nu}{k_b T}} - 1 \right)} \quad (2.10)$$

When the radiative energy emission is perfectly coupled to the local thermodynamic

energy ($\lim_{\kappa_{abs} \rightarrow +\infty}$) the emission is said to be “blackbody,” and radiative intensity is equal to the Planck function as in 2.11.

$$I_\nu(s, \mu, \theta) = B_\nu \quad (2.11)$$

When the radiative energy emission is uncoupled from the thermodynamic energy ($\lim_{\kappa_{abs} \rightarrow 0}$), the radiative intensity is completely unaffected by the local thermodynamic energy.

Finally, wall absorptivity and emissivity are similar to the medium absorptivity and emissivity in that they are the coupling between the thermodynamic energy of the wall and the electromagnetic energy of the medium. Wall reflectivity is the measure of the amount and direction that radiation of the medium is reversed by the wall back into the field [31]. The emissivity, absorptivity, and scattering properties are dependent on frequency, temperature, material, and surface condition [48, 112, 114].

2.2.3 Band Modeling

To properly calculate the absorption coefficients and blackbody emission, a spectral model must be employed. Methods such as the Weighted Sum of Gray Gas (WSGG) can be linked to various spatial modeling techniques such as the DOM and RT Method, but they offer limited accuracy in frequency resolution, which can adversely affect the accuracy of the calculations [37, 68, 102, 101]. Additionally, Statistical Narrow Band (SNB) Methods can be quite spectrally accurate, but they only apply to path-based methods with low spatial variation [36, 41, 74]. Many endeavors have sought to rectify these issues for spatial variation and frequency resolution [38, 64] The most promising to date are the full-spectrum and narrow-band correlated-k methods on which all of the spectral models in this work are based [67, 76, 103, 110].

The band method employed is a simplified two-point narrow-band c-k spectral

model. Whereas detailed multi-species c-k methods are very accurate, they can require large amounts of computational time to generate all of the cell specific quantities. This time can be reduced by using pre-computed spectral tables, but these tables can be large to the point of being unusable in a realistic computational system [110]. Many simplifications to the c-k method have been developed to compromise between accuracy, time, and memory requirements [76, 78].

All frequency-based models assume that the total intensity is calculated by a frequency integration of the spectrally-resolved intensity as given in Eq. 2.12.

$$I(s) = \int_{\nu_{min}}^{\nu_{max}} I_{\nu}(s) d\nu \quad (2.12)$$

For considering the spectral resolution, realistic mixed-gas spectra are very complex, with hundreds of millions of spectral lines that depend on temperature, pressure, and species concentration. The most rigorous method is the Line By Line (LBL) method, which allows for the arbitrarily fine computation of the spectral absorptivity at any frequency [75, 76]. However, the LBL method is computationally expensive enough to be impractical in any large-scale design study [36, 83]. Narrow-band methods are significantly faster. Narrow-band methods divide the absorption spectrum into bands of given spectral width. In the case of this work, 25 cm^{-1} wide bands are employed. Generalized absorption characteristics are calculated for each band using the arbitrarily fine absorption spectrum as calculated by the LBL method.

The c-k method transforms the fine-resolution absorption spectrum from the LBL method into an ordered monotonic absorption spectrum, which can be approximated with a handful of quadrature points, as in Eq. 2.13, where “ g ” is the quadrature weight, “ l ” is the quadrature index, and “ k ” is the spectral band index. The extreme simplification of this approach is to take a quadrature point at the statistical average of the absorption band and set the quadrature weight equal to 1 for the single point

in the band [21].

$$I(s) = \sum_k^{N_{band}} \sum_l^{N_{quad}} g(l) I_\nu(s, k, l) \Delta\nu(k) \quad (2.13)$$

A step up from a band-averaged approach would be to choose two equally weighted quadrature points ($g = 0.5$) at one standard deviation above and below the mean band absorptivity [20]. A true c-k method would require the reordering of the absorption spectrum of each band and numerically calculating the weighted value for both standard deviation locations. A simplified method involves setting the quadrature point values as those of the standard deviations in the error function as in Eq 2.14, where “ $\bar{\kappa}$ ” is the band-averaged absorption, “ σ ” is the standard deviation of the band absorption, and “ c_1 ” is a tuning parameter between 0 and 1.

$$\kappa_\nu(s, l) = \bar{\kappa}_\nu(s) \left(1 + ERF \left(\frac{\pm\sigma_\nu(s)}{\bar{\kappa}_\nu(s)} \right) c_1 \right) \quad (2.14)$$

Because all bands are assumed independent for narrow-band methods, and Raman cross-scattering is assumed to be insignificant, the total integration can be computed as the sum of the spectrally resolved flux, as given in Eq. 2.13. However, the quadrature points within the sub-bands are not necessarily independent, but all information regarding the cross-correlation is lost when these methods are applied. Therefore, the quadrature absorption values are assumed to have no cross-correlation with the other quadrature points in their own band, and they are assumed to have perfect correlation with the same quadrature points for absorption values at other locations.

The calculation of absorption coefficients is performed with a LBL calculation for all species of interest at representative pressures and temperatures pertinent to the conditions inside a scramjet. The individual lines are extracted from the HiTemp database using JAVAHAWKS at a pressure of 2 Atm and temperatures of 500, 1000, 1500, 2000, 2500, and 3000 K, respectively [92]. The individual lines are processed

at regular intervals for the summation of Lorentz line profiles using the procedure laid out in Section 2.3 of the thesis by Irvine[50]. The extracted data are used to calculate a series of optical depths for each species at each temperature with a spectral resolution of 0.01 cm^{-1} , which, in turn, are used to create the band statistic needed for the spectral model, resulting in a series of fast spectral lookup tables for each species. The lookup tables can be used to directly evaluate the species absorption as in Eq. 2.15, where “ n ” denotes the species index, “ S_ν ” denotes the species absorptivity extracted from the lookup table, “ $X(i, n)$ ” represents the mole fraction, and “ $\xi_n(i)$ ” represents the relative number density normalized to the number densities used to calculate the lookup tables. With this process in place, the absorption coefficient can quickly be calculated for any combination of species concentration mixtures at a wide range of temperatures.

$$\kappa_\nu(i, l) = \sum_n^{N_{spec}} S_\nu(T(i), n, l) X(i, n) \xi_n(i) \quad (2.15)$$

2.3 Sensitivities and Errors

One of the main motivations for the current work is to determine the uncertainty in the amount of thermal radiation in the combustion chamber.

The types of uncertainty can be classified as two major categories: epistemic and aleatory uncertainties. Epistemic uncertainty is defined as uncertainty resulting from a lack of knowledge of the system. Aleatory uncertainty results from variation within the system. Additionally, the error resulting from the numerical approximations inherent to the system may be treated as uncertainties when the known calculation error has been bounded [93].

The main uncertainty from lack of information in the system is based on the spectral model. First, there is an inherent measurement uncertainty associated with all spectral lookup tables [74, 92]. Second, the band models employed have an associ-

ated modeling and approximation error. Mathematically, the proper choice of values for the model would result in a perfect agreement of the spectral model with the raw LBL lookup tables. However, the precisely matching values for banded spectral models are not known and can only be approximated. As such, the numerical and modeling errors of the spectral model are folded into the epistemic uncertainty along with the experimental table error, as they all directly affect the knowledge of the correct values of “ κ_ν ” as given by Eq. 2.14.

One additional source of error that can be treated as a lack of knowledge is the error stemming from numerical approximations and spatial and angular mesh modeling. Mathematically, a perfectly refined angular and spatial grid with a proper numerical scheme will give the exact solution for a location of interest given standard convergence [90]. However, the exact grid and method is unknown and infeasible. As such, the current grid can be treated as an approximation of uncertain accuracy.

The uncertainty from variations in the system comes from several sources. One source of variation is the flowfield being processed. The medium can vary widely in temperature, pressure, and species concentration for any location. For this case, there is no one correct value for the flowfield, even when inlet conditions match experimental data exactly. The reason being is that the flowfield undergoes time-varying turbulent fluctuations. Therefore, a wide variety of instantaneous solutions are valid and may be considered as a probability distribution. If only time-steady information is known, then the Root Mean Square (RMS) values of the fluctuating quantities can be considered to construct an estimated probability distribution. Additionally, the boundary conditions of the system may vary due to material properties and manufacturing uncertainty. Given the thermal cycling of the system, and the possibility of fowling, the values of the boundary conditions may vary from run-to-run or even within a run, meaning that no exact number may be applicable. Therefore, a range of boundary conditions must be considered in order to account for the total probability

distribution. These ranges are considered as the limits of the temperatures and emissivities of the materials considered as well as for the range of any material deposition which may occur during combustion. In order to incorporate the aleatory probability distributions, a series of design studies and sampling points is considered for which statistical distributions may be constructed [47]. The different types of uncertainty can be combined using a statistical analysis method of comparing Cumulative Distribution Function (CDF) curves of different conditions [9, 106, 24].

Design studies require a knowledge and selection of important input parameters to the system. A sensitivity analysis is required to determine the factors of greatest influence on the system. The factors being considered are the medium characteristics and the boundary conditions. Flowfield and medium sensitivities are calculated with a discrete adjoint sensitivity method as discussed below [107] With the sensitivities known, the important variables of consideration can be determined.

2.3.1 Sensitivities

The sensitivity analysis is required to make proper decisions on the parameter variation study of the system since it provides a mathematical basis of importance to factors in the system. The use of a discrete adjoint implementation gives direct sensitivities based on the solution method and model [94]. The method under consideration in this work is the DOM, which calculates the intensity for an entire domain and lends itself to adjoint analysis [73, 95].

In order to determine the most pertinent factors affecting the overall wall radiative heat flux, a discrete adjoint sensitivity method is employed for the three-dimensional DOM. The adjoint method allows for the local derivatives of a computed quantity to be calculated simultaneously with respect to numerous inputs. In this case, sensitivity of the wall radiative heat flux is calculated with respect to the temperature, pressure, and partial pressures within each cell as represented by the matrix equation, Eq. 2.16.

In Eq. 2.16, the transpose of the adjoint matrix solution, “ $-\Psi^T$,” relates the wall heat flux, “ F ,” to the individual numerical cell intensity residuals, “ R_I ,” and “ $\left[\frac{\delta R_I}{\delta u}\right]$ ” relates the cell intensity residuals to the individual cell quantities, “ u .”

$$\left[\frac{\delta F}{\delta u}\right] = -\Psi^T \left[\frac{\delta R_I}{\delta u}\right] \quad (2.16)$$

Equation 2.17 is the matrix representation of Eqs. 2.4 and 2.2, where “ A ” is the coefficient matrix of the intensity vector, “ I ,” and “ Q ” is the intensity source vector. The matrix equation includes intensities at all locations, ordinates, and frequencies. The individual entries in Eq. 2.17 can be analytically differentiated with respect to the local cell quantities allowing for “ $\left[\frac{\delta R_I}{\delta u}\right]$ ” to be calculated quickly.

$$R_I = AI_\nu + Q \quad (2.17)$$

The adjoint matrix is calculated iteratively using Eq. 2.18, where all terms have the same meaning as they do in Eqs. 2.16 and 2.17. A useful description of the discrete adjoint sensitivity method and the means of calculating the adjoint matrix is given by Fidkowski and Darmofal [26].

$$A^T \Psi + \left[\frac{\delta F}{\delta I_\nu}\right]^T = 0 \quad (2.18)$$

The advantage of performing the sensitivity analysis this way is that the location and magnitude of flow-field sensitivities can be calculated for the cost of one additional matrix solution. This calculation allows simulations to focus on probing the most pertinent locations and quantities.

2.3.2 Uncertainty Estimation

In order to calculate the uncertainty of the radiative heat flux, different methods are employed for the different sources of uncertainty. For the epistemic spectral uncertainty, a perturbation-based uncertainty is employed. For the epistemic uncertainty stemming from mesh convergence, an estimated post-processed multiplier is employed. For boundary and medium-based aleatory uncertainties, a parameter variation study is employed.

The uncertainty stemming from the epistemic spectral uncertainty is divided into two parts that both affect the absorption coefficient in Eq. 2.1. The first part is the experimental uncertainty inherent in the spectral lookup tables, which is given along with the spectral absorptivity for each entry. The second form of uncertainty is the modeling error introduced by reducing the system into a series of bands. The uncertainty is calculated in Eq. 2.19, in which “ ΔI_ν ” is the local intensity uncertainty, and “ E_ν ” is the variation in the absorption coefficient defined by the combination of modeling and measurement uncertainty as defined by Eq. 2.20.

$$\Delta I_\nu(s, \mu, \theta) = I_\nu((E_\nu \kappa_{abs}), s, \mu, \theta) - I_\nu(\kappa_{abs}, s, \mu, \theta) \quad (2.19)$$

$$E_\nu = 1 \pm (E_{\nu 1} + E_{\nu 2}) \quad (2.20)$$

In Eq. 2.20, the value of “ $E_{\nu 1}$ ” is the measurement error given with the experimental reference tables. The value of “ $E_{\nu 2}$ ” is calculated for the modeling error and is estimated by the use of a unit problem. The unit problem is a one-dimensional homogeneous medium with no scattering and purely absorbing boundary conditions. When Eqs. 2.1 and 2.2 are subjected to these conditions, they are reduced to what is known as Beer’s Law, as given in Eq. 2.21, for a specific frequency [65]. To determine the intensity over a frequency band, Eq. 2.21 can be spectrally integrated using Eq.

2.13. When the band intensity is calculated for two schemes at two resolutions, different band specific intensity may occur for either calculation. A comparison between the absorptivity of the schemes is computed as follows.

$$I_\nu(s, \mu, \theta) = B_\nu(T(s))(1 - e^{-s\kappa_{abs}}) \quad (2.21)$$

The goal is to find the effective difference between the absorptivity, “ κ_{abs} ,” for two spectral schemes of different resolution over the same domain and frequency band.

The spectrally integrated band intensity, “ $I(s, k)$,” for a known homogeneous domain can be treated with Beer’s Law, as given by Eq. 2.22, where “ k ” is the band index, “ κ_{eff} ” is the effective band absorptivity, and “ \bar{B}_ν ” is the band average of Planck’s function in Eq. 2.23.

$$I(s, k) = \Delta\nu(k)\bar{B}_\nu(T(s), k)(1 - e^{-s\kappa_{eff}(k)}) \quad (2.22)$$

$$\bar{B}_\nu(T(s), k) = \int_{\nu_{min}(k)}^{\nu_{max}(k)} B_\nu(T(s))d\nu/\Delta\nu(k) \quad (2.23)$$

From this step, Eq. 2.22 can be rearranged into Eq. 2.24 by defining “ $\epsilon_{2\nu}$ ” as a factor of the absorptivity of high and low spectral resolution methods as defined in Eq. 2.25 (“ $\kappa_{high}(k)$ ” and “ $\kappa_{low}(k)$,” respectively.) The relative absorption uncertainty for a particular solution can be defined as long as the spectral band, “ $\Delta\nu(k)$,” is not too broad and “ $\kappa_{high}(k)$ ” is considered an accurate result. When a solution to a non-unit problem is desired, the values of “ $E_{\nu 2}$ ” can be inserted back into Eqs. 2.19 and 2.20 in order to garner an estimated value of the intensity change caused by the potential error in the spectral model.

$$\kappa_{eff}(k) = -\ln\left(1 - \frac{I(s, k)}{\Delta\nu(k)\bar{B}_\nu(T(s), k)}\right) \frac{1}{s} \quad (2.24)$$

$$E_{\nu 2}(k) = \frac{\kappa_{low}(k)}{\kappa_{high}(k)} - 1 \quad (2.25)$$

The aleatory uncertainty is accounted for in two manners. The first manner is the boundary conditions, as defined by Eq. 2.2. The factors of emissivity, “ ϵ_{ν} ,” reflectivity, “ r_{ν} ,” wall temperature, “ $T(s_{wall})$,” and redistribution factor, “ f_{ν} ,” are varied for their physically possible ranges to determine a range of effects from the boundary conditions. With no knowledge of the probability for the material characteristics, the associated Probability Density Function (PDF) is assumed to be of uniform density. Additionally, the flowfield quantities can be varied in a correlated manner based on their turbulent characteristics. This method necessitates running a number of simulations that can result in a compiled PDF of the results. The probability assigned to each flowfield is found by the following analysis. With the mean and RMS values of the flow known, a probability can be given for the value in each cell. Given that there are a large number of cells, the total superposition of all of the distribution function results in a normal distribution as per the Central Limit Theorem. The CDF is given in Eq. 2.26, in which “ $C(t)$ ” is the value of the CDF for the particular variation, “ $u(i, t)$ ” is the cell-specific flow quantity, “ $\bar{u}(i, t)$ ” is the time-averaged cell-specific flow quantity, “ $u_{rms}(i, t)$ ” is the RMS of the cell-specific flow value, and “ N_{cell} ” is the number of cells (entries in the i -dimension of the matrix).

$$C(t) = \sum_{i=1}^{N_{cell}} \left[1/2 + ERF \left(\frac{u(i, t) - \bar{u}(i, t)}{\sqrt{2}u_{rms}(i, t)} \right) / 2 \right] \frac{1}{N_{cell}} \quad (2.26)$$

2.3.3 Combined Errors

With two types of uncertainties known in the system, a method of combining the effects is needed. The first issue to be addressed is that the CDF of the flowfield in Eq. 2.26 does not directly translate into the CDF of the final radiative intensity, given the non-linear nature of the radiative intensity solution. The relative weighting

of the individual flowfields can be assigned to each radiative solution by taking the derivative of the CDF at the known value, as given in Eq. 2.27, where “ $\Phi(t)$ ” is the probability density of the given flowfield.

$$\Phi(t) = \sum_{i=1}^{N_{cell}} \left[\frac{1}{\sqrt{2\pi}u_{rms}(i, t)} \exp \left(-\frac{(u(i, t) - \bar{u}(i, t))^2}{2u_{rms}(i, t)^2} \right) \right] \frac{1}{N_{cell}} \quad (2.27)$$

Then, the individual radiative solutions to the radiative intensity calculations can be ordered in a monotonic manner based on a chosen criterion within the solution. This ordered grouping of radiative solutions becomes the final PDF of the design study, which can be numerically integrated into a CDF, as given in Eq. 2.28, where “ $C(t)$ ” is the CDF, “ F ” is the flux of interest, “ F_{max} ” is the maximum flux of interest from simulations, “ t ” is the index for the simulation of interest, and “ t' ” is the index for all simulations in the summation.

$$C(t) = \sum_{t' \quad F(t') < F(t)} \Phi(t') / \sum_{t' \quad F(t') < F_{max}} \Phi(t') \quad (2.28)$$

In order to incorporate the epistemic uncertainty in the final intensity CDF as given by Eq. 2.28, an uncertainty and sensitivity method proposed [9, 24, 106]. To apply the method, the simulations are rerun with the altered spectral data as presented in Section 2.2. A new CDF is then created from this altered data. Additional uncertainties from the mesh and numerical methods may be added to these final values with the intention of moving the new intensity CDF farther from the unperturbed CDF. The differences between the perturbed epistemic CDF and the nominal values can be interpreted as the effects of that which cannot be known in the system. The probability box created by the curves can be superimposed to create the total CDF.

2.4 CFD Modeling

The radiative mediums of concern are three-dimensional turbulent-reacting flowfields [5, 70]. The individual test cases are run using three separate flowfield solvers. Each flowfield solver is written and run independently of the other solvers. Each solver is a turbulent-reacting compressible CFD code which is run in an uncoupled manner from the radiative simulations. The outputs of all simulations give temperature, pressure, species concentration, velocity, density, and Mach Number.

The first code is a three-dimensional unstructured Reynolds Average Navier-Stokes (RANS) program run by Vincent Terrapon at Stanford University. The CFD code uses a nine species progress-based hydrogen-air flamelet model and a $k-\omega$ turbulence model to simulate the combustion chamber of the HyShot-II experiment [81]. Further details are given in Chapter III.

Additional simulations are run by Jiwen Liu at the AFRL using an unstructured three-dimensional turbulent reacting RANS CFD simulation code. The code employs a twenty-two-species hydrocarbon combustion model and a $k-\epsilon$ RANS turbulence model [70, 85]. The code is specifically used for simulations of the HIFiRE Direct Connect Rig (HDCR) at National Aeronautics and Space Administration (NASA), Langley. More details on the simulations are given in Chapter III.

The final set of CFD simulations are run by Ivan Bermejo-Moreno at Stanford University with an unstructured three-dimensional turbulent-reacting Large Eddy Simulation (LES) CFD simulation code [58, 61]. The code employs an eleven-species flamelet hydrocarbon combustion model [82]. The main advantage of the LES over the RANS simulation is that the LES gives both instantaneous time-step data as well as temporal flow statistics. Additionally, LES is far more accurate at shock-boundary layer interaction predictions. The main advantage of RANS simulations over LES is that RANS simulations gives reasonable time-averaged data with a greatly reduced computational cost over the LES [44]. The individual LES results are discussed in

more detail in Chapter V.

2.5 Experimental Setup

The experimental emission measurements were taken by Michael Brown of the AFRL on the HIFiRE Direct Connect Rig (HDCR) in the Arc-Heated Scramjet Test Facility (AHSTF) at NASA Langley. The experimental setup was calibrated by Andrew Crow and Michael Brown at the AFRL, with a procedure given in Appendix A. The HDCR was constructed and operated to provide ground-test support for Flight 2 of the HIFiRE program using the same flowpath lines as the flight engine [11]. A two-dimensional schematic of this flowpath appears in Fig. 2.2 [52].

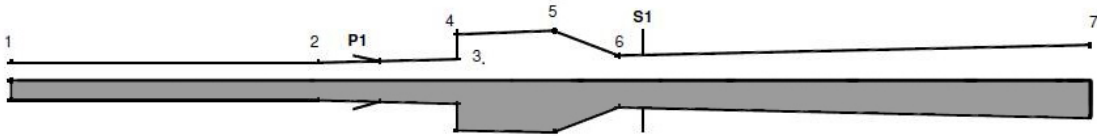


Figure 2.2: Schematic of flowpath: Flow is left to right. The isolator extends from station 1 to 2, the cavity flameholder extends from from 3 to 6. Primary and secondary fuel injection sites are denoted by P1 and S1, respectively. Emission measurements are made at the exit of the combustor, denoted as station 7. The CFD domain is denoted in gray.

An optical diagnostics flange and attendant hardware were attached to the engine at the exit of the combustor (station 7 in Fig. 2.2). The primary function of the optical hardware was to execute tunable diode laser absorption measurements along 16 lines of sight across (and adjacent to) the combustor exit. Three diode lasers were sequentially tuned across multiple water spectral features in the neighborhood of 1.4 microns (7143 cm^{-1}) with the aim of determining the temperature and water concentration fields at the exit plane [8]. The absorption measurements were conducted

in such a way that for every 1 ms of data collection, approximately 100 μ s of signal due just to the nascent hot gas emission was also collected. The emission signals are captured using InGaAs photodetectors with a narrow infrared spectral bandwidth of 1.1-1.8 microns ($5556\text{-}9091\text{ cm}^{-1}$). A silicon filter removed emission at wavelengths below 1.1 microns (9091 cm^{-1}). (The filter is necessary to maintain good signal-to-noise ratios in the absorption measurements.) A photograph of the optical hardware attached to the HDCR is shown in Fig. 2.3. Sixteen photodetectors and associated transimpedance amplifiers were split between two electronics boxes, one positioned on the body (top) side of the combustor exit and one on the port (left) side of the combustor exit. This arrangement permitted collection of the emission from 8 vertical views and 8 horizontal views that share some common overlap with respect to their solid angles of emission collection. In Fig. 2.4, a scaled schematic is shown of the location of the 16 individual photodetectors with respect to the combustor exit, which was 0.05 m tall and 0.10 m wide. Apertures located between the photodetectors and combustor exit limited the solid angle of light collection. Specific values of the light collection (field of view and sheet thickness) for each photodetector are given in Table 2.1. The photodetectors and all optics associated with the experiment are calibrated using a single tunable diode laser with a known power. Further results are discussed in Chapters IV and V.

Sensor Number	Orientation	Field of View (deg)	Sheet Thickness (deg)	y-Position (m)	z-Position (m)
1	Horizontal	48.3	3.9	-0.038	0.168
2	Horizontal	45.2	3.9	-0.027	0.168
3	Horizontal	23.9	3.9	-0.016	0.174
4	Horizontal	23.9	3.9	-0.005	0.174
5	Horizontal	23.9	3.9	0.005	0.174
6	Horizontal	23.9	3.9	0.016	0.174
7	Horizontal	45.2	3.9	0.027	0.168
8	Horizontal	49.0	3.9	0.038	0.168
9	Vertical	49.8	4.0	0.139	0.062
10	Vertical	20.1	4.0	0.146	0.027
11	Vertical	20.2	4.0	0.146	0.016
12	Vertical	21.4	4.0	0.146	0.005
13	Vertical	21.4	4.0	0.146	-0.005
14	Vertical	20.2	4.0	0.146	-0.016
15	Vertical	20.2	4.0	0.146	-0.027
16	Vertical	50.0	4.0	0.139	-0.062

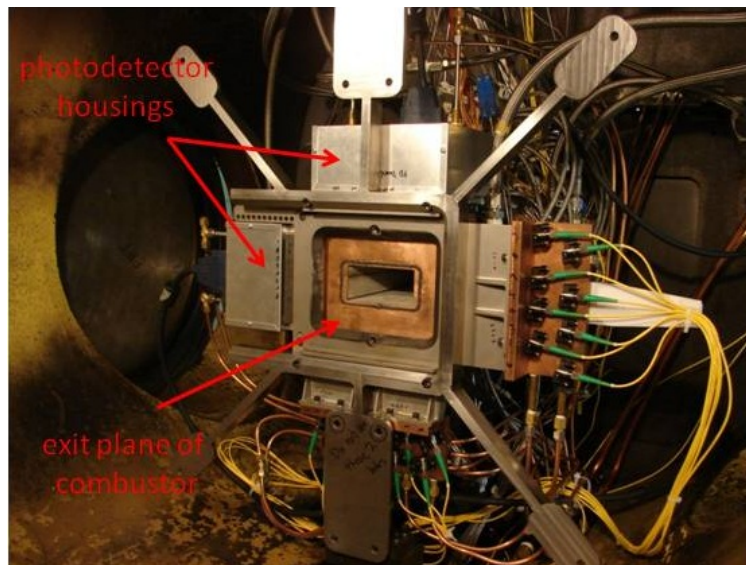


Figure 2.3: Optical hardware mounted to the exit plane of the HDCR combustor. The 16 photodetectors used in the emission measurements are located in two housings as indicated. (Flow is right to left.) Photo courtesy of Michael Brown at the AFRL.

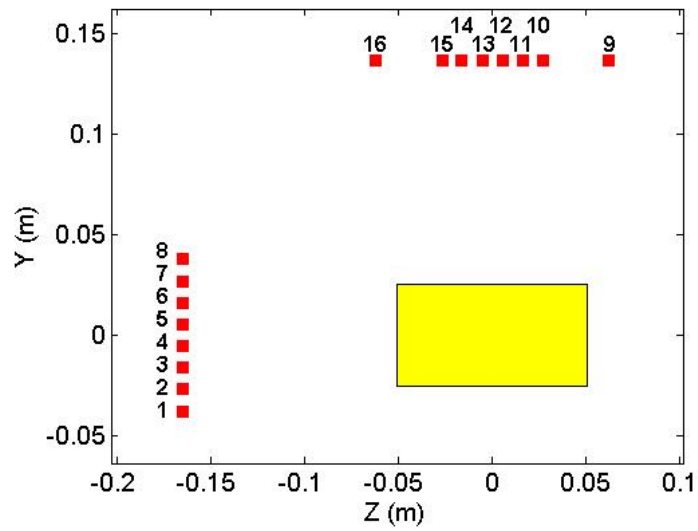


Figure 2.4: Location of the emission photodetectors with respect to the exit of the combustor shown in yellow. Flow is out of the page. Image courtesy of Michael Brown at the AFRL.

2.6 Conclusions

The simulation of thermal radiation within scramjet combustion chambers are performed using several methods as described in Section 2.4. First, the scramjet flowfields for both HyShot-II and HIFiRE-2 are run uncoupled from the thermal radiative solution using both RANS and LES flow solvers. All flow solvers are turbulent compressible reacting CFD codes, providing flow characteristics such as temperature, density, pressure, and species concentration. The LES provides time-resolved flowfields, whereas the RANS simulations provide only time-averaged quantities.

The flows are post-processed using two three-dimensional radiative solutions codes, as described in Section 2.2. The DOM code, “GRASP,” is a lower spatial fidelity code that can provide spectrally-resolved solutions of the entire flowfield. The code is also capable of examining scattering and variable boundary conditions. Additionally, it is augmented for adjoint sensitivity analysis. The Ray Tracing (RT) method is an arbitrarily accurate spatial method that solves spectrally resolved thermal radiative flowfields for a specific location.

Both radiative codes employed a multipoint correlated-k style band spectral method as described in Section 2.2. The individual bands are based on statistics gathered from the HiTemp database [92]. The model allows for the individual assignment of spectral absorption coefficients for each location, with the coefficient being dependent on temperature and multiple radiative species concentrations. The spectral model can be made arbitrarily fine, and each band is solved independently of other bands allowing for both computational codes to be parallelized to handle multiple bands simultaneously.

The epistemic and aleatory uncertainties are calculated using methods described in Section 2.3. The epistemic uncertainty is the combination of experimental uncertainty inherent in all measurements and the spectral uncertainties predicted by one-dimensional unit problems. The epistemic uncertainties are predicted by per-

turbing the spectral model by an estimated uncertainty and rerunning the entire simulation. The aleatory uncertainties are predicted by a parameter variation study of possible flow conditions. These flowfields are simulated with radiative solvers to create a CDF of possible radiative intensity outputs.

The epistemic and aleatory uncertainties can be combined by calculating the aleatory CDF for both the perturbed and unperturbed spectral models and comparing the final distributions.

The final comparison is made between the computational simulations and laboratory experiments performed at the HDCR at NASA Langley, as described in Section 2.5. The plane along the combustion chamber exit output flowfield is studied experimentally with tunable diode lasers and infrared photodetectors. The calibrated photodetectors give absolute measurements of the thermal radiation within the flowfield with a known calibration error.

CHAPTER III

Parameter Sensitivity Studies

3.1 Introduction

With design and sensitivity studies presented in further chapters, an examination of possible test cases is presented in the current chapter. Two test geometries are being considered. The first test geometry is the HyShot-II scramjet combustor, a relatively small hydrogen-air combustor flown in 2002 [5]. The second geometry is the HIFiRE-2 scramjet combustor, a larger hydrocarbon-air combustor flown in 2012 [104]. Both geometries were intended to explore the physical phenomena inside the combustion chamber during flight, but they were not intended to produce a net thrust to power their respective craft.

The examination in the following sections discusses the importance of geometric approximations, flowfield medium, parametric selection, radiative boundary conditions, and the necessity of coupling the thermal radiation to the calculations of the medium.

With thermal radiation being a geometry-dependent phenomenon, a number of questions arise as to the approximations and implications of geometry. One issue is the validity of lower-dimensional approximations, which often prove useful in certain applications such as atmospheric modeling [46, 65]. Additionally, the physical size of the test case is an issue that may have a strong impact on importance of radiative heat

transfer in the combustion chambers. The chamber geometry and size are examined to determine the validity of a number of approximations.

With thermal radiation being a medium-dependent phenomenon, a number of questions arise as to the sensitivity of individual physical factors within the medium. Many medium properties are shown to be very important in specific modeling regimes but not in other regimes. The importance of various radiative contributing properties and the sensitivities of the overall simulation outputs to the physical properties is examined for the purpose of selecting appropriate factors for parameter variation studies presented in later chapters.

With thermal radiation being a boundary condition-dependent phenomenon, an examination of possible boundary conditions is required to determine the impact on the final radiative quantities within the simulation. Widely varied boundary conditions are a possibility, even within the same test run in a scramjet combustion chamber, which can greatly alter the radiative characteristics [69]. A number of possible boundary conditions are considered to examine the impact of the design studies in further chapters.

Finally, with thermal radiation being a phenomenon physically coupled to the thermal energy of the medium, a number of questions arise as to the necessity of direct coupling of thermal radiation to the flowfield simulations. Radiative heat transfer can cause significant temperature changes within a combustion chamber, which in turn, can affect all portions of an engine flowfield [35]. The effect of thermal radiation on the medium temperature and the necessity of thermal coupling is examined. This knowledge is used to determine the necessity of coupling to the flowfield solvers in future work.

3.1.1 HyShot-II

The HyShot-II combustor is a hydrogen-air supersonic combustion experiment flown by the University of Queensland in 2003 with continuing ground experiments run by the German Aerospace Center (DLR). The main combustion chamber, as given in Fig. 3.1, has a rectangular cross section with dimensions of 75 mm wide by 9.8 mm high. The chamber is 300 millimeters long with a series of four evenly-spaced injection ports 58 mm downstream of the combustion chamber entrance. The exit of the combustion chamber is attached to a 12° vertically expanding nozzle. Not shown in the diagram is the vehicle tip and compression ramp, which begin 450 mm upstream of the chamber entrance.

The flow-path of the combustor was intended to have a supersonic air stream enter and undergo a series of compressive shocks before fuel enters the stream at the injection ports. The fuel ignites, burning through the combustion chamber before being accelerated in the expansion nozzle. The particular test case considered in this work has free-stream conditions that correspond to those of the ground experiments performed by Karl et al., with a pressure of 1813 Pa, a temperature of 242 K, a density of 0.0260 kg/m^3 , a velocity of 2313 m/s, and a Mach number of 7.4 [56] Fuel is injected at an equivalence ratio of 0.29 and is evenly distributed across all four injectors.

The flowfield simulation is performed with an unstructured RANS approach with a nine species combustion model as described in section 2.4. The simulation was run on a 6.8 million point unstructured grid, for which only one-eighth of the domain was modeled. The one-eighth model was a result of the even spacing of the injection ports and a high aspect ratio, which allowed for planes of symmetry to be assumed on both the centerlines of the injection ports as well as the plane halfway between the injection ports.

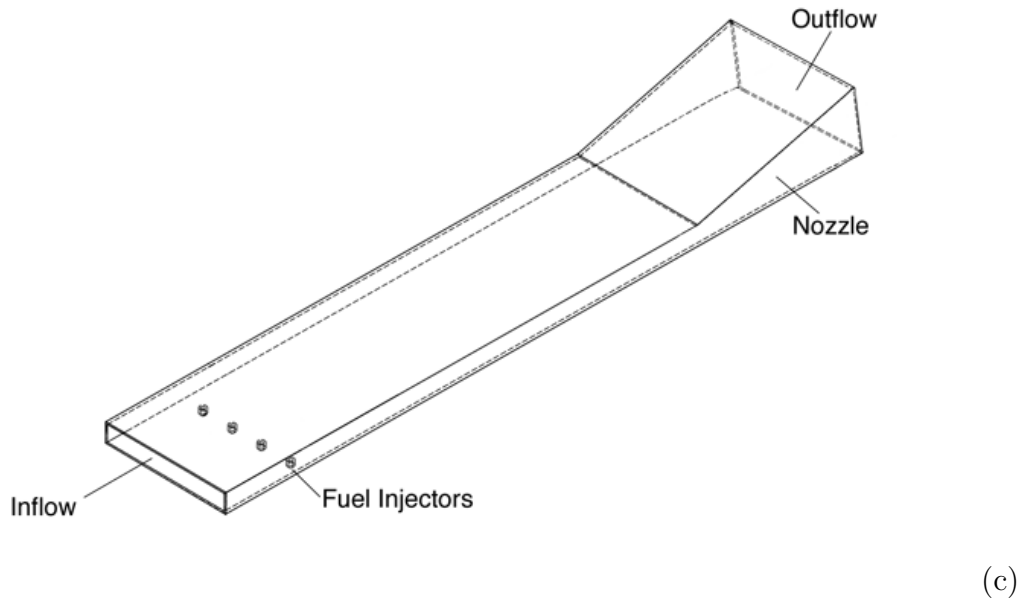
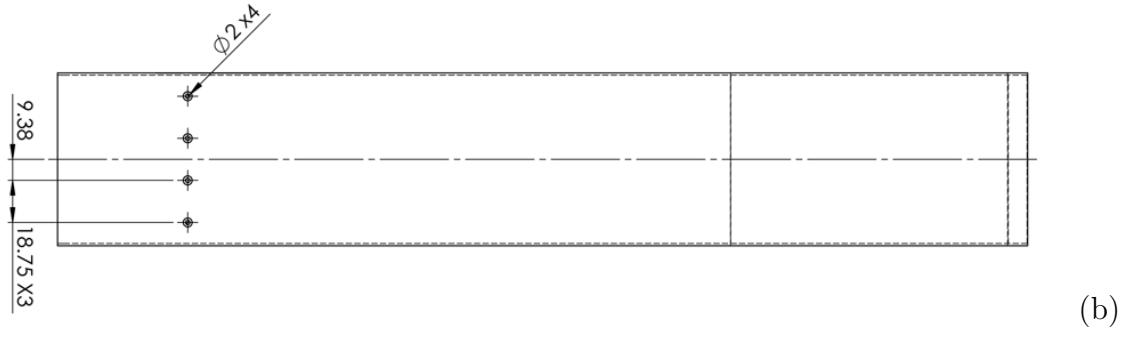
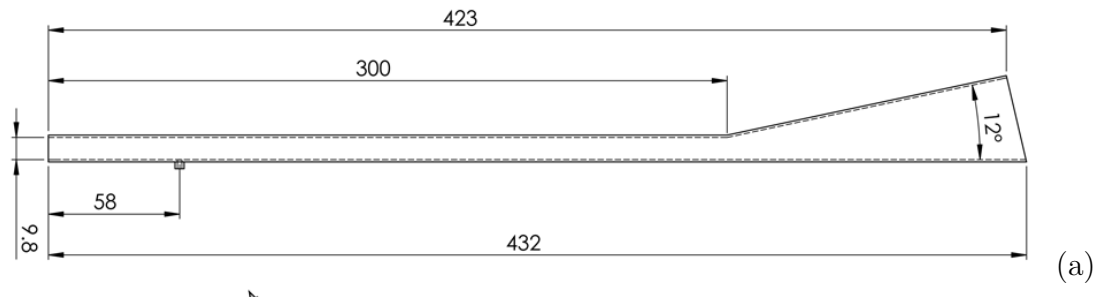


Figure 3.1: HyShot-II combustion chamber geometry. (a) Side, (b) bottom, (c) Orthographic. All dimensions in millimeters. Flow is from left to right.

The flowfield results from the simulations are expanded by mirroring them across their planes of symmetry to show a one-half flowfield view in Figs. 3.2 and 3.3. These simulations are the same datasets used in previous works, and as such, additional analysis may be found in the works by Crow, *et al.* [21, 22]. In these simulations, flow is from left to right with a coordinate system defined as given in Figs. 3.2 and 3.3, with the origin for the x , y , and z directions set at the injection port centerlines, the bottom wall of the chamber, and the chamber centerline, respectively.

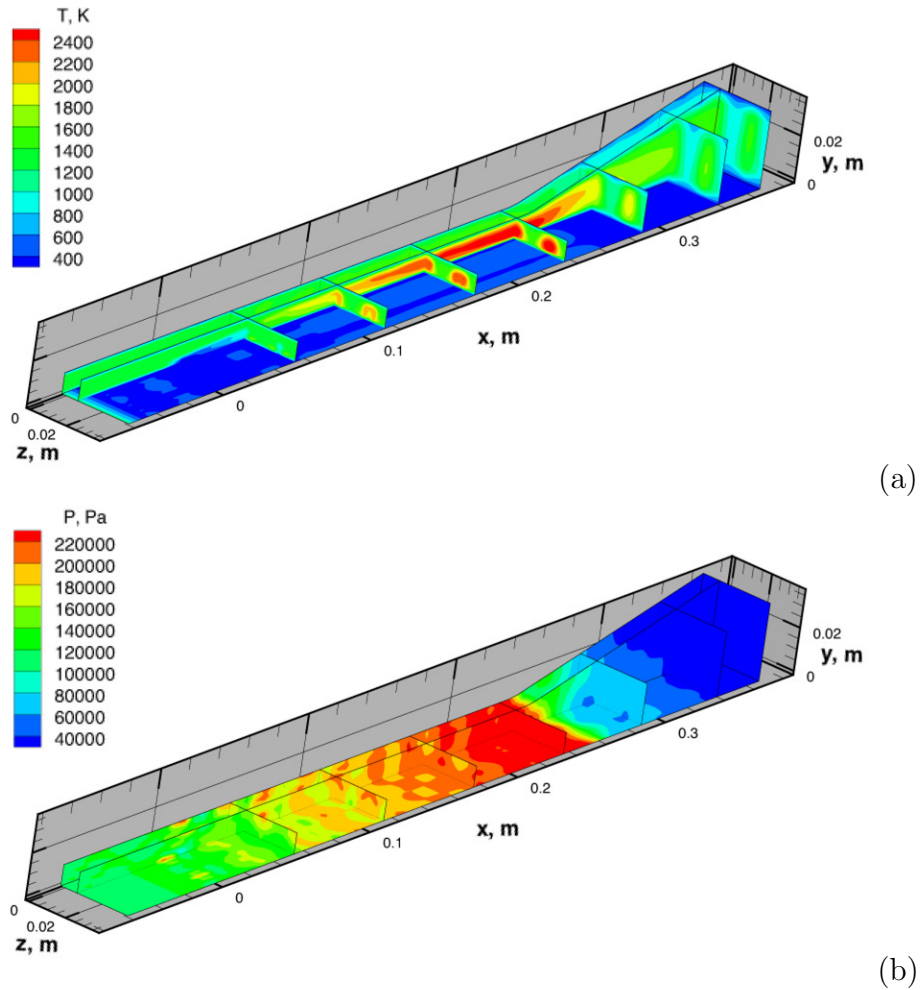


Figure 3.2: HyShot-II combustion chamber RANS calculations (without radiation) for (a) Temperature and (b) Pressure. Flow is from left to right.

The temperature profiles are given in Fig. 3.2 (a), which depicts the cool bottom wall at $y = 0.000$ m, the injection of the cold fuel at $x = 0.000$ m, the formation of a hot

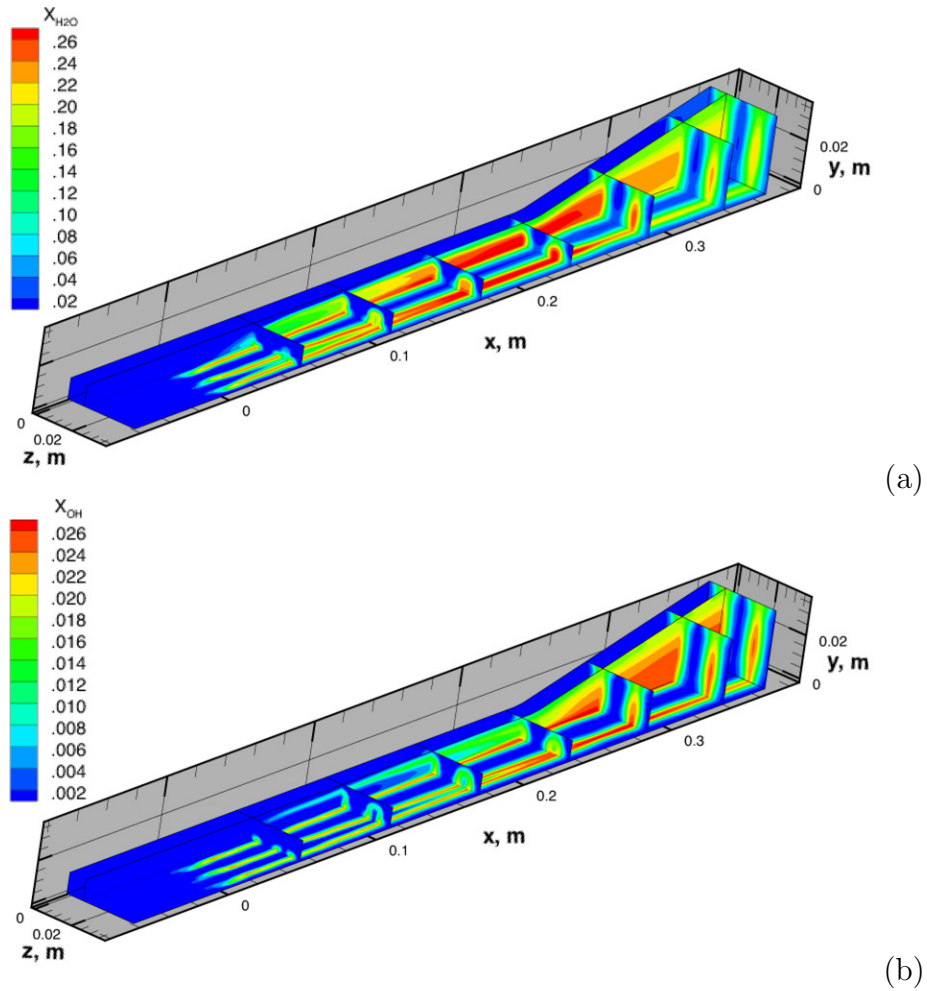


Figure 3.3: HyShot-II combustion chamber RANS calculations (without radiation) for (a) H₂O and (b) OH mole fraction. Flow is from left to right.

three-dimensional flame structure, and the expansion and cooling of the flame in the exit nozzle at $x = 0.25$ m. The entrance temperature into the combustion chamber is 1225 K, which is significantly higher than the free-stream temperature as the vehicle bow-shock (not-shown) and inlet shock train significantly heat the incoming air before the combustion chamber entrance. The peak temperature of the flow is 2550 K near the transition from the combustion chamber to the expansion nozzle ($x = 0.242$ m). The pressure plot is given in Fig. 3.2 (b). The flow at the combustion chamber inlet is about 115 kPa due to the shock compression. The pressure does not have smooth transitions due to numerous internally reflecting shockwaves and the notable

pressure spike at the injection port. The pressure rises to a peak of 241 kPa in the uniform cross-section portion of the chamber as combustion progresses, and lessens in the nozzle as the flow expands.

The mole fractions of two combustion products, water vapor and the hydroxyl radical, are given in Figs. 3.3 (a) and (b), respectively. Other combustion products have only trace fractions and are omitted in the figures. The combustion products form as the flame progresses giving a definite three-dimensional flame structure in the combustion chamber ($x = 0$ to $x = 0.242$ m). However, the products spread and homogenize in the nozzle ($x = 0.242$ to $x = 0.344$ m).

3.1.2 HIFiRE-2

In addition to the HyShot-II combustor, a ground experiment duplicating the HIFiRE-2 combustor is considered in this work [39, 104]. The main reason for the consideration of the HIFiRE-2 combustor is the low importance of thermal radiation in the HyShot-II combustion chamber [21]. It is anticipated that the radiative component of wall heat flux will be higher in the HIFiRE-2 combustor due to two effects: First, the HIFiRE-2 combustor uses hydrocarbon fuel that generates significant quantities of radiating species, such as carbon dioxide, that are absent from HyShot-II; and second, the HIFiRE-2 combustor is significantly larger in volume than the HyShot-II combustor.

The main simulation domain is based on the experiment described in section 2.5 and attempts to duplicate the HDCR at NASA Langley, not the exact flight vehicle. However, the HDCR does attempt to duplicate the flow characteristics of the flight experiments [10]. A diagram of the HDCR is given in Fig. 3.4, where the flow is from right to left, and the facility nozzle is visible. The entire domain has a rectangular cross section with a 4 inch width (z -direction) and a variable, symmetric vertical dimension (y -direction). The coordinate system is defined in Fig. 3.4 with

the vertical, “ y ,” and horizontal, “ z ,” origins being set at the facility centerline with the streamwise, “ x ,” origin being significantly upstream of the nozzle.

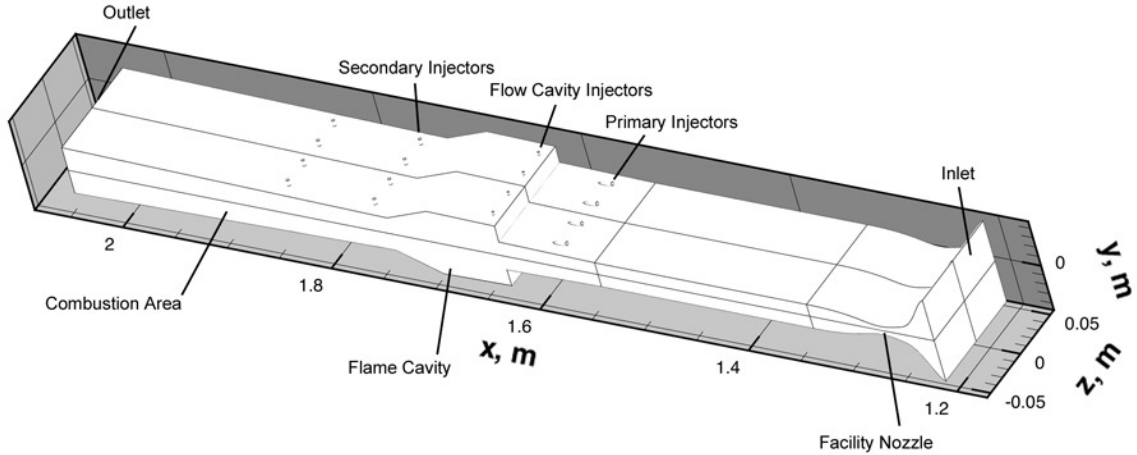


Figure 3.4: HDCR domain: Illustration of the facility nozzle, flame holding cavity, injection ports, and outlet. Flow is from right to left.

In the current chapter, an examination of the HDCR is based on the AFRL RANS simulations using the computational solver described in Section 2.4. The simulation utilized a 1.4 million point mesh to capture a one-quarter domain with planes of symmetry about the vertical, “ y ,” and horizontal, “ z ,” axes.

The computational results simulate the HDCR in an attempt to duplicate the Mach 6.5 flight of the HIFiRE-2 scramjet. The equivalence ratio is 1.0 for a 0.36-0.64 methane-ethylene fuel mixture. The results are given in Figs. 3.5 through 3.7.

The temperatures given in Fig. 3.5(a) shows a peak in the flame holder around 2800 K and remains between 2000 K and 2800 K for the remainder of the combustion chamber. The wall temperature peaks around 1900 K for the slow regions around the injection ports and at the back edge of the flame holding cavity. The wall temperature generally stays between 1200 K and 1400 K for areas not in contact with the cold fuel stream. The cooling due to fuel injection can be seen around the injection ports and extends to the chamber exit. The pressure, as given in Fig. 3.5 (b), lies between

300 and 400 kPa in the flame holder and lessens as the flow expands until it reaches a minimum of 140 kPa at the exit. The density, as given in Fig. 3.5 (c), is between 0.7 and 0.4 kg/m³ in the combustion chamber with a reduction to less than 0.2 kg/m³ at the chamber exit. The density has a notable rise in the boundary layers and around the injection ports as given by the increases of up to 2 kg/m³ at the walls. The Mach number, as given in Fig. 3.5 (d), is generally above 1 for most of the flow except for the locations by the sidewalls and in the flame holder. The Mach number increases to 1.5 at the chamber centerline for the exit plane, but it never recaptures the peak of Mach 2.0 that exists before the fuel injectors.

The number densities for the radiative species of interest are given in Fig. 3.6 and Fig. 3.7 in units of mole/m³. The two major radiative species are water vapor and carbon dioxide as given in Figs. 3.6 (a) and (b), respectively. Water vapor displays a high molar concentration in the recirculation region of the flame holding cavity with values of up to 2 moles/m³ around the fuel injectors. Water vapor has almost no concentration upstream of the injection, but after combustion it generally has a concentration between 0.5 mole/m³ and 1 mole/m³, with the exception of around the fuel injectors and in the boundary layer. Carbon dioxide behaves very similarly to water vapor as far as molar concentration is concerned, with the exception that it does not reach as high levels as water vapor does in the chamber. Also, carbon dioxide undergoes a reduction in concentration in the hot flame regions downstream from the fuel injectors, whereas water vapor undergoes an increase in concentration. The resulting higher temperature of water vapor serves to make it the dominant radiative species in the simulation.

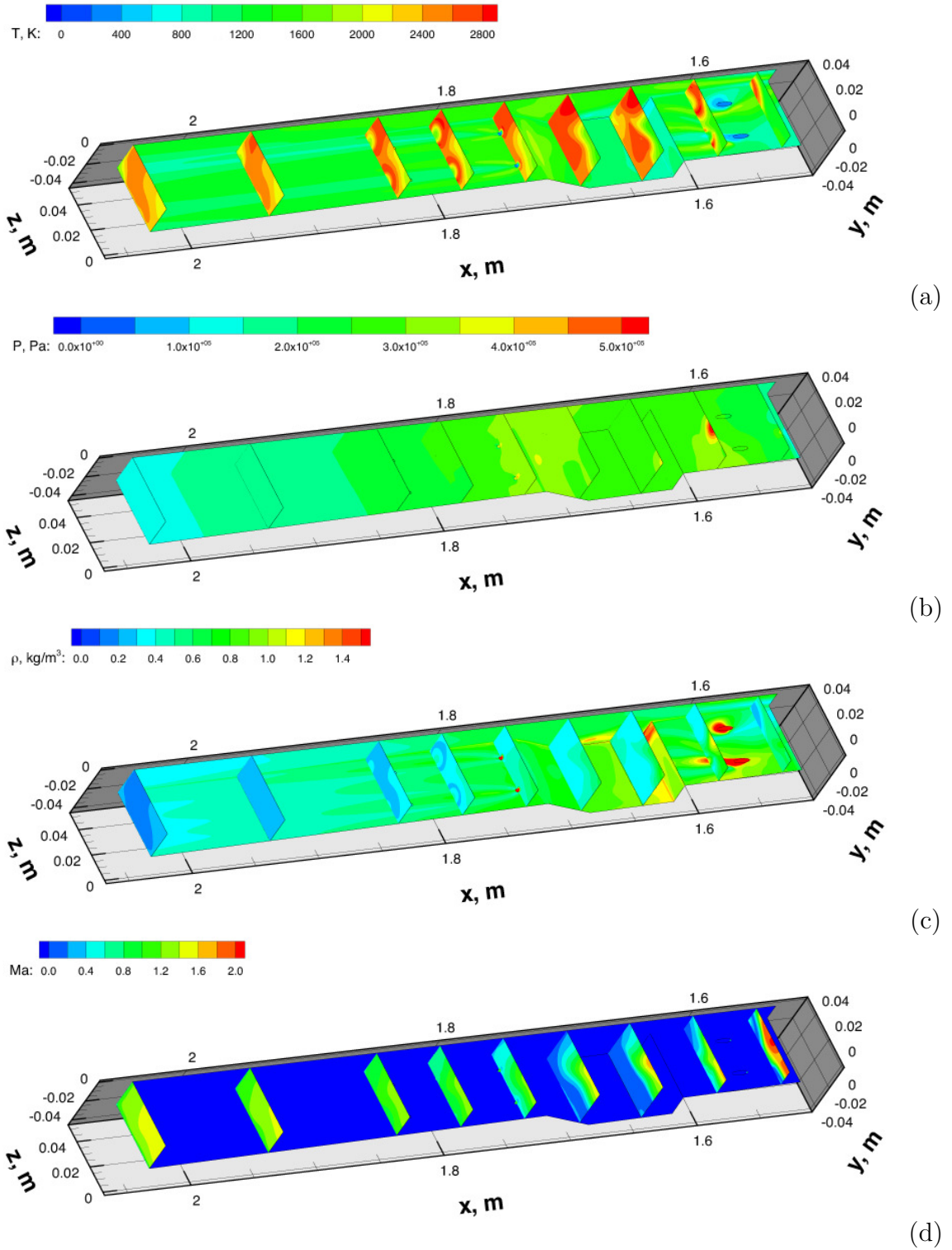


Figure 3.5: HDCR temperature (a), pressure (b), density (c), and Mach number (d) from the AFRL CFD simulation (without radiation). Flow is from right to left.

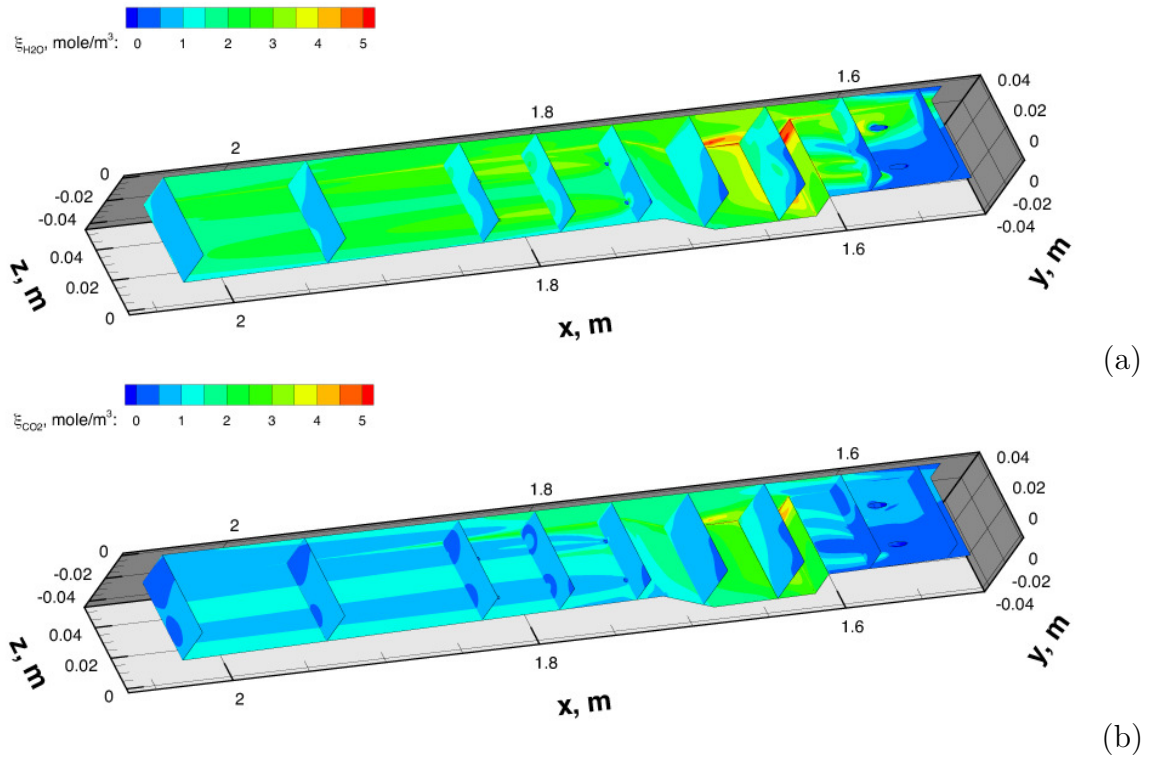


Figure 3.6: HDCR molar concentrations of water vapor (a) and carbon dioxide (b) from the AFRL CFD simulation (without radiation). Flow is from right to left.

The molar concentrations of minor radiative species are given in Fig. 3.7, with the hydroxyl radical (a), carbon monoxide (b), and methane (c) being chosen as the most pertinent species. The hydroxyl radical, being an intermediate reaction species, only exists in concentrations of up to 0.25 mole/m^3 in the flame holder and the edges of the flames [62]. Unlike water vapor, the hydroxyl radical builds up on the outside of the flame structure as opposed to within. This location may serve to lower its importance as a radiator because it exists more in the cooler regions of the flow. Carbon monoxide tends to only exist in the incompletely combusted fuel stream, and it does not build up concentrations in the flame holder. Having values as high as 0.6 mole/m^3 downstream of the fuel injectors and up to 2.0 mole/m^3 around the fuel injectors, the overall concentration of carbon monoxide decreases significantly over the length of the chamber. Being mainly located in the hottest region of the flame, carbon monoxide can play a significant role in localized wall heating. Finally, methane is injected in high concentrations as a fuel at the injection ports. The injection concentrations are as high as 50 mole/m^3 but quickly disperse and diminish as they undergo combustion. While likely not a major contributor of heating to other parts of the flow, methane is considered in this analysis as a possible means of transferring heat into the cold fuel stream.

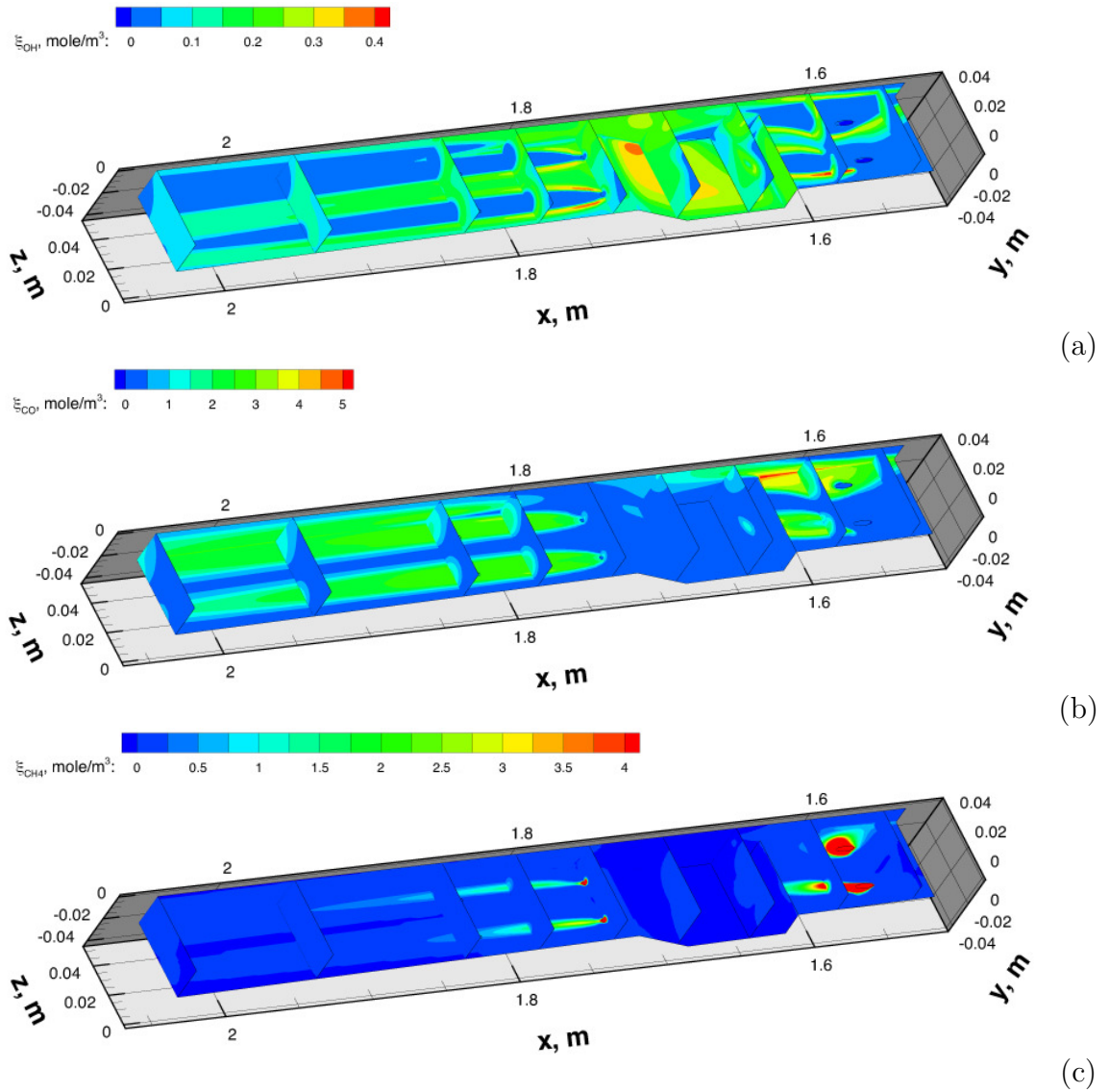


Figure 3.7: HDCR molar concentrations of the hydroxyl radical (a), carbon monoxide (b), and methane (c) from the AFRL CFD simulation (without radiation). Flow is from right to left.

3.2 Geometric Approximation

In the previous examinations of thermal radiation of the HyShot-II combustor, several important factors have been studied that warrant a reexamination in this work. The two factors in this section are both geometric simplifications that have been useful in the past [21, 22]. The first examination is a comparison of the geometric simplification of a plane-parallel representation of the HyShot-II combustion chamber versus a fully three-dimensional spatial model. The goal behind this modeling approximation is to justify plane-parallel and simplified one-dimensional geometries as representative unit problems in order to gather data on the radiative field. Such data include frequency resolved optical path length, species sensitivity, and overall heat flux. The second examination is a consideration of the importance of overall physical problem size and pertinent composition when considering a scramjet combustion chamber. Previous work has found that thermal radiation within a scramjet varies greatly due to combustion chamber size and flow composition, and the work has found that thermal radiation can be a significant mechanism for heat transfer [77]. The flow conditions of the previous works differ greatly from conditions in the HyShot-II [5]. Therefore, additional simplifications are made to allow direct comparisons to the HyShot-II combustion chamber.

3.2.1 Simulation Dimensions

With the goal of using one-dimensional unit problems as representative surrogates for a portion of a medium, a comparison between a one-dimensional method and a three-dimensional method is required. One-dimensional methods have been demonstrated in previous works as a good gauge of system behavior, especially in atmospheric simulations, but it is helpful to determine the applicability for the cases of interest [46]. The two methods employed are the three-dimensional RT method and the one-dimensional DOM method. Both employ identical spectral band models. The

RT method is described in detail in Section 2.2. The one-dimensional DOM is a vast simplification of the flowfield geometry. The medium is assumed to be plane-parallel in that the medium is homogeneous and infinitely wide in the planes parallel to the surface of interest. However, the medium can vary in the direction normal to the surface of interest. A one-dimensional DOM grid is used to approximate the parallel planes employing an S_n weighting scheme [28]. For both cases, the only radiative species considered are water and the hydroxyl radical.

The individual meshes are extracted from the CFD flowfield for points given in Table 3.1. All points of interest are along the lower wall ($y = 0.0$ mm), with the corresponding meshes extending into the flowfield. The points are either at the flow centerline ($z=0.0$ mm) or in a combustive region ($z = 6.0$ mm). The points are located in the main combustion chamber ($x = 42$ and 92 mm), at the combustion chamber exit ($x = 242$ mm), and in the expansion nozzle ($x = 292$ and 342 mm). All physical boundary conditions are assumed to be non-reflective and perfectly absorbing ($T_{wall} = 0$, $r_\nu = 0$, and $\epsilon_\nu = 1$).

For the RT method, a series of traces are taken, intersecting each point of interest in a structured manner. The hemisphere solid angle is discretized into 72 evenly spaced azimuthal, “ θ ,” directions and 18 evenly spaced vertical, “ ϕ ,” directions. The medium is sampled along each direction’s line of sight at intervals of 0.5 mm. For the DOM method, a singular trace is taken normal to the bottom of the combustion chamber for each point of interest. The flowfield is sampled along individual traces with spacing between 0.05 and 0.12 mm.

The individual heat flux results are given in Table 3.1 for both methods at several locations. Several notable trends are present in the comparison of methods. The first notable trend is that along the centerline there are significant disparities between the RT and DOM stemming from the flame not propagating into the centerline until the expansion nozzle. Even then, only a negligible amount of radiative material is present

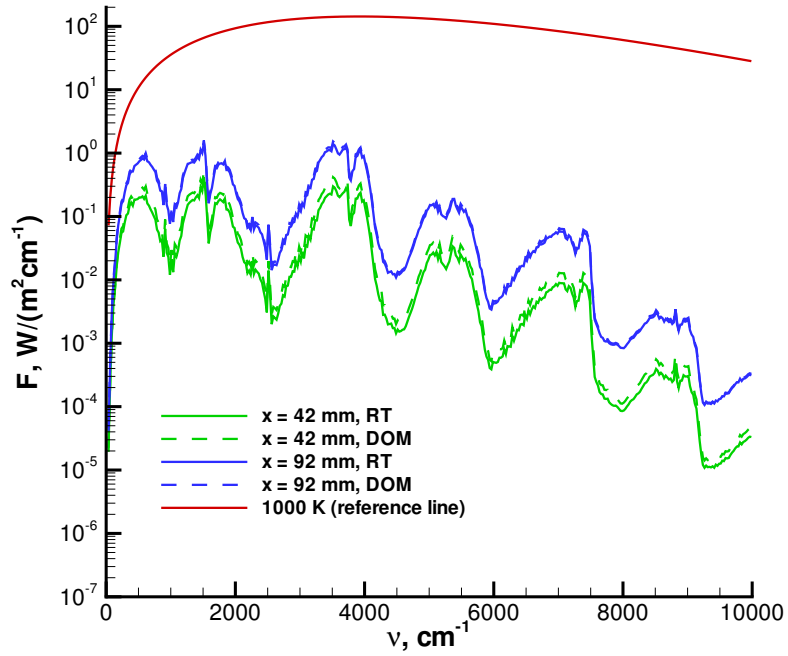
directly above the centerline. Without radiative material directly above the point of interest, the one-dimensional trace cannot take into account the local radiative material. This trend greatly diminishes the merit of the one-dimensional DOM as a predictive tool when compared to the ray tracing method, which can also take into account radiative material adjacent to the point of interest in the simulation. The second trend is that, within the flame, the methods match to within 40% of each other at corresponding locations. This trend, also, does not support the use of one-dimensional DOM as a highly accurate predictive tool in three-dimensional flame environments. However, it does support that, when chosen properly, an individual one-dimensional profile can give a rough estimation of the overall character of the flow. The final trend is that the convective heating from the RANS simulation is three to four orders of magnitude higher than the radiative heat flux predictions, a trend which has been noted in multiple publications, with a full three-dimensional DOM examination showing that no notable radiative hot-spots emerge [22]. Thus, the trend does not justify a further investigation of thermal radiation in the HyShot-II combustion chamber as a significant means of heat transfer [21].

Table 3.1: Comparison of convective and radiative heat fluxes using the 1D DOM and the 3D RT methods at the lower wall ($y=0.0$ mm)

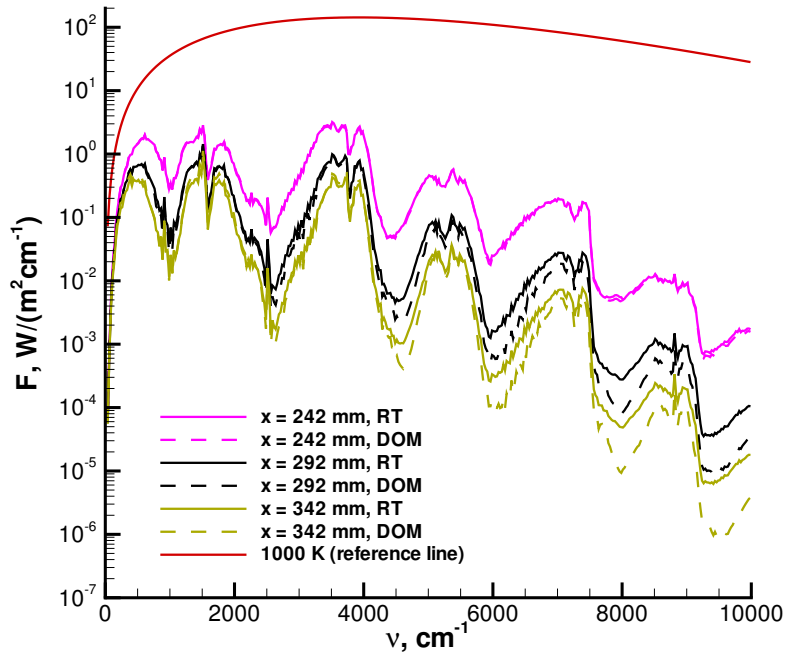
x	y	F	F	F/F	F	F/F
(mm)	(mm)	(RT)	(DOM)	(DOM)/(RT)	(Conv.)	(Conv.)/(RT)
		(W/m ²)	(W/m ²)	(%)	(MW/m ²)	(%)
42	0.0	363	0	0.0%	4.05	0.0090%
92	0.0	1090	0	0.0%	4.23	0.0258%
242	0.0	2589	0	0.0%	4.77	0.0542%
292	0.0	1260	1	0.0%	2.42	0.0521%
342	0.0	591	1	0.2%	1.28	0.0461%
42	6.0	431	587	136.2%	3.94	0.0109%
92	6.0	1982	2182	110.0%	5.80	0.0342%
242	6.0	4903	5056	103.1%	6.38	0.0768%
292	6.0	1433	1346	93.9%	2.05	0.0698%
342	6.0	670	765	114.3%	2.61	0.0256%

The usefulness of one-dimensional profiles for predicting the overall behavior depends not only on the absolute heat flux transmitted but also on the reliability of the spectral profile, as the ability to predict the character of a three-dimensional error based on the variations shown in a one-dimensional profile is crucial to the error propagation method given in Section 2.2. The spectral heat flux profiles are presented in Fig. 3.8 for the RT and DOM predictions located at 6.0 mm from the centerline as given in Table 3.1.

The trends given in Fig. 3.8 show that the overall spectral features remain consistent between methods and even among different locations with significantly different radiative heating. These predictions hold to within 50% for the corresponding location and the adjacent centerline location. This comparison indicates that a one-dimensional profile can characterize the heat flux and spectrum for a given three-dimensional region. This correlation is demonstrated in thin-walled flame profiles such as the locations of $x = 42$ and 92 mm, as well as in completely solid flame profiles such as at $x = 242$ mm. Additionally, the correlation is demonstrated in more diffuse locations, such as $x = 292$ mm, and even when geometry limits the field of view of the three-dimensional methods, such as at the location of $x = 342$ mm. Once again, it is emphasized that these profiles must be chosen to be representative of the flow, containing a similar temperature, radiative species concentration, and characteristic length of the flow feature being considered, which, in this case, is the flame structure. Additional rigor for choice and representation of a one-dimensional profile is discussed in Section 4.2. The justification of these parameters is given in subsequent sections of this chapter.



(a)



(b)

Figure 3.8: Spectral heat flux profiles for the using DOM (dashed) and RT method (solid) at the lower wall ($y=0.0 mm$) for various locations given in Table 3.1.

3.2.2 Size Approximations

The final lesson of the HyShot analysis is that the one-dimensional profiles are useful in justifying further investigation into different types of scramjets. An earlier work behind scramjet radiative analysis found that thermal radiation within a hydrogen-fueled scramjet could be as high as 10% of the total heat flux [77]. However, those simulations were demonstrated to vary significantly based on physical chamber dimensions. Additional work in similar supersonic combustive flows discovered that radiation could overtake convection as the primary means of heat transfer if the flow becomes large enough [72].

The comparison is made between the HyShot-II combustion chamber and a hypothetical combustion chamber presented by Nelson, which was found to have significant radiative properties. The geometries and compositions of the two cases do not match, and the HyShot-II simulations are non-homogeneous, whereas the hypothetical combustion chamber is homogeneous. As such, a one-dimensional problem is chosen to compare the simulations. The one-dimensional profile is advantageous because it allows for a direct comparison for characteristic length, and inhomogeneous profiles properties can be characterized by their averages, as is similar to the procedure of the Curtis-Godson Approximation [36]

The single DOM profile taken at $x = 242$ mm and $y = 6.0$ mm is treated as the representative HyShot-II profile, and several homogeneous flowfields are sampled from the work by Nelson. The sizes chosen are the height of the HyShot-II combustion chamber (9.8 mm) and the smallest scaled length in the hypothetical combustion chamber (66.5 mm). In order to change between the two chamber lengths, the cell sizes are scaled accordingly. The profile for the HyShot-II case is left inhomogeneous, whereas the hypothetical profiles are homogeneous profiles in all simulations. The boundary conditions are two parallel, cold, non-reflective plates ($T_{wall} = 0$, $r_\nu = 0$, and $\epsilon_\nu = 1$).

Table 3.2: Comparison of variation between data from Nelson [77]. and the HyShot-II test cases. The temperature, pressure, and mole fraction quantities for the HyShot simulation are averages. The quantities for the Nelson cases are uniform throughout the flow domain.

Flow-field Data	z (mm)	F (W/m ²)	T (K)	P (Pa)	X _{H2O}	X _{OH}
HyShot Exit (Averaged)	9.8	5.06×10^3	1970	2.19×10^5	0.137	0.0113
HyShot Exit (Averaged)	66.5	2.94×10^4	1970	2.19×10^5	0.137	0.0113
Nelson Mach 14	9.8	2.65×10^4	2920	4.75×10^5	0.205	0.0200
Nelson Mach 14	66.5	1.44×10^5	2920	4.75×10^5	0.205	0.0200
Nelson Mach 9.77	9.8	5.71×10^4	3090	8.89×10^5	0.269	0.0290
Nelson Mach 9.77	66.5	2.85×10^5	3090	8.89×10^5	0.296	0.0290
Nelson Mach 7.67(a)	9.8	2.34×10^4	2720	5.76×10^5	0.204	0.0200
Nelson Mach 7.67(a)	66.5	1.25×10^5	2720	5.76×10^5	0.204	0.0200
Nelson Mach 7.67(b)	9.8	4.51×10^3	1960	2.90×10^5	0.110	0.0150
Nelson Mach 7.67(b)	66.5	2.54×10^4	1960	2.90×10^5	0.110	0.0150

The resulting heat fluxes and flowfield characteristics for all mediums and geometries are given in Table 3.2. For the cases of the 66.5 mm geometry, all radiative conditions are significantly higher than with the 9.8 mm geometry. Additionally, a comparison of the geometric (and spectral) differences from the current one-dimensional work to the previous work (given in Table 3.3) demonstrates that the single profiles can still approximate the general order of magnitude of the radiative heat flux.

Table 3.3: Comparison of variation between data from Nelson [77]. and current the one-dimensional approximations of the flowfields presented in this work.

Flow-field Data	z (mm)	F (Nelson) (W/m ²)	F (1-D) (W/m ²)
Nelson Mach 14	66.5	1.44×10^5	1.254×10^5
Nelson Mach 9.77	66.5	2.85×10^5	1.396×10^5
Nelson Mach 7.67(a)	66.5	1.25×10^5	8.31×10^4
Nelson Mach 7.67(b)	66.5	2.54×10^4	1.61×10^4

Across all cases, the changes in geometry demonstrate a significant increase in radiative heat flux with the increase in combustion chamber size. This trend is expected in a situation where the thermal radiation can be considered optically thin

[22]. With the changes in geometry, the hypothetical profiles still garner a higher radiative heat flux than that of HyShot-II. The exception is the Mach 7.67(b) example, which generally behaves similarly to the HyShot-II example for both geometry sizes. These behaviors are similar, even when comparing the spectrally resolved heat fluxes, as given by Fig. 3.9. The agreement or lack-there-of between the HyShot case and the hypothetical cases can be explained only by the variations in flowfield properties. With a predictable agreement with three-dimensional solutions and an ability to directly compare flow regimes for both size and quantities, the one-dimensional approximation can work as a reasonable predictive tool.

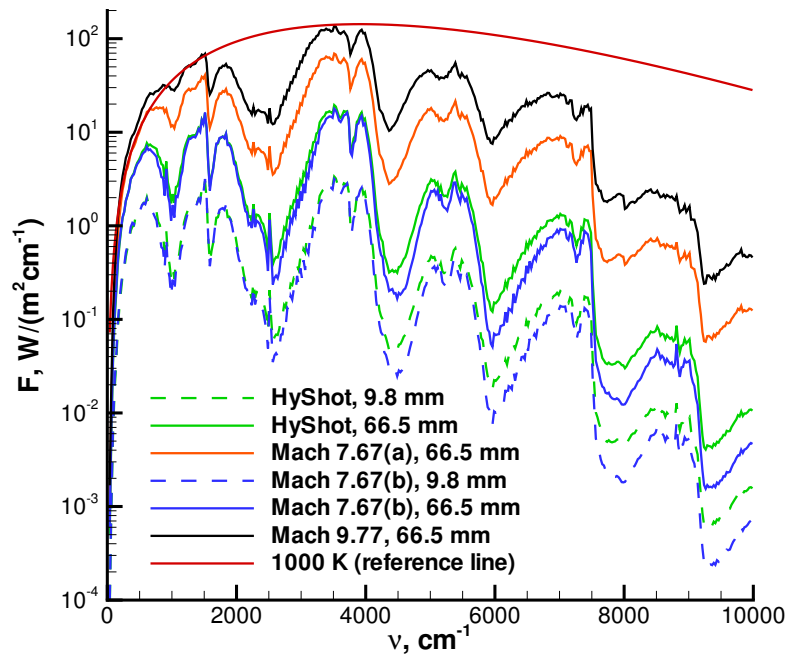


Figure 3.9: Spectral heat flux profiles using DOM for various conditions given in Table 3.2

3.3 Flowfield Parameters

Even with geometric constraints, it has been shown in the previous section that the range of what is considered reasonable for scramjet flowfields can result in greatly differing radiative heat fluxes. As such, an investigation into the important flowfield factors, whose variation affects the final output, are considered. The main goal of this section is to determine the magnitude of the effects of individual flowfield parameters and use these quantified effects to make decisions as to which parameters are to be considered for parametric variation studies.

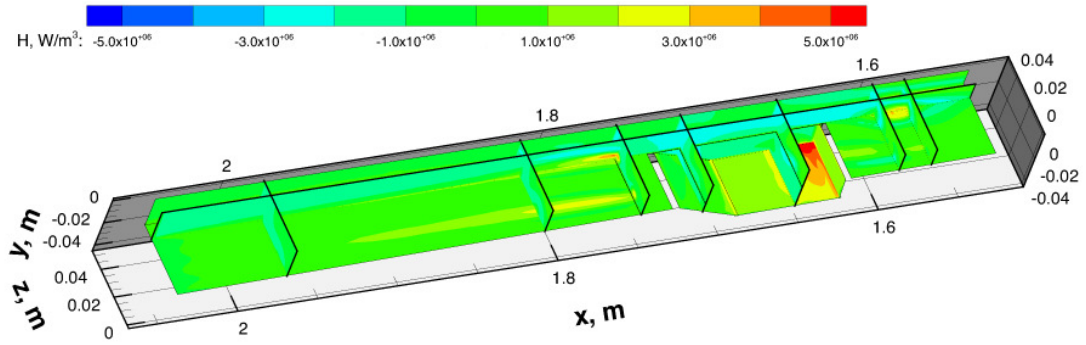
The flowfield under consideration is the Mach 6.5 HIFiRE-2 RANS simulation discussed earlier in the chapter. The flowfield is sampled with a coarse mesh consisting of a 89 thousand point hexahedral structured grid, which is simulated using the GRASP DOM code with a two-point banded spectral model ranging from wavenumbers of 25 to 10000 cm^{-1} and a bandwidth of 25 cm^{-1} . Five radiative species are studied: water vapor, carbon dioxide, carbon monoxide, the hydroxyl radical, and methane. An S_8 weighting scheme is used for the simulation [29] The simulation encompasses one quarter of the physical domain with reflective boundary conditions at the vertical and horizontal centerlines, $y = 0$ m and $z = 0$ m, respectively.

The fluid inflow and outflow are taken as perfectly absorbing, non-emitting walls. The physical walls are simulated as fully absorbing non-emitting ($T_{wall} = 0$, $r_\nu = 0$, and $\epsilon_\nu = 1$). The resulting heat flux calculations are given in Fig. 3.10. The radiative volumetric heating, given in Fig. 3.10 (a), depicts the flow cooling at a maximum of 5 MW/m^3 in the flame holder and a more general heat loss between 1 MW/m^3 to 4 MW/m^3 downstream of the cavity. The volumetric heat loss is smallest in the fuel streams and it even becomes a heat gain directly around the cold fuel injection ports. The total radiative wall flux, given in Fig. 3.10 (b), depicts the highest amount of radiative heat transfer at 56 kW/m^2 in the flame holder with a reduction to 20 kW/m^2 at the chamber exit. The downstream radiative heating does not have as much of a

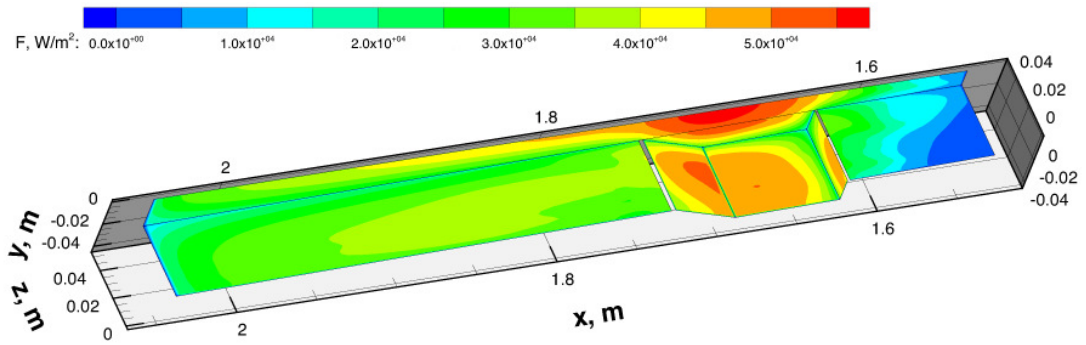
localized effect as does convective heating as given in Fig. 3.10 (c). Upstream of the fuel injection, the effects are negligible.

The convective wall heating, as taken from the CFD simulation, is depicted in Fig. 3.10 (c) with peak heat transfer of up to 3 MW/m^2 around the fuel injection ports and at the back edge of the flame holding cavity. The convective heat transfer is lowest within the stagnation region of the flame holding cavity. When the radiative heat transfer is compared to the convective heat transfer, as given in Fig. 3.10 (d), it is found that radiative heat transfer has the highest relative values directly around the injection ports and in the stagnation region of the flame holding cavity, with values over 10% of those of the convective heat transfer. This phenomenon is mainly due to the low convective heat transfer in these regions. Where convective heat transfer is higher, radiative heat transfer levels off to between 2 to 3% of the convective heat transfer. With localized values of up to 10% of the convective heat transfer, HIFiRE-2 may still be a worthwhile radiative test case.

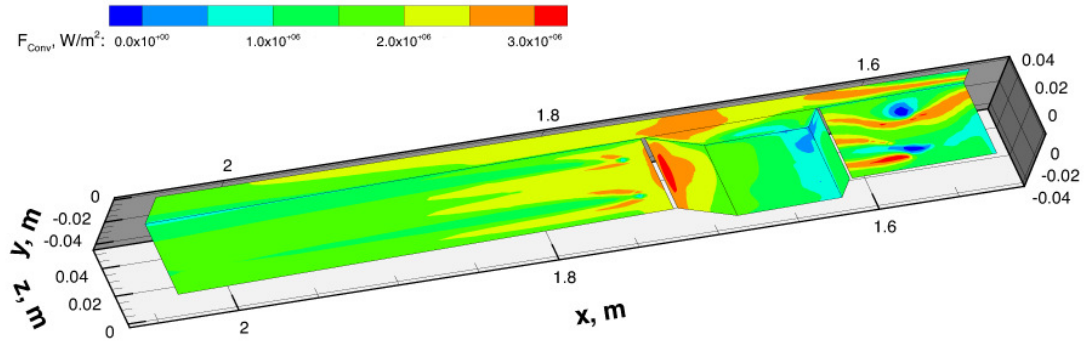
An adjoint sensitivity analysis is performed in order to gather a direct quantification of both the location and magnitude of the effects of flowfield properties of interest. The adjoint method tracks the importance of flow variables to the final heat flux.



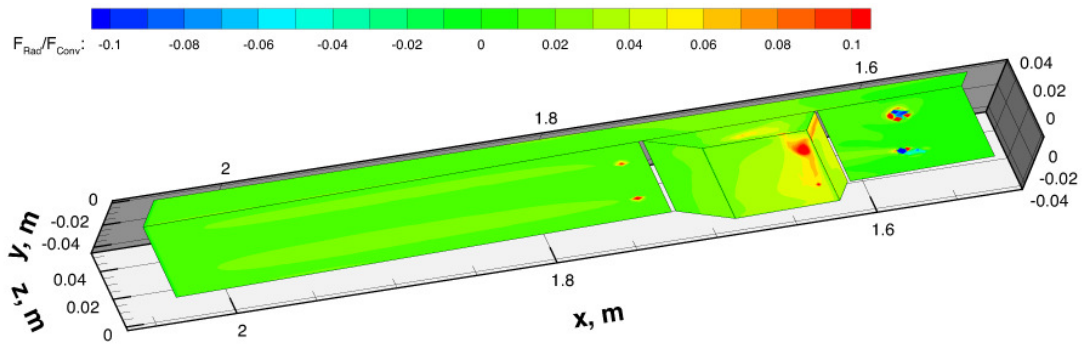
(a)



(b)



(c)



(d)

Figure 3.10: DOM solutions to HIFiRE-2 for (a) volumetric radiative heat loss per cell, (b) radiative heat flux at the wall, (c) convective heat flux at the wall, and (d) the ratio of radiative to convective heat flux at the wall. Flow is from the right to left.

3.3.1 Sensitivity Analysis

The importance of individual parameters is determined by a sensitivity study of the flowfield. A discrete adjoint sensitivity method is employed to determine the sensitivity of radiative wall heat flux to the flowfield quantities in local parameter space. The quantities of interest are the interior cell temperatures, total pressures, and concentrations of the radiative species studied. The results, given in Figs. 3.11 and 3.12 for each of the cell quantities, are the first-order prediction of the effect of the individual cell value on the average wall flux. The quantity is calculated by multiplying the per-unit flux sensitivity of each cell by the corresponding cell quantity as in Eq. 3.1. The resulting calculations allow for a direct comparison between the calculated values in any cell. The cell averages for each flow quantity's estimated flux contribution are given in Table 3.4

$$\Delta \overline{F}_u = \frac{\delta \overline{F}_u}{\delta u} / u \quad (3.1)$$

Table 3.4: Cell averaged contribution to wall averaged heat flux for each flow quantity

$\Delta \overline{F}_T$	$\Delta \overline{F}_P$	$\Delta \overline{F}_{H_2O}$	$\Delta \overline{F}_{CO_2}$	$\Delta \overline{F}_{OH}$	$\Delta \overline{F}_{CO}$	$\Delta \overline{F}_{CH_4}$
(W/m ²)	(W/m ²)	(W/m ²)	(W/m ²)	(W/m ²)	(W/m ²)	(W/m ²)
0.928	0.419	0.324	8.72×10^{-2}	3.07×10^{-3}	4.17×10^{-3}	2.30×10^{-4}

The notable trend for the importance of the individual quantities are as follows. The relative importance of temperature within a cell increases with increasing temperature due to the nonlinear relationship of temperature to thermal radiation. Additionally, because all species concentrations are directly proportional to pressure, the relative effect of pressure can be used as a gauge of the importance of all species. In this particular case, due to mole concentrations of up to 2.0 mole/m³ and strong spectral lines, the contributions of water greatly outweigh all other contributions [92]. Carbon dioxide, with weaker lines and a mole concentration of up to 1.3 mole/m³,

has a significantly smaller contribution to the overall heat flux. Carbon monoxide, whereas having similar molar concentration to that of water vapor in certain regions, has a significantly weaker line-strength and, therefore, contributes an order of magnitude less. The hydroxyl radical has a mole concentration of only up to 0.25 mole/m³ and weaker lines than water vapor resulting in maximum contributions of less than 1 percent of that of water vapor. Methane has a very strong concentration in the injection streams, but it has much weaker line structure than any other species. However, it is the dominant species for radiative heat transfer in the unburnt fuel stream. The information gathered is that, as expected, species with stronger line strengths and higher concentrations tend to have a larger total flux contribution. As such, when making a general property selection these factors need be taken into account.

It should be noted that the averages used in Table 3.4 compare the averaged effect of every cell when quantifying the effect of a species. Therefore, a species such as carbon dioxide may only have a total contribution of 13% of that of water, as given in Table 3.4, and a peak value of only 21% that of water as given by Fig. 3.11 (b) and (c). However, closer examination of the figure shows that in the high heat flux region of the flame holder, the contribution of carbon dioxide is on the order of 50-90% of that of water vapor. Thus, regions of importance should be probed before a decision is made on whether or not to include a variable.

The full heat flux sensitivity results are given in Figs. 3.11 and 3.12. As given by parts (a-c), the sensitivity regions of temperature, pressure, and water vapor concentration are highly correlated with each other. This correlation has two general explanations. The first explanation is that temperature rise and water vapor creation are both results of the same combustive process. Examination of Figs. 3.5 and 3.6 shows that this is not a perfect correlation, however, and the correlation does not explain the correlation of pressure.

The other explanation is that radiative emission relies on the local thermody-

namic energy, indicated by the temperature, and the concentration of species that can emit the energy from the local internal energy to the radiative energy. Since water concentration is the dominant emitter, and is directly proportional to pressure, the radiation will be most greatly affected by regions with high levels of both of these factors. However, higher temperatures make these regions more effective emitters. As such, regions with high concentrations of water, (brought on by high pressure) and high temperature show up on all sensitivity results as the most sensitive regions.

In general, the temperature has the greatest effect directly around the injection ports and down-stream in the burning interface of the fuel stream. The effects of temperature tend to even-out as the flow moves downstream. It should be noted that the overall effect of temperature is nonlinear. Therefore, the linear estimation employed in the adjoint analysis tends to over-predict the effect of temperature as indicated by it having a greater predicted effect than that of linear factor pressure.

Both water vapor and carbon dioxide tend to have a significant influence in the cavity holder, and carbon dioxide approaches the same level of emission as water vapor as indicated by Fig. 3.12 (c-d). Water vapor has notable regions of high sensitivity around the burning fuel stream downstream of the flame holder and in some regions within the flame holder. Carbon dioxide has regions of highest sensitivity at the end of the flame holder and in areas away from the burning fuel stream. Unlike water, whose sensitivity correlates mainly with the presence of higher temperature, carbon dioxide's sensitivity correlates more strongly only with regions of high carbon dioxide. This trend is mainly because carbon dioxide is not present in the regions of higher temperature as water vapor is, but it is mainly present in regions of more consistent temperature. Therefore, the patterns in carbon dioxide sensitivity are not as affected by local variations in temperature.

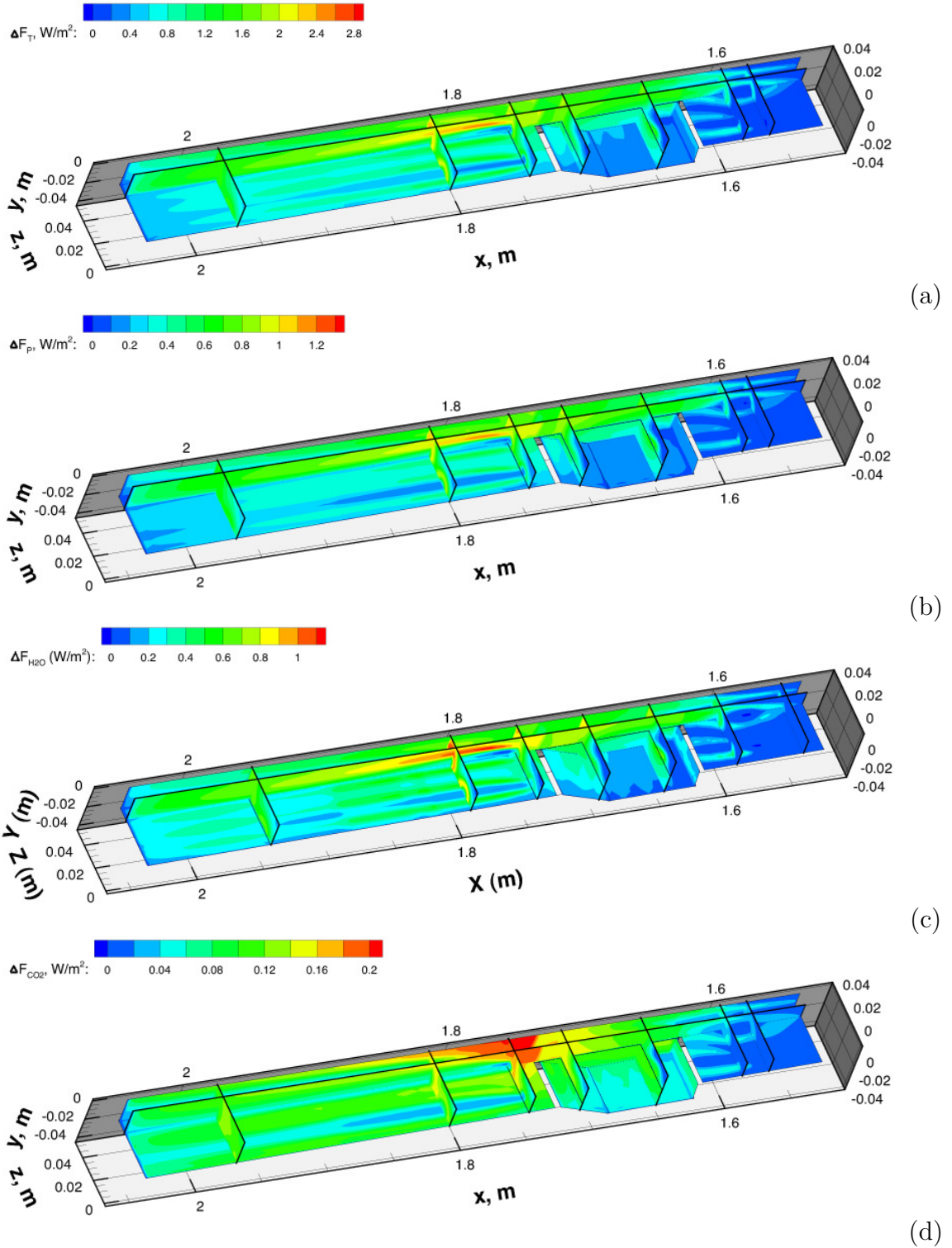


Figure 3.11: Relative contribution of an individual cell quantity to wall heat flux for (a) temperature, (b) pressure, (c) water vapor, and (d) carbon dioxide. Flow is from right to left.

The species with minor predicted contributions are the hydroxyl radical, carbon dioxide, and methane, and they are presented in Fig. 3.12. The radiative sensitivity of the hydroxyl radical is presented in Fig. 3.12 (a). The overall sensitivity tends to peak around areas of highest temperature as with water, but the maximum contribution of hydroxyl is only 1% of that of water. The radical does have some predicted radiative effects in the flame holder, where it serves an important role in the reaction mechanism for the chemistry. Its presence in the hot flamefront is an explanation as to why hydroxyl is most emissive there.

Carbon monoxide only has regions of predicted effects directly encasing the burning fuel and none in the flame holder. This pattern is expected as carbon monoxide is mainly present within the fuel stream. Thus, only the outer regions of carbon monoxide have high enough temperatures to contribute notably to the wall heating. Additionally, some cold regions within the unburnt fuel undergo a mild amount of radiative heating as indicated by a negative sensitivity to carbon-monoxide. These values tend to be negligible, though. The peak predicted contribution of carbon monoxide is about 2.6% that of the peak predicted contribution of water and 12% of the peak contribution of carbon dioxide.

The final species under consideration is methane as given in Fig. 3.12 (c). The peak predicted heat contribution for methane is three times higher than that of carbon dioxide, and it is about 6.5% of the peak contribution of water, mainly due to high concentrations around the fuel injectors. Furthermore, the predicted contributions of methane are limited to a very small spatial region directly around and downstream of the injection ports, resulting in a very small contribution to the wall. However, within the unreacted portion of the fuel stream, methane is the dominant emitter, as indicated by comparing the region directly downstream of the secondary fuel injectors in Fig. 3.12 (c) to the same region in the sensitivity plots of other species, where there is a small gap in the concentrations of other species where only methane exists.

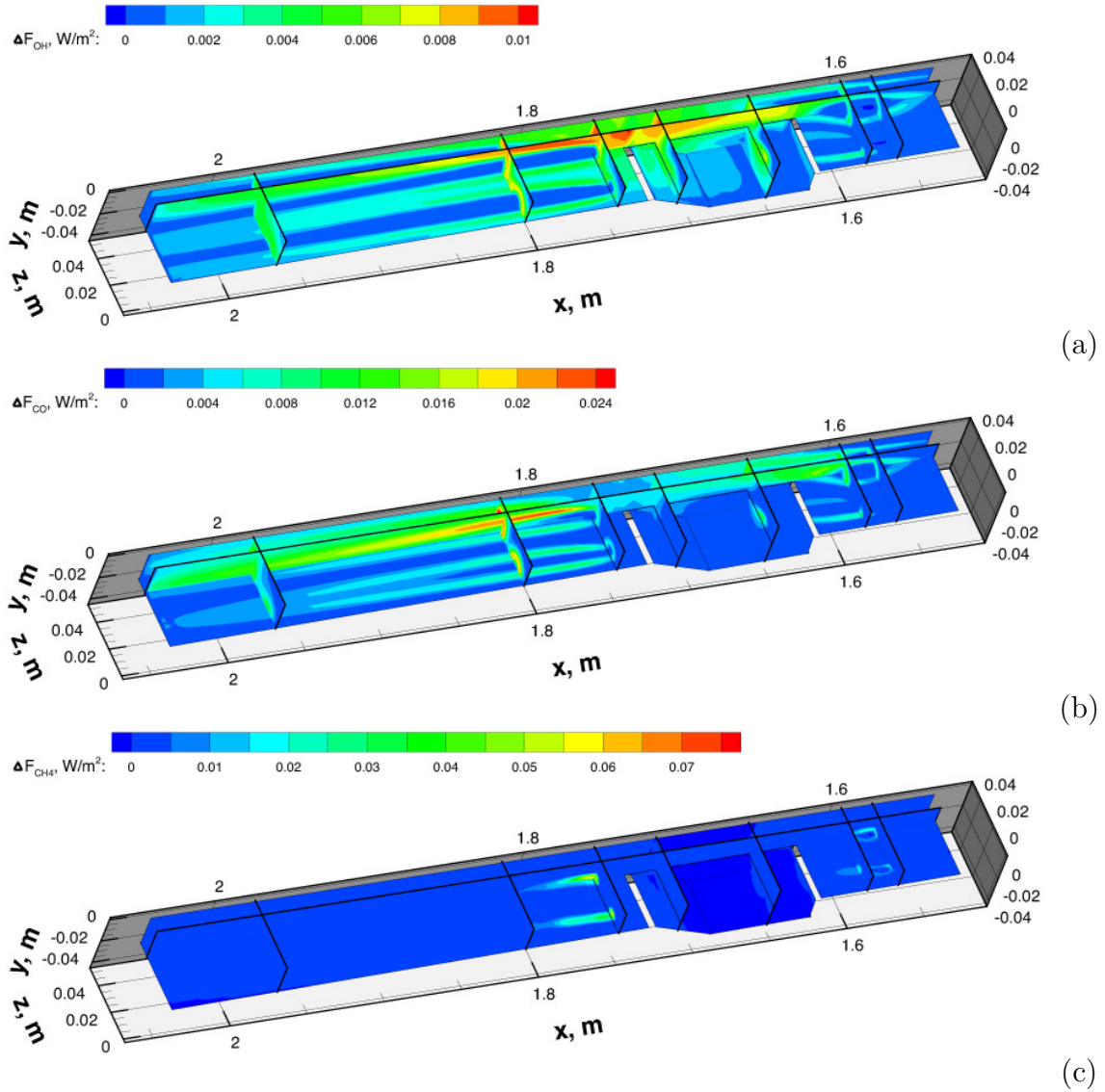


Figure 3.12: Relative contribution of an individual cell quantity to wall heat flux for partial pressure of (a) hydroxyl radical, (b) carbon monoxide, and (c) methane. Flow is from right to left.

This phenomenon is only a small contribution to the overall system, and methane is only included to determine if it would be a mechanism to heat the fuel stream. Whereas certain areas of the flow around the injection ports show a predicted net heat gain by methane, the values are still an order of magnitude smaller than the predicted heat loss immediately downstream of the injection port, thus indicating that the radiative heating of fuel may not have an effect on shortening combustion time.

3.3.2 Property Selection

The choice of flowfield properties for the current work now focuses on the consideration of several species as well as other flowfield parameters. Currently, the model only takes into account species concentration and temperature in calculating radiative heat flux. The contribution of pressure and density only serve to determine the species concentration, and pressure broadening effects are neglected in the band model. Temperature, as demonstrated in the previous section, is a significant non-linear contributor to the overall heat flux. Water vapor and carbon dioxide concentrations tend to make up the bulk of the radiative contributions with the other species being only minor contributors but with enough of an overall contribution to remain part of future radiative calculation.

With the criteria in place to select species of interest, the additional species in the flowfield are also examined for potential inclusion into the calculation. As mentioned in Section 2.4, the CFD model employed a twenty-two species hydrocarbon combustion model, of which only five are currently being represented. Minor species are short-term intermediate reaction products, many of which do not form in concentrations large enough to have a mole fraction of over 0.005. These species are neglected due to small concentrations. Several species, however, do have large concentrations. Such species are included in Table 3.5, which gives the Planck mean spectral con-

tributions of several species. The Planck mean is a means of estimating the overall radiative contribution of a species at a given temperature [115]. The Planck mean is calculated using the spectral convolution of the Planck function and the spectral band strength and dividing by the spectral integration of the Planck function, as given in Eq. 3.2. Table 3.5 gives the Planck mean values (in 1/m) for several temperatures as taken from the HITEMP 2010 database [92].

$$\overline{S(T)} = \int_0^{\text{inf}} (B(\nu, T)S(\nu, T)d\nu) / \int_0^{\text{inf}} (B(\nu, T)d\nu) \quad (3.2)$$

All species that have been previously neglected have Planck mean values less than those of carbon monoxide, which is found to be a very small contributor despite having mole fractions on the same levels water vapor. However, several fuel species are present in high enough concentrations around the injection ports to where they can affect the local thermal radiation. These species are relatively cold compared to the rest of the flow with injection temperatures between 300 and 400 K, and they do not travel far down stream as they react with the oxidizing flowfield. These species may play an important role in heat transfer around the injection ports. Under the current study, this region is very small. However, if coupled to a chemically reacting simulation, the heat transfer around the injection ports could affect the initial fuel temperature and reaction progress.

One final species, acetylene, is a non-minor intermediate species which is present in mole fractions of over 0.01 through the entire combustion chamber. The species is, however, far less radiative than carbon dioxide, and never present in nearly as large quantities. As such, acetylene is assumed to be a small contributor to the overall heat radiative heat flux of the system.

An additional consideration is the result of interspecies effects. One possible contributor to infrared thermal radiation in atmospheric conditions is the water dimer

Table 3.5: Comparison of the Planck Mean function of several major flow species at various temperature as calculated from the HITEMP 2010 Database [92]. CH₃ and C₂H₄ not present in the database.

Species	\bar{S} (500 K) 1/m	\bar{S} (1500 K) 1/m	\bar{S} (2500 K) 1/m
H ₂ O	1.88×10^{-6}	2.16×10^{-7}	6.12×10^{-8}
CO ₂	3.05×10^{-6}	9.85×10^{-7}	2.06×10^{-7}
OH	7.90×10^{-7}	4.96×10^{-8}	1.34×10^{-8}
CO	3.18×10^{-7}	9.16×10^{-8}	1.99×10^{-8}
CH ₄	6.24×10^{-9}	3.98×10^{-8}	8.74×10^{-9}
CH ₃	N/A	N/A	N/A
C ₂ H ₆	8.48×10^{-9}	3.37×10^{-8}	6.15×10^{-10}
C ₂ H ₄	N/A	N/A	N/A
C ₂ H ₂	2.60×10^{-8}	8.11×10^{-9}	1.21×10^{-9}
N ₂	1.91×10^{-18}	4.90×10^{-17}	5.39×10^{-17}
O ₂	1.50×10^{-16}	3.66×10^{-15}	2.68×10^{-14}

[65]. Whereas the pressures within the combustion chamber would support a population of water dimers, the chemical equilibrium for the water dimer is inversely related to temperature. Based on the predictions of Scribano et al., water dimer prediction models only extend to temperatures below 400K. An extension of the model to the temperatures within a scramjet yields a negligible concentration [97]. Other possibly radiating species such as NO_x were not included in the CFD chemistry model and present in the flowfield.

Two final decisions remain for the selection of parameters whose variation influences the thermal radiation inside of a scramjet. The first decision is the selection of which species to include in any the simulations. The species which must be included are water vapor and carbon dioxide. Species which may give a small contribution, but will not greatly affect the total magnitude of the problem, are carbon monoxide, the hydroxyl radical, methane, and ethane. Carbon monoxide and the hydroxyl radical are the strongest emitters and are present through the entire chamber. Therefore, will be included in all simulations. Ethane is only present in small amounts in small areas and can be neglected if the areas are not of specific interest. Methane is present

in large amounts in specific areas and may be a minor species worth including with contributions on the same order as hydroxyl or carbon monoxide. Methane may become an important contributor to radiative simulations that are coupled to chemically reacting fluid simulations as a significant increase in temperature in a fuel can reduce the ignition delay time in combustion [62]. However, the chemistry effects will not be a major concern in the current work, and methane does not affect the direct wall heating in any significant manner.

The second decision is which species to account for when examining flowfield variation studies. Priority should be given to the species with the greatest radiative contribution. Water vapor and carbon dioxide stand out at the largest contributors. Other minor species are significantly smaller contributors, even when combined. They constitute an additional set of parameters for very little possible variation in the final outcome. Additionally, it is shown in Section 4.2 that the errors associated with minor species may overshadow any variation they can have in a flowfield.

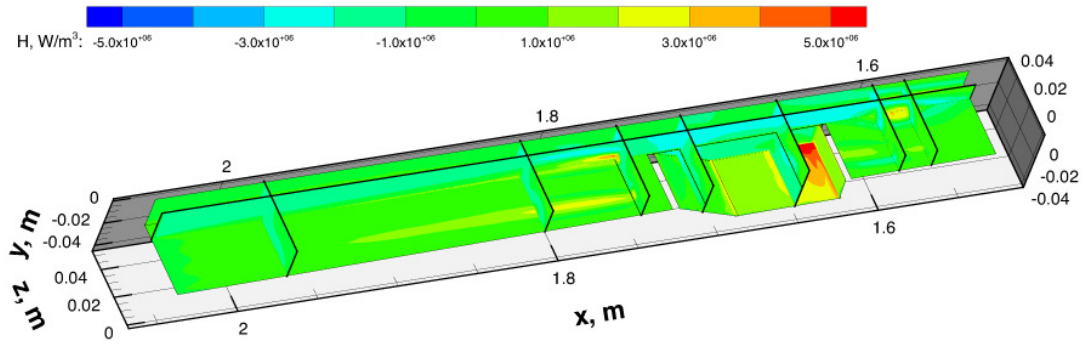
3.4 Boundary Conditions

In addition to flow variables, boundary condition variables can greatly affect the overall radiative field. The boundary conditions can vary greatly given different materials, temperatures, and material conditions. For example, the copper used to construct the interior walls of the HyShot-II combustion chamber can vary from an emissivity of 0.04 to 0.80 [48, 100]. The HIFiRE-2 combustion chamber is an uncharacterized stainless steel whose emissivity can be reasonably expected to vary from 0.17 to 0.76 [48, 69].

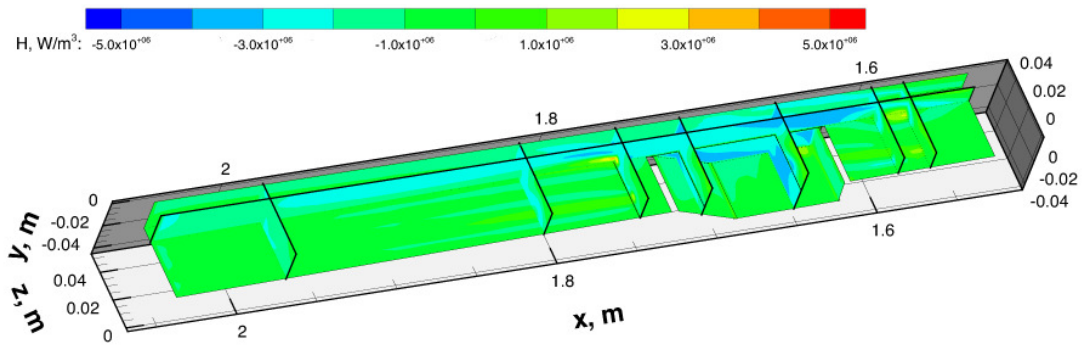
Given the large variance in the thermal characteristics of the combustion material, no particular limitation can be imposed on the combustion chamber boundary conditions. As such, the HIFiRE-2 simulations are re-run using a variety of boundary conditions.

The conditions given in this section are for blackbody walls ($\epsilon_\nu = 1.0$, $r_\nu = 0.0$) for cases with 0 K (effective outflows) walls and walls at the same temperature as the flow edge. Additional boundary conditions are half-black and half-spectrally reflecting ($\epsilon_\nu = 0.5$, $r_\nu = 0.5$) walls with temperatures equal to that at the edge of the flow. Finally, completely reflective wall boundaries ($\epsilon_\nu = 0.0$, $r_\nu = 1.0$) are employed. All simulations are run on the same mesh as described in the previous section. The overall heating rate per unit volume is given in Fig. 3.13, and the net radiative heat flux to the wall is given by Fig. 3.14. In all cases, the flow inlets and outlets are treated as radiative outflows.

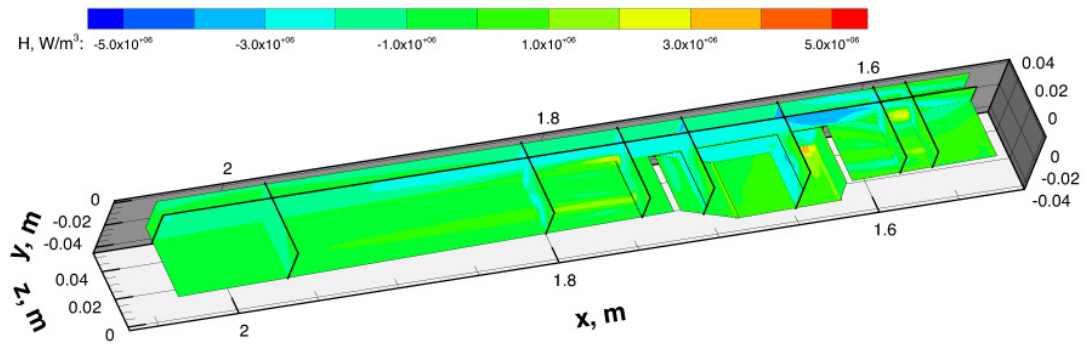
The overall volumetric heating in the cold case (Fig. 3.13 (a)) is almost entirely negative, with the exception of the region directly around the injection ports. This trend is greatly changed by two factors. The first factor is the blackbody radiation from the hot walls. In the purely blackbody case (Fig. 3.13 (b)), the walls emit a significantly higher amount of radiation than they receive from the flow. As such, they create a large increase in the overall thermal radiation of the system. This thermal radiation mainly passes through the domain undisturbed due to the low optical depth of the system, but some of it is absorbed by the medium lowering the net heat loss, even causing some portions of the flow to encounter a net heat gain. The second factor is the reflectivity of the walls. In the purely reflecting case (Fig. 3.13 (d)), the thermal radiation emitted from the flow is reflected continuously among the surfaces until it is either reabsorbed by the medium or exits out the physical fluid inflow or outflow. In this case, thermal radiation still has a net cooling effect on the flow (less so than any other cases), and the heating of the cool parts of the flow around the injection ports is higher than for any other case. As discussed in the previous section, these are the areas with the highest concentration of hydrocarbon fuel.



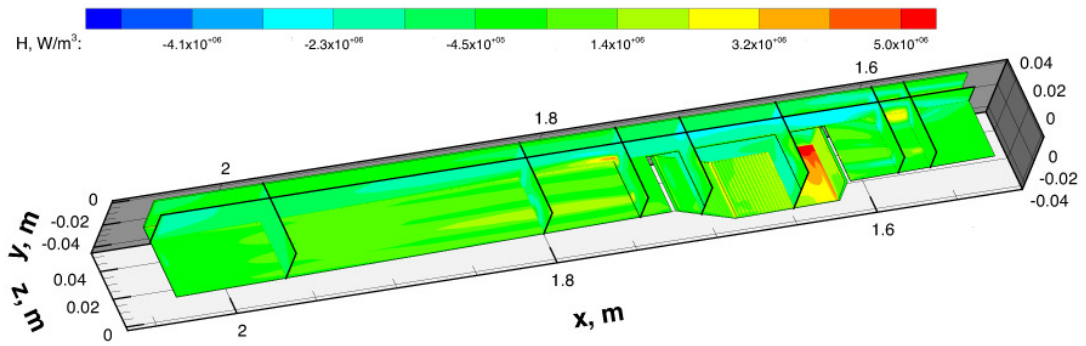
(a)



(b)



(c)



(d)

Figure 3.13: Net volumetric radiative heating for (a) absorbing non-emitting (cold), (b) blackbody, (c) half-emissive, and (d) completely reflective boundary conditions. Flow is from right to left.

A combination of cooling and heating is present, and it shows a hybrid characteristic as given in Fig. 3.13 (c). The trends in this examination show that hot boundary conditions, regardless of emissivity, serve to reduce the cooling of an optically thin flow. These trends are discussed in the next section where the temporally integrated flow cooling is considered.

The net radiative heating presented in the purely outflow case (Fig. 3.14 a) only amounts to at most 56 kW/m^2 . However, the introduction of hot walls (and accounting for the radiative surface emission) increases the net wall heating to up to 400 kW/m^2 in some areas and introduces net wall cooling up to 500 kW/m^2 in the purely blackbody case (Fig. 3.14 b). Since all of the thermal radiative heat flux is absorbed by the walls in both the blackbody and purely outflow cases, this dramatic increase in heat transfer is attributed solely to the blackbody emission of the hot chamber walls. The effects of wall high and low temperature, especially around the fuel injection ports, are apparent in the data. Regions of high temperature see a net heat loss, whereas regions of low temperature see a net heat gain. With such heating rates, wall-to-wall heating may be a significant and dominant means of heat redistribution inside of a combustion chamber. For combustion chambers with longer run-times, this wall heat distribution may have a significant effect on surface temperature, and thus, boundary layer conditions [43]

Adding reflectivity to the chamber walls has a reducing effect on the net heat flux to the wall despite increasing the volumetric heating. For the half-reflective case (Fig. 3.14 c), the net wall heat flux is reduced by roughly a factor of two from the pure blackbody case. The trends of the surface temperature features are still present and dominant in this case as well. Of course, for purely reflecting walls (Fig. 3.14 d), no thermal radiation is absorbed.

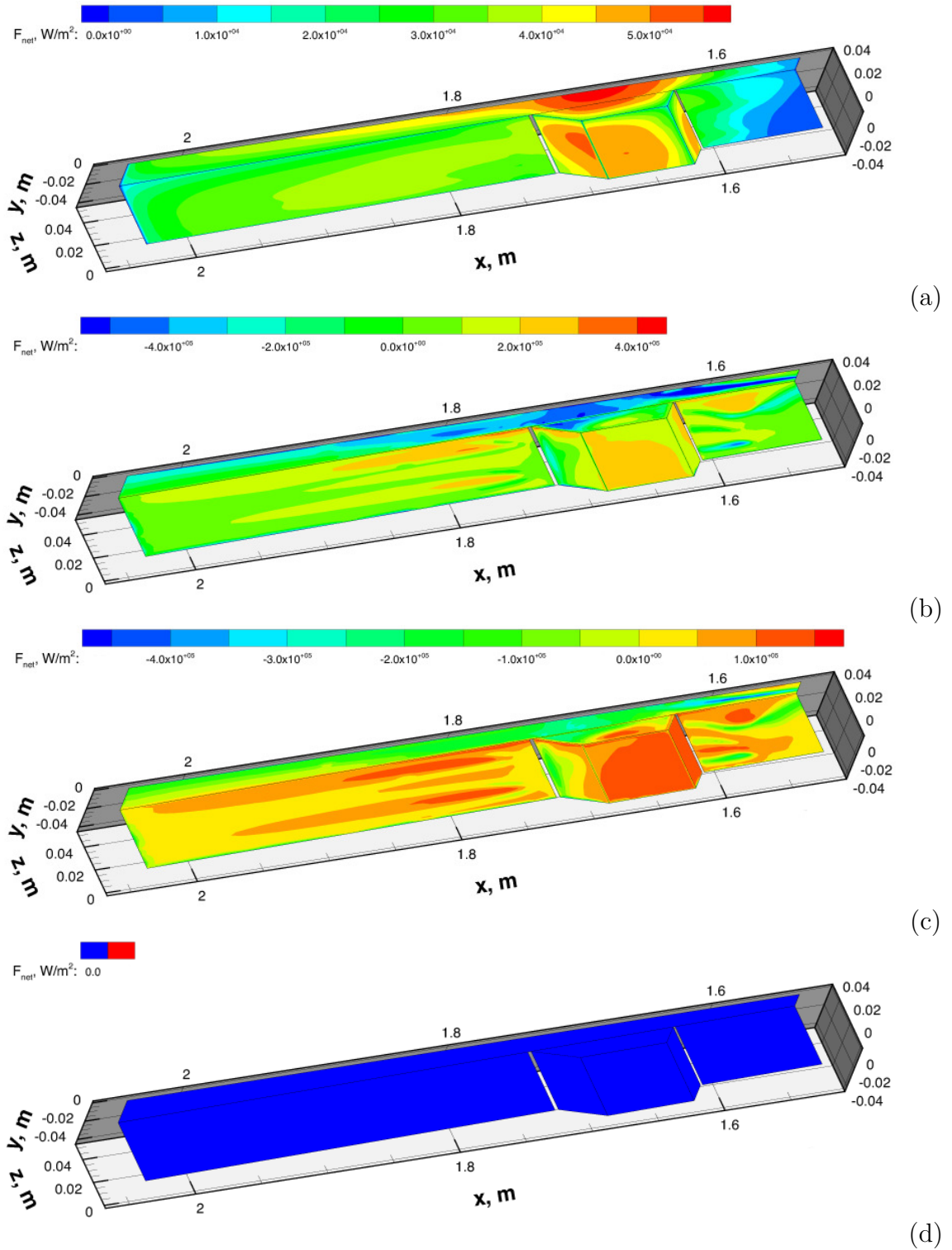


Figure 3.14: Net heat flux for (a) absorbing non-emitting (cold), (b) blackbody, (c) half-emissive, and (d) completely reflective boundary conditions. Flow is from right to left.

Whereas these trends show that wall radiation may dominate a system, a similar study found that even without the inclusion of wall emission, the overall thermal radiation of a system was greatly affected by wall absorption and reflectivity [69]. As such, when making a selection of parameters for design studies, variations in wall temperature and emissivity cannot be ignored as they have significant effects on the uncertainty in the total heat transfer.

3.5 Flowfield Temperature

As discussed in the previous section, the radiative heat transfer from one part of the flow to another may be significantly affected by the physical boundary conditions. One way in which this can manifest itself is in temperature changes within the flow-stream. Studies of subsonic combustion chambers have found shifts of 100s of degrees due to radiative cooling [35]. Additionally, studies of supersonic flows of pure turbulent steam have shown strong coupling of radiation to flow energy [34]. However, given the significantly shorter residence time of a scramjet combustion chamber and the large amount of non-emitting thermal mass (mainly in the form of nitrogen) the current thermal radiation may have a significantly smaller effect on the overall fluid properties.

Previous studies have found radiative flow cooling to be insignificant in scramjets with short flow residence times [21, 20, 22]. Thus, a post-processing stream-trace prediction is employed. If the flow is found to have temperature changes on the order of 10 to 100 K due to radiative cooling, then a direct coupling may need to be employed if the changes in temperature create a change in combustion completion on the same order as the residence time.

To investigate the effects of thermal radiative heat transfer on flow, a series of stream-traces are examined. The individual traces are chosen for different locations within the domain, and some are entrained in the flame holding cavity while others

pass quickly through the chamber. An example of these traces is given in Fig. 3.15 with different types of stream-traces displayed.

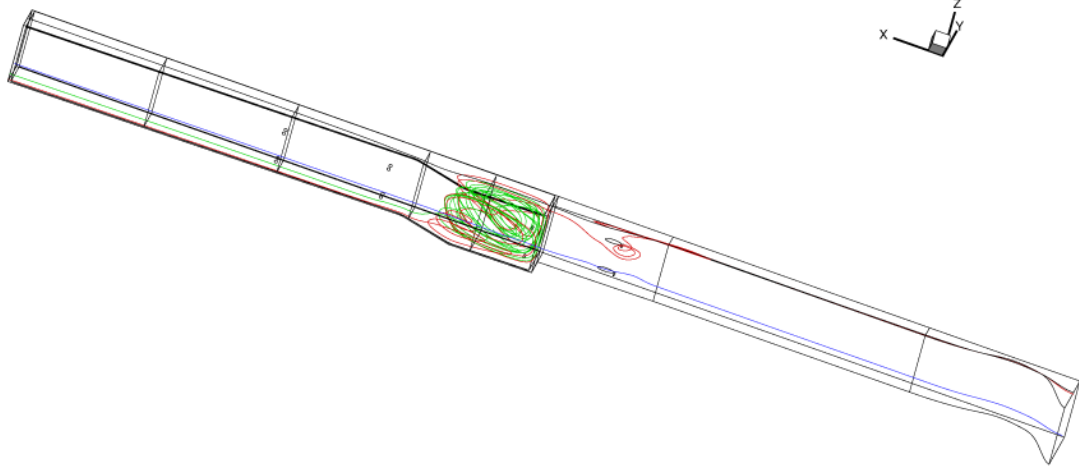


Figure 3.15: Path traces of a highly entrained stream-trace (green), mildly entrained stream-trace (red), and un-entrained stream-trace (blue). Flow is from right to left.

The cooling rate properties and overall heat losses are determined for each stream-trace by first determining the temperature change per unit time, as given in Eq. 3.4, where “ c_v ” is the volume constant specific heat, “ H ” is the local volumetric radiative heating rate, “ ρ ” is the local density, and “ $\frac{dT}{d\tau}$ ” is the time rate change of temperature. The path can then be integrated using the formula given in Eq. 3.4.

$$\frac{dT(s)}{d\tau} = \frac{H(s)}{c_v(s)\rho(s)} \quad (3.3)$$

$$\Delta T = \int_0^{s_{max}} \frac{dT(s)}{d\tau} / \frac{ds}{d\tau}(s) ds \quad (3.4)$$

The results are given in Figure 3.15 as total cooling for 29 individual traces and their respective residence times. The individual flowfield streamtraces and associated properties are taken from the CFD RANS simulations. The volumetric cooling rates

are taken from the four radiative intensity solutions from the four boundary conditions used in the previous section. All calculations for flow cooling are strictly post-processed from the CFD and radiative solutions and do not feed back into the cell temperature, flow quantities, or cooling rate.

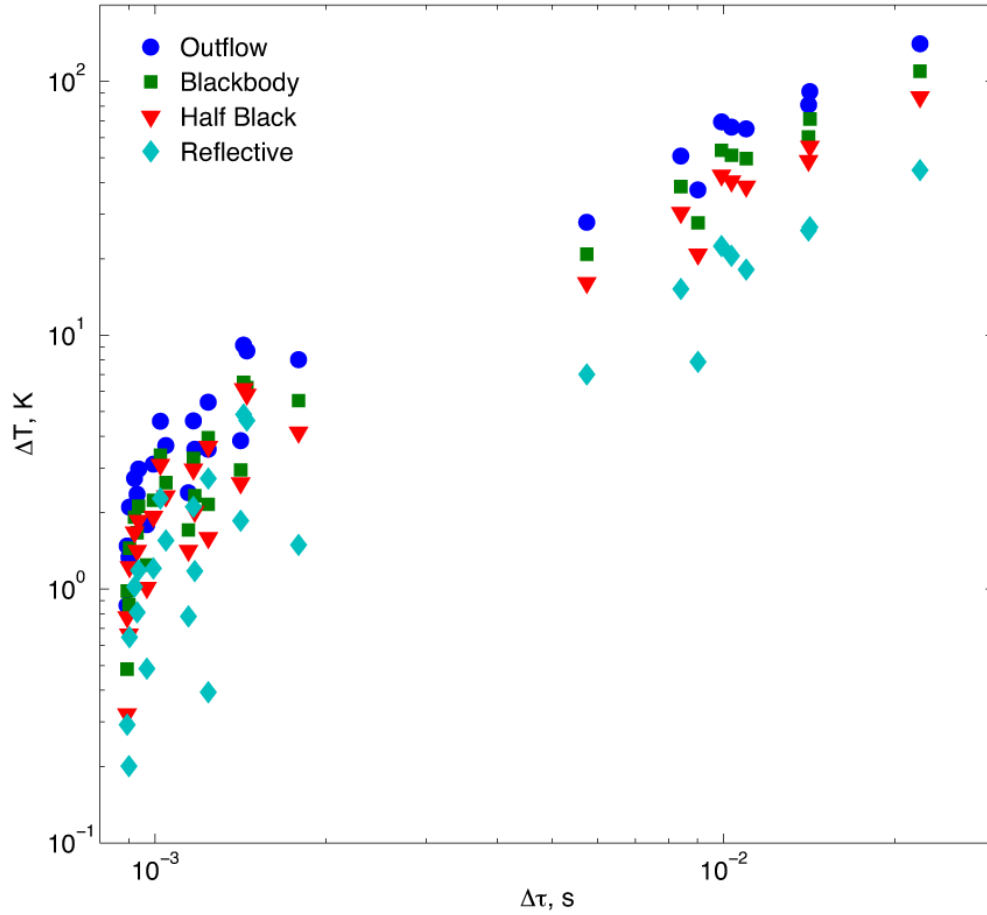


Figure 3.16: Temperature loss ($-\Delta T$) vs. residence time (τ) along stream-traces for radiative outflow, blackbody, half-black half-reflective, and reflective conditions.

The path integrated cooling for any stream-trace is always highest for the radiative outflow condition, with successively reduced cooling for blackbody, half-black half-reflective, and reflective cases, respectively. This is a trend suggested by Fig. 3.13.

Both the amount and variation of flow cooling depending on the same conditions. In extreme cases, a stream-trace may have a temperature reduction by over 145 K, with a corresponding variation of heat reduction of over 99 K due to effects of boundary conditions, whereas other stream-traces show temperature change of less than 1 K for all conditions. The main correlation factor is the residence time of the fluid element in the stream-trace. There is some variation due to the properties of the individual flow path taken, and in one completely reflective case, a stream-trace rises negligibly in temperature. As shown in Fig. 3.15, some stream-traces become entrained in the flame holding cavity or stagnation point upstream of the injectors, whereas other stream-traces pass quickly through the system. The overall residence time varies by several orders of magnitude as does the corresponding flow cooling. These values differ greatly from the analysis of the HyShot-II combustion chamber, which had no flow cavities or stagnation points, and as such, the chamber had no significant flow temperature change [22].

With a large change in temperature predicted due to radiative cooling, examination of the feedback of thermal radiation to the CFD solver may be justified for further investigation. Furthermore, the use of predicted temperature changes within stream-traces can be a telling metric of the uncertainty within a calculation as they greatly change with boundary and flowfield conditions, and unlike wall heat flux, give results even with purely non-absorbing walls. Finally, the justification of using boundary conditions as a sensitivity parameter is even more greatly reinforced as they have strong and consistent effects on the flowfield cooling.

3.6 Conclusions

A number of radiative analysis techniques are employed to process CFD flowfield solutions of both the HyShot-II and HIFiRE-2 scramjet test cases. The goals of the radiative modeling are to establish tools and parameters for examination of the

variations within flowfields. Such goals include the justification of simplified modeling and geometric approximations as well as the selection of quantifiable metrics for uncertainty. Additional selections are made for the specific flowfield and boundary parameters used in further studies.

Analysis is first performed by comparing both one-dimensional and three-dimensional radiative solutions of the HyShot-II scramjet combustion chamber. The resulting traces show that, when properly chosen, a one-dimensional trace can give a 50% accurate prediction of the character of a region within a combustion chamber with a representative spectrum. These approximations may be employed as representative unit problems when examining order of magnitude effects in simulations before undertaking a full three-dimensional radiation solution. In addition to predicting flowfield character, the one-dimensional traces allow for a direct scaling and comparison between flowfields of greatly different geometry, thus allowing isolation of the size effects from flowfield effects.

Flowfield effects can be directly quantified using adjoint sensitivity techniques. Through a linearized approximation, the cell-average effect that a flowfield variable has on the radiative heat flux to the walls can be directly estimated without rerunning the simulation with slight perturbations for each variable. Furthermore, the source locations of the greatest influence on heat flux are directly quantifiable. The resulting analysis for HIFiRE-2 found that temperature, water vapor concentration, and carbon dioxide concentrations comprise the greatest contributions to the wall heat flux, and thus, will be considered in future design studies. The analysis also shows that, while still significant in overall contribution to the radiative heat flux, methane, carbon monoxide, and the hydroxyl radical are insignificant enough to indicate that the uncertainty in their concentrations may not be large enough to warrant consideration in a parameter study.

With a quantifiable measure of radiative contribution of wall heat flux, two notable

trends become present. The first trend is that larger concentrations of a species correlates with larger contributions to the overall radiative heat flux. The second trend is that stronger spectral line-strengths also correlate with larger contributions to the overall radiative heat flux. The parameters are a useful means of examining other flowfield species for possible inclusion in simulations. Using mole fraction as a means of comparing concentrations, and Planck mean absorption as a means of comparing spectral line-strengths, it is found that the current species under consideration are orders of magnitude more important than almost all other species in the simulation.

The physical boundaries are examined for multiple conditions. It is found that with wall temperatures in the same regime as the flowfield temperatures, the wall-to-wall radiative heat transfer far outweighs any radiative flow-to-wall interactions, given the optically thin nature of the flow. Additionally, reflective wall conditions are found to decrease the overall radiative heat flux to the wall. The variation of boundary conditions also shows large effects in the estimation of radiative flow cooling. In this case, a strong trend is demonstrated that radiative cooling decreases with increased wall temperatures and with increased wall reflectivity. These effects appear to be constant over the entire range of flow conditions. The flow cooling predictions vary greatly in their associated heat losses, not just due to boundary conditions but also due to local flow conditions and residence time. The overall residence time shows a strong correlation with overall heat loss and can vary greatly between central stream-traces that pass quickly through the combustion chamber and edge stream-traces that become entrained in the cavity holder.

Finally, radiative flowfield cooling is a candidate as a metric for design studies, and radiative boundary conditions are a potential parameter for design studies.

CHAPTER IV

Model Uncertainty

4.1 Introduction

The current chapter looks at the epistemic uncertainty in the simulated radiative heat transfer of scramjet engines. The particular test case of interest is the HIFiRE-2 scramjet combustor. Epistemic uncertainty is defined by lack of knowledge of the system as a whole. The two major sources of epistemic uncertainty are the spectral model parameters and numerical grid refinement parameters. These individual uncertainty sources can be estimated numerically resulting in a quantifiable verification of the spectral and numerical methods used.

The spectral model uncertainty comes from two sources. The first source is the experimental measurements. The spectral model is based on physical atomic and molecular structures, which can only be determined to within the physical limits of the measurement apparatus employed. Although experiments are continually ongoing to refine the precision of the measurements, uncertainties are still present in the data [91, 92]. High-fidelity uncertainty studies have found that even with a relatively well-understood substance as water, a reasonably large amount of uncertainty in the radiative heat flux prediction stemming from the experimental measurements can persist in the HIFiRE-2 combustion chamber [50]. The second source of uncertainty is that which the simplified two-point c-k model created. As demonstrated in Section

4.2, the choice of spectral quadrature points has a large impact on the overall accuracy of a radiative simulation, but optimized quadrature points may never be known.

A means of estimating the spectral uncertainty comes by perturbing the spectral database by a pre-calculated amount. The difference of the output from the nominal case is taken as the error estimation. The perturbation of the spectral model involves a combination of the experimental measurement error in the spectral databases and modeling error derived by comparing low and high-fidelity spectral models applied to simplified unit problems. The use and justification of unit problems, as compared to full three-dimensional simulations, is addressed in the next section.

Additional epistemic uncertainty comes from grid refinement. Whereas exact convergence requires an infinite number of grid points, a well-chosen set of grid points can give convergence to within a high degree of accuracy [27]. However, these points are unknown, and the accuracy can only be estimated, meaning that the grid errors can be treated as an epistemic uncertainty. Unlike Computational Fluid Dynamics (CFD), the Discrete Ordinates Method (DOM) has both angular and spatial grid refinements to consider.

Grid refinement error can be investigated with classical convergence studies, in which points can be added to the spatial domain as seen fit. Grid refinement for this particular case has a two-fold issue for convergence. The first issue is that the schemes employed are based on post-processing a pre-computed CFD solution that must be sampled in order to be used in the DOM simulation. The sampling has an associated resolution, which, if too coarse, may not gather all of the important flow features. Second, once the flowfield is sampled, the numerical grid used for calculating the radiative field must be properly refined. The grid does not need to be of the same resolution as the sampling scheme and may be higher or lower resolution based on the numerical convergence requirements. Angular refinement can be considered by comparing predefined angular discretization schemes in a convergence study.

Additional refinement may be addressed by using a scheme such as the Ray Tracing method, which has an arbitrarily high limit of sampling, numerical grid density, and angular refinement. Such comparisons have been used in previous works where Ray-Tracing is employed as a truth method to determine the reliability of the DOM in numerous simulations [22, 55].

With both of the numerical domain and spectral sources of error quantified, they can be combined to create an evaluation of both the system and its associated uncertainty prediction. A means of evaluating the system is to use a high-fidelity spatial and spectral model. However, the high-fidelity simulations are still based on tabulated databases and computational fluid predictions. An alternative means of evaluating the model and error predictions is to directly compare the radiative predictions with experimental measurements. As such, the measurements taken at the HDCR are numerically modeled using a Ray Tracing method based on the CFD simulations.

4.2 Spectral Accuracy

The direct evaluation of spectral accuracy requires the modeling of an exact physical domain. The verification of the spectral model can be performed on an arbitrary physical domain by comparing spectral models of varying fidelity. These direct comparisons yield a domain-specific error that can be used to estimate the uncertainty a spectral model contributes to other more physically complex simulations.

Several spectral models are available for radiative heat flux predictions, such as Weighted Sum of Gray Gas (WSGG), correlated-k, and line-by-line methods. The use of WSGG models leads to large inherent errors compared to other full spectrum and banded models, and it will not be considered in this work [75, 86, 101]. Correlated-k models can have an arbitrary spectral resolution, and a derivative of c-k is the main spectral model used in this work as described in Chapter II. The LBL methods are considered robust and can be arbitrarily accurate, but they have a large computational

expense compared to other methods [73]. Because they are arbitrarily accurate, the LBL methods are used in calculating lookup tables from spectral databases, and these computed tables can have low or high-fidelity spectral model depending on their resolution. These tables are used as fast numerical references for other spectral methods. For the purpose of the current work, tables with a spectral resolution of 0.01 cm^{-1} are considered high-fidelity, whereas tables with a spectral resolution of 25 cm^{-1} are considered low-fidelity.

The goal of the current section is to develop a comparison method between higher and lower-fidelity spectral models and to quantify the possible effects of different spectral models on the overall radiative output. The primary method of comparing spectral models is to apply them to identical domains. In the current case, a homogeneous one-dimensional domain is used for comparing spectral models. Due to the computational expenses incurred with high-fidelity methods, it is impractical to perform a full three-dimensional DOM comparison for the entire spectral range of interest. The resulting error estimations from the one-dimensional unit problems can be compiled in spectral error estimation tables. These error tables are used to perturb the low-fidelity spectral models in full three-dimensional simulations, giving an estimation of the uncertainty introduced by the low-fidelity spectral model.

With the simplified error estimators calculated, the question arises as to the validity of translating one-dimensional homogeneous calculations into three-dimensional inhomogeneous flowfields. The use of a one-dimensional domain to predict the behavior of three-dimensional domains is shown in Section 3.2 to have some validity in predicting integrated radiative heat flux, but the spectral constancy of the estimation still needs to be addressed. The evaluation of the methods is performed in several manners. All manners center around performing a computationally expensive high-fidelity spectral model calculation and taking the difference of the results from the low-fidelity spectral model to garner an actual error. These actual errors are

compared to the error estimators generated from the one-dimensional simulations. If the actual errors and the predicted estimators are within an acceptable value of each other, then the error estimator is considered accurate for the current flowfield. Once an acceptable error table is found, it can be used repeatedly without recalculating the high-fidelity spectral simulation for any perturbation in the flow.

4.2.1 Model Comparison

The particular models under consideration are spectrally banded models. These models are chosen over WSGG models because they are considered significantly more accurate in modeling combustion processes. In certain studies, the WSGG method is shown to have spectral errors of up to 20%, whereas c-k methods are found to have spectral errors of only 1 to 2% [86, 110].

As mentioned in Section 2.2, a fine-spectral-resolution set of data is extracted from the HiTemp database under conditions similar to those found in a combustion chamber [92]. The procedure for extraction processes the partition functions of the spectral lines in a species and finds the summation of all Lorentz line profiles along evenly spaced wavenumbers as with the procedure given in the thesis by Irvine [50]. This data is used in establishing a coarse spectral database. The lines employed for gathering statistics on carbon dioxide, the hydroxyl radical, carbon monoxide, and methane constitute all of the lines in the HiTemp database with regards to the species concerned. The lines employed for water vapor are given a specific cutoff threshold for which lines below a certain strength are not selected. Given the selection criteria laid out by Irvine, the cutoff is found to have less than a 0.01% effect on the cumulative radiative heat flux [50].

The fine spectral database can be used as a banded model in its current state if in Eq. 2.13, $g = 1$, $N_{quad} = 1$, and $\delta\nu = 0.01 \text{ cm}^{-1}$. However, to establish a spectral range from 25 to 10,000 cm^{-1} , 997,500 bands are necessary, which can be impractical

for all but the simplest of problems. With the goal of reducing the number of spectral bands, the high-fidelity spectral database is reduced into 399 bands of a width of 25 cm^{-1} each. The band width is chosen as it matches to the narrow-band range of many comparative methods [65, 110]. The individual bands can have multiple quadrature points as calculated with Eq. 2.14. Tables are established for five species (water vapor, carbon dioxide, carbon monoxide, the hydroxyl radical, and methane), with all species having two quadrature points for each band. The tables (given in units of $1/\text{m}$) are normalized for partial pressures of 1 atm (101.325 kPa). The tables are given for temperatures of 500, 1000, 1500, 2000, 2500, and 3000 K. Further optimization studies may further refine this scheme in the future.

For temperatures between the tabulated values, the spectral linestrength is interpolated using a third-order spline. The choice of only one pressure point to represent a large range of pressures is justified by previous works that find the spectrum is mainly sensitive to density effects in the scramjet regime, and pressure effects are found to be negligible [50]. The selection of the individual quadrature points, “ g ,” varies per species.

The use of a singular quadrature point at the band statistical average has been employed in works of the past [21, 22]. However, when compared to the high-fidelity spectral model over a 0.10 m, one-dimensional homogeneous domain of water vapor with a partial pressure of 0.1 atm (10.133 kPa), spectral modeling errors are found to be upward of 49%, which is calculated as the difference between the high-spectral fidelity and low-spectral fidelity simulations. The comparisons between the high-fidelity spectral ($\Delta\nu = 0.01 \text{ cm}^{-1}$) model and the low-fidelity spectral ($\Delta\nu = 25 \text{ cm}^{-1}$) single-point model are given in Fig 4.1 for pure water vapor. The temperatures are 500, 1000, 1500, 2000, 2500, and 3000 K with relative spectrally integrated errors of 49.76, 19.53, 8.33, 4.12, 2.28, and 1.38%, respectively.

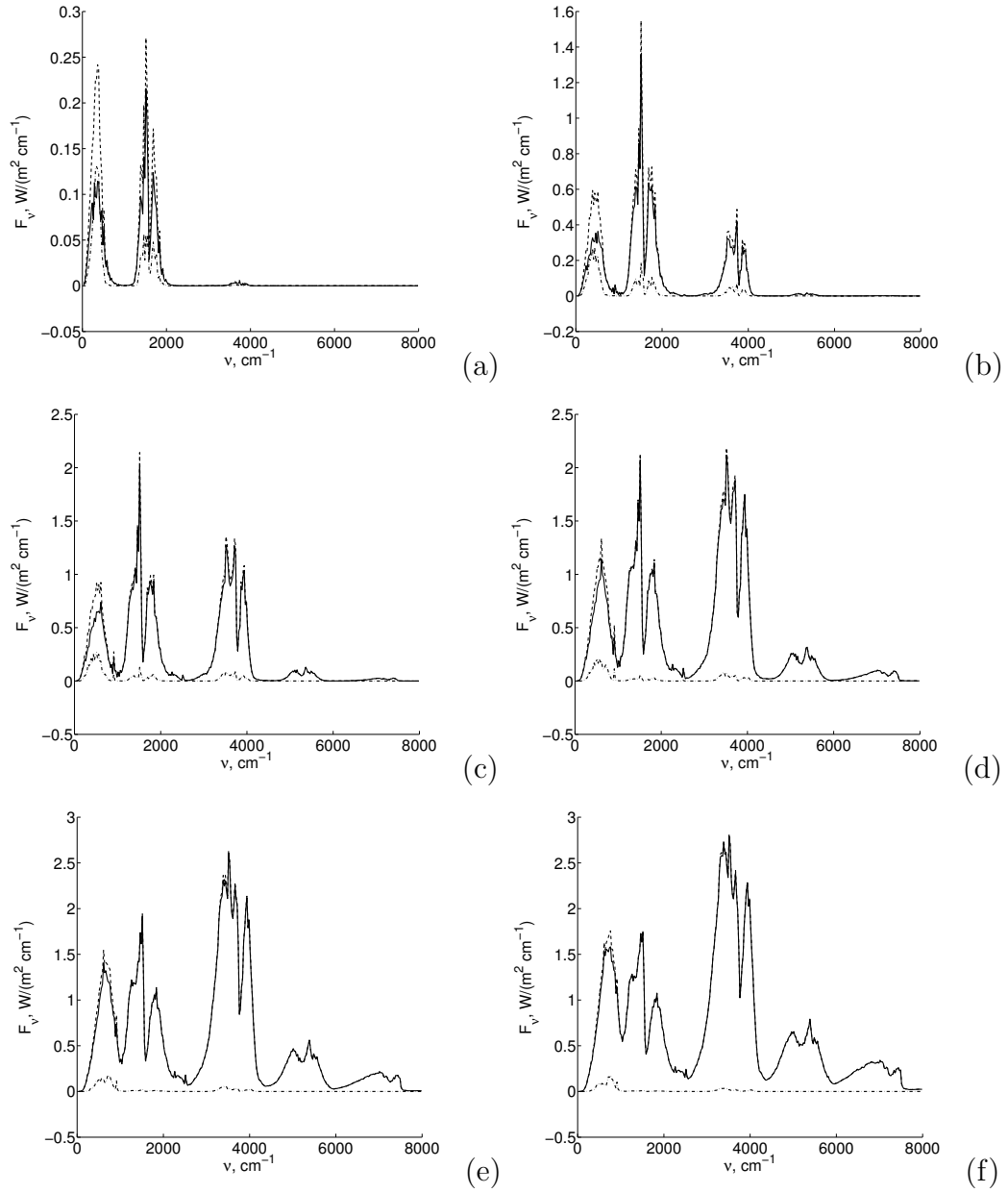


Figure 4.1: Spectrally resolved radiative heat flux of water vapor for the high-fidelity spectral ($\Delta\nu = 0.01 \text{ cm}^{-1}$) model (solid line) and a low-fidelity spectral ($\Delta\nu = 25 \text{ cm}^{-1}$) one-point c-k model (dashed line). Differences are displayed (dash-dot line). All simulations have a one-dimensional path of 0.10 m, at a partial pressure of 0.1 atm (10.133 kPa). Temperatures are at (a) 500 K, (b) 1000 K, (c) 1500 K, (d) 2000 K, (e) 2500 K, and (f) 3000 K.

A significant improvement over the one-point model is a two-point model with the points averaging to the arithmetic mean of the band strengths. The reason for maintaining the arithmetic mean is that, as the optical depth approaches zero, the effect of the absorption coefficient approaches that of the mean of the absorption coefficients. This is demonstrated with the RTE as given in Eq. 4.1.

$$\lim_{(x_{max}-x_{min})\rightarrow 0} \int_{\nu_{min}}^{\nu_{max}} \int_{x_{min}}^{x_{max}} (B(x) - I(x)) \kappa_{\nu} d\nu dx = \int_{x_{min}}^{x_{max}} (B(x) - I(x)) \int_{\nu_{min}}^{\nu_{max}} \kappa_{\nu} d\nu dx \quad (4.1)$$

The weighting parameter given in Eq. 2.13 and tuning parameters given in Eq. 2.14 are chosen to minimize the error of the low-fidelity spectral model when compared to the high-fidelity spectral model over a one-dimensional problem. The current set of parameters has each of the quadrature points set to a weight of $g = 0.5$ for all bands and species. All of the tuning parameters are given a value of $c_1 = 0.9$, as it is found to reduce error in a number of the model problems examined. The exception is carbon monoxide, for which the tuning parameter is set at $c_1 = 1.0$. The reasoning is that the low-fidelity and high-fidelity spectral model results of carbon monoxide match better over the model problem with the revised tuning factor.

Comparisons for a model unit problem are given in Fig. 4.2 for a pure homogeneous water vapor case, in Fig. 4.3 for a case of water vapor with temperature layers, and in Fig. 4.4 for a layered case with multiple species. All boundary conditions are purely absorptive and non-emissive.

In Fig. 4.2, the spectrally resolved radiative heat flux along a one-dimensional case is given for water vapor with a partial pressure of 0.1 atm (10.133 kPa), and temperatures of 500, 1000, 1500, 2000, 2500, and 3000 K. The high-fidelity and low-fidelity spectral models have relative spectrally integrated differences of 23.29, 10.67, 4.35, 1.94, 0.95, and 0.49%, respectively.

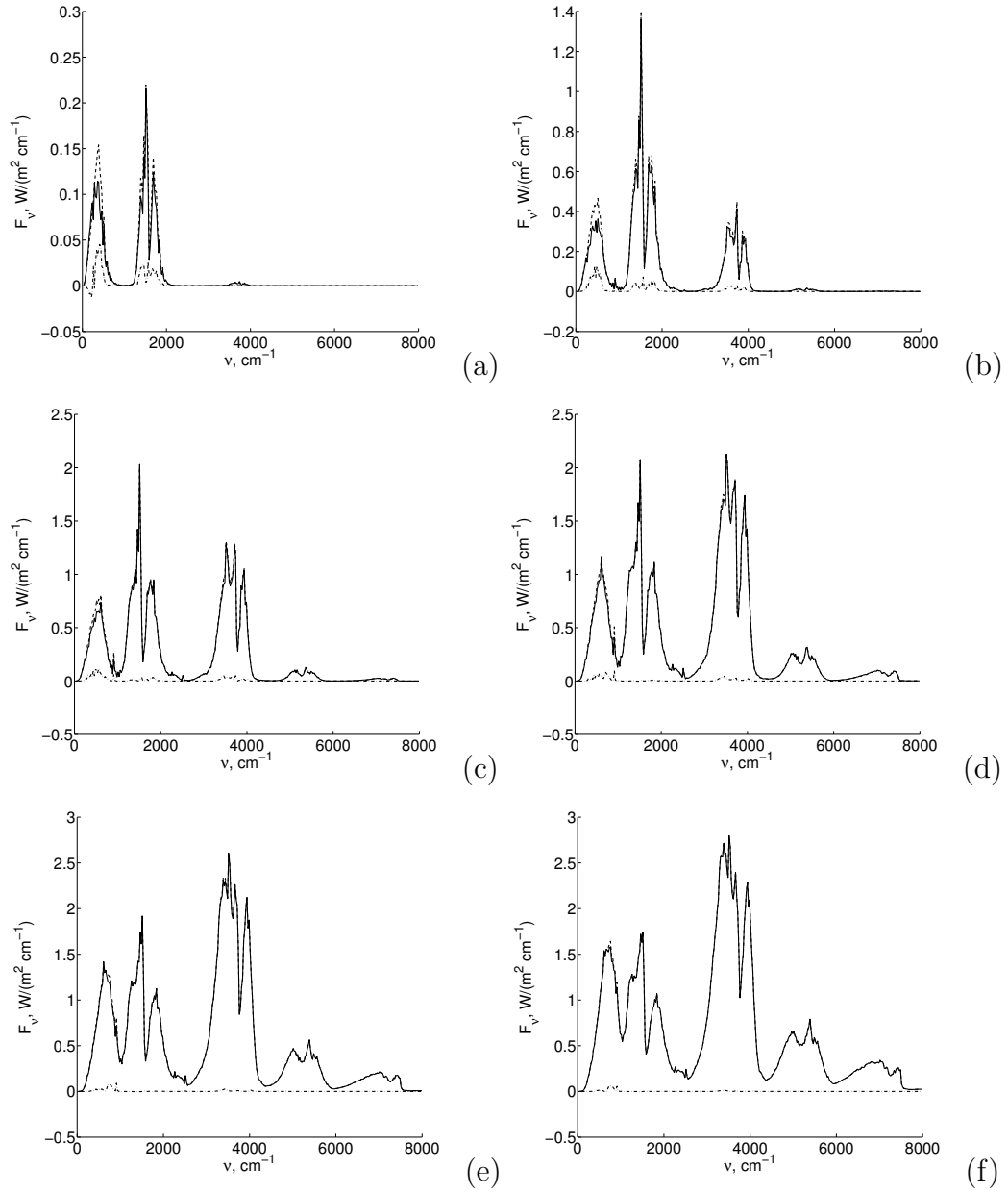


Figure 4.2: Spectrally resolved radiative heat flux of water vapor for the high-fidelity spectral ($\Delta\nu = 0.01 \text{ cm}^{-1}$) model (solid line) and a low-fidelity spectral ($\Delta\nu = 25 \text{ cm}^{-1}$) two-point c-k model (dashed line). Differences are displayed (dash-dot line). All simulations have a one-dimensional path of 0.10 m, at a partial pressure of 0.1 atm (10.133 kPa). Temperatures are at (a) 500 K, (b) 1000 K, (c) 1500 K, (d) 2000 K, (e) 2500 K, and (f) 3000 K.

In Fig. 4.3, the spectrally resolved radiative heat flux along a one-dimensional case is given for water vapor with a partial pressure of 0.1 atm (10.133 kPa). The domain consists of four 0.10 m thick layers with temperatures of 500, 1500, 2000, and 2500 K, respectively. The resulting spectrally integrated spectral heat flux error is 16.36%.

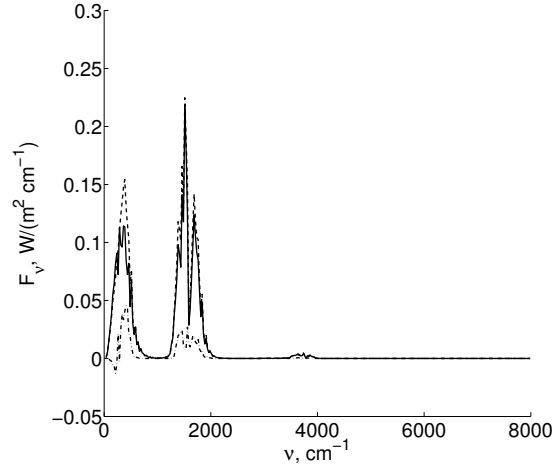


Figure 4.3: Spectrally resolved radiative heat flux of water vapor for the high-fidelity spectral ($\Delta\nu = 0.01 \text{ cm}^{-1}$) model (solid line) and a low-fidelity spectral ($\Delta\nu = 25 \text{ cm}^{-1}$) two-point model (dashed line) over four, 0.10 m layers with temperatures of 500, 1500, 2000, and 2500 K. The partial pressure is 0.1 atm (10.133 kPa) over the one-dimensional path. Radiative wall heat flux differences are given for each simulation (dash-dot line).

In Fig. 4.4, the spectrally resolved radiative wall heat flux is given for a one-dimensional domain. The temperatures are homogeneous for each simulation, but change between simulations with values of 500, 1000, 1500, 2000, 2500, and 3000 K. The species are placed in four distinct layers, each with thicknesses of 0.10 m. The order of the species are water vapor, carbon dioxide, the hydroxyl radical, and carbon monoxide, each with a partial pressure of 0.1 atm (10.133 kPa). The high-fidelity and low-fidelity spectral models show integrated spectral heat flux errors of 16.36, 8.84, 3.64, 1.62, 0.79, and 0.40% for each temperature, respectively. These results are notable because the addition of other radiative species actually decreases the spectral

modeling error from the strictly water vapor case, indicating that the models become more reliable as the system becomes more complicated.

The results of the errors are given in Table 4.1 for homogeneous one-dimensional paths. The partial pressure for radiative species in all cases is 0.1 atm (10.133 kPa), and the path length is 0.10 m. The species are water vapor, carbon dioxide, the hydroxyl radical, carbon monoxide, and methane. The temperatures for each simulation are 500, 1000, 1500, 2000, 2500, and 3000 K, respectively. Water vapor has the lowest spectral modeling error in this situation, whereas carbon monoxide has the highest spectral modeling error. However, carbon monoxide has a significantly lower overall contribution to the radiative heat flux than water vapor does. The error decreases with increased temperature. These issues are considered when establishing error tables in the following section.

Table 4.1: Errors associated with simplified two-point c-k model vs LBL at various temperatures. All species partial pressures are 0.10 atm. All path lengths are 0.10 m.

	H ₂ O	CO ₂	OH	CO	CH ₄
Temperature	Error	Error	Error	Error	Error
(K)	(%)	(%)	(%)	(%)	(%)
500	23.3	3.31	138	70.9	-6.23
1000	10.7	-2.00	172	110.	20.76
1500	4.35	-0.64	145	97.0	30.03
2000	1.94	0.48	123	79.3	18.09
2500	0.95	0.60	105	64.1	7.29
3000	0.49	0.41	90.6	52.1	2.61

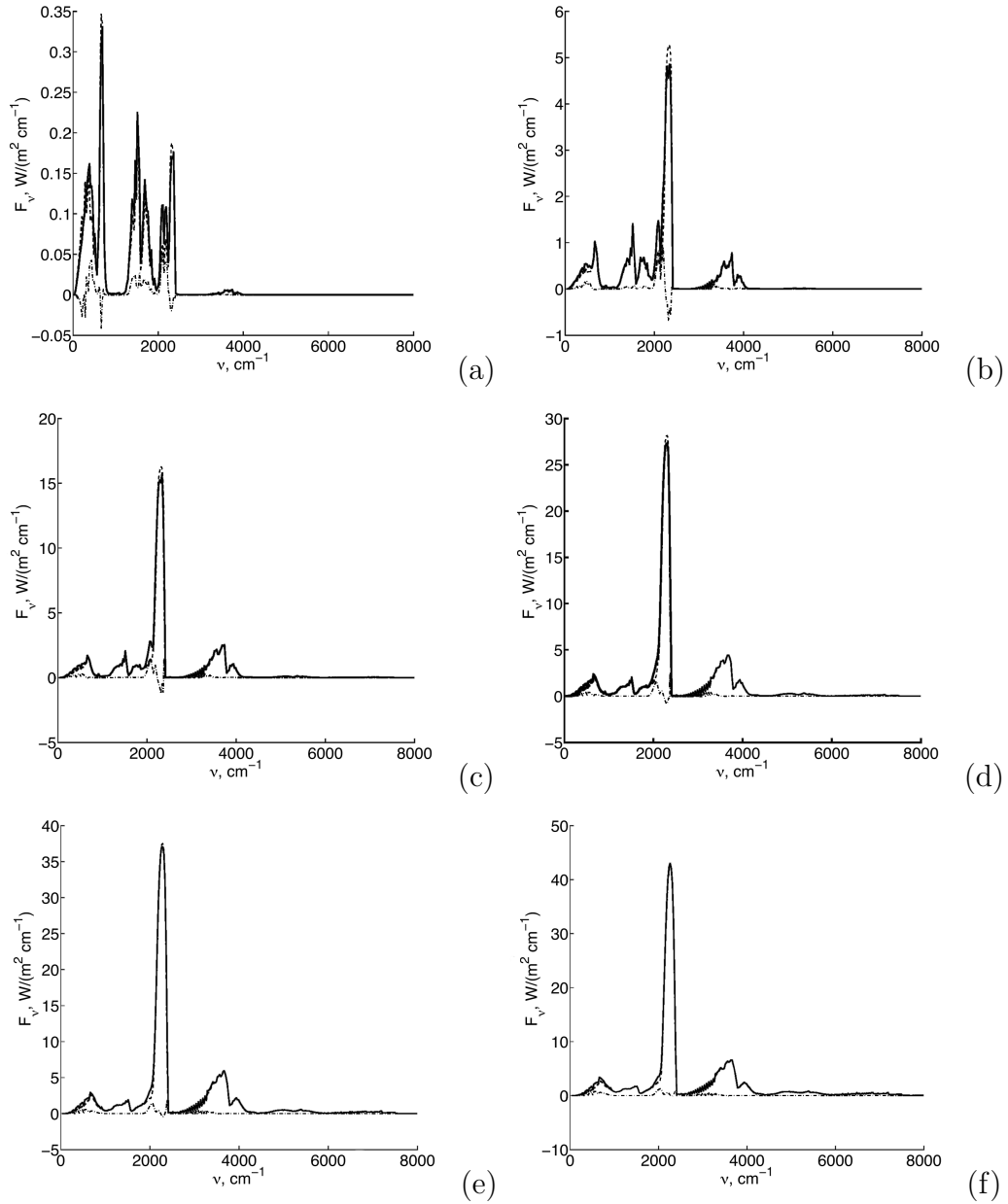


Figure 4.4: Spectrally resolved radiative heat flux for the high-fidelity spectral ($\Delta\nu = 0.01 \text{ cm}^{-1}$) model (solid line) and a low-fidelity spectral ($\Delta\nu = 25 \text{ cm}^{-1}$) two-point model (dashed line) over four 0.10 m layers with species of water vapor, carbon dioxide, carbon monoxide, and the hydroxyl radical, respectively. The partial pressure is 0.1 atm (10.133 kPa) over the entire one-dimensional path. Radiative wall heat flux differences are given for each simulation (dash-dot line). Temperatures are (a) 500 K, (b) 1000 K, (c) 1500 K, (d) 2000 K, (e) 2500 K, and (f) 3000 K

The main explanation for water vapor being the easiest to characterize is that it has a significantly more dense band structure than the other species do. Additionally, as the temperature rises, the individual spectral lines become activated, which increases the overall spectral density of a species [36, 92]. Bands with larger spectral line densities are more accurately modeled with a handful of quadrature points because their features tend to have less spectral variation needing to be captured. Bands that are not as spectrally dense have more distinct features, which are harder to capture with only one or two quadrature points [59]. The mixture of species tends to decrease spectral modeling error because multiple species add more spectral lines than any one species has, thus making the spectral band easier to model with only two points.

With such large differences in relative error among species, and even among temperature bands, the validity and reliability of the method is called into question. The current method is tuned to reduce the relative spectral error of high temperature water vapor and carbon dioxide, which are the main contributors to radiative heating as explained in Chapter III. Furthermore, the incoming flow is mostly above 1000 K, meaning that the simulations mostly draw from the tables with lower estimated errors. Even though the minor species have large relative errors relative to their contributions, their overall contributions are predicted to be small.

When considering other spectral modeling methods, most previous studies completely neglect minor radiative species when calculating radiative heat flux in combustion chambers, and the performance of the major emitters of water vapor and carbon dioxide do not show significant improvement in accuracy by using a more complicated model in the temperature range of interest. The works of Modest, Wang, Pal and others have found that various c-k methods can reduce the error to as low as 1% in a one-dimensional combustion chamber settings, but these methods only examine water vapor and carbon dioxide [76, 79, 78, 110, 111, 112]. Additionally, work

by Strohle et al. has found that for 1000 K water vapor only using an exponential wide-band model, errors in radiative heat flux can range between 0.6 and 23.3% [105]. Various c-k and fictitious gas methods are examined by Riviere et. al, using water vapor with path lengths of 10 to 20 cm at various temperatures. These examinations show a 1 to 2% spectral modeling error over the 1500 K range. Works by Liu et al. have examined statistical narrow-band modeling of water vapor and carbon dioxide in combustion environments of similar length and have found that errors range from 1 to 2% when temperatures approach 1800 K, but spectral modeling errors can be as high as 20% depending on the model employed [66, 67]. Studies by Porter et al. have found that the spectral modeling error for a combustion environment modeling only water vapor and carbon dioxide with a wide range of temperatures in the environment maintains an error of only 1 to 2% for full spectrum c-k models [86]. This study indicates that there is still much room for improvement in the spectral model on the lower end of the temperature range. However, due to the temperatures within the combustion chamber, these discrepancies may not be an issue. Examinations in the following sections address the impacts of the spectral modeling errors.

4.2.2 Error Tables

Given the inherent errors from the spectral model employed, a means of prediction is needed to estimate the uncertainty that the model contributed to the thermal radiative simulations. As discussed in the previous section, the spectral modeling error can change greatly depending on both species and temperature. As such, any uncertainty predictions will need to take both factors into account. An additional question considered is the optical depth of the system and its effect on the spectral modeling errors. As the optical depth approaches zero, the spectral modeling errors approach zero, provided that the spectral model averages to the mean absorptivity of the band in question per Eq. 4.1. As the optical depth approaches infinity, any

error in absorptivity will only affect the difference between the value of the actual thermal radiation intensity and the associated value of the blackbody intensity of the medium. However, as optical depth approaches infinity, the thermal radiation approaches blackbody, meaning that the difference (and, thus, the possible spectral modeling error) diminishes. With this in mind, the effects of optical depth are examined.

The method of calculating the spectral modeling errors is given by Eqs. 2.19 through 2.25 in Section 2.3. As with the spectral model tables, the error tables are generated for all radiative species at temperatures of 500, 1000, 1500, 2000, 2500, and 3000 K with an associated pressure of 1 atm (101.325 kPa). The optical depth requires further investigation.

The flow regime of the HIFiRE-2 combustion chamber is considered as a representative case. The species of greatest concern are water vapor and carbon dioxide, both of which have molar concentrations ranging from 1 to 5 mole/m³. When calculating the tables, number density is not directly used. Instead, partial pressure is employed. The justification for this change in variables is that the pressure of the system remains much more consistent than the number density does, as given by Figs. 3.5 through 3.7. As such, a table calculated on constant pressure would have a more general application than a table based on constant density. The table based on constant pressure accounts for density variations with the use of the ideal gas law (as given in Eq. 4.2), knowledge of the temperature, and a pressure multiplier. The partial pressures of consideration for the major species range from 8 to 45 kPa. The resulting depths are 0.8 to 45 kPa-m. For the purposes of the tables employed, the pressure is normalized by 1 atm (101.325 kPa), resulting in a path length range of 0.008 to 0.44 m for the HIFiRE-2 scramjet combustor. In order to examine this range, a series of simulations is run with associated lengths ranging from 0.001 to 1 m.

$$\rho = P/RT \quad (4.2)$$

The resulting spectral error prediction tables vary greatly based on temperature, frequency, and species. Additionally, the predicted spectral modeling error values can vary by two orders of magnitude for different path lengths with same temperature and frequency of water vapor. The statistics of the error tables are given in Appendix B.

In order to determine which path length is representative of the current work, a review is made of the work by Irvine, in which a series of one-dimensional traces were extracted from a CFD RANS solution of the HIFiRE-2 scramjet [50]. The CFD solution is identical to the solution presented in Chapter III. The lines compare the spectral model presented in this work with a higher fidelity Implicit Monte Carlo (IMC) method [30]. The findings show that when only water vapor is considered, the spectral method presented here is within 3% of the higher fidelity model for most cases and is within 6% of the higher fidelity model for the cases of lowest thermal heat flux. Given the mean data in Table B.1, the most appropriate choice of lengths is the 1 m path, which is used for the rest of this section.

An additional source of uncertainty is the experimental uncertainty present in the tables of the HiTemp database [92]. The data in the tables can vary the Lorentz line profiles by a significant amount. A study in previous work by Irvine has examined the propagation of the HiTemp database uncertainty through a radiative simulation of the HIFiRE-2 combustor using an Implicit Monte Carlo method [50]. The study found that for spectrally integrated radiative heat transfer, only the uncertainty in the linestrengths affected the overall radiative heat flux in a significant manner. The results found that for the pure water vapor case the spectral database error translated to error predictions of 20 to 25% of the total radiative wall heat flux. These numbers can be used as the database error prediction, “ $E_{\nu 1}$,” from Eq. 2.20 in Section 2.3.

The application of the database error has its own constraints. As far as verification of any set of simulations is concerned, the database error is meaningless because it would affect all models and simulations identically. However, when evaluation of the datasets is considered, either by comparing the simulation results to experiments or to simulations based on different spectral databases, the database uncertainty must be incorporated in order to account for the variation that uncertainty may contribute to the simulation of interest. Since all simulations in this work are based on the HiTemp database, simulation-to-simulation comparisons will not include the database error prediction. However, any comparisons to experiments and estimations of absolute uncertainty must incorporate the database error predictions.

4.2.3 Error Propagation

With spectral error prediction tables generated for one-dimensional cases, the question of their applicability to the full three-dimensional simulation must be addressed. Unfortunately, a total spectral integration of the full domain with the high-fidelity spectral model is more computationally intensive than the low-fidelity model within both the DOM or RT methods. Several manners of reduced comparison are possible. One such method is to use a stochastic sampling of the spectral domain using an IMC selection. However, due to memory constraints, this method is only available for the water vapor simulations with no other species included.

A direct comparison between the IMC simulation of the DOM analyses of the HIFiRE-2 combustor are presented for a pure water vapor case by Irvine [50]. Both sets of simulations use 720,000 sample points. The boundary conditions are pure radiative outflows on all physical walls and specular reflection along planes of symmetry. The HIFiRE-2 domain is taken from the RANS CFD simulations provided from the AFRL and are identical to the flowfields used in the previous section.

The results of both calculations are given in Fig. 4.5. The results of the IMC

simulation, which are provided from Irvine’s thesis, are given in Fig. 4.5 (a) and are treated as a truth model in this case [50]. The IMC method employed 10 million particles and a spectral sampling resolution of 0.01 cm^{-1} with a 26-temperature, single-species lookup table.

The DOM simulation results for radiative heat flux are given in Fig. 4.5 (b) and employ the low-fidelity spectral two-point banded model with a resolution of 25 cm^{-1} . The DOM simulation employs an S_8 quadrature scheme. The error estimation scheme is chosen to provide the limits of possible error as suggested by the error lookup tables. For the case of the HDRC geometry, the optical depth is low enough to where the total radiative heat flux can be assumed to be a linear superposition of the individual species concentrations from each cell. This assumption is further supported in Section 3.3, in which the additive sensitivities of all of the individual radiative species partial pressures is approximately equal to the sensitivity of the radiative wall heat flux to the total pressure. With all cell quantities having approximately independent effects, all of the linestrengths contribute mainly to emission and not to absorption. As such, the relationship between linestrength and total radiative wall heat flux is approximately linear and positive. Thus, the possible range of radiative heat flux contributions from a spectral line is calculated from the maximum and minimum possible linestrengths. In order to calculate the upper and lower bounds of the spectral uncertainty, all table entries are perturbed in the same manner simultaneously.

If a probability curve is desired, then the table entries for the most radiative species (water vapor and carbon dioxide) can have their individual entries sampled with a structured design study. This study becomes more useful when the system optical depth increases making the radiative contributions non-linear. However, only a cumulative error estimation is desired in this work. Thus, all spectral model error predictions are performed by taking the difference of the radiative heat flux predictions associated with maximum, minimum, and nominal possible spectral table values.

In general, the DOM result has many of the same features as does the IMC result. However, in the DOM, the spectrally banded model tends to under-predict the radiative heat flux. When the water-only results in Fig. 4.5 are compared with the full species results of Fig. 3.10 (b), the same general features are observed in both figures, such as the location of the peak heat flux in the flame holding cavity and a lack of radiative heat flux upstream of the fuel injectors. However, due to the absence of other radiative species, the water-only case has a reduction in radiative wall heat flux of up to 50% compared to full-species simulations.

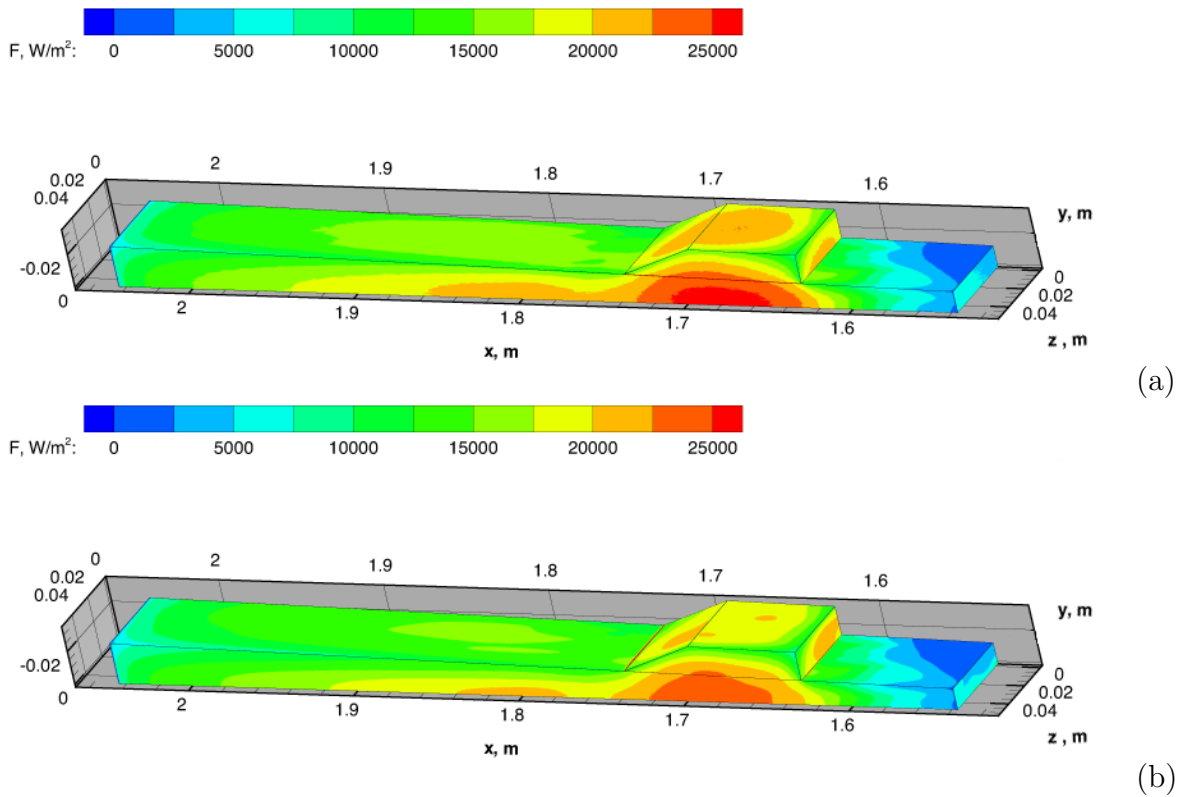


Figure 4.5: Radiative wall heat flux for a water vapor simulation of the HIFiRE-2 combustion chamber. Solutions from (a) the IMC method and (b) the DOM on identical grids. Flow is from right to left.

The comparison between the IMC data provided by Irvine and a DOM dataset performed for the current work is given in Fig. 4.6 (a). The figure displays the difference between the radiative wall heat flux of the two methods divided by the

radiative heat flux as calculated by the IMC method. The two simulation methods are notably different in two ways. The first difference is that the IMC uses a stochastic, high-fidelity frequency sampling method, whereas the DOM uses the low-fidelity two-point banded method as presented in this work. Additionally, the IMC has a stochastic directional sampling, whereas the DOM uses a predetermined S_8 ordinates method [29]. The relative differences remain below 20% of the computed IMC values over most of the wall. In lower flux regions near the primary injectors, the relative error rises significantly, but the absolute error is still small.

An error estimation is performed for the low-fidelity spectral banded model using the DOM simulations and the spectral modeling error tables calculated in the previous section. First, the DOM simulation is performed. Then, the spectral tables for the banded model are perturbed by multiplying them by the error tables. The simulations are rerun, and the relative difference is given in Fig. 4.6 (b). The spectral modeling error estimator gives a much more spatially consistent prediction than the actual error with estimations ranging between 3 and 5% of the computed DOM radiative heat flux values. The error estimator can be significantly higher or lower than the actual error predicted by taking the difference of the IMC and the DOM predictions.

The ratio of the values of Fig. 4.6 (b) (estimated error) divided by the values in Fig. 4.6 (a) (actual error) is given in Fig. 4.6 (c). The DOM spectral modeling error estimator tends to greatly over-predict the actual error near the centerline, and it tends to under-predict the error in the corners. However, most of these under-predictions are within 50% of the value of the actual error. This trend suggests that, although the error estimator may not be able to be used as a correction factor, it can still give an order-of-magnitude prediction for the overall system error. As suggested by the large changes in spectral modeling error prediction of the tables in Appendix B, the predicted error can easily fluctuate by several orders of magnitude over different length scales for otherwise identical problems. Thus, any knowledge of the spectral

error to within a reasonable accuracy can be useful.

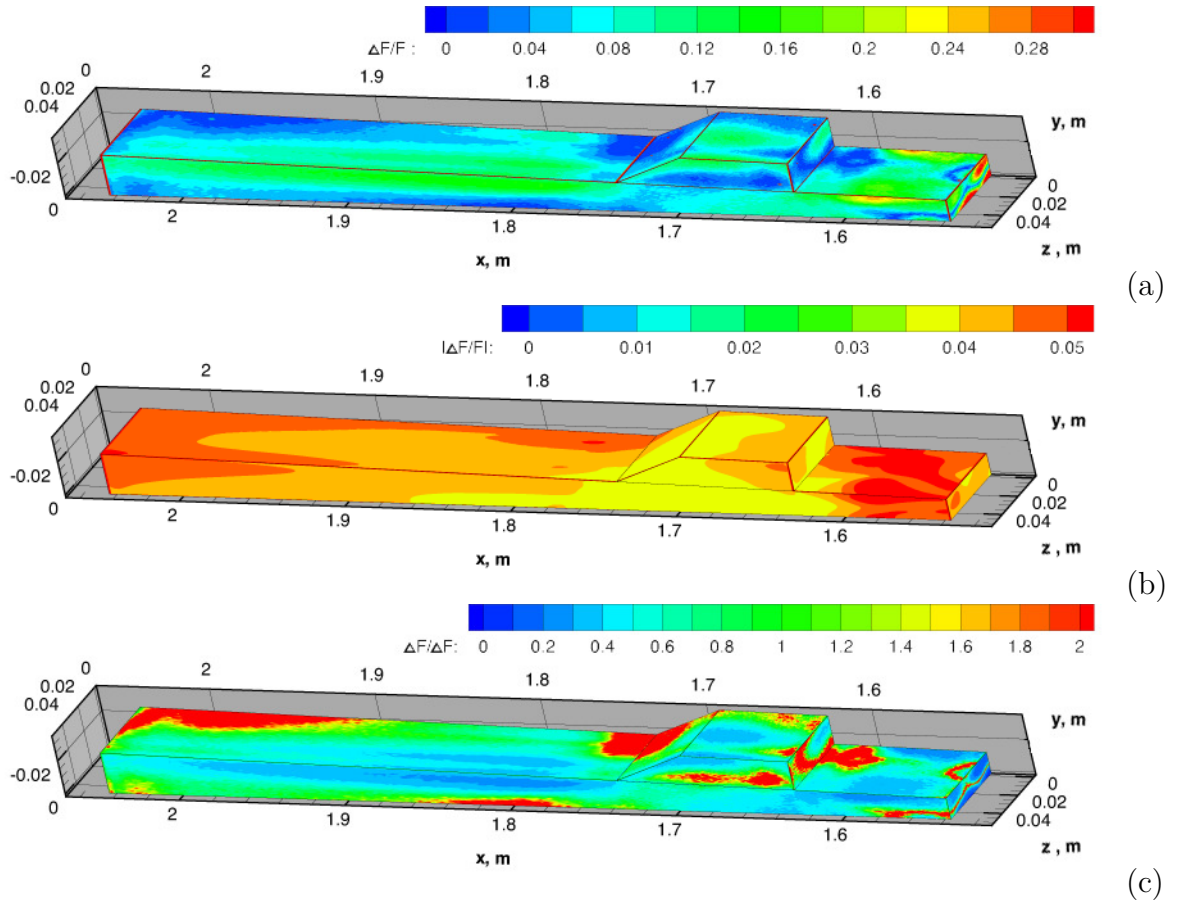


Figure 4.6: Relative error of a radiative simulation of the HIFiRE-2 combustion chamber for water vapor. (a) The relative change between the base level high-spectral-resolution IMC simulation and the low-spectral-resolution DOM simulation. (b) The error estimated with the low-spectral-resolution DOM error tables. (c) The ratio of the error estimated with DOM error tables to the actual error computed from the high-spectral-resolution IMC simulation. Flow is from right to left.

As stated previously, there is a significant difference between the angular model used in both simulations, whereas the DOM is limited by a mathematically structured angular mesh. The IMC is able to employ an arbitrarily fine angular mesh. In order to account for this, a number of simulations are run with the RT method. The RT method allows for arbitrarily fine sampling of the field of view for any one point within the domain. However, the spatial resolution necessitates that the RT and DOM simulations employed a different sampling of the CFD simulation flowfields. A direct computation is performed for a number of points on the physical wall surface using only the banded water model with an angular spacing of 2.5° in a rectangular pattern and a path resolution of 0.5 mm. The simulations are rerun with a perturbed spectral model and compared to the original simulations. Additionally, the results of the IMC simulations are sampled at the locations of interest. All data are given in Table 4.2.

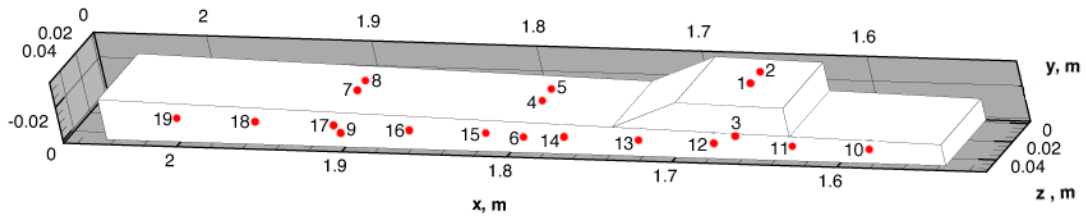


Figure 4.7: Locations of sample points in the HIFiRE-2 combustion chamber corresponding to Table 4.2. Sample points are denoted by red dots. Flow is from right to left

The locations of all of the points are shown in Fig. 4.7. The first three samples lie within the flame holding cavity region. The next three samples are near the exit of the flame holding cavity. The following three samples are midstream down the length of the combustion chamber, and the remaining ten samples run the length of the side of the domain from the fuel injectors to the exit plane. The final ten samples are the same points used in the IMC to DOM comparisons in Figures 5.5 to 5.7 from the

Table 4.2: Radiative heat flux evaluated at different wall locations for the HIFiRE-2 test case. The two methods employed are a high-fidelity spectral IMC model F_{IMC} and a RT method with a banded spectral model F_{RT1} . The spectral error is estimated using a perturbed banded spectral model F_{RT2} . The estimated error from the perturbed RT model and the actual error from the IMC are given.

	x	y	z	F_{RT1}	F_{RT2}	F_{IMC}	$\frac{\Delta F_{RT}}{F_{RT1}}$	$\left \frac{F_{RT1} - F_{IMC}}{F_{IMC}} \right $
	(m)	(m)	(m)	(W/m ²)	(W/m ²)	(W/m ²)		
1	1.660	-0.0326	0.0254	2.13×10^4	2.19×10^4	2.22×10^4	0.028	-0.041
2	1.660	-0.0326	0.0127	2.02×10^4	2.10×10^4	2.12×10^4	0.039	-0.043
3	1.660	-0.0100	0.0508	2.31×10^4	2.40×10^4	2.48×10^4	0.036	-0.068
4	1.750	-0.0175	0.0254	1.38×10^4	1.44×10^4	1.44×10^4	0.043	-0.042
5	1.750	-0.0175	0.0127	1.18×10^4	1.24×10^4	1.24×10^4	0.047	-0.049
6	1.750	-0.0040	0.0508	1.89×10^4	1.97×10^4	2.03×10^4	0.038	-0.067
7	1.900	-0.0209	0.0254	1.46×10^4	1.52×10^4	1.55×10^4	0.043	-0.060
8	1.900	-0.0209	0.0127	1.44×10^4	1.50×10^4	1.53×10^4	0.044	-0.065
9	1.900	-0.0040	0.0508	1.72×10^4	1.79×10^4	1.87×10^4	0.040	-0.082
10	1.581	-0.0092	0.0508	7.93×10^3	8.32×10^3	9.21×10^3	0.050	-0.139
11	1.627	-0.0099	0.0508	1.90×10^4	1.97×10^4	2.06×10^4	0.038	-0.079
12	1.673	-0.0106	0.0508	2.34×10^4	2.43×10^4	2.51×10^4	0.036	-0.065
13	1.717	-0.0113	0.0508	2.08×10^4	2.16×10^4	2.21×10^4	0.036	-0.057
14	1.766	-0.0120	0.0508	1.69×10^4	1.76×10^4	1.84×10^4	0.039	-0.083
15	1.812	-0.0127	0.0508	1.67×10^4	1.74×10^4	1.88×10^4	0.041	-0.114
16	1.858	-0.0134	0.0508	1.58×10^4	1.65×10^4	1.75×10^4	0.042	-0.099
17	1.904	-0.0141	0.0508	1.48×10^4	1.54×10^4	1.63×10^4	0.043	-0.090
18	1.951	-0.0148	0.0508	1.37×10^4	1.43×10^4	1.50×10^4	0.044	-0.085
19	1.997	-0.0155	0.0508	1.21×10^4	1.27×10^4	1.32×10^4	0.045	-0.080

thesis by Irvine [50]. Depending on the location of the sampling point, a number of phenomena are noticeable. The predicted spectral errors are taken as the difference between the IMC and RT method simulations. For points 1 through 3, the values of all predicted spectral errors are within 50% of the values of the actual spectral errors. For points 4 through 6, which lie directly behind the flame holding cavity, the error prediction agrees to within 3% of the actual error value for the upper wall and within 43% for the side wall. For points 7 through 9, a location significantly farther downstream of the cavity, the error is within about 32% of the actual error value for the top wall and within about 51% of the actual error value at the side wall. For

the range of points spanning the length of the side wall (points 10 through 19), the predicted error is within 65% of the values of the actual error for all locations. The location of the worst error estimator is within the low flux region, where the actual error is the least consequential.

Another notable trend is that, in all cases, the banded spectral model under-predicted both the radiative heat flux and the relative error for all sample points. A full comparison shows that there are regions where the banded spectral model can over-predict as well [50].

To examine the consistent trend of under-prediction, the possibility of dimensional errors is considered. The spectral error tables are constructed using one-dimensional unit problems, which may not directly translate into three-dimensional problems. In a previous study, the points at locations 10 through 19 of the Table 4.2 were examined using a one-dimensional problem [50]. The one-dimensional traces were calculated for each point considering only water vapor. The problems were calculated using one-dimensional IMC and DOM simulations on identical grids. As before, the IMC employed a much finer spectral resolution than did the DOM. The spectral error was found to be 2 to 3% of the value of the high-fidelity spectral radiative heat flux prediction for all of the locations except for location 10, which is a lower flux region than most of the domain, having an actual error of 6% of the radiative heat flux predicted by the high-fidelity spectral model. Comparing these results to the three-dimensional results, it is found that the three-dimensional errors for the same points are between two to four times larger than those of the one-dimensional results. As such, it is suggested that spectral errors increase as the simulations go from one to three dimensions. Furthermore, the spectral modeling errors predicted by the narrow-banded ray-tracing simulations are larger than the actual spectral modeling error of the one-dimensional comparisons, but they are smaller than the actual spectral modeling errors of the three-dimensional comparisons. Although the RT simulations are three-

dimensional, their error predictions are based upon one-dimensional estimations. As such, the error predictions for three-dimensional simulations are of similar magnitude to those of one-dimensional simulations. As established earlier in the section, a one-dimensional domain tends to have a spectral modeling error that is smaller than that of a three-dimensional domain by a factor-of-two. Basing a three-dimensional error prediction on a one-dimensional unit problem results in a consistent under-prediction in spectral modeling error. However, the order of the under-prediction remains relatively consistent among points. For the current case, a simple correction of doubling the predicted spectral modeling error is proposed to compensate for the dimensional change. This error doubling is applied to the spectral modeling error tables before the simulations are run.

Additional investigation using strictly DOM simulations with limited spectral bands gives a similar trend, suggesting that spatial model resolution does not change the factor-of-two change in error introduced by switching from one to three dimensions. This factor-of-two does not affect the spectral database uncertainty that is addressed in the previous section, since the database uncertainty is an uncertainty that affects all models and simulation domains equally, regardless of dimensions or optical depth.

4.3 Numerical Accuracy

In addition to spectral accuracy, the numerical accuracy of the solution method is also under consideration. Numerical accuracy for the current case is addressed using mesh refinement studies. The current DOM program does not include the ability to consider flux schemes with an order higher than one, and therefore, such numerical issues are not addressed. The refinement of the numerical system can be considered with two types of refinements. The first refinement is to consider the grid used to sample the flowfield domain. The domains under consideration are CFD simulations

with several times more points than is practical to use in a DOM simulation. As such, the domain is sampled using a much coarser, structured mesh. The scheme used to sample the CFD domain is referred to as the “CFD sampling mesh” in the current section. This mesh may have an arbitrary refinement in order to adequately capture all of the features of concern. Sampling mesh refinement is addressed by comparing spatial radiation meshes with identical structures but different CFD sampling mesh fidelities.

The resolution of the radiative domain must be high enough in order to execute the simulation in an accurate manner. The mesh used for calculating the radiative heat flux has two refinement components: the first being spatial referred to as the “spatial radiative mesh,” and the second being angular referred to as the “angular quadrature scheme.” These meshes differ from the CFD sampling mesh in that they represent the numerical discretization used by the DOM program to calculate the radiative heat transfer within a domain. The level of accuracy is addressed by comparing grids of different refinement for both spatial and angular radiative meshes in order to find the spatial modeling error. These refinements can be addressed not only for the mesh convergence of radiative heat flux, but also for the convergence of the spectral error prediction method employed in Section 4.2.

Current limits of the DOM program, GRASP, prevent an arbitrary refinement of the numerical “spatial radiative mesh” or the “angular quadrature scheme.” If the numerical grid convergence limit is unable to be found within the limits of the DOM program, then an alternate modeling scheme is necessary to estimate the numerical modeling error inherent within the system. A numerical truth model can be assessed with the use of the RT method. The RT method has an arbitrarily fine CFD sampling mesh, spatial radiative mesh, and angular quadrature scheme refinement. Additionally, it can use the same spectral scheme as the DOM simulation, thus removing any spectral variation. The RT method can be employed to compare all forms of spatial

and angular convergence at once.

All simulations in the current section employ the two-point banded spectral method discussed in Section 4.2, with all five radiative species (water vapor, carbon dioxide, the hydroxyl radical, carbon monoxide, and methane) and a 25 cm^{-1} spectral resolution spanning from 25 to $10,000 \text{ cm}^{-1}$. The simulations are run using the HDCR CFD domain described in Section 3.1 and used throughout the current chapter. For all cases, the physical boundaries are treated as non-emissive, non-reflective radiative outflows ($T_{wall} = 0$, $r_\nu = 0$, and $\epsilon_\nu = 1$). The planes of symmetry are treated as perfect specular reflecting surfaces.

4.3.1 Grid Refinement

The first comparison of interest is for the various CFD sampling resolutions used to determine the inputs into the DOM simulations. For this comparison, a 710,000 point spatial radiative mesh is employed for all simulations. An S_8 quadrature scheme is employed as the angular radiative mesh for all simulations. The first simulation uses a fine CFD sampling mesh that matches directly to the spatial radiative mesh. The second simulation uses a coarser CFD sampling mesh that samples only one point in the CFD solution for every eight points in the spatial radiative mesh. The manner of sampling is as follows. The sampling resolution is reduced by half for all three spatial dimensions, and the corresponding points are sampled directly onto the reduced CFD sampling mesh. The mesh is then doubled in resolution for each dimension, and the values of the existing points are projected onto the seven new points. The choice of the points is such that if the domain were divided into hexahedrons with grid-points at their vertices, the original grid-point would be at the same corner for all hexahedrons and all other points within the hexahedron would have the same flowfield values as the original point. The resulting CFD sampling mesh directly coincides with the spatial radiative mesh. The resulting comparisons are given in Figs. 4.8 and 4.9.

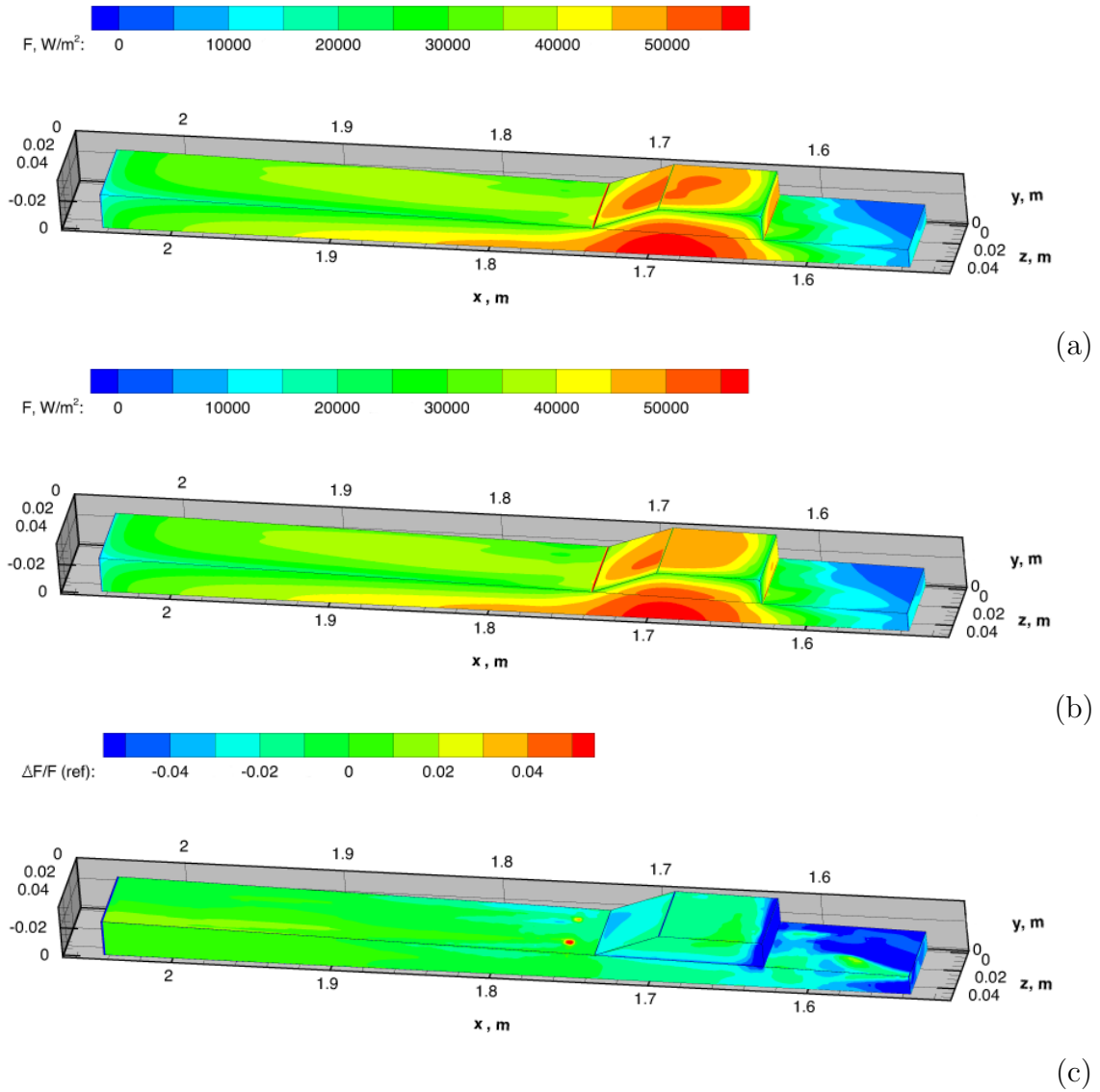


Figure 4.8: DOM solutions for fine spatial sampling with an S_8 angular quadrature scheme comparing the radiative wall heat fluxes for (a) the fine and (b) the coarse CFD sampling meshes. The relative difference between the simulations is given in (c), in which the difference between the two simulations is normalized by the values from the fine grid sampling. Flow is from right to left.

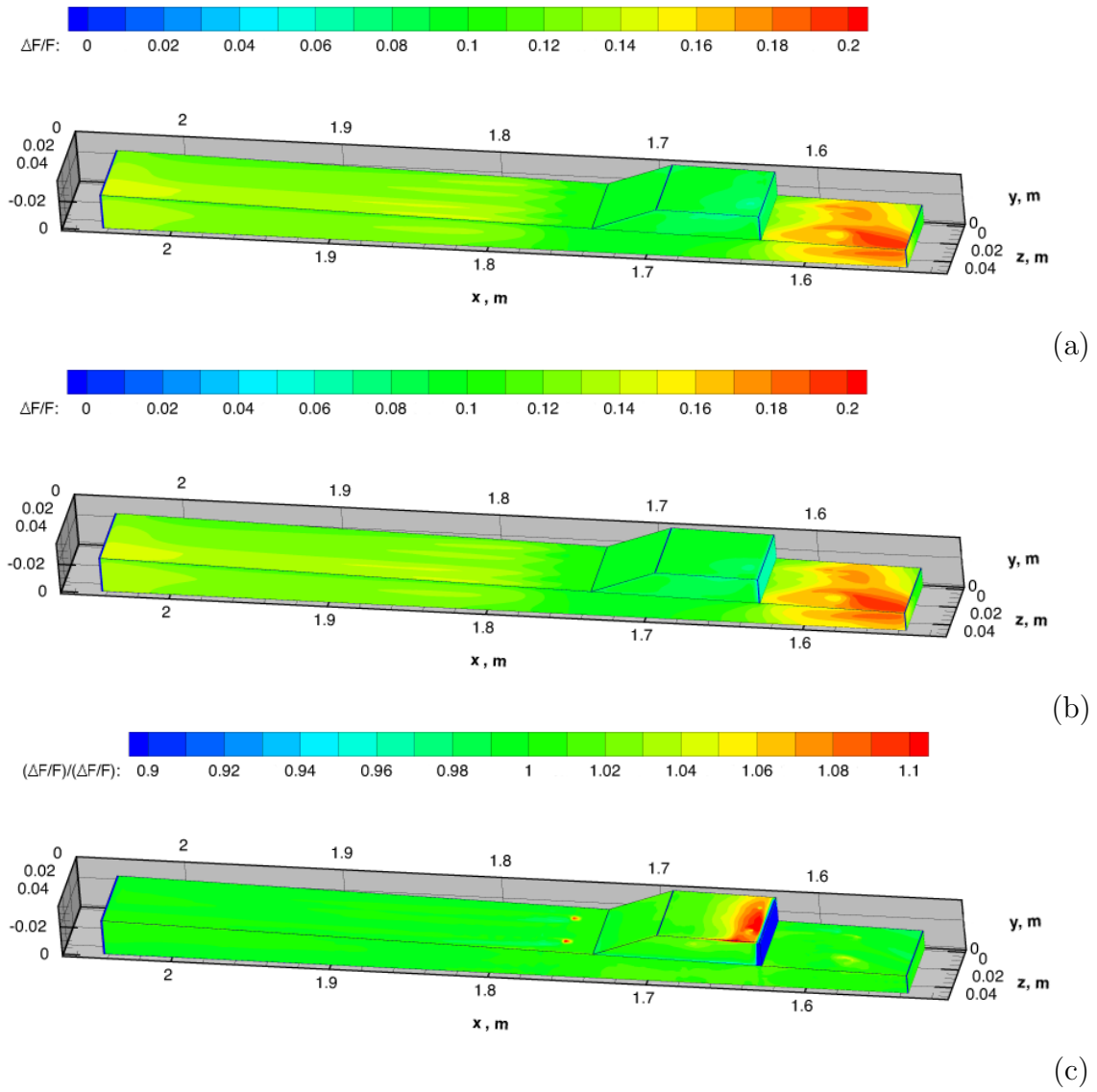


Figure 4.9: DOM solutions for fine grids and an S_8 angular quadrature scheme comparing the radiative wall heat fluxes for (a) the fine and (b) the coarse CFD sampling meshes. The relative difference between the simulations is given in (c) and is normalized by the fine grid sampling values. Flow is from right to left.

The radiative wall heat fluxes given in Figs. 4.8 (a) and (b) represent the solutions for the fine and coarse CFD sampling meshes, respectively. The simulations with the finer CFD sampling mesh show a slightly higher radiative heat flux within the flame holding cavity as opposed to the coarser CFD sampling mesh. The radiative heat flux peaks around 56 kW/m^2 in the flame holding cavity and reduces to about 20 kW/m^2 near the combustion chamber exit. Upstream of the fuel injection, the thermal radiative heat transfer is negligible. Downstream of the flame holding cavity, large variations in radiative heat distribution are not apparent. Near the primary fuel injectors, any differences in radiative heating appear small in magnitude relative to the rest of the domain. The relative difference between the radiative heat fluxes garnered from both simulations, as normalized by the values of the radiative wall heat flux from the fine CFD sampling mesh, are given in Fig. 4.8 (c). The simulations show agreement to within 3% of the total radiative heating values for most of the chamber. Near the primary fuel injection ports the relative difference is over 5%, although the absolute difference in radiative heat flux is small in magnitude. This difference is mainly attributed to the thin wall flame structures, which are not properly captured by the coarse CFD sampling mesh. As mentioned before, there are relative differences in radiative heat flux of over 5% in the flame holding cavity, mostly resulting in the coarser CFD sampling mesh being unable to account for the boundary gradients near the chamber walls. The highest difference in radiative heat flux lies at the front face of the flame holding cavity. The issues with the local flowfield gradients are most apparent on the front wall because the field of view is limited mostly to the adjacent section of the cavity, which has the most notable gradients. The radiative heat flux has small relative differences downstream of the cavity, with the exception of the location of the secondary fuel injectors. The cold stream around the secondary fuel injectors is not properly captured by the coarse mesh. Therefore, the simulation overestimates the thermal radiation at those exact points. The comparison suggests

that a fine CFD sampling mesh will resolve some features more accurately, but it will not improve the radiative heat flux estimate by more than 4% for most areas.

The predicted spectral modeling errors in Figs. 4.9 (a) and (b) represent the solutions for the fine and coarse CFD sampling meshes, respectively. The estimated spectral modeling errors for both CFD sampling meshes appear practically identical with the solutions from the coarse CFD sampling mesh having a slightly higher predicted error in some locations. The overall predicted spectral modeling error is significantly higher than the water-only prediction presented in Fig. 4.9 (a). The main cause of this difference is additional species included in the current simulations. Whereas Section 4.2 suggests that spectral error is reduced with the addition of new species, the spectral model incorporates all species errors in a linear manner, thus giving the maximum possible effect of spectral errors.

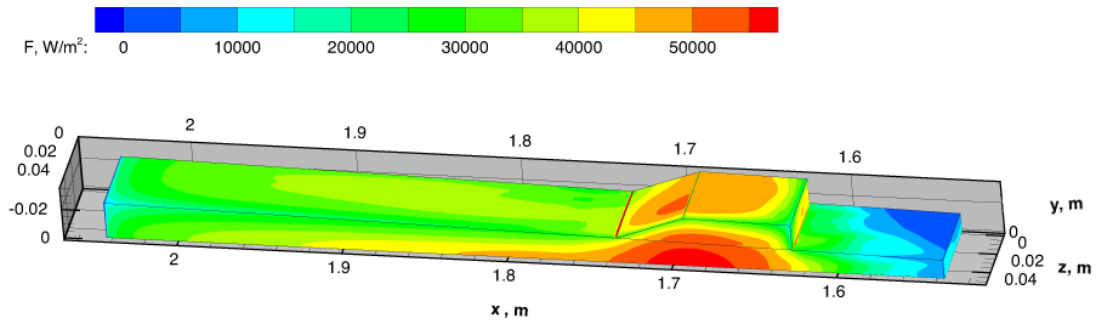
The largest contributor to the spectral modeling error prediction is carbon monoxide, which when included can contribute about 10% of the radiative heat flux in addition to contributing a spectral modeling uncertainty of almost equal value. With all species contributing to the expected radiative heat flux, the predicted spectral modeling error ranges between 0 and 15 % of the radiative wall heat flux for most of the chamber with significantly higher relative (but not absolute) value around the primary fuel injectors.

The ratio of the predicted spectral modeling errors is given in Fig. 4.9 (c), which depicts the predicted spectral modeling error of the coarse CFD sampling mesh divided by that of the fine CFD sampling mesh. The ratio of the predicted errors is almost 1 for most of the combustion chamber. This consistency suggests that the spectral modeling uncertainty affects all radiative simulations of the same domain equally regardless of their CFD sampling mesh resolution. This insensitivity can be attributed to the constancy in temperature and molar concentration between the two sampling schemes. There are exceptions around the fuel injectors and near the wall of

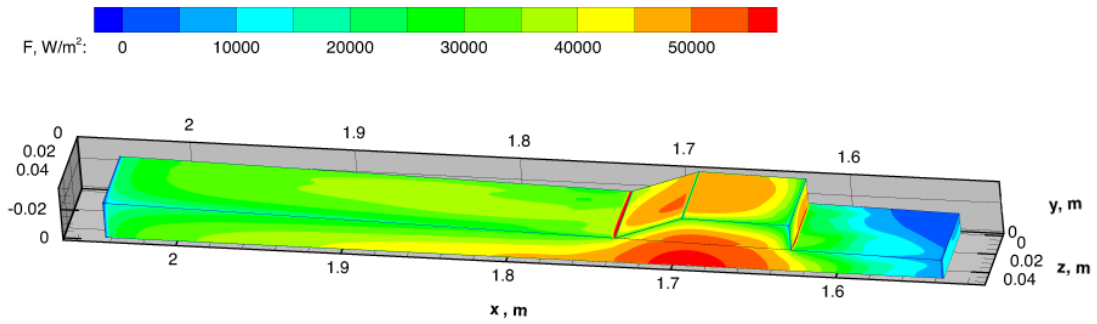
the flame holding cavity, where the coarse CFD sampling mesh is unable to capture sharp changes in temperature and concentration. As such, for those few locations, different values from the error tables are employed, resulting in slightly different predicted errors when calculating the spectral modeling error.

With the CFD sampling addressed, the question of numerical grid refinement in the radiation simulations remains. The two issues of concern are the spatial and angular refinements. The first issue of concern is the spatial refinement, which is addressed by comparing simulations using different spatial radiative meshes. The two grids employed are a 710,000 point and a 90,000 point structured spatial radiative mesh. The coarser spatial radiative mesh is a reduction by half in all three dimensions of the number of points in the fine spatial radiative mesh. Both meshes use the coarse CFD sampling mesh discussed earlier in this section. All simulations for this study employ an S_8 angular quadrature scheme. The resulting comparisons are given in Figs. 4.10 and 4.11.

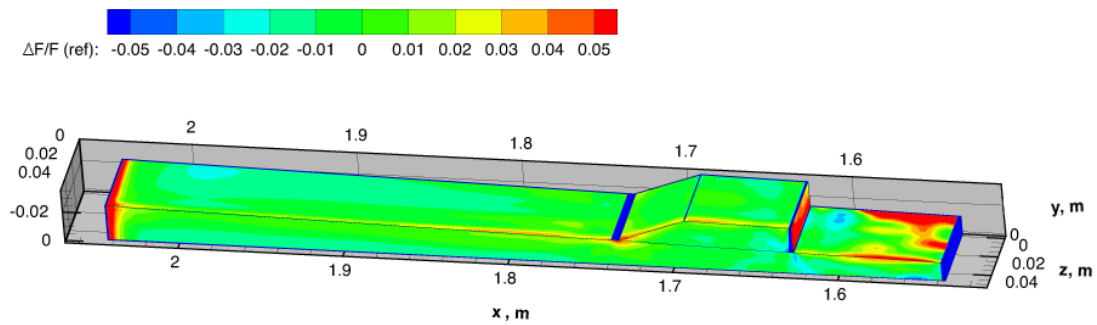
The radiative wall heat fluxes given in Figs. 4.10 (a) and (b) represent the solutions for the fine and coarse spatial radiative meshes, respectively. The radiative heat fluxes have similar features. The solutions to the coarse radiative spatial mesh show slightly reduced radiative heat fluxes compared to the solutions for the fine spatial radiative meshes. The radiative heat flux on the front face of the flame holding cavity for the coarse spatial radiative mesh in Fig. 4.10 (b) is significantly higher than that of the fine spatial radiative mesh in Fig. 4.10 (a). The radiative heat flux for the coarse spatial radiative mesh is closer in magnitude to the radiative heat flux of the fine CFD sampling mesh given in Fig. 4.8 (a).



(a)



(b)



(c)

Figure 4.10: DOM solutions for coarse CFD sampling mesh and an S_8 quadrature scheme comparing the radiative wall heat fluxes for (a) the fine and (b) the coarse spatial radiative meshes. The relative difference between the simulations is given in (c) and is normalized by the fine grid sampling values. Flow is from right to left.

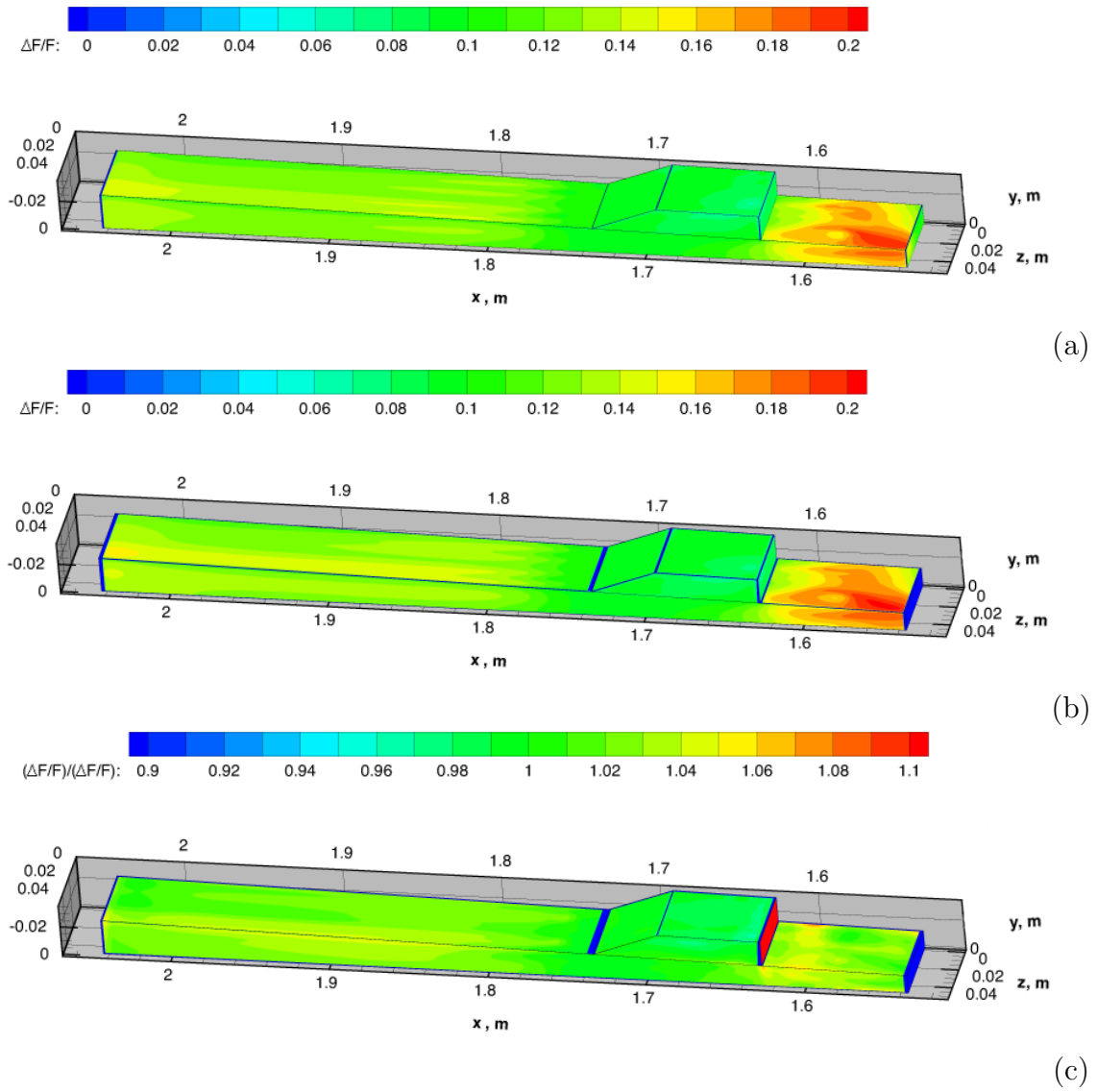


Figure 4.11: DOM solutions for coarse CFD sampling mesh and an S_8 quadrature scheme comparing the spectral error predictions for (a) the fine and (b) the coarse spatial radiative meshes. The relative difference between the simulations is given in (c) and is normalized by the fine grid sampling values. Flow is from right to left.

This issue may be the result of a sub-optimal projection of the coarser CFD sampling mesh onto the finer spatial radiative mesh. The projection can maintain the original value from the CFD sampling mesh, but the values of the points adjacent to the spatial radiative mesh can vary depending on the projection scheme. This variation in mapping the spatial radiative mesh with a projection from the CFD sampling mesh can result in shifted locations and thicknesses of gradients and flow features. These features are especially relevant in the flame holding cavity. This change suggests that the projection method employed for mapping the CFD sampling mesh to a spatial radiative mesh is as important as the CFD spectral mesh resolution.

The relative difference between the radiative heat fluxes garnered from both simulations, as normalized by the values of radiative wall heat flux from the fine spatial radiative mesh, are given in Fig. 4.8 (c). The relative change in the radiative heat flux when changing from a fine to a coarse spatial radiative mesh with identical CFD sampling mesh resolutions is at most 2% in the flame holding cavity. This value is smaller than the relative change presented for the CFD sampling mesh refinement given in Fig. 4.10 (c), suggesting that the majority of the refinement error in the flame holding cavity is mainly due to sampling and mapping. The area downstream of the flame holder displays relative differences of up to 3% of the radiative heat flux. As such, numerical grid refinement error is slightly higher than in the previous test case comparison given in Fig. 4.8 (c).

The predicted spectral modeling error in Figs. 4.11 (a) and (b) represents the solutions for the fine and coarse spatial radiative meshes, respectively. The predicted spectral modeling error from the coarse spatial radiative mesh solution is slightly higher than that of the fine spatial radiative mesh solution. The relative difference between the predicted spectral modeling errors garnered from both simulations, as normalized by the values of the predicted spectral modeling error from the fine spatial radiative mesh, are given in Fig. 4.11 (c). The areas within the flame holding cavity

agree to within 2%, but locations downstream have differences as high as 5%. The relative change around the fuel injectors rises to the level of 7%. These changes are significantly more pronounced than those in Fig. 4.9 (c), suggesting that changes in the prediction of the spectral modeling error are more dependent on numerical solution than flowfield sampling. The relative errors on the front face of the flame holding cavity are not constant, mainly due to the shifted gradients the the mapping from the CFD sampling mesh to the spatial radiative mesh discussed above.

Finally the angular mesh refinement is considered. Two sets of simulations are run on the coarse grid described in the current section. The angular refinement of the simulation is either an S_6 or an S_8 angular refinement. The resulting comparisons are given in Figs. 4.12 and 4.13.

The radiative wall heat fluxes given in Figs. 4.12 (a) and (b) represent the solutions for the S_8 and S_6 angular meshes, respectively. The radiative features and peak values do not change much between the two ordinate schemes. However, the S_6 scheme does have more concentrated peaks. These peaks are a result of the S_6 scheme concentrating its radiative intensity along fewer, more widely spaced ordinates. The system does not show angular convergence with these methods. However, there is an upper limit on angles that can be employed in this situation because the scheme must be performed repetitively for numerous cases. The relative difference between the radiative heat fluxes garnered from both simulations, as normalized by the values of radiative heat flux from the S_8 scheme, are given in Fig. 4.12 (c). The relative difference introduced by reducing the angular ordinates is generally less than 10% of the radiative wall heat flux except for the low radiative heat flux regions near the primary fuel injectors. The rest of the variations are concentrated around areas of higher spatial gradients for the radiative wall heat flux. The differences around the gradients are attributed to the higher flux concentrations given by the S_6 scheme.

The predicted spectral modeling error in Figs. 4.13 (a) and (b) represent the

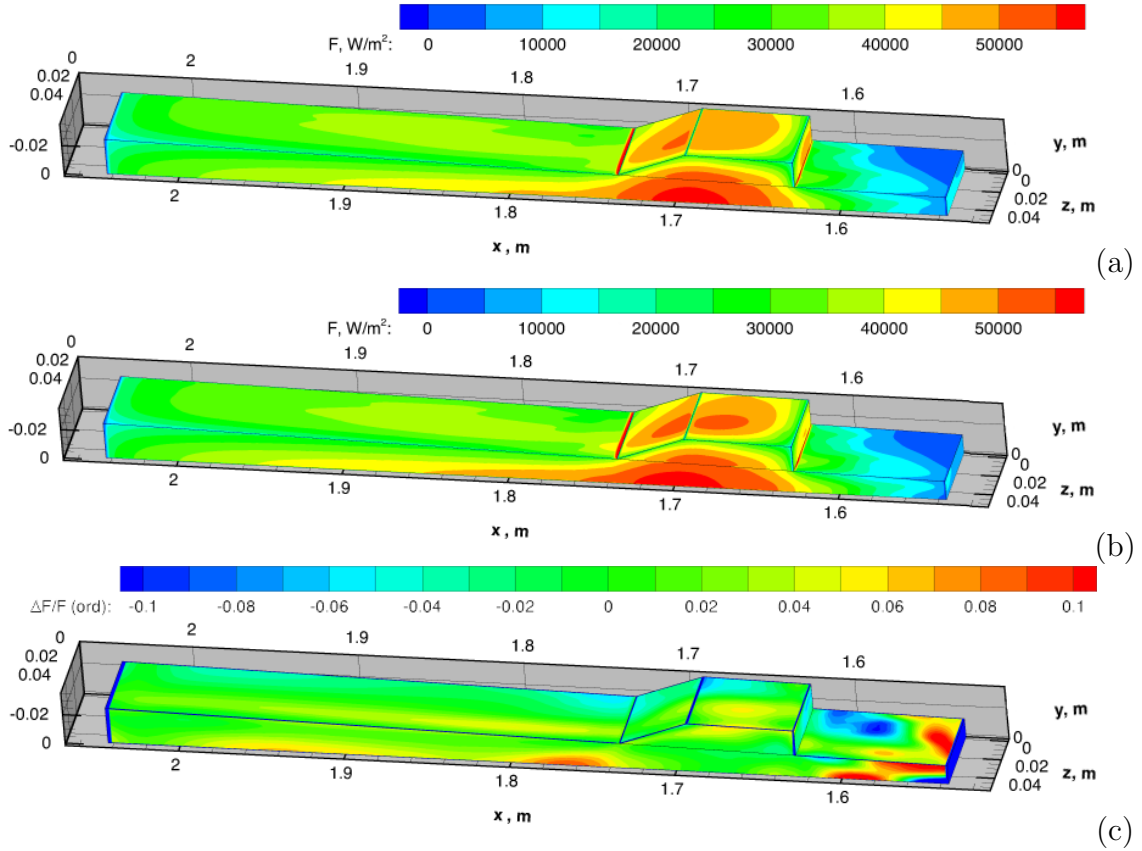


Figure 4.12: DOM solutions for a coarse grid comparing the radiative wall heat flux for (a) the S_8 quadrature scheme and (b) the S_6 quadrature scheme. The relative difference between the simulations is given in (c) with and is normalized by the S_8 quadrature scheme values. Flow is from right to left

solutions for the S_8 and S_6 meshes, respectively. In both cases, the predicted spectral modeling errors are very similar, showing that spectral modeling error has more to do with the spatial location than the overall angular resolution. In general, the errors depend on the source cell. A change in angular resolution may change the location of a cell's contribution to radiative wall heat flux, but it does not change the magnitude of the contribution be it either nominal or perturbed. As such, the overall error contribution does not change significantly.

The relative difference between the predicted spectral modeling errors garnered from both simulations as normalized by the values from the S_8 simulation, are given

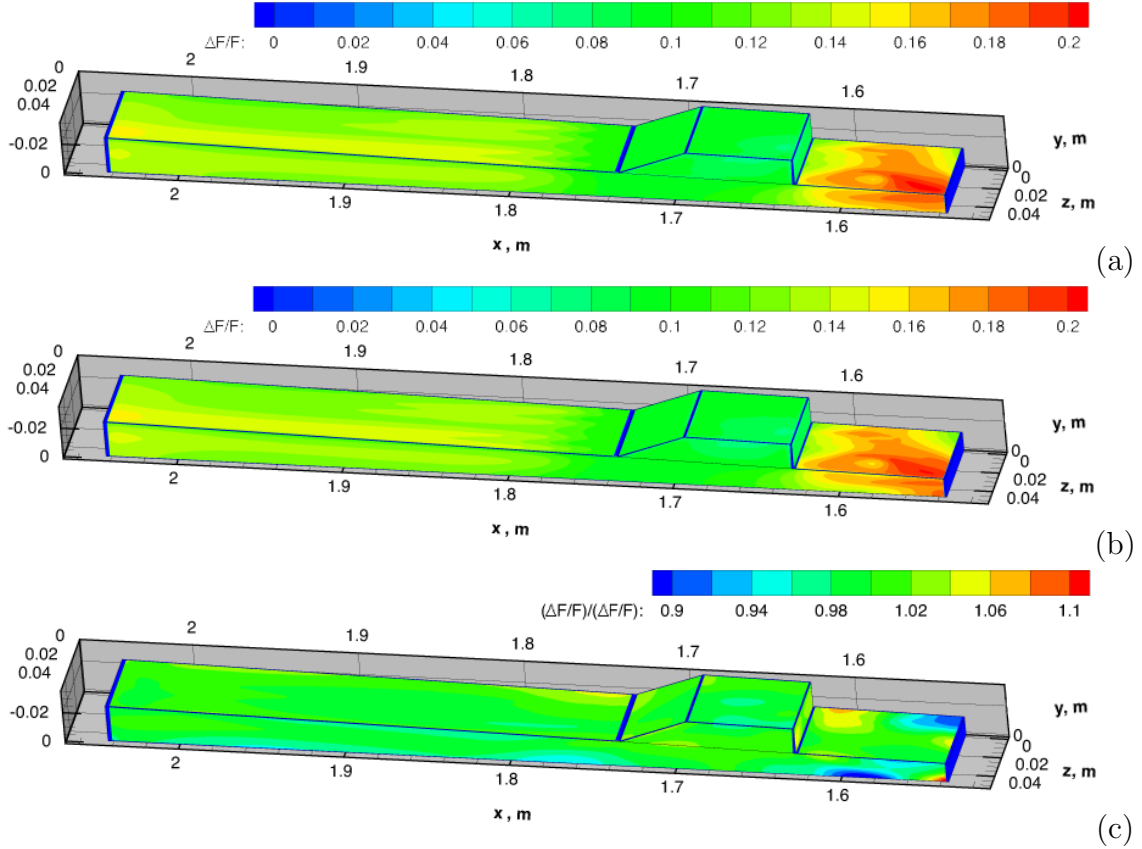


Figure 4.13: DOM solutions for a coarse grid comparing the spectral error predictions for (a) the S_8 quadrature scheme and (b) the S_6 quadrature scheme. The relative difference between the simulations is given in (c) with and is normalized by the S_8 quadrature scheme values. Flow is from right to left

in Fig. 4.13 (c). The ratio of the predicted errors shows that most predicted spectral modeling errors are within 2% of each other regardless of the angular method employed. The notable exception is in the low flux region with high gradients. In small areas of high gradients, predicted spectral modeling error can change by 12% of its value. Altogether, the radiative wall heat flux is quite sensitive to changes over the range of angular resolution possible. However, the perturbations caused by estimated spectral modeling error are stable and can be readily substituted for each other in most cases. Therefore, investigations strictly into spectral modeling uncertainty can be performed at a lower angular resolution than investigations into radiative wall heat

flux. This observation may serve to reduce computational times of design studies.

When all studies are compared, it is found that the largest changes in radiative heat flux are more directly related to CFD sampling mesh refinement and mapping than to spatial radiative mesh refinement, suggesting that as long as the appropriate domain values are used in the simulation, the spatial sensitivity of the radiative solution can be quite robust. However, if the angular quadrature scheme refinement is not adequate, then the thermal radiative heat transfer may not be distributed equitably along the walls, resulting in spurious hot spots. The predicted spectral modeling error appears to be affected mostly by the spatial radiative mesh refinement, and neither CFD sampling mesh refinement nor angular quadrature scheme refinement have much of an effect on it.

4.3.2 Numerical Method Comparison

The convergence study suggests that the system is not fully converged, even with the finest spatial radiative mesh. Further angular and spatial refinements are possible with the DOM, but they would not be practical for a large number of simulation runs as is planned in the parameter variation study detailed in Chapter V. Additionally, the inherent limitations within GRASP are currently being employed for spatial and angular meshes. The current sets of results from the previous sections, neither suggest that the current mesh is completely converged, nor does it suggest that the current mesh will achieve mesh convergence with the same order magnitude of points as is currently available. As such, an estimate of the combined spatial and grid error is required. A truth model is available to spot-check specific points. The Ray Tracing method employed in the previous section can be used to determine the absolute grid and sampling error of a simulation.

Two sets of simulations are employed. The first set is a pair of DOM simulations. Two meshes are used with 710,000 and 90,000 grid points for the fine and coarse

spatial meshes, respectively. (For the current set of simulations, the spatial radiative meshes are identical to the CFD sampling meshes.) Both simulations employ an S_8 ordinate angular quadrature scheme. The second set is a series of Ray Tracing method simulations using an angular resolution of 2.5° and a spatial sampling and resolution of 0.5 mm. The flux is transmitted with a first-order upwind scheme, although it is found that increasing the method to a second order upwind scheme does not affect the output. A convergence study shows that increasing angular resolution does not significantly change the output of the system. Therefore, the method is assumed to be converged in angular space. Both the RT and DOM simulations employ the two-point banded spectral method discussed in Section 4.2 with all five radiative species (water vapor, carbon dioxide, the hydroxyl radical, carbon monoxide, and methane) and a 25 cm^{-1} spectral resolution spanning from 25 to $10,000 \text{ cm}^{-1}$. The simulation results are compared in Table 4.3.

For most locations, the radiative wall heat fluxes predicted by the DOM on the fine and coarse spatial radiation meshes are within 3% and 5% of the RT predictions, respectively. These values suggest that all of the mesh refinement errors from the refinement studies are not necessarily additive. The angular and sampling studies suggest larger errors in certain areas, but the resolution under consideration appears to be reliable. Previous studies have found that comparing the DOM to higher fidelity methods has given mesh refinement errors ranging from 2 to 20% when simulating combustion environments [53, 55, 54]. Therefore, the simulations appear to give a lower amount of predicted uncertainty than the literature on the methods would suggest. As such, if using a coarse spatial radiative mesh for the DOM simulation, an error bar of $\pm 5\%$ can be used in the higher flux regions, and an error bar of $\pm 10\%$ can be used in lower flux regions. If a finer spatial radiative mesh is employed for the DOM simulations, an error bar of $\pm 3\%$ can be used in the higher flux regions, and an error bar of $\pm 8\%$ can be used in lower flux regions.

Table 4.3: Radiative heat flux evaluated at different wall locations for the HIFiRE-2 test case. The two methods employed are the RT method (F_{RT}) and the DOM with a banded spectral model (F_{DOM}). The fine and coarse spatial radiative meshes for the DOM are denoted by “1” and “2,” respectively. The relative difference in radiative wall heat flux is given and normalized by the radiative wall heat flux from the RT simulations.

	x	y	z	F_{RT}	F_{DOM1}	F_{DOM2}	$\frac{\Delta F_1}{F_{RT}}$	$\frac{\Delta F_2}{F_{RT}}$
	(m)	(m)	(m)	W/m ²	W/m ²	W/m ²		
1	1.660	-0.0326	0.0254	2.13×10^4	1.96×10^4	1.94×10^4	-0.082	-0.091
2	1.660	-0.0326	0.0127	2.02×10^4	2.00×10^4	1.95×10^4	-0.013	-0.036
3	1.660	-0.0100	0.0508	2.31×10^4	2.28×10^4	2.22×10^4	-0.015	-0.039
4	1.750	-0.0175	0.0254	1.38×10^4	1.40×10^4	1.37×10^4	0.013	-0.006
5	1.750	-0.0175	0.0127	1.18×10^4	1.25×10^4	1.23×10^4	0.054	0.039
6	1.750	-0.0040	0.0508	1.89×10^4	1.92×10^4	1.89×10^4	0.016	-0.001
7	1.900	-0.0209	0.0254	1.46×10^4	1.44×10^4	1.42×10^4	-0.010	-0.024
8	1.900	-0.0209	0.0127	1.44×10^4	1.47×10^4	1.44×10^4	0.022	0.004
9	1.900	-0.0040	0.0508	1.72×10^4	1.78×10^4	1.74×10^4	0.037	0.016
10	1.581	-0.0092	0.0508	1.75×10^4	1.71×10^4	1.68×10^4	-0.027	-0.045
11	1.627	-0.0099	0.0508	4.32×10^4	4.23×10^4	4.06×10^4	-0.023	-0.062
12	1.673	-0.0106	0.0508	5.66×10^4	5.58×10^4	5.44×10^4	-0.015	-0.040
13	1.717	-0.0113	0.0508	5.12×10^4	5.14×10^4	5.05×10^4	0.003	-0.014
14	1.766	-0.0120	0.0508	3.91×10^4	3.79×10^4	3.73×10^4	-0.033	-0.047
15	1.812	-0.0127	0.0508	3.65×10^4	3.55×10^4	3.51×10^4	-0.027	-0.037
16	1.858	-0.0134	0.0508	3.50×10^4	3.40×10^4	3.37×10^4	-0.030	-0.038
17	1.904	-0.0141	0.0508	3.35×10^4	3.25×10^4	3.23×10^4	-0.030	-0.035
18	1.951	-0.0148	0.0508	3.17×10^4	3.07×10^4	3.06×10^4	-0.030	-0.034
19	1.997	-0.0155	0.0508	2.87×10^4	2.83×10^4	2.80×10^4	-0.017	-0.027

4.4 Comparisons to Measurements

With the expectation of several sources of variance and uncertainty stemming from the studies in Sections 4.2 and 4.3, a question arises as to how well the simulations predict reality given their variations. A validation study is performed using experimental measurements taken by Dr. Michael Brown at the AFRL on the HDCR at NASA Langley Research Center. The measurement setup is described in Section 2.5. For reference, Fig. 2.4 is presented as Fig. 4.14.

The measurements are taken over a 16 second timespan with two seconds of measurements before fuel is ignited, 10 seconds of combustion, and 4 seconds of cool-down

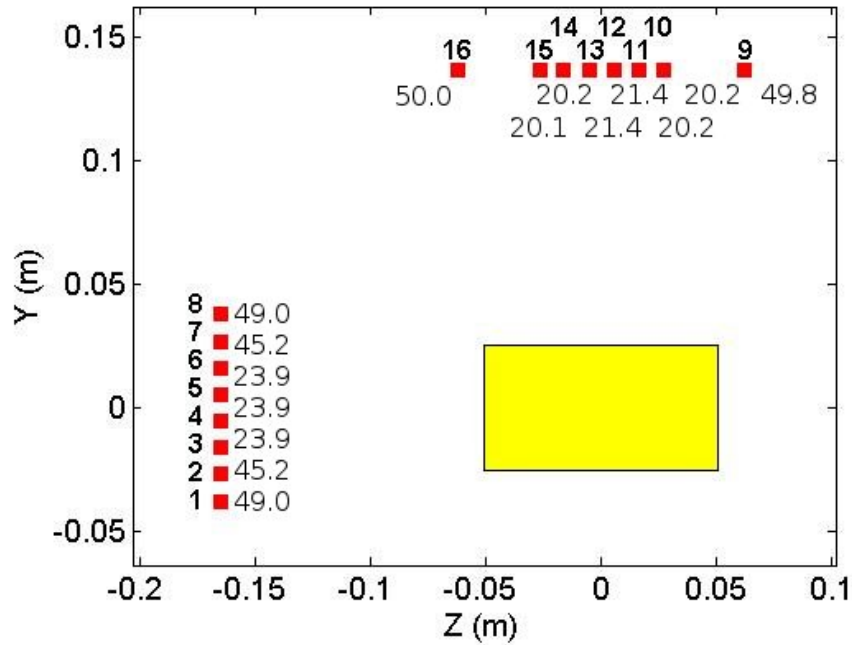


Figure 4.14: Location of the emission photodetectors with respect to the exit of the combustor shown in yellow. Flow is out of the page. Associated angular widths given for each detector in degrees. Image courtesy of Michael Brown at the AFRL.

after the flame is extinguished. The conditions of the experiment are designed to duplicate a Mach 6.5 flight of the HIFiRE-2 combustor. The total radiative heat flux is measured by sixteen infrared photodetectors viewing the flow through a silicon window. The photodetector signals are translated directly into radiative heat flux through a calibration procedure given in Appendix A. The experimental measurements, with appropriate compensation for ambient heating and silicon filtering, are given in Fig. 4.15.

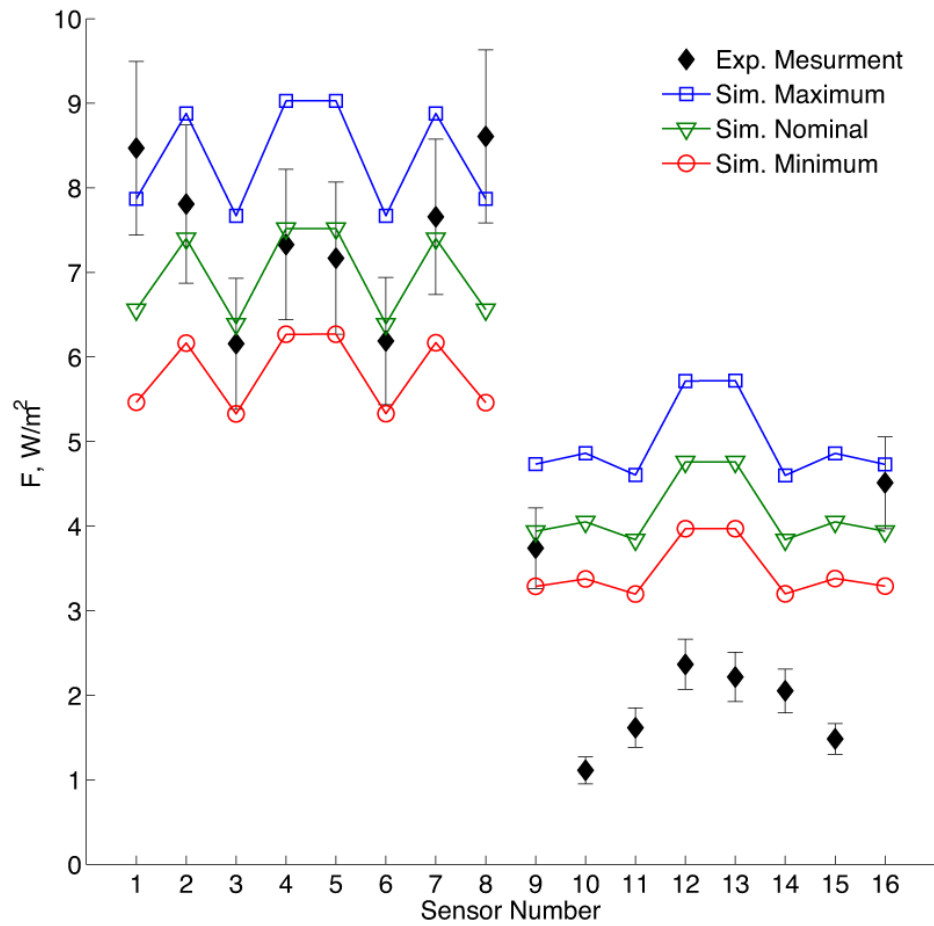


Figure 4.15: Comparison of the net radiative heat flux to the wall at the experimental exhaust port. Experimental results presented with experimental measurement uncertainty. RT simulations presented with computational uncertainty predictions.

The experimental conditions are simulated using a RT method with a narrow-banded spectral model. The physical domains of the simulations are intended to duplicate the exact field of view for each sensor, given the position of the sensor and the geometry of the mounting hardware. The details are given in Table 2.1. The simulations employ an angular resolution of 0.5° along the solid-angle field of view and a spatial resolution of 0.5 mm along each trace path. The spectral model employs 138 bands ranging in frequencies from 5550 to 9100 cm^{-1} with an evenly distributed spectral resolution of 25 cm^{-1} . This range corresponds to the combined effects of the physical sensor response function and the silicon filtering window. The resulting predictions are given in Fig. 4.15.

In addition to the spectral modeling error calculated in Section 4.2, the spectral database error coming from the original HiTemp spectral database also needs to be included. The spectral modeling error employed, “ $E_{\nu 2}$,” is calculated over the 1 m path length as described above. The spectral database error is computed by adding a factor of 20% to the existing spectral model, resulting in a value of $E_{\nu 1} = 0.20$. The spectral model is perturbed as in Eq. 2.19.

In Fig. 4.15, the experimental measurements are given with individual symbols and corresponding error bars, as each measurement is taken individually, and the factors affecting the certainty of the measurement may vary from detector to detector. The simulations are given as correlated curves because all simulations use an identical spectral model. Therefore, any error in the spectral model would appear in all simulations. As such, all simulations would either be perturbed high or low due to spectral uncertainty but never with a mixture of results.

The simulation results have agreement within experimental uncertainty for sensors 9 and 16 of the vertical photodetectors and for sensors 2 through 7 of the horizontal photodetectors. The vertical sensors 10 through 15 show similar relative trends between experiment and simulation, but they do not overlap in any absolute sense.

Sensors 1 and 8 show an agreement with the highest simulations predictions fitting into the experimental error bars, but this overlap does not match the trend presented by sensors 2 through 7.

The explanation as to why only certain sensor simulations correlate with experiments may lie in the flowfield. The experimental flowfield is characterized for water vapor mole fraction and temperature by Brown et al [8]. The flowfield shows large temporal variation, which has been found in previous studies to cause significant differences between time averaged and time resolved radiative heat transfer predictions [15, 16]. Additionally, the temperature and water vapor distribution do not closely match those predicted by the CFD RANS predictions. For the purpose of comparison, the exit plane temperature and water vapor mole fraction are given in Fig. 4.16 for the CFD simulation results and Fig. 4.17 for the experimental results (reprinted with permission).

The results from the CFD simulation differ greatly from those of the experimental measurements. The temperature forms a hot ring around the edges in Fig. 4.16 (a), whereas the experiment shows no structure in Fig. 4.17. The simulated water vapor mole fraction given in Fig 4.16 (b) is significantly less evenly distributed than would be suggested by experimental results given in Fig. 4.17 (b). The differences between the simulated and experimental flowfields can account for differences in the radiative heating. If the flows are equal in combustion completion and heat release, then their differences would mainly be due to the spatial distribution of the flowfield quantities. Sensors that view a large amount of the flowfield would be unaffected by the changes in distribution. Due to their orientation and fields of view, sensors 1 through 8, 9, and 16 view almost all of the flow. Thus, it is hypothesized that this is the reason the simulations of these sensors yield results close to the experimental measurements. The edge of the flow has a significant amount of mixing with the external surrounding air, which is not accounted for in the simulations as they end at the exit plane. Thus,

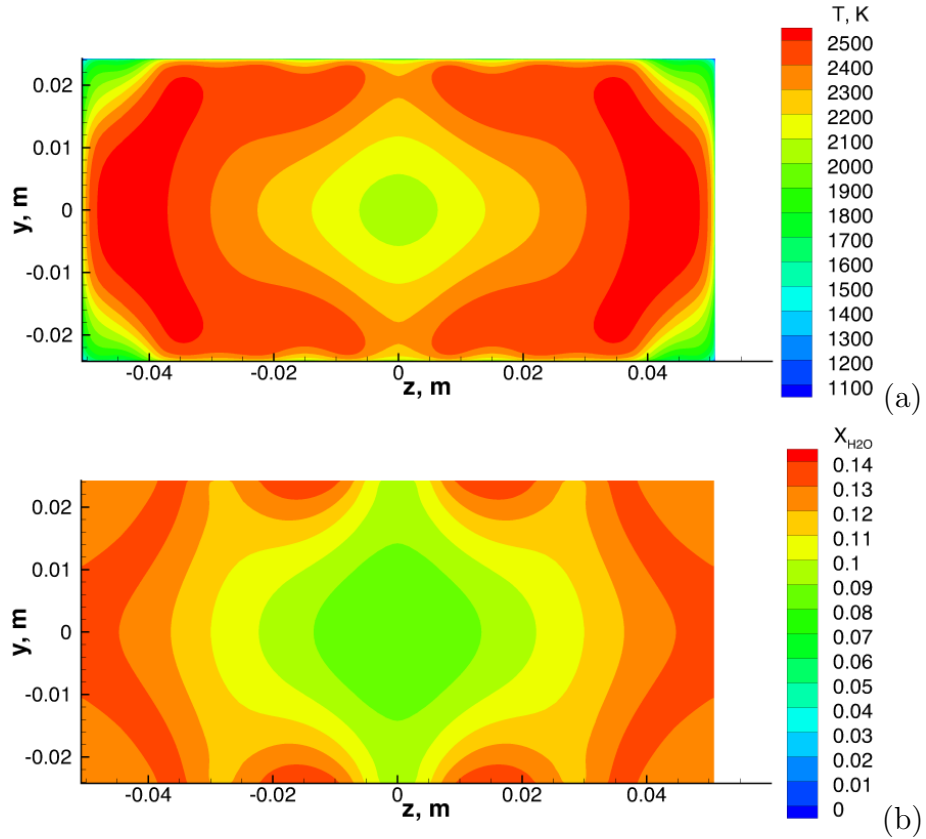


Figure 4.16: Exit plane profiles for a CFD RANS simulation of the HDCR experiments for (a) temperature and (b) water vapor mole fraction. Flow is out of the page.

the sensors may see more radiative material in their fields of view than the simulation can predict. Sensors 9 through 16 only view a narrow column. As such, any small shift in flowfield distribution causes a significant change in the radiative material in their fields of view. Sensors 12 and 13 have fields of view containing the highest quantities of water vapor at the exit planes, according to the simulation, resulting in them having higher predicted radiative heat fluxes than the other vertical sensors. However, there is no such spike present in the experimental measurements. These areas of high concentration are not present in the experiments. Thus, there is a large disparity between the simulated prediction and the experimental measurements for these sensors.

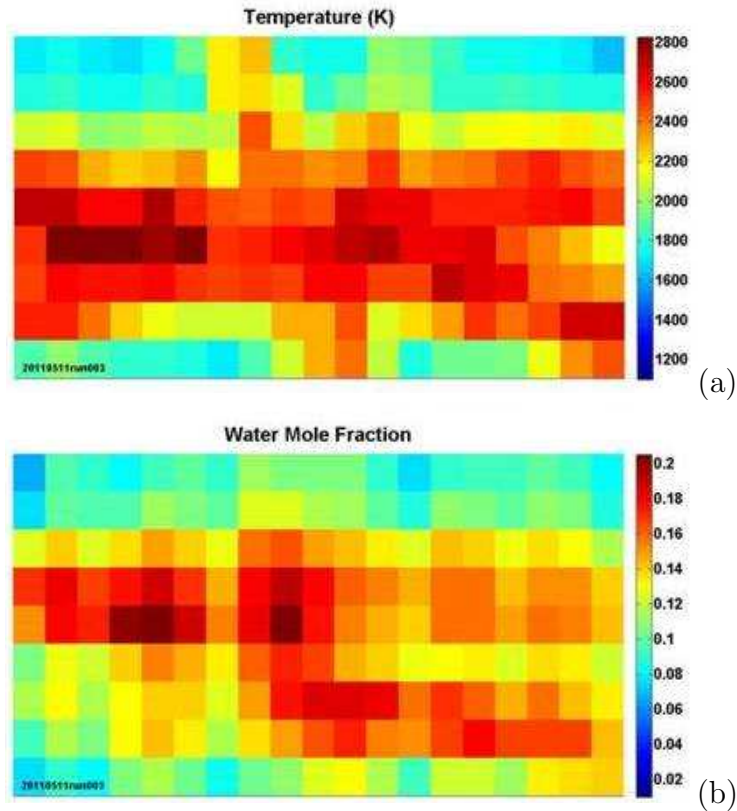


Figure 4.17: Exit plane profiles measured from the HDCR experiments for (a) temperature and (b) water vapor mole fraction. Flow is out of the page. Images courtesy of Michael Brown at the AFRL [8].

The agreement of radiative heat flux between the experiment and the simulations presented in Fig. 4.15 support that proper modeling is taking place in the system. Currently, there are no previous experimental comparisons of hydrocarbon-fueled scramjets available to validate a thermal radiative simulation. The datasets are partially validated for wide-field of view sensors, and they support the belief that the simulations are reasonably accounting for the overall thermal radiation and heat transfer within the system. This belief holds even with wide changes in the flowfield and a number of uncertainties brought on by modeling and simulation.

However two issues remain. The first issue is that of the limited spectral and spatial range over which the simulations have been measured. The expansion of these ranges necessitates additional experiments. Secondly, with such large differences

between the simulation and experimental flowfield for the narrow-view sensors, the temporal and spatial variation will need to be accounted for by looking at reasonable variations in the flowfield. The study in Chapter V takes such variations into account.

4.5 Conclusions

Several sources of uncertainty in scramjet radiation computation are addressed, and the means of quantifying their impacts on future studies are examined. Spectral model and numerical mesh refinement errors are quantified with comparative studies, and their combined effects are partially validated using experimental measurements.

The spectral model tables are generated for all species for a range of 6 temperatures using a spectral resolution of 25 cm^{-1} . The model is tuned for higher temperature water and carbon dioxide at 1 atm (101.325 kPa), with conditions similar to the scramjet combustion chambers. With this tuning, the accuracy of the water and carbon dioxide models agree within the bounds of with previous studies. Minor species do not yield nearly as good performance. The individual tables have a number of factors that can be tuned to optimize accuracy and computational efficiency, including the number of quadrature points, quadrature point weighting, quadrature point values, and spectral resolution. Many of these values can be varied by species or by band. However, the optimization of the method is left for a future study, with the error simply to be predicted and documented in the current work.

For the purpose of predicting spectral modeling errors, a series of error tables are generated using one-dimensional model problems with conditions similar to those found in the HIFiRE-2 scramjet combustion chamber. The error tables have identical delineations for temperature, species, and frequency as the spectral tables have. Studies applying the predicted spectral modeling error tables to a number of simulations of the HIFiRE-2 combustion chamber give errors of 6 to 8% for water-only conditions and 10 to 15% for all radiative species. Comparisons of low-fidelity to

high-fidelity spectral models show that the error tables based on one-dimensional problems underestimate the relative spectral modeling error by a factor-of-two. This phenomenon appears to be a result of the transition from one-dimensional predictions to three-dimensional domains, as it does not appear in purely one-dimensional comparisons. In future studies, a correction factor-of-two may need to be applied to the error predictor either before or after the simulation is completed.

The numerical grid refinement errors are examined with a series of studies employing DOM simulations. Not only is the convergence of the radiative heat fluxes examined in the studies, but the convergence of the predicted spectral modeling error is examined as well. Radiative heat flux is found to be most affected by the CFD sampling mesh used to extract data from the CFD solutions, and it is less affected by the spatial radiative mesh of the system. Coarse angular quadrature schemes tend to create spurious hotspots. Thus, finer angular quadrature schemes are preferred for radiative heat flux predictions. The spectral modeling error predictor appears to be affected mainly by spatial radiative mesh refinement and not by the CFD sampling mesh or angular quadrature scheme refinements. The trend suggests that error prediction is generated and propagated evenly in the HIFiRE-2 combustor case, provided that the physical radiative paths can be properly resolved numerically. A highly refined truth study employing the RT method finds that the radiative heat flux predicted by the coarse spatial radiative mesh DOM simulations is accurate to within 5% of a highly refined spatial model over most of the domain with spatial refinement errors rising to 10% in the lower flux region. The same comparison applied to finer spatial radiative mesh simulations find the DOM accurate to within 4% of a highly refined spatial model over most of the domain with spatial refinement errors rising to 8% in the lower flux region. These errors line up closely to previous studies and are included in further parts of this work by the use of error bars [53].

Finally, high-spatial-resolution RT simulation results are compared to experimen-

tal measurements taken in the HDCR. Currently, these values are the first published direct quantitative measurements of radiative heat transfer in a hydrocarbon scramjet. The experiments agree with the simulations for the photodetectors with wider fields of view, suggesting that the overall CFD simulations and radiative simulation methods are adequate. This trend can be used as a partial validation of the modeling methods. However, for the sensors with narrow fields of view, the simulations and experiments do not agree even when experimental measurement error and computational uncertainty are taken into account. This trend suggests that the CFD simulations are not completely resolving the spatially and temporally varying features in the flow, even though they are accurately modeling the flow progress as a whole. As such, a parameter study looking at the variations in the computational flowfield solutions and the effects on radiative heat transfer is described in Chapter V. The study attempts to rectify the differences between the experiment and simulation, as well as investigate the total combined computational uncertainty that may be introduced into a large flowfield simulation of a scramjet engine.

CHAPTER V

Flowfield Variation

5.1 Introduction

The current chapter studies the thermal radiative heat transfer for the HIFiRE-2 combustion incorporating all contributors to computational radiative uncertainty as discussed in the previous chapters. The methodology for predicting the epistemic uncertainty contributions of spectral modeling, spectral databases, and numerical modeling are established in previous chapters, but the overall combined effects remain uncharacterized. Additionally, the effects of temporal flowfield parameter variation are yet uncharacterized.

As demonstrated in Section 4.4, even with spectral uncertainty characterization and reduced error for the radiative numerical modeling, the radiative predictions do not entirely capture the effects of the physical flowfield. One possible explanation is that the flowfield itself is not fully characterized by the RANS CFD simulations, as it is found in previous works that the time-averaged radiative properties of a time-varying flow are not necessarily equal to the radiative properties of a time-averaged flow [15, 16]. Thus, the effects of temporal variation are examined in the current chapter. Since a well-characterized turbulent flow will always have variation, the uncertainty associated with such instantaneous time variations is classified as aleatory.

In order to incorporate the temporal variations of the HIFiRE Direct Connect

Rig (HDCR), a variable time-series of computed flowfields is taken as the input to the radiative heat flux code. Unlike previous studies, the work of the current chapter is based on a Large Eddy Simulation (LES) of the HDCR. These different flowfield snapshots present a correlated variation of different parameters of interest. The time-varying flowfield snapshots are taken as input flowfields to be processed by the DOM code providing a temporal series of thermal radiation solutions.

The radiative solutions based on temporal variations can differ depending on their boundary conditions and spectral model, as demonstrated in Chapters III and IV, respectively. As such, the effects of these changes on the radiative heat flux prediction of a time-varying flowfield are also examined. A new series of radiative heat fluxes results from each change in boundary condition and spectral modeling.

These multiple time-series can be compared among each other in a statistical manner. The associated radiative heat flux values vary for each time-series being considered. As such, for any particular value of heat flux, the associated probability can change among time-series. Thus, the probability of any particular value of heat flux occurring is a combination of the probabilities from all of the time-series considered. The particular quantities examined are the radiative wall heat flux and the streamline flow cooling. Finally, a reexamination of the experiments discussed in Section 4.4 is included with a combined uncertainty analysis.

5.2 Flowfield Examination

The CFD flowfield under examination in the current chapter is a Large Eddy Simulation of the HDCR performed by Ivan Bermejo-Moreno at Stanford University. The simulation differs from the CFD results presented in previous chapters that employ a time-steady RANS CFD simulation. The LES computation employs a 20 million point unstructured mesh to resolve one quarter of the physical domain of the HDCR with numerical planes of symmetry at the vertical and horizontal centerlines.

The code employs an eleven-species flamelet hydrocarbon combustion model [82]. The HDCR is modeled at Mach 6.5 conditions with an equivalence ratio of 1.

The simulation is time-resolved with each timestep equivalent to 30.0 or 36.6 ns of physical time. The simulation is run for 500,000 timesteps with flowfield snapshots recorded at every 10,000 timesteps, equivalent to a physical domain run time of 0.0173 s. The temporal snapshot spacing ranges from 0.300 to 0.366 ms. Of the 50 snapshots available, the latter 41 are employed as a time-series for flowfield variation. The first 9 are omitted as the system may not have fully developed into a proper turbulent regime during the earlier timesteps. The CFD boundary conditions are modeled as adiabatic walls.

The individual cell values for each flowfield quantity vary among all snapshots. As such, the total effect of flowfield variation on the parameters of importance needs to be addressed. The main parameters of concern for the variation are temperature, water vapor concentration, and carbon dioxide concentration as discussed in Section 3.3. The individual flowfield snapshots can be used as inputs to the radiative simulations in a manner similar to how the CFD RANS simulations are employed in Chapters III and IV. These results can be examined for both overall effects of thermal radiation as well as for completeness of statistics.

5.2.1 Initial Large Eddy Simulation Examination

The flowfield is initially examined for several flow quantities varying among the time-resolved flowfields. The 41 initial flowfields generated from the LES snapshots are processed using the Discrete Ordinates Method (DOM) code GRASP.

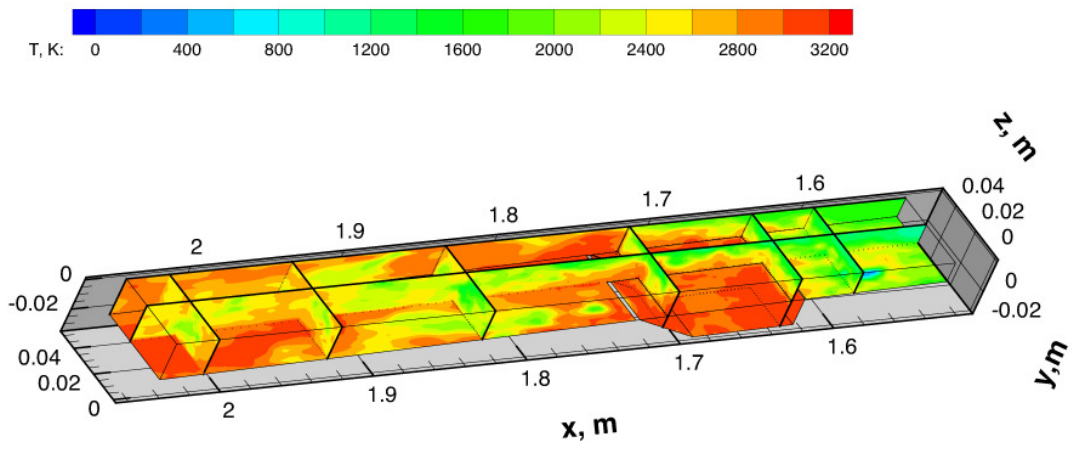
The overall character of the LES simulations is given with the temperature profiles in Fig. 5.1. Two instantaneous temperature snapshots are given in Figs. 5.1 (a) and (b). The time-averaged temperature profile is given in Fig. 5.1 (c). The individual temperature snapshots show a wide variation in overall flow character. However, the

time-averaged temperatures give a smooth profile similar to the RANS simulations in Chapters III and IV. The temperatures peak at over 3000K in the flame holding cavity and near the wall at the exit. The centerline temperature in the time-averaged case remains between 1500 and 2200 K for most of the flow. However, the instantaneous temperatures at the centerline can be as high as 2600 K. Given the nonlinear relationship that temperature has to radiative heat flux, the time-resolved simulations may have significantly higher radiative heat fluxes than those of the steady-state predictions, as suggested by previous works [15, 16]. This phenomenon is examined in Section 5.3 in reference to radiative wall heat transfer at various locations.

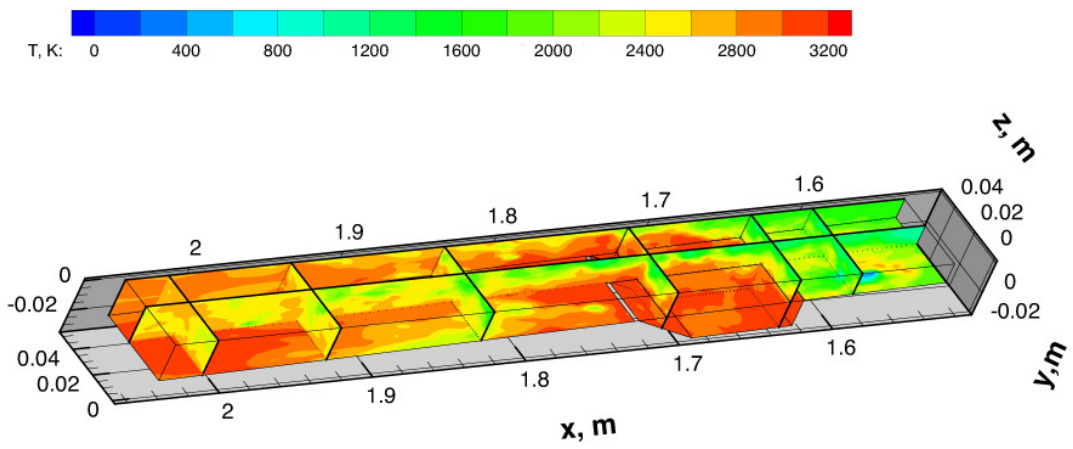
With the exit pane being of greater interest due to the experimental radiative heat flux measurements, the flowfields predicted by the CFD LES are more closely examined in Figs. 5.2 and 5.3 for temperature and water vapor mole fraction, respectively.

The temperature for the combustion chamber exit varies from 1700 K in the center to 3000 K along the edges for LES flowfield snapshots. The lower temperature in the center indicates that the radiative heat flux coming from these regions may not be as important as would be predicted in the steady-state case. The time-averaged LES temperature profile given in Fig 5.2 (d) appears to be generally hotter and more evenly distributed than the RANS flowfield calculations given in Fig. 4.16.

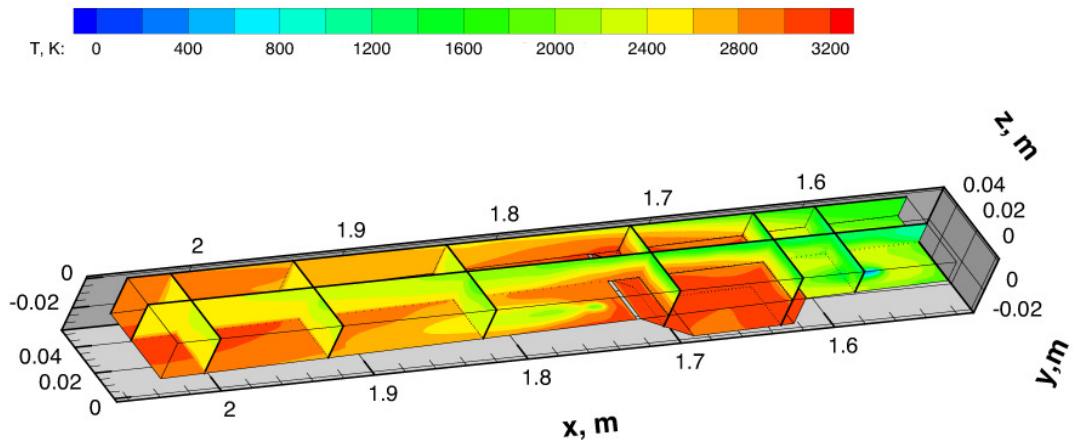
When considering the water vapor mole fraction given in Fig. 5.3, the instantaneous flowfield values vary from 0.3 to 0.12. The central part of the flows undergoes fluctuations from 0.03 to of 0.11, and the areas around the edges undergo fluctuations from 0.07 to 0.12. Despite these large variations, many well-defined structures are present in the time-averaged flowfield as given in Fig. 5.3 (d). The well-defined structures, however, are lower in magnitude and in relative spatial variation than are those from the RANS simulation flowfields, presented in Fig 4.16 (b). These more evenly distributed flowfields may serve to reduce some of the peaks seen in the narrow field-of-view sensor simulations discussed in Section 4.4.



(a)



(b)



(c)

Figure 5.1: Flow temperature, for LES flowfield snapshots of the HDCR (a and b) and time-averaged LES flowfield (c). Flow is from right to left.

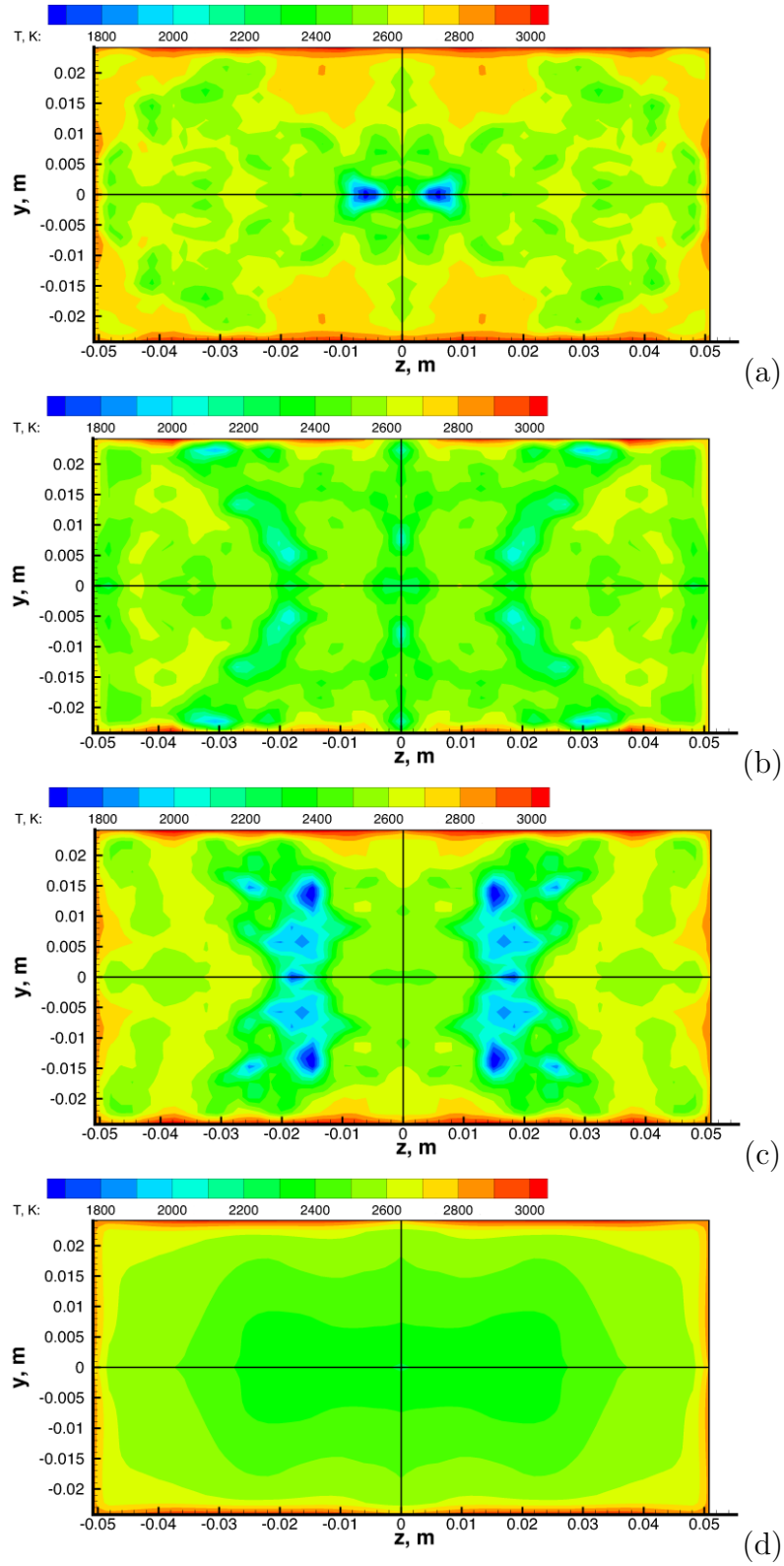


Figure 5.2: Flow temperature at the HDCR exit plane, for various LES flowfield snapshots (a - c) and time-averaged LES flowfield (d).

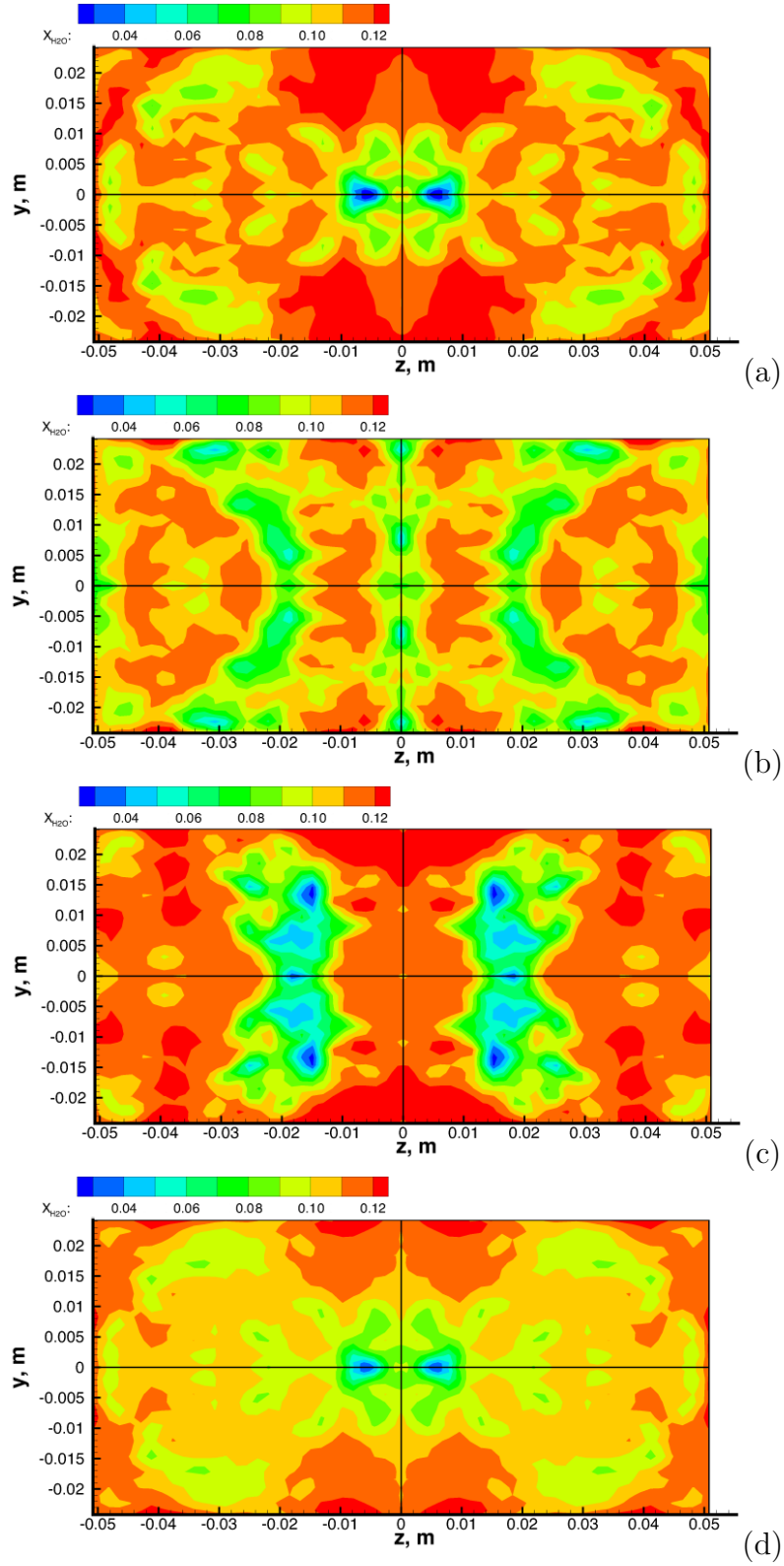


Figure 5.3: Flow water vapor mole fraction at the HDCR exit plane, for various LES flowfield snapshots (a - c) and time-averaged LES flowfield (d).

5.2.2 Large Eddy Simulation Radiative Heat Fluxes

In order to further compare the LES flowfields, the individual flowfield snapshots are run on the radiative DOM solver, GRASP. The time-averaged LES flowfield is examined as well. The flowfields are sampled and run on a 90,000 point three-dimensional structured mesh with an S_8 angular quadrature scheme. For all simulations, the CFD sampling and spatial radiative meshes are identical. All simulations employ five radiative species (water vapor, carbon dioxide, the hydroxyl radical, carbon monoxide, and methane) with the two-point spectral method introduced in Section 4.2. The spectrum for all simulations is divided into 399 bands of 25 cm^{-1} ranging in wavenumber from 25 to $10,000 \text{ cm}^{-1}$.

The spatially averaged radiative heat fluxes for several regions along the combustion chamber walls are calculated for all of the LES flowfield snapshots that are discussed in the previous section as well as for the time-averaged LES flowfield. In all cases, the wall boundary conditions are radiative outflows ($\epsilon_\nu = 1$, $T = 0$), and the centerlines are spectrally reflective planes. Example profiles of the radiative wall heat fluxes are given in Fig. 5.4 for representative LES flowfield snapshots and for the time-averaged LES flowfield.

The instantaneous radiative heat flux near the combustion chamber exit fluctuates by over 10 kW/m^2 , as given in Figs. 5.4 (a-c). Additionally, the radiative heat flux in and around the flame holding cavity can fluctuate by over 5 kW/m^2 . The fluctuations constitute a change of 10 to 30% of that of the time-averaged flowfield presented in Fig. 5.4 (d).

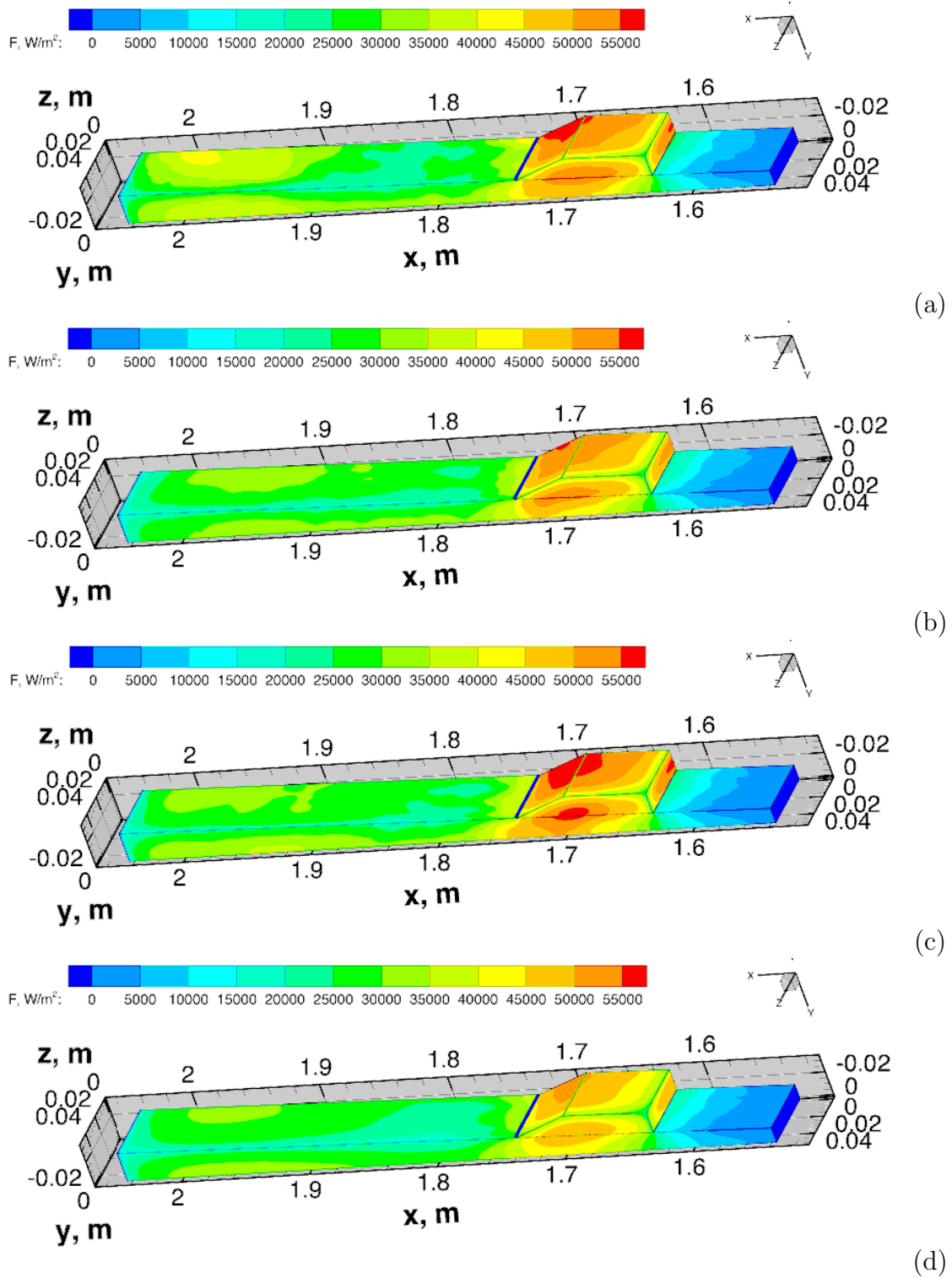


Figure 5.4: Radiative wall heat flux profiles for non-radiative outflow walls, for various LES flowfield snapshots (a-c) and time-averaged LES flowfield (d). Flow is from right to left.

The LES flowfield snapshots can also have significantly higher radiative heat flux than the time-averaged LES flowfield at the combustion chamber exit and in the flame holding cavity. Given the variations near the combustor exit and in the flame holding cavity, these regions are chosen to examine the temporal effects of the flowfield variations. Additionally, the temporal variations do not show nearly as well-defined structures for radiative wall heat fluxes as they do for raw flowfield quantities.

The computed radiative heat fluxes are tabulated in histograms in Fig. 5.5. The histograms give the spectrally integrated radiative heat flux averaged over specified wall sections of the HIFiRE-2 combustor as displayed in Fig. 5.6. The results for simulations of the flowfield snapshots are sorted into bins at a resolution of 500 W/m^2 .

The area-averaged radiative heat flux over the back wall of the flame holding cavity is presented in Fig. 5.5 (a). The area is depicted in Fig. 5.6. The heat fluxes range from 47.5 to 51.0 kW/m^2 providing 8 bins. The associated levels show a single mode around 49.0 kW/m^2 and no areas of low population bins, indicating that the 41 radiative simulations of the original LES flowfield snapshots are adequate.

The area-averaged radiative heat flux over the side wall of the flame holding cavity is presented in Fig. 5.5 (b). For the particular measurement of concern, the area does not extend in the vertical, “y,” direction into the flame holding cavity, but it remains in the flow stream as depicted in Fig. 5.6. The stream-wise, “x,” bounds range from values of 1.62 to 1.73 m . The heat fluxes range from 41.5 to 46.5 kW/m^2 providing 11 bins. Some of the associated bins are unpopulated, and while a large mode is present around 43.5 kW/m^2 , additional modes are present. Such variations indicate a need for more flowfield samples.

The area-averaged radiative heat fluxes near the combustion chamber exit are presented for the side and top walls in Figs. 5.5 (c) and (d), respectively. Both averages span the widths of their respective walls and extend over stream-wise (x) locations from 1.93 to 2.04 m , as indicated in Fig. 5.6. Both histograms have 49

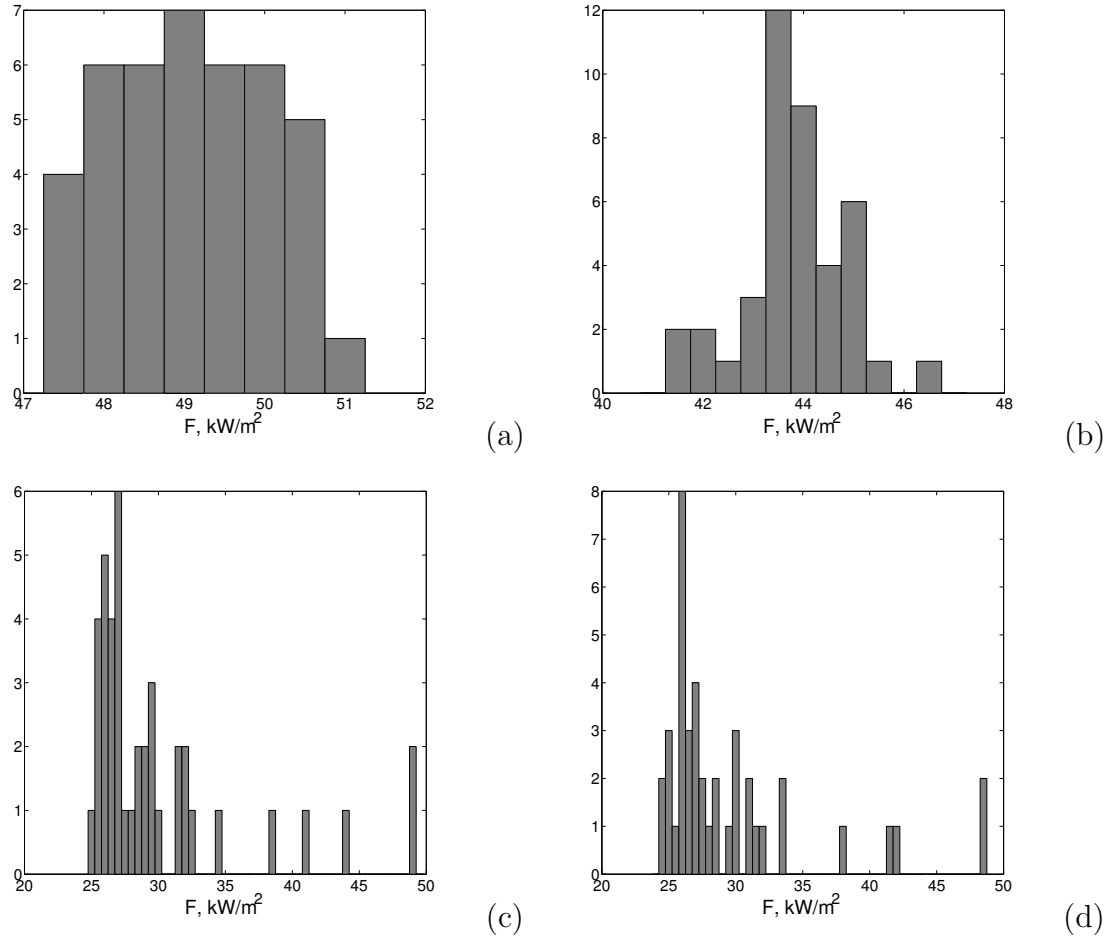


Figure 5.5: Histograms of the spectrally integrated spatially averaged heat fluxes, for various LES flowfield snapshots. Locations are for (a) the back of the flame holding cavity, (b) the sidewall near flame holding cavity, (c) the sidewall near the flowfield exit, and (d) the top wall near the flowfield exit.

bins, spanning from 25.0 to 49.0 kW/m^2 and 24.5 to 48.5 kW/m^2 , respectively. Both histograms show a strong mode around 26.0 kW/m^2 but do not have any definite structure, and both histograms have many unpopulated bins.

The large gaps in some of the bins indicates that the flow statistics either need to be increased by further sampling or that they need to be augmented with weighted probability. A means of flow weighting is given by Eq. 2.27 in Chapter II. The weighting scheme examines how far the individual cell quantities deviate from the

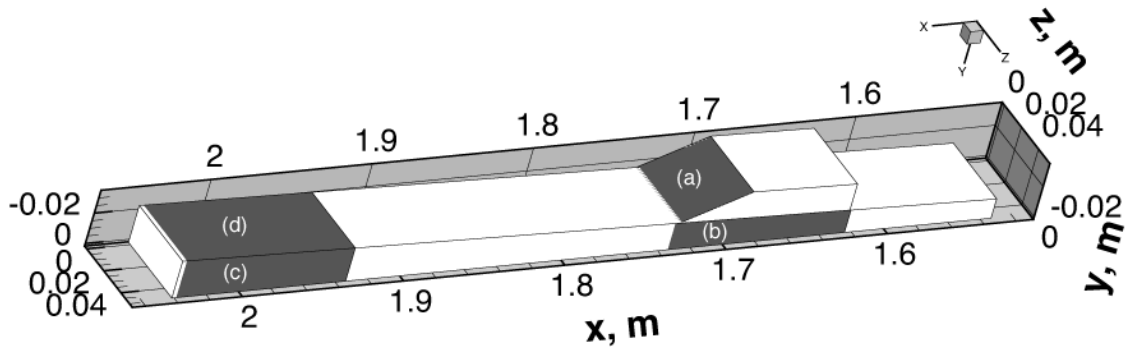


Figure 5.6: HIFiRE-2 wall areas used for spatial averaging of radiative heat flux in the histograms of Fig. 5.5

time-averaged cell quantity. As discussed in Section 3.3, temperature, water vapor concentration, and carbon dioxide concentration are the flowfield quantities which have the largest impact on radiative heat flux. Therefore, they should be the ones considered for flow statistics. The average of Eq. 2.27 is taken among the three flowfield quantities as is given in Eq. 5.1.

$$\bar{\Phi} = \sum_{t=1}^3 \left[\sum_{i=1}^{N_{cell}} \left[\exp \left(-\frac{(u(i,t) - \bar{u}(i,t))^2}{2u_{rms}(i,t)^2} \right) \right] \right] \frac{1}{3N_{cell}} \quad (5.1)$$

The individual LES flowfield snapshots are processed with Eq. 5.1, and the results are given in Fig. 5.7. The probabilities range between 0.68 and 0.82. These values allow for weighting of the individual LES snapshots when time-series statistics and distribution functions are being considered. Given the relatively steady range of associated probabilities, a correlation to any one radiative feature may not become apparent. However, if further flow statistics are desired, any additional flowfield snapshots can be compared with the current set of data to determine if the snapshot is in line with the current dataset.

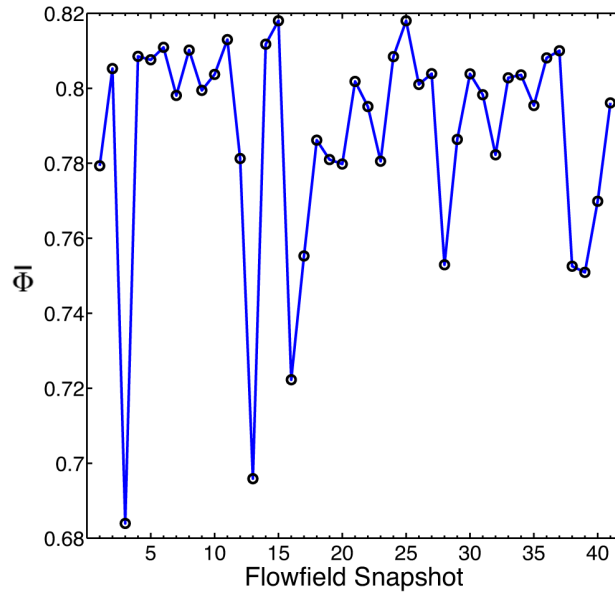


Figure 5.7: Probability of individual LES flowfield snapshots

The LES snapshots provide a wider possible range of flowfields than a RANS simulation. As such, the total variation of the system can be examined in light of the variations in the LES with appropriate statistical weighting also considered. The overall radiative heat fluxes vary in time, and the average radiative heat fluxes of the individual snapshots may not be equal to the radiative heat flux of a time-averaged flowfield. Even though the LES flowfield snapshots provide a reasonable description of the flow characteristics, many of the areas of interest are not fully resolving their range of outputs. Additional samples may be required to fully understand the effects of flowfield variation. However, the current samples are probabilistically characterized, and can be used to generate CDFs for uncertainty analysis.

5.3 Uncertainty Incorporation

In order to determine a total uncertainty of the system, all of the previously discussed uncertainty factors are combined into a Cumulative Distribution Function

(CDF), as discussed in Section 2.3. Both the aleatory flowfield uncertainty and the epistemic modeling uncertainties are taken into account.

The radiative heat flux values of the individual LES flowfield snapshots may differ greatly from the calculations based on the a steady-state RANS flowfield used in Section 4.4. The average of the radiative heat flux calculations from the LES snapshots may not coincide with the radiative analysis of the RANS simulation. If the fluctuations due to the time varying LES flowfields have a large enough effect on the radiative heat flux distribution at the exit of the combustor, then the discrepancies between the experimental radiation measurements and the simulated radiative heat flux prediction based on the time-steady RANS CFD flowfield solutions may be explained.

The spectral model uncertainty is accounted for by perturbing the spectral lookup tables before a simulation is run with the procedure discussed in Sections 2.3 and 4.2. The resulting spectral error predictions are taken as the spectral uncertainty. Numerical uncertainty is accounted for with a post-processed perturbation of the simulation predictions. Boundary conditions are varied as well. Each change to the spectrum and boundary condition requires a reprocessing of the LES flowfield snapshots, which generates a new probability curve for any radiative quantity of interest. The quantities of interest are the radiative wall heating along certain parts of the combustion chamber walls as well as flow cooling along specific streamtraces.

5.3.1 Radiative Modeling Uncertainty

The predictions for radiative wall heating can change for both time variation and model perturbations. In order to consider the combined effects of flowfield and modeling uncertainty, the series of LES flowfield snapshots are run with the nominal spectral model and the perturbed spectral model. All of the simulations are run using the GRASP DOM radiative heat transfer code, with identical spatial and sampling

meshes of 90,000 points. The spectral model is perturbed by the methodology established in Section 2.3. The modeling error, “ $E_{\nu 2}$,” is set to twice the values calculated in Section 4.2, and the experimental database error, “ $E_{\nu 1}$,” is set to a value of 0.25. All simulations employ five radiative species (water vapor, carbon dioxide, the hydroxyl radical, carbon monoxide and methane) with the two-point spectral method introduced in Section 4.2. The spectrum for all simulations is divided into 399 bands of 25 cm^{-1} ranging in wavenumber from 25 to $10,000 \text{ cm}^{-1}$.

As with the previous section, four specific wall regions are examined for average radiative heat transfer. The specific regions are near the combustion chamber exit and in the flame holding cavity as indicated in Fig. 5.6. The CDF curves for each region for the nominal spectral conditions along with the associated epistemic perturbations are given in Fig. 5.8. To incorporate the epistemic perturbation, the simulations are run with the spectral model perturbed according to the methodology given in Section 2.3. Additionally, the CDF curves of the spectrally perturbed calculations are shifted by 5 % of their values to incorporate the grid refinement error, coming from the comparisons to the RT method solutions in Table 4.3. The vertical lines in Fig. 5.8 represent the radiative heat fluxes calculated from the time-averaged LES flowfields.

Unlike the histograms presented in Fig. 5.5, the CDF curves in Fig. 5.8 employ a probability weighting for each sample as based on Eq. 5.1. The sharp jumps in the statistics are still apparent, but the overall nature of the curve is displayed. The epistemic uncertainty is given as the difference between the nominal curves and their associated limits.

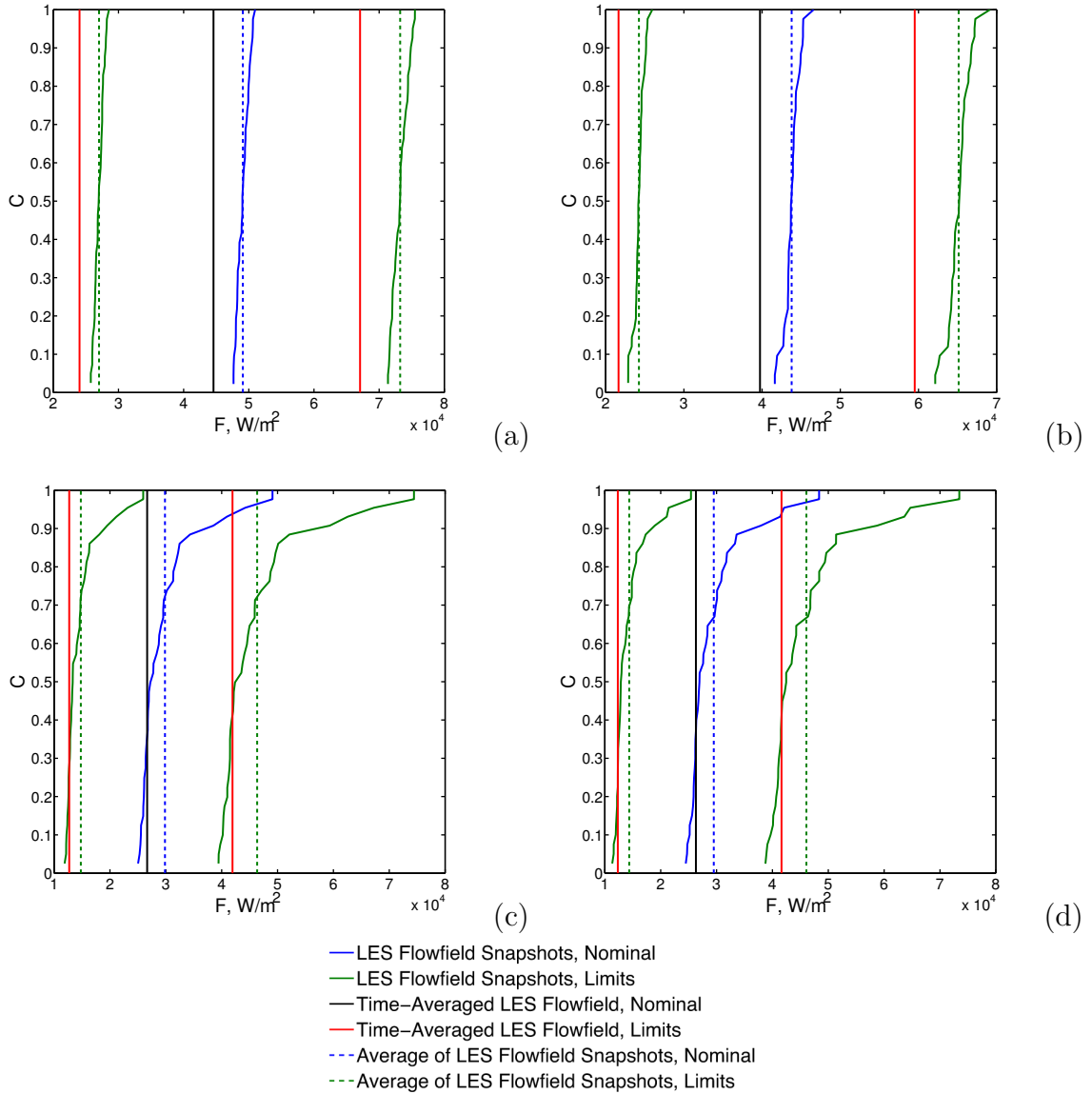


Figure 5.8: Cumulative distribution function of the spectrally integrated spatially averaged heat fluxes, for various LES flowfield snapshots. Locations are for (a) the back of the flame holding cavity, (b) the sidewall near flame holding cavity, (c) the sidewall near the flowfield exit, and (d) the top wall near the flowfield exit. Wall boundary conditions are radiative outflows.

For the radiative simulations of the time-averaged LES flowfield (indicated by solid vertical lines in Fig. 5.8), the epistemic uncertainty of the radiative wall heat fluxes ranges between ± 50 and ± 58 % of the nominal heat flux value. The LES flowfield snapshots (indicated by solid curves in Fig. 5.8) have epistemic uncertainty of the radiative wall heat fluxes ranges between ± 48 and ± 59 % of the nominal values. The probability weighted average heat fluxes of the LES flowfield snapshots (indicated by dashed vertical lines in Fig. 5.8) have epistemic uncertainty of the radiative wall heat fluxes ranges between ± 49 and ± 56 % of the nominal values.

The aleatory uncertainty may be considered as the instantaneous uncertainty that can be measured by the range of any one CDF curve. The relative instantaneous uncertainty is low for the flame holding cavity cases given by Figs. 5.8 (a) and (b), but it can be quite large with values of up to ± 40 % of its mean for areas near the combustion chamber exit given by Figs. 5.8 (c) and (d).

Given that the effects of heat transfer are often time integrated, an additional manner of incorporating flowfield uncertainty is more applicable in the current situation. The approach is to take the difference between radiative heat flux of the time-averaged LES flowfield, and the weighted average of the radiative heat flux calculations of each of the LES flowfield snapshots. This method negates the effects of the time-varying aleatory flowfield uncertainty, but it introduces an additional epistemic flowfield uncertainty. The uncertainty for the time integrated radiative heat flux ranges between 10 and 12 %. The change of 10 to 12 % agrees with previous works that find time-resolved flowfields can cause increases in radiative heat fluxes of 2.9 to 13.6 % over their steady-state counterparts [16].

The combined epistemic radiative heat flux uncertainties for the entire system can be measured as the difference between the lower limit of the time-averaged LES flowfield radiative heat flux and the upper limit of the weighted-average radiative heat flux from LES flowfield snapshots. For the regions in the flame holding cavity, the

combined uncertainty varies between -46 and +64 % of the time-averaged nominal case. For regions near the exit, the combined uncertainty varies from -53 to +75 % of the time-averaged nominal case. An overall combined radiative wall heat flux uncertainty map of the entire flowfield is given in Fig. 5.9.

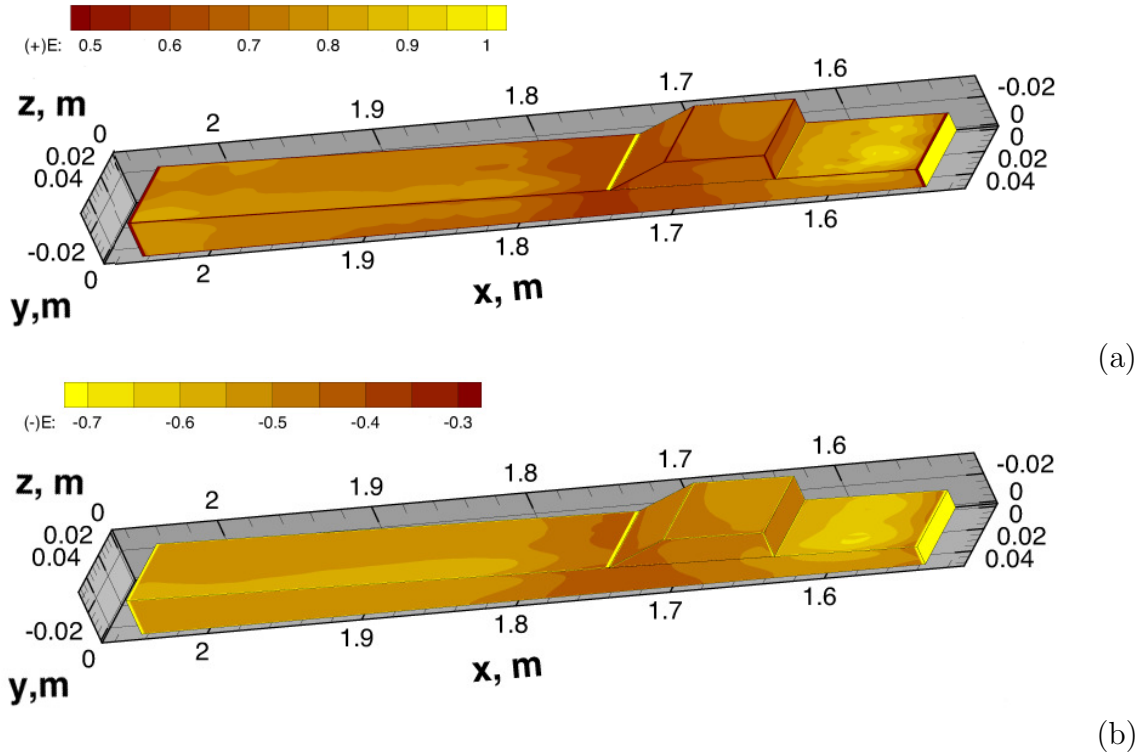


Figure 5.9: Combined epistemic uncertainties for radiative wall flux using strictly wall outflow boundary conditions. Uncertainties are for (a) upper uncertainty limit and (b) lower limit uncertainties relative to LES time-averaged nominal condition.

The overall epistemic uncertainty of the system is between -70 and + 95 % of the local radiative heat flux. The largest combined epistemic uncertainty of the radiative wall heat flux is in the low-flux region in which the spectral uncertainty is shown to be highest (as described in Section 4.2). The uncertainty is lowest at the back end of the flowfield cavity and rises to values ranging from -65 to +80 % along the length of the combustion chamber. The uncertainty also rises in the flowfield-cavity to values ranging from -50 to +70 %.

With the combined epistemic uncertainty quantified, the overall system uncertainty for a purely radiative case is a significant portion of the total radiative wall heat flux. In order to lower the individual uncertainties, the system uncertainty needs to be addressed. The predicted grid refinement error, is a flat $\pm 5\%$ uncertainty applied to the entire output, which can be improved with great expense by increasing the overall grid refinement (as described in Section 4.3). The flowfield uncertainty of ± 10 to $\pm 12\%$ can be decreased by examining the consistency of the overall flowfield simulations. If a singular time-averaged value of radiative uncertainty can be set, and the flowfield simulations can be validated with experiment, then the factor can be reduced. The spectral modeling accounts for the remainder of the radiative heat flux uncertainty. A value of roughly $\pm 25\%$ is attributed to the spectral databases (as described in Section 4.3). The experimental database error requires cross examination of other experimental databases or new experimentation to properly correct. Beyond these factors, the remaining uncertainty is attributed to the spectral modeling errors. As discussed in Section 4.3, the overall errors may be overestimated by the current method of linearly adding the errors of all species under consideration. Improvement in this method may lower the predicted spectral modeling errors significantly. Additional improvement in the model through either increased resolution or fine-tuning of parameters may lower the large spectral modeling errors completely.

With the uncertainty of a purely outflow radiative condition characterized, the question of the effects of varied boundary conditions remains. These boundary conditions are shown in Sections 3.5 and 3.4 to have a much greater effect on radiative wall heating and flow cooling than the combined uncertainty suggested by Fig. 5.9.

5.3.2 Boundary Condition Uncertainty

Additional factors to consider in radiative heat flux are those of the boundary conditions with respect to the flow cooling and radiative wall heating as discussed in

Sections 3.4 and 3.5. Wall temperature is found to produce large changes in radiative wall heat flux and radiative flow cooling. The combined effects of wall temperature variation, along with spectral and numerical uncertainty are addressed.

All of the simulations in the current section are run using the GRASP radiative solver and have identical numerical and flowfield sampling schemes to those of the previous sections in the current chapter. The spatial radiative mesh is identical to the CFD sampling mesh, each being a 90,000 point three-dimensional structured mesh with an S_8 angular quadrature scheme. The spectral method is a 399 band two-point banded model with bandwidths of 25 cm^{-1} and a spectral range of 25 to $10,000 \text{ cm}^{-1}$.

One issue of concern is the effect of radiative wall boundary conditions on radiative wall heating. As is established in Section 3.4, radiative wall heating has the greatest effect on wall heat transfer when the walls are blackbody emitters at the same temperature as the flowfield. The radiative wall heat transfer is minimum when the walls are purely reflective, resulting in a radiative wall heat flux of zero. In order to establish a CDF of the radiative outputs, a series of flowfield samples is processed. The chosen flowfields are the LES flowfield snapshots discussed in Section 5.2. The radiative analysis for the series of flowfields is repeated for several boundary conditions, the first being the purely radiative outflow condition ($\epsilon_\nu = 1$, $r_\nu = 0$, $T = 0$), performed in order to establish a baseline. The second condition is for blackbody walls ($\epsilon_\nu = 1$, $r_\nu = 0$) at the same temperature as the instantaneous flowfield. However, in a physical system, the thermal mass of the walls will prevent the walls from precisely matching the instantaneous flowfield temperature. Thus, the simulations are run for a third condition of blackbody walls having a temperature held constant to the local time-averaged flow-temperature. In the last series of simulations, the flowfield still varies among simulations, but the wall temperatures do not change.

In order to determine the effects of spectral sensitivity, the spectral model is perturbed by the methodology established in Section 2.3. The spectral modeling

error, “ $E_{\nu 2}$,” is set to twice the values calculated in Section 4.2, and the experimental database error, “ $E_{\nu 1}$,” is set to a value of 0.25. The six resulting CDFs of radiative heat flux for four areas of the HIFiRE-2 combustor walls are displayed in Fig. 5.10.

The particular locations of the radiative heat fluxes are those established in Fig. 5.6. Several trends are immediately noticeable. The blackbody radiative wall heat flux creates a significant change in net radiative heat flux with values of over 1.2 MW/m². Additionally, the hot radiative walls can undergo a net cooling rate of up to 1.1 MW/m². The average radiative wall heat flux of the CDF curves for the LES flowfield snapshots with time-averaged walls are -459, 852, -136, and -567 kW/m² in Figs. 5.10 (a), (b), (c), and (d), respectively. The average radiative wall heat flux of the CDF curves for the LES flowfield snapshots with time-varying walls are -465, 897, -131, and -566 kW/m², in Figs. 5.10 (a), (b), (c), and (d), respectively.

The introduction of the spectral perturbation is minor in comparison to any radiative wall changes. The spectral perturbation for the outflow case is one to two orders of magnitude smaller in effect as that of the blackbody walls. Additionally, due to the non-linear effects of thermal radiation, as the blackbody radiation becomes larger, the overall contribution of the flowfield to thermal radiation becomes smaller. Thus, any perturbations of the thermal radiative contribution to the flowfield also become smaller. For pure-blackbody cases, the spectral modeling error is practically negligible. The epistemic uncertainty arising from boundary temperature ranges from the high radiative heat flux values of time-averaged blackbody walls, to the values with pure outflow walls ($T = 0$ K). The magnitude of the epistemic uncertainty due to spectral model perturbations scales with the blackbody wall temperature effects.

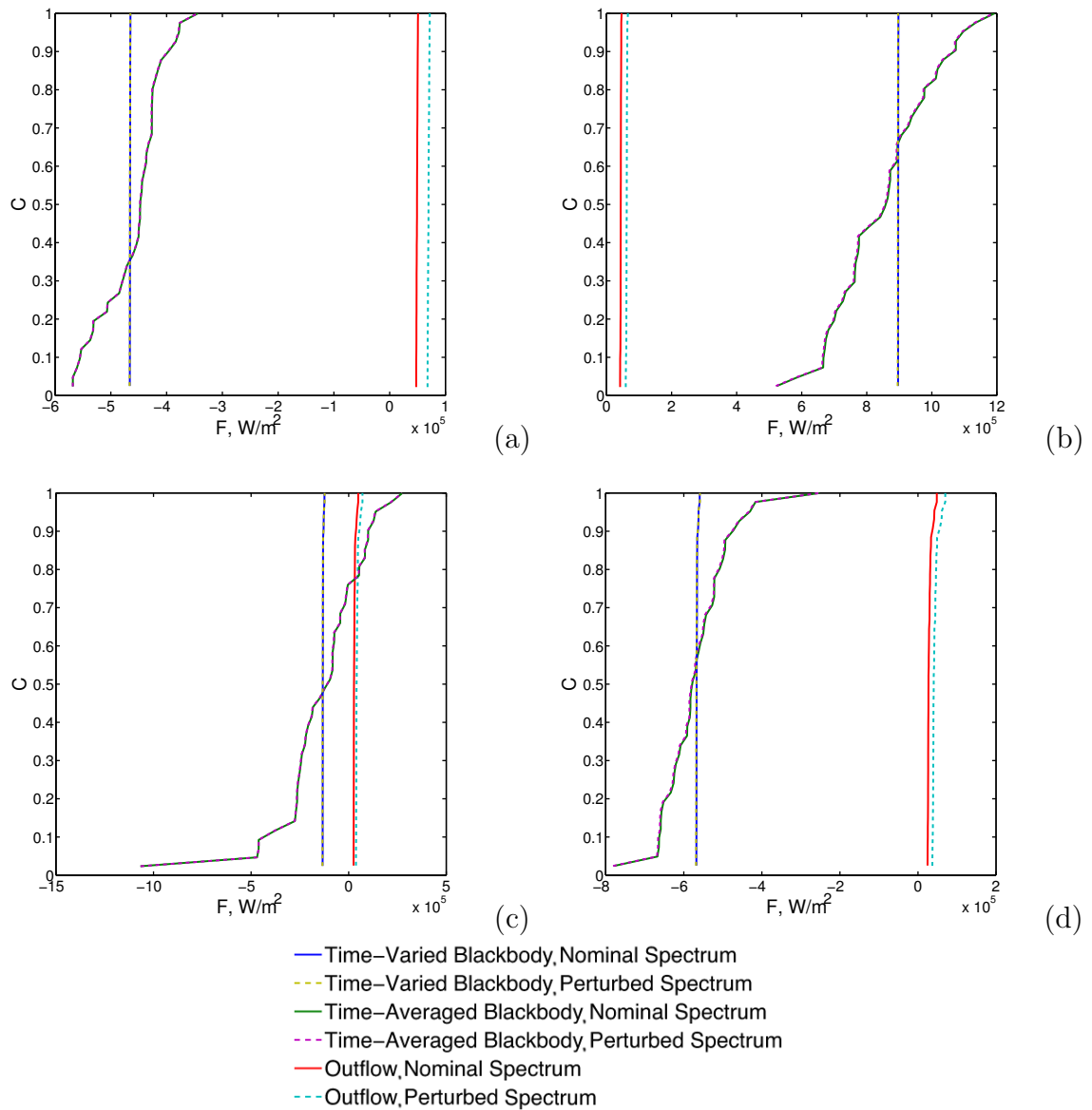


Figure 5.10: Cumulative distribution function of the spectrally integrated spatially averaged heat fluxes, for various LES flowfield snapshots. Locations are for (a) the back of the flame holding cavity, (b) the sidewall near flame holding cavity, (c) the sidewall near the flowfield exit, and (d) the top wall near the flowfield exit. Three boundary conditions are given along with a spectral perturbation comparison.

The varying aleatory uncertainty of the wall temperature fluctuations is given as the ranges of the time-varied blackbody CDF curves in Fig. 5.10. If the temperatures of the walls perfectly match the temperature at the edge of the flowfield and the walls are blackbody, then the uncertainties are 48, 75, 102, and 93 % of the mean radiative heat flux values in Figs. 5.10 (a), (b), (c), and (d), respectively. As the temporal response of temperature reduces from an instantaneous response to a perfect time average, the spectrally changing aleatory radiative heat flux reduces to a value of 0.

Finally, as established in Section 3.4, increasing the wall reflectivity, and decreasing the wall emissivity serves to reduce the overall absorbed radiative heat flux. As reflectivity approaches 1 the radiative wall heat flux, and therefore, the total uncertainty approaches 0.

For reference, the net radiative wall heating for a single LES flowfield snapshot is given in Fig 5.11, for physical wall boundary conditions of radiative outflows, time-averaged blackbody walls, and time-resolved blackbody walls.

In addition to radiative wall heating, radiative flow cooling is of interest. Radiative flow cooling may cause temperature changes of over 100 K, as discussed in Section 3.5. In order to address flow cooling, a series of 123 streamtraces are stochastically sampled from the time-averaged LES flowfield values. The time-averaged values are selected because the instantaneous velocity fields taken from the LES flowfield snapshots change drastically in the time required for a fluid element to traverse the length of the combustor. Thus, no exact path can be established. The radiative heat flux results do have instantaneous effects, as such the temporally resolved heat flux values can be projected onto the stream-traces, and the integrated flow cooling can be predicted. However, these values also change creating a fair amount of uncertainty to the overall prediction.

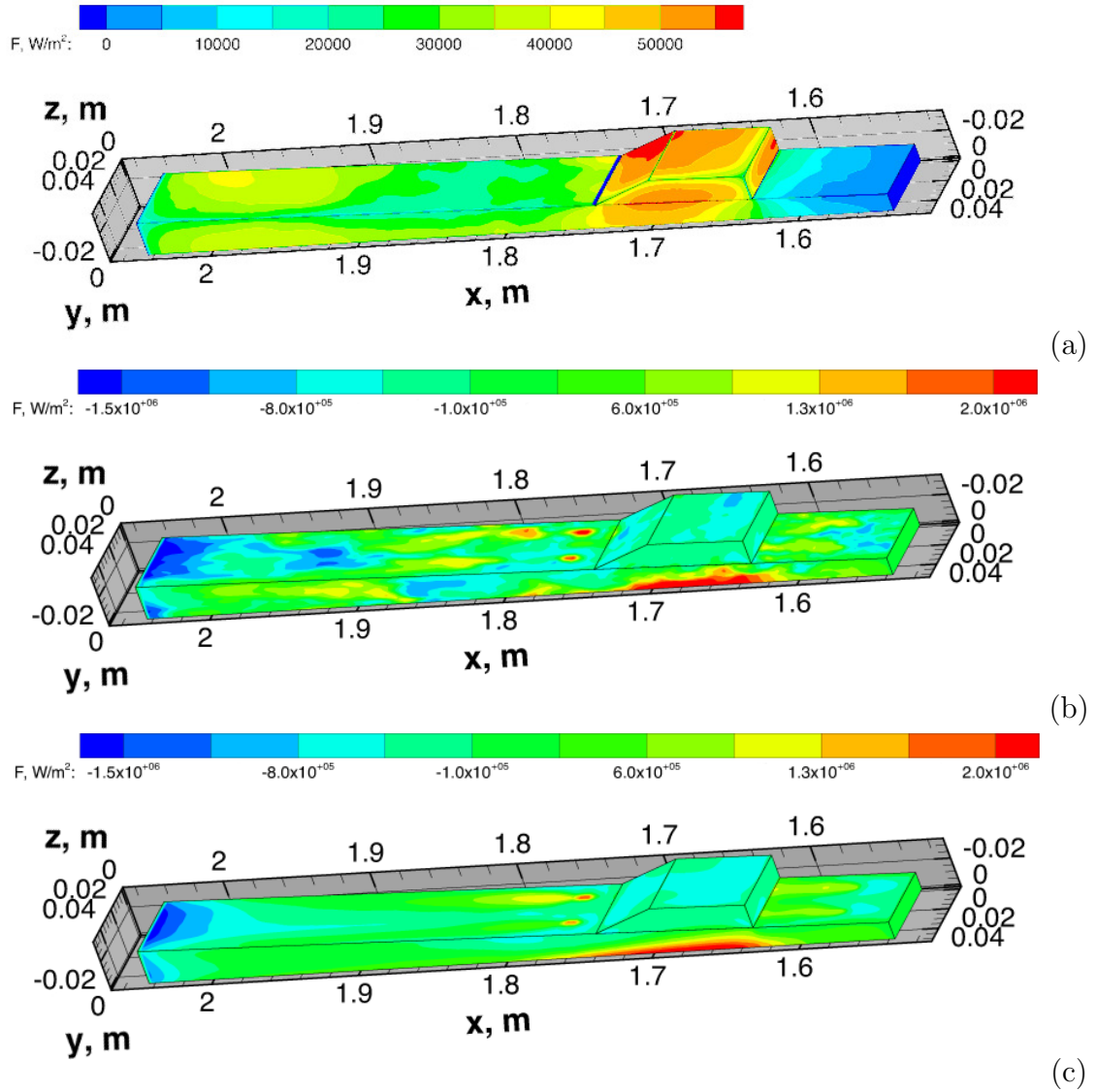


Figure 5.11: Radiative wall heat fluxes for a single LES flowfield snapshot with (a) radiative outflow, (b) time-resolved blackbody and (c) time-averaged blackbody radiative wall conditions.

The radiative flow cooling is calculated for all 123 flowfield traces on all 41 LES flowfield snapshots. The simulations have pure radiative outflow boundary conditions at the physical walls and planes of reflection at the centerlines. The temperature loss and residence time for each streamtrace is given in Fig. 5.12. Each of the radiative simulations based on the LES flowfield snapshots produces a different predicted temperature change. Thus, only the minimum, maximum, and mean values are given.

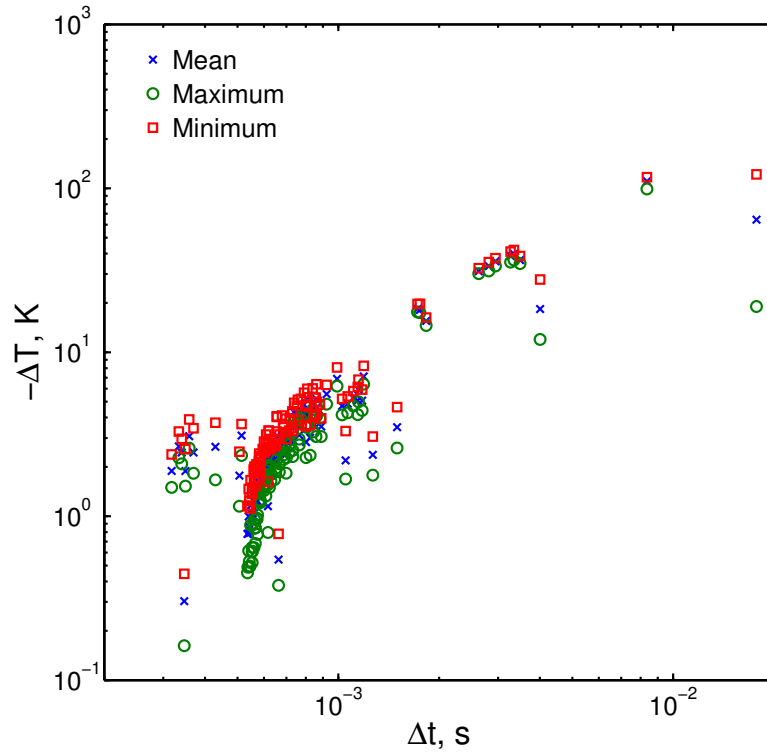


Figure 5.12: Predicted radiative temperature loss versus residence time for various streamtraces with radiative outflow boundary conditions. The minimum, maximum, and mean values based on multiple flowfield snapshots are given.

The trend in Fig. 5.12 suggests that the temperature change along a streamline is mostly determined by the fluid element residence time. However, many data-points suggest that strong variations in flowfield can influence these results. The range of temperature losses for a single stream-trace can vary from less than 1 K to over 80

K depending on the instantaneous flowfield conditions. Additionally, many flowfield traces have cooling from 1 to 4 K despite having a wide range of residence times.

With such a large possible range in temperature changes and residence times, a representative sample of flowfield traces is taken to be more fully examined. The sample consists of four flowfield traces with residence times of 0.6, 3.3, 1.1, and 17.7 ms, respectively. The traces are used to predict the temperature change due to flow cooling in a series of radiative simulations corresponding to 41 LES flowfield snapshots. The various results are computed into Cumulative Distribution Function curves for physical wall boundary conditions of pure radiative outflow, blackbody walls with time-averaged temperatures, and blackbody walls with time varying temperatures, which are given in Fig. 5.13. The CDF curves give the range between the high and low predicted spectral errors with an additional curve shift of $\pm 5\%$ due to numerical grid error.

Several trends appear in Figure 5.13. One trend is that no matter the magnitude of the predicted radiative heat flux of the outflow conditions, the addition of the blackbody radiation from the walls serves to reduce the overall flow cooling. In the case of Fig. 5.13 (a), the wall radiation serves to heat the flow slightly. This heating is much larger than that suggested by the radiative analysis of the steady-state RANS simulations discussed in Section 3.5.

An additional trend is that the overall variation in flow cooling is significantly smaller for the blackbody wall conditions than it is for the outflow conditions. This trend is especially notable in Fig. 5.13 (b), in which the range of radiative heat loss changes from about 40 K to about 2 K.

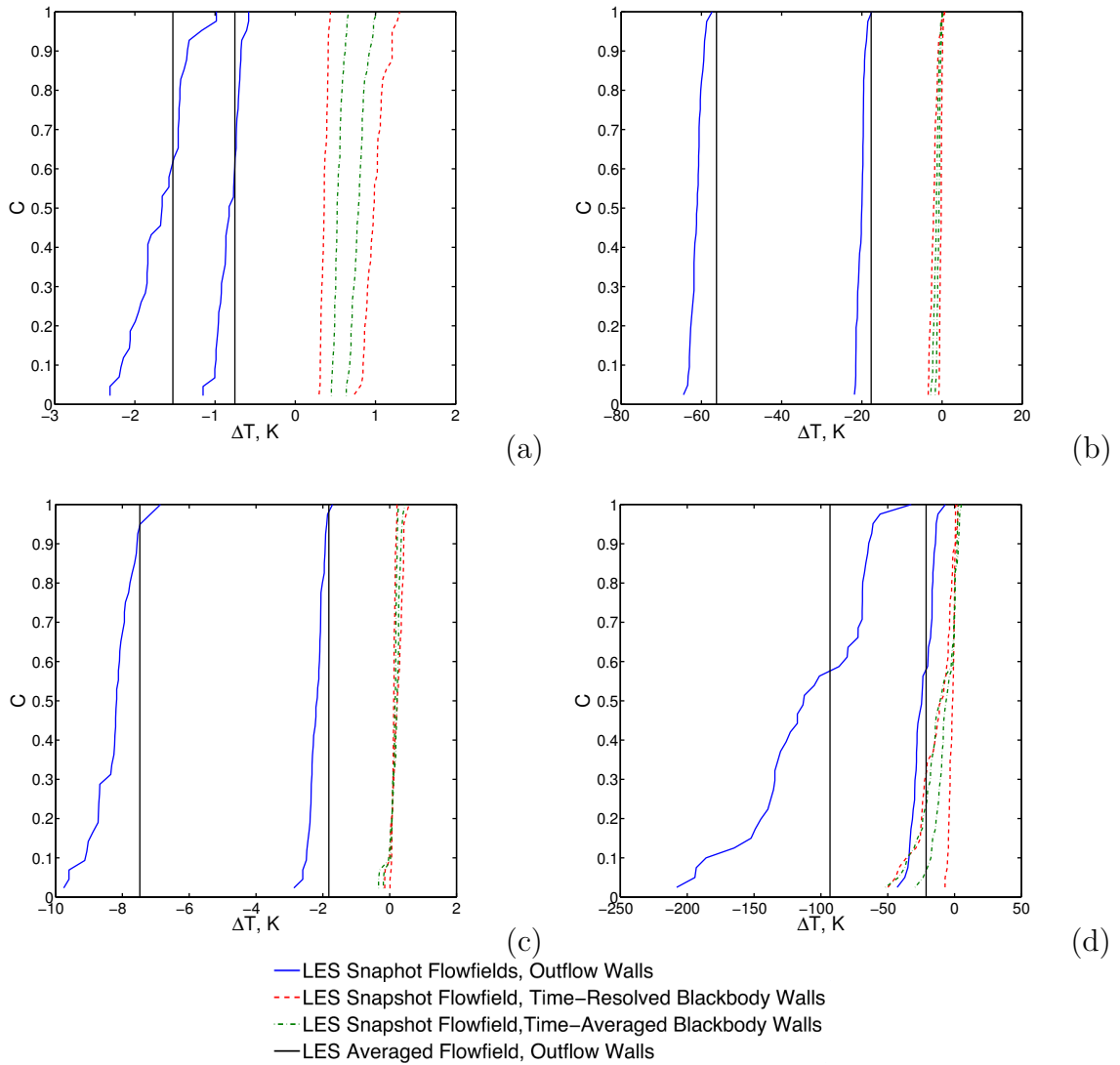


Figure 5.13: Cumulative distribution functions over a range of flowfield snapshots for streamtraces with residence times of (a) 0.6, (b) 3.3, (c) 1.1, and (d) 17.7 ms. The ranges due to spectral modeling and numerical grid uncertainty are presented for simulations with various physical wall boundary conditions. Simulations corresponding to a time-averaged, steady-state flow are given with black vertical bars.

The measure of the aleatory flowfield uncertainty is given by the temperature range over which the individual CDF curves are spread. With the flowfield changing over the residence time of a fluid element, the exact flow (or even the average effect) cannot be known. Thus, the flowfield cooling cannot be reduced to a single value as the wall heating can be. Additionally, unlike for the investigation of radiative wall heating, the blackbody radiation serves to lower the overall aleatory uncertainty of the temperature loss, as the individual curves cover a smaller range of possible temperature losses. The cases with the blackbody walls set at the time-averaged temperature of the LES snapshots have the smallest aleatory uncertainties, as their greatest radiative contributions are set to a constant for all radiative simulations.

The measure of the epistemic uncertainties is taken as the temperature difference between the high and low CDF curves. The differences between the high and low curves corresponding to the outflow boundary conditions are significantly higher than those of the blackbody CDF curves. The CDF curves with time-resolved blackbody walls bracket the CDF curves with time-averaged blackbody walls. This trend indicates that the lower average radiative heat loss caused by the time-averaged blackbody walls translates into a lower combined epistemic uncertainty, as most epistemic uncertainties scale with the absolute magnitude of radiative effects.

Unlike the radiative wall heat fluxes, which can be found exactly with the proper flow modeling, the flow cooling can never be precisely known for any one stream-trace because the flowfield changes during the fluid element residence time. As such, the temporal effects are treated as aleatory uncertainties. The manner of combining aleatory and epistemic uncertainty, as incorporated within Fig. 5.13, is to take the vertical difference between the upper and lower curves. The resulting normalized distribution is the combined PDF as given in Fig. 5.14 for the outflow cases.

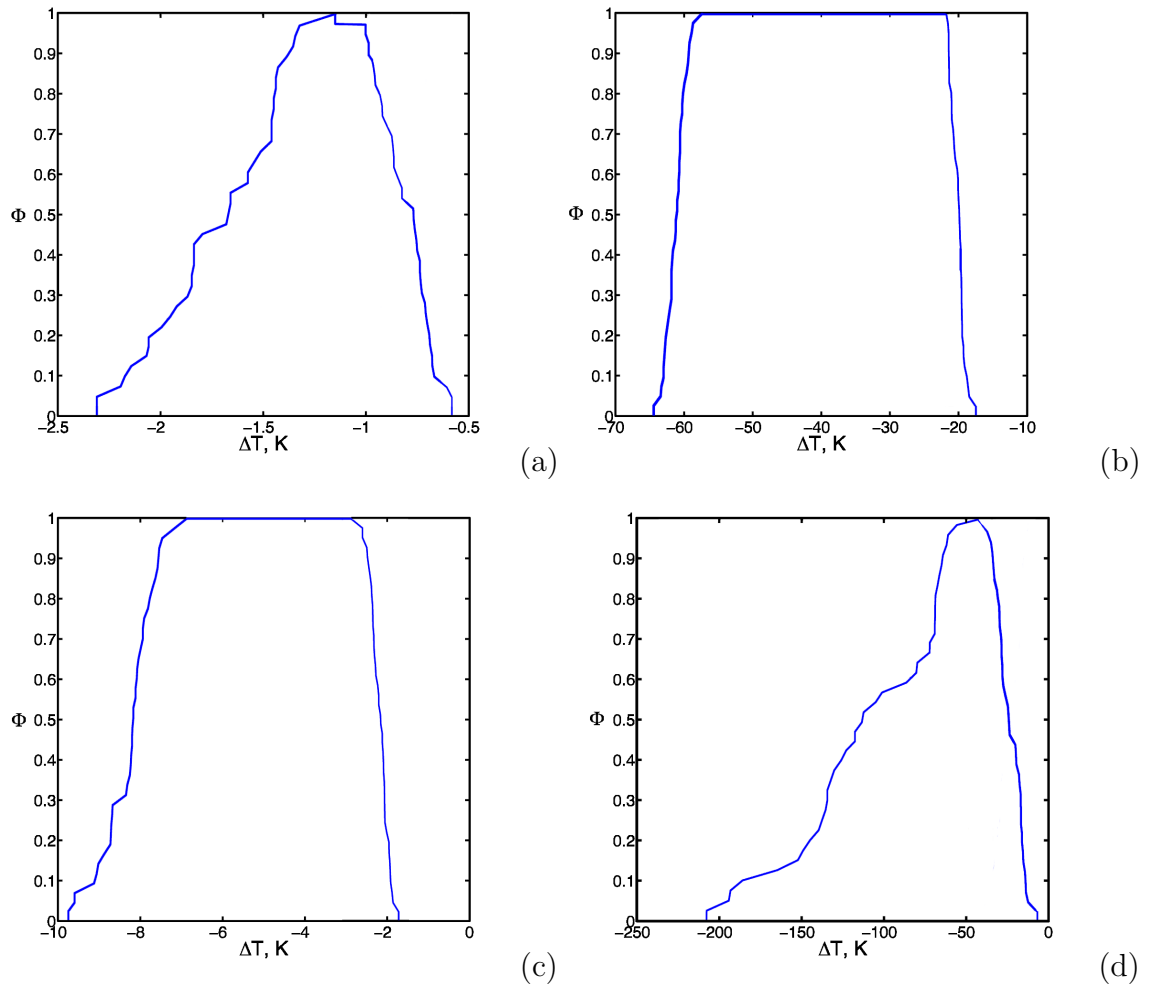


Figure 5.14: Normalized probability density functions over a range of flowfield snapshots for streamtraces with residence times of (a) 0.6, (b) 3.3, (c) 1.1, and (d) 17.7 ms. The combined epistemic and aleatory uncertainties are presented for all factors. Simulations corresponding to outflow boundary conditions.

In cases with larger temperature changes the aleatory flowfield uncertainty tends to dominate over the epistemic modeling uncertainty for the blackbody CDF curves, indicating that flowfield changes are more important than spectral changes for simulations with blackbody walls. However, when residence times and temperature changes become small, the effects of the walls are not able to completely overcome uncertainties in the flowfield, as indicated in Fig. 5.13 (a).

The epistemic modeling uncertainty for outflow cases is generally higher than the aleatory flow variation uncertainty, indicating that the changes in flow have a smaller impact on the radiative flow cooling than changes in the spectral model. However, this trend does not hold to for all stream-traces as shown in Fig. 5.13 (d).

In all cases, the blackbody radiation serves to reduce the effects of flowfield variation and spectral uncertainty, as the flowfield absorbs some of the thermal radiation from the wall, offsetting the overall temperature loss. The wall and flow are not of the same temperature resulting in a small amount of heat transfer and temperature change, whose rate is directly affected by uncertainties in the spectral model. However, these uncertainties do not have nearly as large an effect in the blackbody wall case as they do in the radiative outflow case because the rates of temperature change are greatly offset by the blackbody radiation.

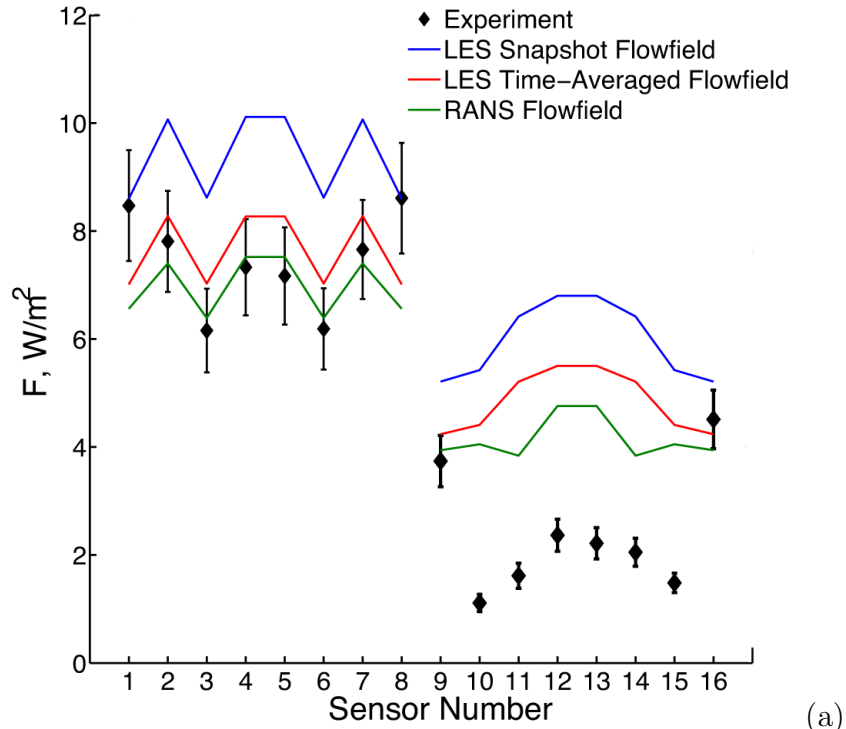
Finally, a comparison can be made between the CDF curves of the radiative flow cooling for the time-varying LES flowfield snapshots (indicated by blue curves) and the time-steady LES average flowfields (indicated by black vertical lines). In all cases, the time-steady solutions indicate a lower overall temperature loss than does the median of the time-resolved simulations ($C = 0.5$). These differences can range from 8 to 21% of temperature change predicted by the time-averaged flowfield simulations. Additionally, due to the higher averaged radiative heat fluxes for the time-resolved radiative flux simulations, the epistemic uncertainty for the time-resolved flowfield simulations is slightly higher than it is for the time-averaged flowfield simulations.

5.3.3 Sensor Prediction Uncertainty

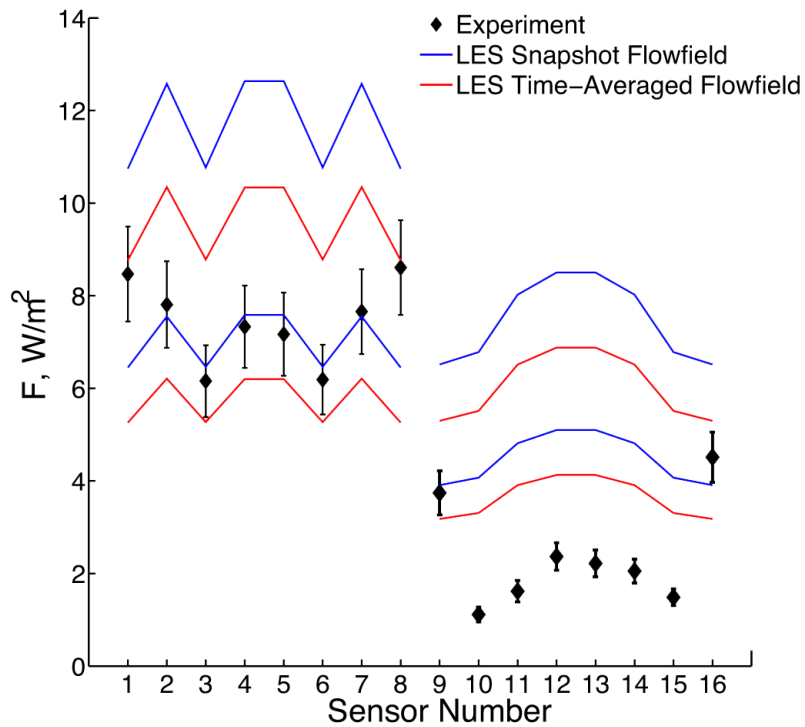
The incorporation of uncertainty into the wall boundary conditions and radiative heat flow gives very large variations in the thermal quantities of interest. With these large uncertainties, many of which come from the temporal variations in the LES simulations, previous examinations may need to be revisited. One such examination is the experimental measurement of radiation using photodetectors on the HIFiRE Direct Connect Rig discussed in Section 4.4. The radiative simulations for the photodetectors are now run using the LES flowfield as an input instead of the CFD RANS simulation flowfield.

According to Fig. 5.12, the residence time for most fluid elements is less than 2 ms with very few residing longer than 10 ms. The LES constitutes a flow simulation time of 13.7 ms with 41 flowfield snapshots. Additionally, the experimental data is sampled for a duration of 2 seconds with 17,500 samples. These sampling times indicate that the flowfield is cycled multiple times for both the LES and the experimental measurements. Additionally, the experimental measurements have very rigorous flow statistics. The cycling of the flowfields is important as flowfield statistics are not greatly affected by the turbulent autocorrelation.

The radiation generated in the experimental conditions is simulated using a RT method with a narrow-banded spectral model. The physical domains of the simulations are intended to duplicate the exact field of view for each sensor, given the position of the sensor and the geometry of the mounting hardware. The details are given in Table 2.1. The simulations employ an angular resolution of 0.5° for the solid-angle field of view and a spatial resolution of 0.5 mm along each trace path. The spectral model employs 138 bands ranging in wave numbers from 5550 to 9100 cm^{-1} , with an evenly distributed spectral resolution of 25 cm^{-1} . This range corresponds to the combined effect of the physical sensor response function and the silicon filtering window.



(a)



(b)

Figure 5.15: Comparison of the net radiative heat flux to the wall at the experimental exhaust port. Nominal values of different CFD modeling predictions are given in (a), RT simulations presented with computational uncertainty predictions in (b) for time-averaged LES flowfield and averaged radiative heat flux of LES flowfield snapshots. Experimental results presented with experimental measurement uncertainty.

The radiative heat flux for all 16 photodetectors is given in Fig. 5.15 (a) for the radiative prediction of the time-averaged LES flowfield, and for the average heat flux of all LES flowfield snapshots. The difference between the two curves can be considered a form of aleatory uncertainty, as it is uncertain to the exact character of the flowfield. In addition to the radiative heat flux predictions for the LES simulations, the radiative simulation of the RANS flowfields and the experimental data points are given. These additional data are identical to those given in Fig. 4.15. The trends for sensors 1 through 8 do not change significantly when considering the LES flowfield. Although, the radiative prediction for the time-averaged LES flowfield is slightly higher than for that of the RANS prediction, and the average of the time-resolved LES snapshots is significantly higher than either predictions, with a difference of about 2 W/m^2 .

For sensors 9 through 16, the radiative flowfield predictions are higher than those based on the RANS flowfields. However, the overall trends do not line up. The most obvious example is that for the radiative simulations based on the RANS flowfields, the predicted heat fluxes at sensors 11 and 14 are lower in value than those of sensors 10 and 15. In all of the other cases (including the experiment), the predicted radiative heat fluxes at sensors 10 and 14 are greater than the values for sensors 10 and 15 but lower than the values for sensors 12 and 13.

If not for the offset of about 4 W/m^2 for the radiative predictions based on the LES flowfields, the trends for sensors 10 through 15 would match the trend of the experiment. One possible explanation of the discrepancy in the values for sensors 9 through 15 is that, unlike the other sensors which have a standoff value from the silicon filter of approximately 1 mm, sensors 9 through 15 have a standoff distance of over 3 mm. The back end of the silicon filter is textured resulting in a scattering of the infrared light passing through it. It is possible that the scattering caused by the silicon filter is not strong enough to greatly affect the radiative measurements

with a 1 mm standoff, but it is strong enough to effect a measurable change in the thermal radiation measurements with a 3 mm standoff. This phenomenon can be shown mathematically for a number of scattering schemes, but the overall scattering is yet to be characterized experimentally.

The closer relative agreement in the trends is expected as the temperature and water vapor mole fraction distributions predicted by the LES simulations for the exit plane of the combustor do not show the strong structure predicted by the RANS simulations in Fig. 4.16. The LES exit profiles given in Figs. 5.2 and 5.3 are more evenly distributed like the experimental profiles given in Fig. 4.17.

The spectral modeling error employed, “ $E_{\nu 2}$,” is calculated over the 1 m path length as described in Section 4.2. The spectral database error is computed by adding a factor of 25% to the existing spectral model, resulting in a value of $E_{\nu 1} = 0.25$. The spectral model is perturbed as in Eq. 2.19.

The ranges of the epistemic uncertainties for both the RT simulations based on the time-averaged LES flowfield simulations and the average radiation of all the LES flowfield snapshots are given in Fig. 5.15 (b). The overall characters and magnitudes of the uncertainties are similar for both sets of data. The total combined uncertainty can be taken as the range between the uppermost and lowermost computational radiative curves. Given the consistency between the curves, it is predicted that any curve lying within the range will have roughly the same shape as the boundaries. The experimental measurements are included for reference.

The epistemic uncertainties of the system are combined into a series of CDF curves for a variety of conditions. For strictly outflow wall conditions ($\epsilon_{\nu} = 1$, $r_{\nu} = 0$, $T = 0$), the epistemic modeling uncertainty dominates the uncertainty of the flowfield variations. The combined uncertainty spans from -70 to +90 % of the radiative heat flux in low flux regions, but it can be as large or small as a range of -45 to +60 % of the radiative heat flux in regions near the flame holding cavity exit. The

major contributors to uncertainty in these cases are spectral modeling error and spectral database error. The minor contributors are grid refinement error and flowfield variation uncertainty.

The effects of changing boundary conditions introduce a large uncertainty into the system. The effects of blackbody walls negate spectral modeling error on radiative wall heating in most cases. Wall temperature fluctuations can greatly increase or decrease the effects of radiative blackbody walls. However, wall temperature fluctuations will not change as quickly as the flowfield temperature fluctuations. Highly reflective walls negate the radiative wall uncertainty effects completely.

The radiative flow cooling is dependent on residence time and can range in values from less than 1K to over 100 K for radiative outflow conditions. Spectral uncertainty and numerical modeling uncertainty can introduce uncertainties in the predict flowfield cooling on the same order as the nominal flow cooling value. The flow cooling and associated modeling errors are reduced with the introduction of blackbody radiative wall heat flux, but the epistemic uncertainties are not made negligible as they are for the radiative wall heating considerations. The flowfield properties fluctuate greatly over the residence time of a fluid element. Thus, any flow cooling prediction is subject to an aleatory uncertainty associated from the flowfield fluctuations. The aleatory flowfield uncertainty associated with the temporal fluctuation in the flowfield can have effects on the predicted temperature changes that are either smaller or larger than the epistemic modeling uncertainty.

Finally, the LES flowfields are added to the radiative predictions of the experimental measurements presented in section 4.4. The RT predictions based on the LES flowfields give a better prediction of the flowfield character than those based on the RANS simulations. However, for a number of sensors, the radiative simulations of the LES flowfields even more greatly over-predict the radiative heat flux than do the radiative simulations based on the RANS flowfields.

5.4 Conclusions

The combined uncertainty for the thermal radiative simulations of the HIFiRE Direct Connect Rig (HDCR) is presented. In order to account for temporal effects of the turbulent flowfield, LES simulations of the HDCR were performed by Ivan Bermejo-Moreno at Stanford University. The individual LES flowfield snapshots and the time-averaged flowfield are processed with the DOM code, GRASP. The turbulent flows create a much more widely varied set of structures than the time-averaged flowfield would suggest. Despite the more varied snapshots, the LES time-averaged flowfields are less defined when compared to the RANS predictions presented in previous chapters. Additionally, the mean temperatures are higher and the water mole fractions are lower than for the RANS predictions presented in previous chapters. All of these phenomena are most apparent at the combustor exit plane.

The individual LES flowfield snapshots show radiative heating peaks over 5 kW/m^2 higher than those of the time-averaged LES flowfield. Additionally, the clearly defined structures in the LES snapshot temperature profiles translate into more spatially even radiative wall heat flux profiles. The spatially averaged temporal variations of radiative heat flux in the flame holding cavity range from 41 to 51 kW/m^2 with reasonably well-defined modes and ranges given the 41 LES flowfield snapshots considered. The spatially averaged temporal variations for radiative heat flux near the combustor exit are not as well-defined. The heat fluxes range from 24 to 49 kW/m^2 with the modes near 27 kW/m^2 . However, many features suggest the need for more flowfield samples before the system is fully characterized.

The individual simulations have associated probabilities assigned to them, and these probabilities can be used to find weighted time-averages of the radiative heat flux and thus construct Cumulative Distribution Functions (CDFs) of output quantities of interest. The radiative outflow quantities of interest are wall heating and flowfield cooling. The CDF curves can be combined with other forms of uncertainty

to garner a total uncertainty. The uncertainties sources of concern are the spectral modeling error, numerical modeling error, and flowfield uncertainty. All spectral error predictions are applied before the radiative simulations are processed. The numerical modeling error is applied after all simulations are processed, and the flowfield uncertainty is taken as the difference between the radiative calculations using different flowfields.

The overall uncertainty of the HDCR is characterized for a number of factors, and further investigation is suggested for each one. For the case of radiative wall heating, the flowfield uncertainty is taken as the difference between the average radiative heat flux for all of the LES flowfield snapshots and the thermal radiative heat flux for the time-averaged LES flowfield. When all uncertainties are combined, the total radiative uncertainty ranged from -70 to +95 % of the radiative heat flux in the low-flux regions and from -50 to +60 % downstream of the flame holding cavity. The breakdown of the uncertainties attributed approximately as follows: 25 % to the experimental database, 5 % to the numerical grid model, 12 % to the flowfield model, and the remaining uncertainty is attributed to the spectral model. With the spectral model contributing the largest uncertainty, and it being the most readily adjustable parameter in the simulation, future investigation should first examine optimizing the spectral model and the associated error prediction.

The introduction of blackbody wall radiation changes the radiative wall heat flux from -1.5 to 2.0 MW/m², indicating that wall emissivity and temperature are the largest factors for uncertainty in radiative wall heating. The spectral model error is not only much smaller than the uncertainty due to boundary conditions, but it actually diminishes due to increases in the radiative wall temperatures. It is assumed that the walls have a much slower temporal fluctuation than does the flowfield. The overall uncertainty of the system with emissive walls ranges from the maximum of perfectly emissive blackbody walls at the flowfield time-averaged temperature, to purely reflec-

tive walls with no radiative wall heat flux at all, giving an uncertainty range of up to 2 MW/m^2 for some areas of the system. In order to properly predict radiative wall heating, temperature and wall emissivity must be properly characterized for all test cases.

The examination of flow cooling along stream-traces is shown to have uncertainty stemming from many factors. As established in Section 3.5, the flow cooling depends greatly on wall boundary conditions and residence time that can vary the mean flow cooling from less than 1 K to over 90 K. Given that the flowfield changes greatly over the residence time of a fluid element, the uncertainty attributed to the flowfield is taken as the range of the associated CDF of the cooling curve. These aleatory flowfield uncertainties can vary from less than 1 K to over 150 K, depending on the streamtrace and boundary conditions. The use of blackbody walls greatly reduces the radiative flowfield cooling and the associated uncertainty. However, the spectral and numerical modeling errors never become negligible for flow cooling predictions as they do for wall heating predictions. The combined uncertainties from the spectral model and boundary conditions range from 3 to 90 K depending on the streamtrace. With such large and varied ranges in flow cooling for a variety of uncertainty sources, future investigations of radiative flow cooling may require a direct coupling of the radiative solver to the flowfield solutions, as the temperature changes may greatly affect the flow character.

Finally, the temporal effects are examined using a Ray Tracing method for the thermal radiation prediction of the flowfield sensors from the HDCR experiment discussed in Section 4.4. The LES simulations are found to have higher radiative heating predictions than either the RANS simulations or the experimental measurements. The introduction of spectral modeling uncertainty brings roughly half of the individual sensors into agreement with experiment. Additionally, the shift from the average of the radiative heating prediction of the individual LES snapshots to the radiative

heating of the time-averaged LES flowfield moves the agreement even closer. Some of the radiative trends in the experiment are more closely matched by the radiative predictions of the LES flowfields as opposed to the RANS flowfield. However, some sensors still have a very large margin of disagreement regardless of the flowfield. These differences suggest that further experimental characterization of the silicon filter may be necessary for the full explanation of the experimental measurements.

CHAPTER VI

Conclusions and Looking Forward

6.1 Project Goals

The goal of the current work was to explore the computationally uncertainties of thermal radiation as it pertains to a pair of scramjet combustion chambers. The goal was accomplished over the chapters of the current work.

Chapter I introduced the concept of the scramjet as a supersonic combustion chamber employing shockwave compression. The chapter described the goal of uncertainty quantification with respect to one of the major issues of scramjets, unstart. The chapter also discussed the concept of thermal radiative heat transfer as a way of coupling electromagnetic energy to internal thermal energy, which can be employed as a means of thermal management within the system. Finally, it reviewed how thermal radiation has been studied for scramjets in prior works.

Chapter II introduced the equations and methodology used in the investigation. The RTE was described as a means of spatially modeling radiation, and the RT and DOMs were presented as numerical discretizations for a three-dimensional radiative heat transfer domain. A two-point banded spectral model was introduced, and a means of estimating its modeling uncertainty was discussed. An adjoint sensitivity methodology was described for determining important parameters, and a probability function was discussed for weighting all simulations. Finally, an experimental test rig

(the HDCR) was described.

Chapter III discussed the geometry and operating conditions of the HyShot-II scramjet combustor. A numerical comparison of the radiative heat transfer of different combustion chamber sizes and geometries was performed with respect to HyShot-II. The chapter also introduced the details of the HDCR CFD simulations. The combustor was numerically evaluated to quantify the effects that individual flowfield quantities have on radiative wall heat transfer. Additionally, the combustor was analyzed to quantify how boundary conditions affect the radiative wall heating and flow cooling within a combustion chamber.

Chapter IV discussed the sensitivities and accuracies of the radiative modeling techniques with respect to the RANS CFD simulations of the HDCR. The spectral model along with a means of estimating its uncertainty was evaluated for the three-dimensional geometry. Additionally, refinement of radiative grid and flowfield sampling meshes was performed for the DOM simulations of the HDCR. Finally, a series of experimental datapoints was compared to a series of RT simulations of the HDCR exit plane.

Chapter V discussed the combination of all of the uncertainties presented in the current work. These uncertainties were put in the context of the radiative simulations for a series of LES flowfield snapshots of the HDCR. The combined uncertainty for radiative wall heat flux was evaluated for multiple boundary conditions including spectral perturbations. The uncertainty boundaries for the flow cooling prediction of multiple stream traces was calculated. Finally, the radiative analysis of the LES flowfield simulations was compared to the experimental measurements with their associated error bars and uncertainties included.

The remainder of the current chapter discusses the main conclusions and contributions of the current work. Finally, the current chapter examines possible future lines of investigation, including suggestions to further improve the current set of in-

vestigations as well as expand on the scope of the work.

6.2 Conclusions

The evaluation of the thermal heat transfer for two different scramjet combustion chambers is accomplished using numerical radiative simulations. The current study predicts radiative heat transfer to range from insignificant values to a dominant means of heat transfer depending on a variety of conditions.

The impact of the radiative heat transfer predictions can affect a large number of factors for the sustainability of a scramjet. The thermal radiative heat transfer may greatly affect wall heat loads, which may affect the structural integrity and geometry of a scramjet. Additionally, the wall heating loads may distort the supersonic boundary layer of a scramjet, affecting many of the compressible flow characteristics of a scramjet. Whereas these effects are found to be small for purely outflow wall conditions in the HDCR (20 to 56 kW/m² for the nominal case), the effects of hot radiating wall conditions can contribute greatly to the overall heat loads, creating wall-to-wall heating rates of up to 2 MW/m². Additionally, it is shown that the scramjet combustion chambers under consideration are relatively small and optically thin. The chambers, being experimental test cases, are much smaller than any powerplant for a sustained flight vehicle. Because radiative heat transfer scales with size, whereas convective heating is relatively constant, an increase in combustion chamber size to that of a sustainable flight combustion chamber may greatly increase the additive heat load from radiation on the combustion chamber walls.

Additionally, the impact of radiative heating on internal flow temperature can have a great effect on combustion rates. For the case of the HDCR, the post-processed radiative streamtrace integration finds that temperature reduction can range from less than 0.001 K in streamtraces with small residence times to over 100 K in streamtraces that become entrained in recirculation zones. Additionally, the magnitudes of

the temperature changes are greatly influenced by the spectral model uncertainty, and the boundary conditions create a possible range variation of over 50% of the nominal temperature change. The importance of the high temperature changes in the recirculation zones is that the main recirculation zone is in the flame holding cavity, an area intended to facilitate combustion. A change of 20 to 100 K in the flame holding cavity due to thermal radiation may greatly change the rate of combustion.

This knowledge of thermal loading and heat transfer may guide further designs of scramjets to incorporate the thermal effects of radiative heat transfer. Additionally, the requirements and findings of the current work may serve to instruct future research on how to more effectively evaluate a scramjet and on what knowledge remains to be gathered in order to fully evaluate the system.

6.3 Contributions

The main contribution of the current work is the thermal radiative analysis of two scramjet combustors. The work is unique in that it is the first known thermal radiative analysis of a scramjet engine that has been operated in a flight environment. Additionally, the current work is only the third known work to compare thermal radiative predictions to experimental radiative heat flux measurements of a scramjet combustion experiment. Also, it is the only known work to cover scramjet thermal radiation in the 1.1 to 1.8 micron wavelength range, and it is the only one to consider scramjets with hydrocarbon fuels [45, 88]. The simulations are the first to compare the radiative properties of both LES and RANS CFD flowfields for the same flight combustor. Finally, the work is the first to place uncertainty and error bars on the thermal radiative simulations of flight scramjet combustors for an aggregate of uncertainties. The details of the procedural contributions are listed in the current section.

A banded spectral model is introduced with a 25 cm^{-1} spectral resolution based on

the HiTemp 2010 database [92]. The individual spectral bands are given a two-point quadrature scheme and organized into lookup tables based on frequency, temperature, and species. A simple additive system is employed to account for multiple species. The radiative species of interest are water vapor, carbon dioxide, the hydroxyl radical, carbon monoxide, and methane. A means of estimating the accuracy of the individual spectral bands is introduced by taking the difference between high-fidelity and low-fidelity spectral band models as applied to a unit problem. The difference is used to create an error lookup table. The resulting uncertainties for radiative wall heat flux in the HDCR simulations vary between 5 and 30 % of the nominal wall heat flux value.

The current work applies a sensitivity analysis to the radiative flowfield code, GRASP, and it provides an analytical way of determining the net effect that a particular flowfield quantity has on the radiative wall heat flux. The local sensitivity of temperature is found to be the greatest factor in radiative wall heat flux. The species of water vapor is found to be the dominant emitter for thermal radiation. Carbon dioxide is found to have a contribution between 10 and 50 % of that of water for different locations. These three flowfield parameters are determined to be the most important parameters for analyzing flowfield variation within the HDCR. The hydroxyl radical, carbon monoxide, and methane are found to have local, non-negligible effects, but small variations in their values are predicted to be insignificant. Thus, the minor species are not considered in flowfield variation statistics.

The current work applies a simple post-processing model to predict the temperature change due to thermal radiation for CFD flowfield streamtraces. A strong connection between residence time and temperature change is found. Fluid elements with residence times of greater than 10 ms having predicted temperature changes of 10 to 100 K. The effect of boundary conditions can vary these results greatly, with blackbody walls reducing the temperature change by as much as 20 %, and reflective

walls reducing the temperature change by as much as 50% from outflow wall values.

The current work performs a comparison of size variation for the HyShot-II combustor, finding that the optical depth is thin, and the relationship between the linear chamber dimensions and thermal radiative heat flux is almost linear. Additionally, the work examines the approximation of a three-dimensional combustion chamber as a one-dimensional plane-parallel geometry, and it is found, in multiple cases, to approximate the full-three dimensional chamber within a factor of two. This finding is applied to the one-dimensional unit problem used to estimate the spectral modeling errors.

The current work presents a means of combining the uncertainties from different sources into a single bound. The uncertainty from the numerical modeling in the DOM simulations is found to be approximately 5 % of the nominal radiative heat flux values of DOM simulations. This uncertainty is applied to the simulation results in the form of an error bar. The spectral database error is 20 to 25 % of the radiative wall heat flux according to a previous study [50]. This prediction is treated as a perturbation to the spectral model lookup tables. Additionally, the spectral modeling error is found to vary greatly depending on species, temperature, frequency, and optical depth. This prediction is also treated as a perturbation to the spectral model, but the individual perturbations vary based on the individual cell quantities. The variations in wall boundary conditions are examined by taking the extreme of the wall boundary conditions. The uncertainty of the boundary conditions is taken as any calculated radiative value between the extremes.

The individual time-resolved LES flowfields are given probabilities based on how much their individual cell quantities of temperature, water vapor concentration, and carbon dioxide concentration differ from the time-averaged cell mean. The probabilities are used to construct a CDF of the LES flowfield snapshots based on their temporal variation. The implementation of these fluctuations varies depending on

application. For radiative contributions of flow heating to the walls, the uncertainty is taken as the addition of the differences resulting from spectral modeling perturbations. Also added is the difference between the time-averaged radiative heat flux from the individual LES flowfield snapshots and the radiative heat flux from the time-averaged LES flowfield. The resulting uncertainties range from 45 to 95 % of the nominal heat flux value depending on location.

The uncertainties associated with the net radiative wall heating are dominated by the uncertainty in the wall condition. The boundary extremes are taken as a purely reflective wall, which can absorb no thermal radiation, and as the net radiative heat flux for a blackbody wall at the time-averaged flow temperature, which can have radiative heat flux contributions ranging over -1.5 to $+2$ MW/m².

Finally, the individual uncertainties for the flowfield traces are taken as the extremes of the combined perturbations caused by wall boundary condition changes, numerical modeling errors, and spectral modeling errors. Additional uncertainty is derived from the temporal variation in the flowfield, which unlike the situation for wall heating, does not have a time-averaged effect.

The current work, finally, examines a comparison between radiative measurements and RT simulations of the HDCR. The individual measurements are found to agree within the experimental error bars and the modeling errors for the majority of the measurements. The combined method of post-processing of a CFD flowfield with a radiative heat flux prediction is shown to have some validity in the context of a scramjet combustor.

6.4 Looking Forward

With the current contributions in place, numerous issues and future works remain for the current project. Such issues include the further characterization of the physical test cases and a more rigorous reevaluation of the spectral and uncertainty models

employed in the current work. Further investigations of work may be included, such as the application of the methodologies to other test cases and the direct coupling of thermal radiation to the fluid-dynamic flow calculations in these cases.

6.4.1 Revisiting Issues

Several issues remain to be revisited in the current work, several of which pertain to the spectral model. With a number of tuning parameters for the spectral model in place, each band can be optimized for bandwidth to increase spectral accuracy in regions of high spectral variation and lower computational cost in spectral bands of lower spectral variation. Additionally, the flat tuning factors applied to the spectral weighting should be revisited for each combination of species, frequency band and temperature.

The spectral model has many factors that should be fine-tuned in order to increase both the speed and the accuracy of the simulations. The bandwidths, number of quadrature points, and tuning parameters used in the spectral model should be adjusted to minimize the spectral error over a prescribed test problem. Given that the error will necessarily be only driven to zero when the number of bands and quadrature points approaches infinity, an optimization method should be employed to give increased refinement to the system while limiting the increase in computational cost. The adjoint sensitivity method should be further extended to the individual line-strength table entries. Given that the absorptivity is the multiplication of the species concentration and the calculated line-strengths, the sensitivity of the radiative wall heat flux to the spectral linestrengths should be calculated by multiplying the adjoint sensitivity by the derivative of the absorptivity over the linestrengths as in Eq. 6.1. The errors should be calculated by taking the difference of a high-fidelity spectral model and the spectral model of interest over a test problem. The knowledge of which bands have the highest errors directs which linestrengths must be refined, and

the knowledge of the most sensitive linestrength entries directs which modifications provide the largest improvement in spectral error.

$$\begin{bmatrix} \delta F \\ \delta S_\nu \end{bmatrix} = -\Psi^T \begin{bmatrix} \delta R_I \\ \delta \kappa_\nu \end{bmatrix} \begin{bmatrix} \delta \kappa_\nu \\ \delta S_\nu \end{bmatrix} \quad (6.1)$$

The spectral error model prediction has several major areas that should be addressed with future investigations. The current additive perturbation model is shown to overestimate uncertainty predictions in cases with mixed species. A comparison between high and low spectral fidelity models for three-dimensional inhomogeneous domains is required to determine the additive nature of the spectral modeling error. The spectral modeling error tables need not necessarily be applied in a uniform manner. The major contributors should be varied in an design study. The individual frequencies should be studied independently of each other, and the contributors of interest (water vapor, and carbon dioxide) only have six entries each for the current model. As such, a twelve dimensional design study can give a probable range of errors. The number of total design variables can be further reduced if any correlation is found among the individual table entries for any one species.

The final issue with the spectral database is the flat 25 % database uncertainty applied on top of the modeling errors. The spectral database employed contains individual errors predictions accompanying each of the linestrength entries [92]. Re-computing the spectral model table to include the database uncertainties and taking the difference from the current tables would provide a direct measure of uncertainty for the spectral lookup tables. These uncertainties would be specific to each table entry.

In addition to the spectral lookup tables, the particular test cases would benefit from further characterization of the physical domains. The silicon filtering window employed in the experimental measurements has an uncharacterized scattering property, which may be the source of the discrepancy between the simulations and mea-

surements of the radiative heat flux at the exit plane of the HDCR. A calibration study is suggested to determine the scattering function of the silicon window and if the scattering is the cause of the difference. Additional characterizations of the HDCR would be to determine the wall temperature profile, emissivity, and reflectivity as all are shown to have a dominant effect on radiative wall heating and flow cooling.

The use of 41 LES flowfield snapshots as a characterization of the time-varying flow leads to many useful conclusions. However, a direct look at the data showed holes in the overall sampling domain. One possible means of filling in these gaps is the inclusion of more flowfield samples. However, with the computational expense of LES flowfield samples, a Reduced Order Model (ROM) is suggested. A Proper Orthogonal Decomposition (POD) analysis of the flowfield snapshots produces a number of flow modes that can be reconstructed into turbulent flowfields [4, 98]. Perturbations of the flow modes would allow for new, unique flowfields to be constructed quickly in order to augment the current set of LES flowfield snapshots. The measure of flowfield probability can be applied to the new reconstructed flowfields to determine their applicability.

6.4.2 Future Work

In addition to revisiting a number of issues in the current work, the lessons learned can be applied to further test cases. One such set of cases is the historical spectral scramjet measurements made for the NASA Langley Research Center [45, 88]. The past measurements cover a different range of wavelengths than the current experiment, and they provide spectrally resolved outputs over wavelengths of higher heat fluxes. As such, they provide a validation dataset for the current methodology.

One very useful expansion of the current capability would be a direct coupling of the thermal radiative heat transfer code to a LES CFD solver. Given the nonlinear nature of thermal radiation, a direct coupling to any time-averaged CFD solution

is found to be less accurate than an instantaneous coupling. However, given the spatial sampling and numerical solution requirements of the thermal radiative heat transfer methods, a far coarser spatial grid can be applied for the thermal radiation calculations than for the flowfield calculations. Additional investigation is required to determine if the thermal radiation analysis needs to be applied in between every timestep, or if it only needs to be updated after a certain interval of timesteps.

The main need for coupling is the predicted path integrated temperature changes given in Sections 3.5 and 5.3. The criterion to decide whether or not to include radiative cooling in a CFD predictions is if the flow is cooled enough to delay combustion for an appreciable distance along the flowpath. With residence times around one millisecond, an additional combustion delay on the same order could prevent complete combustion within the chamber. With predicted temperature losses on the order of 10 to 100K, the combustion chemistry model of the CFD may be adversely affected [81, 82].

Additionally, if the CFD wall models are described using a more complicated scheme than an adiabatic or isothermal limit, such as one with a given thermal mass and conductivity, then the radiative wall heating will affect the boundary condition temperature and be fed back into the flow calculations. As such, any heat-rate based boundary condition GRASP calculations must incorporate radiative heating as the blackbody wall effects are found to be on the same order as the convective wall heating effects.

If further detail in the angular and spatial mesh are desired, then the method of parallelizing the CFD simulations may need to be addressed. Currently, the simulations are parallelized by spectral band. However, with a large number of ordinates, the simulations must have a limited number of spatial cells to fit within the memory limits of the processors used. If a spatial domain decomposition is implemented, then the entire domain is not required to be stored in the same memory allocation, and it

can be spread among several processors or nodes to allow for a much larger spatial mesh.

Finally, the methodologies given in the current work can be applied to any number of combustion situations. Optically thicker situations will introduce a number of non-linearities into the system, and they may cause a reevaluation of certain methodologies. One such methodology is the adjoint method, which becomes a more useful tool when the optical thickness is high. This increase in the importance of determining the source of the thermal radiation that is incident to the chamber walls is because certain parts of the flow may be very radiative, but their effects may not reach the chamber walls in optically thick regions. A sensitivity analysis will tell if these areas are worth scrutinizing.

6.5 Project Evaluation

The thesis predicted the radiative heat transfer within a scramjet combustion chamber using multiple numerical methods. A number of numerical methods are applied for uncertainty analysis, and a new spectral model for radiative heat transfer is evaluated in the context of the project. The predictions show that, even with large uncertainty bars, the overall effects of radiative heat transfer in a flight scramjet are not negligible. For further investigations of flight scramjet combustion chambers, thermal radiation should be included in the analysis for both wall heating and flow cooling.

APPENDICES

APPENDIX A

Photodetector Calibration

The following appendix covers the procedure used to calibrate the photodetectors used in the experimental setup. The nomenclature of the current appendix differs from the main chapters as follows.

Appendix A Nomenclature

A	Photodetector Area	$[mm^2]$
F_C	Flowfield Heat Flux Incident onto Chamber Wall	$[\mu W/mm^2 = W/m^2]$
P_A	Ambient Power Incident From the Chamber	$[\mu W]$
P_B	Power Emanating from the Diode Laser Beam	$[\mu W]$
P_C	Flowfield Power Incident onto Chamber Window	$[\mu W]$
P_E	Power Incident During Experiment	$[\mu W]$
P_I	Power Incident During Calibration	$[\mu W]$
R_A	Sensor Response to Ambient Measurements	$[V]$
R_E	Sensor Response to Flowfield Measurements	$[V]$
R_I	Sensor Response to Laser Durring Calibration	$[V]$
r	Photodetector Radius	$[mm]$

T_A	Ratio of Final Beam Incident to Photodetector Surface	
T_F	Transmittance of Infra-Red (IR) Filter	
T_L	Transmittance of Collimating Lens	
T_S	Transmittance of Silicon Filter	
V_G	Sensor Gain Response Function	$[V/\mu W]$
w	Gaussian Beam Width	$[mm]$
x	Horizontal Positions Relative to Photodetector Center	$[mm]$
x_0	Horizontal Offset of Laser Beam Center	$[mm]$
x_{max}	Maximum Horizontal Edge of Photodetector	$[mm]$
x_{min}	Minimum Horizontal Edge of Photodetector	$[mm]$
y	Vertical Positions relative to Photodetector Center	$[mm]$
z	Width Factor Multiplier	

A.1 Methodology

A.1.1 Governing Equations

Two setups are employed for measurements. The first is an experimental setup at the HIFiRE Direct Connect Rig (HDCR) used to gather the intensity of the combustion chamber. The second is a calibration setup at the AFRL used to gather baseline power data and photodetector characteristics.

The photodetector sensors are calibrated using a tunable diode laser as a controlled input, with outputs recorded by a data acquisition board [8, 20]. An individual sensor is calibrated by passing a laser beam of known intensity through a collimating lens and an Infra-Red (IR) filter (in order to prevent amplifier saturation) onto the sensor surface as shown in Fig. A.1. The resulting incident power, “ P_I ,” is defined by Eq. A.1.

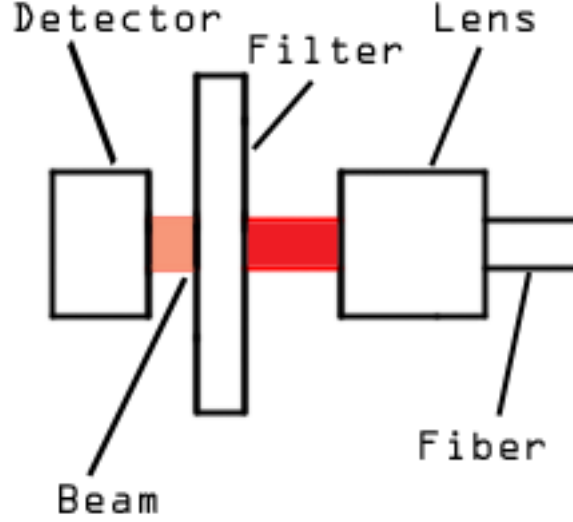


Figure A.1: Optical path of laser beam to photodetector, passing through a collimating lens and neutral-density filter.

$$P_I = P_B T_F T_L T_A \quad (\text{A.1})$$

The power measurement is translated into a voltage response, “ R_I ,” with a tunable gain, “ V_G ,” read by the data acquisition software as defined by Eq. A.2, and this equation can be combined with Eq. A.1 to calculate the gain function with Eq. A.3.

$$R_I = P_I V_G \quad (\text{A.2})$$

$$V_G = R_I / (P_B T_F T_L T_A) \quad (\text{A.3})$$

In the experimental setup, the photodetectors are aimed at the combustion flowfield at the exit of the HDCR combustion chamber. Silicon windows with a measurable transmittance, “ T_S ,” are placed between the combustion flowfield and the photodetectors with the purpose of protecting the photodetectors. The net power incident to and individual photodetector, “ P_E ,” is a combination of the filtered power from the

combustion flowfield, “ P_C ,” and the ambient power from the power of the combustion chamber, “ P_A ,” resulting in Eq. A.4.

$$P_E = P_C T_S + P_A \quad (\text{A.4})$$

Both the total incident power during the experiment and the ambient power to the sensor have measurable response functions as given by Eqs. A.5 and A.6, respectively.

$$R_E = P_E V_G \quad (\text{A.5})$$

$$R_A = P_A V_G \quad (\text{A.6})$$

Equations A.4, A.5, and A.6 can be combined into Eq. A.7 to calculate the unfiltered power from the combustion flowfield, which in turn, can be divided by the photodetector area, “ A ,” to calculate the unfiltered area-specific heat flux to the detector location as given by Eq. A.9.

$$P_C = \frac{R_E - R_A}{T_S V_G} \quad (\text{A.7})$$

$$F_C = P_C / A \quad (\text{A.8})$$

$$F_C = \frac{R_E - R_A}{T_S V_G A} \quad (\text{A.9})$$

A.1.2 Procedure

The laser beam power, “ P_B ,” is measured with a flux meter at two power settings with 40 measurements taken at the lower power setting and 35 measurements taken at a higher power setting. The beam power is assumed constant, whereas the mea-

measurements are assumed to have an error spread. Therefore, the mean measurements are found with 95% confidence intervals. The results are given in Table A.1.

All other measurements are assumed to be physically varying but with precise measurement points resulting in a PDF variation, which is assumed to be Gaussian.

The transmittance of the IR filter, “ T_F ,” is found by measuring the incident beam power to eight different sensors using the following filter combinations: no filter, filter 1, filter 2, and both filters, for a gain of 40 (normalized amplifier-specific scaling). The ratio of the filtered and unfiltered responses are taken as the transmittance. The silicon filter transmittance, “ T_S ,” is found in a similar manner. The results are given in Table A.1.

The collimating lens transmittance, “ T_L ,” is found by taking a measurement with and without the collimating lens. In these cases, a larger diameter photodetector is employed to insure that the sensor is receiving the total beam power within measurement reading error. The ratio of the lensed to the un-lensed beam measurements is taken as the transmittance.

The ratio of total beam power spread incident to the surface of the filter, “ T_A ,” is calculated with a two-step process. The first step involves incrementally taking measurements of the laser beam moving across the surface of the sensor in a radial fashion. These measurements are performed with two Gaussian beam spreads and self-normalized by their peak values taken with the beam at the center of the sensors. The Gaussian beam spreads are taken for a beam with a collimating lens and a beam coming off the raw fiber without a collimating lens. These measurements are taken for eight of the sixteen sensors. The results are given in Table A.1.

Based on the convolution of a Gaussian beam and circular photodetector, the total power incident to the surface can be given by Eq. A.10. The beam width, photodetector radius, and beam offset distance are given by “ w ,” “ r ,” and “ x_0 ,” respectively, as illustrated in Fig. A.2. In all cases, the laser beam is assumed to

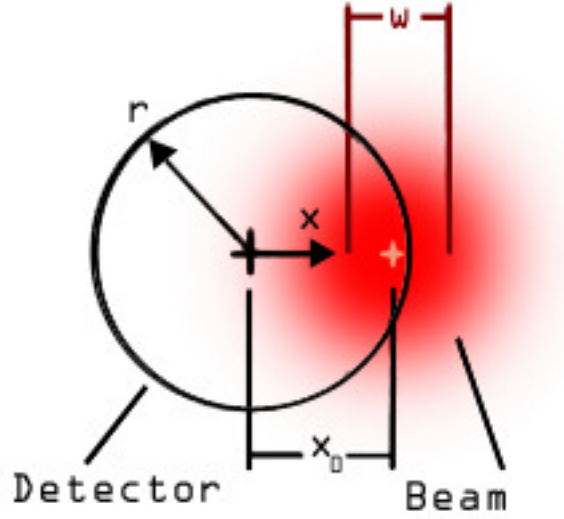


Figure A.2: Layout of photodetector of radius r and laser beam or half-width w offset by distance x_0

be Gaussian [31]. Additionally, a Gaussian width factor multiplier is defined by $z = 1/\sqrt{8 \ln 2}$.

When Eq. A.10 is calculated for two different beam widths and the beam offset value “ x_0 ” is swept across the photodetector, there is one value of “ x_0 ” for which the incident power will be identical. This location can be used to determine the detector width.

$$T_A = \int_{x_{min}(y)}^{x_{max}(y)} \int_{-r}^r \frac{\exp\left(-\frac{1}{2} \frac{(x-x_0)^2}{(zw)^2} - \frac{1}{2} \frac{y^2}{(zw)^2}\right)}{2\pi(zw)^2} dx dy \quad (\text{A.10})$$

With the photodetector radius known, the only remaining unknown is the beam width. The second step of the process is to calculate the beam width with a single-variable curve fit to the calibration data.

A.2 Results

The beam radius is found by sweeping the collimated and uncollimated beam over the edge of eight of the sensors, using 0.01mm step sizes and with a position accuracy of ± 0.001 mm. The sensor measurements are taken with variable gains with a measurement accuracy of 0.0217 V. As given in Fig. A.3, for the same detector with given beam widths, the values of normalized incident beam power will be identical for a one location regardless of beam width. The colored lines in Fig. A.3 are the experimental calibration data with each color corresponding to a different sensor. The point where the same colored lines intersect is the coalescing point discussed above. A series of mathematical solutions to Eq. A.10 are given in Fig. A.3 as a series of black lines, where each line represents a different beam width. The lines in Fig. A.3 (a) correspond to a detector radius of 1.13 mm, and the lines in Fig. A.3 (b) correspond to a detector radius of 1.15 mm. When the experimental measurements are compared to mathematical solutions, the experimental intersection point is found to be greater than that of a photodetector with a radius of 1.13 mm and less than that of a photodetector with a radius of 1.15 mm. A value of 1.14 mm is taken as nominal.

With the photodetector radius known, an additional set of experimental measurements are taken over the the horizontal centerline of eight of the sixteen photodetectors in order to determine the width of the collimated beam. In this setup, filter 1 and the collimating lens are used for all cases. As with the previous measurements, the accuracy of the horizontal position is known to within 0.001mm, and the accuracy of the response function is known to within 0.0217 V. The experimental measurements are self-normalized and given by the symbols in Fig. A.4. The lines in figure Fig. A.4 correspond to the self-normalized mathematical solutions to Eq. A.10. Each line indicates a different possible beam width ranging from a radius of 0.824 mm to 1.060 mm. For the purpose of comparison, the photodetector width, “ r ,” used in generating

Fig. A.4 (a) and (b), is 1.13 mm and 1.15 mm, respectively. Upon examination of the data-spreads, the beam width lies between 0.82 mm and 1.06 mm with a nominal value taken as 0.94 mm.

The total power to the sensor, “ P_I ,” can now be found for the setups with appropriate bounds. As an additional control, the laser power is varied between a high and low setting to insure that the full range of the photodetector response capabilities is being probed. These power levels are delimited with “High” and “Low.” In this case, the limits are found by choosing the either upper or lower limits of each factor going into the power equation (Eq. A.1) to maximize or minimize the cumulative effects of all uncertainties. The results are given in Table A.1

Table A.1: Nominal and upper and lower bound of measured variables

Quantity	Units	Nominal	Upper Bound	Lower Bound
$P_B(\text{High})$	μW	61.89	61.90	61.89
$P_B(\text{Low})$	μW	19.97	19.97	19.96
$T_F(1)$		0.512	0.522	0.502
$T_F(2)$		0.512	0.522	0.502
$T_F(1+2)$		0.263	0.284	0.243
T_L		0.969	0.975	0.963
T_A		0.983	0.996	0.957
r	mm	1.14	1.15	1.13
A	mm^2	4.08	4.15	4.01
w_0	mm	0.94	1.06	0.82
$P_I(\text{High})$	μW	30.18	31.36	28.64
$P_I(\text{Low})$	μW	9.74	10.12	9.24
T_S		0.545	0.576	0.515

In order to find the response function, “ V_G ,” the collimated beam is placed concentric with each of the sensors. The gains are varied from 20 to 120 in increments of 10. Both the high and low laser power signals are used. Filter 1 is used for low power situations. When the signals become saturated, an additional filter is used. It should be noted that the relative uncertainty from one filter is identical to the relative uncertainty from two filters. Therefore, a correction factor is used to put all

signals onto the same scale of one filter without changing the overall uncertainty of the system.

The results are fit with a least-squares regression for each sensor and both beam settings. The curve fits can now be normalized by the measured power. Given the maximum and minimum of different power normalizations for “ P_I ” and the predicted gains from both laser setups, there are four different response functions, “ V_G ,” that can be tried for each sensor. The results are given in Table A.2 for the corresponding sensor gain used in collecting the experimental data. Additionally, the raw responses for the experimental power and ambient power measurements, “ R_E ” and “ R_A ,” respectively, are given in Table A.2.

Table A.2: Possible limits of known gain functions with raw signal responses for each sensor.

Sensor	$V_G(\text{max})$ V/ μW	$V_G(\text{min})$ V/ μW	Gain	R_E V	R_A V
1	1.017×10^{-3}	9.231×10^{-4}	30	2.222	1.678
2	9.957×10^{-4}	9.064×10^{-4}	30	2.012	1.521
3	9.827×10^{-4}	8.836×10^{-4}	40	2.031	1.525
4	1.030×10^{-3}	9.345×10^{-4}	32	2.069	1.492
5	1.037×10^{-3}	9.324×10^{-4}	35	2.000	1.622
6	1.042×10^{-3}	9.449×10^{-4}	40	2.171	1.629
7	1.016×10^{-3}	9.247×10^{-4}	35	2.348	1.774
8	9.482×10^{-4}	8.644×10^{-4}	35	2.479	1.877
9	9.654×10^{-4}	8.653×10^{-4}	35	1.530	1.266
10	9.686×10^{-4}	8.410×10^{-4}	45	0.744	0.645
11	9.665×10^{-4}	8.375×10^{-4}	45	1.028	0.884
12	9.393×10^{-4}	8.451×10^{-4}	40	1.166	0.980
13	9.370×10^{-4}	8.334×10^{-4}	45	1.169	0.975
14	9.539×10^{-4}	8.571×10^{-4}	40	1.062	0.899
15	9.167×10^{-4}	8.309×10^{-4}	60	1.257	1.086
16	8.933×10^{-4}	8.121×10^{-4}	45	2.361	1.979

When the gains and response functions from Table A.2 are applied to Eq. A.5, the total power to the photodetectors during the experiment can be calculated, as is given in Table A.3 along with the overall sensor measurement error, which can be as

high as ± 7 %.

Table A.3: Radiative Power Values to the Photodetectors During the Experiment.

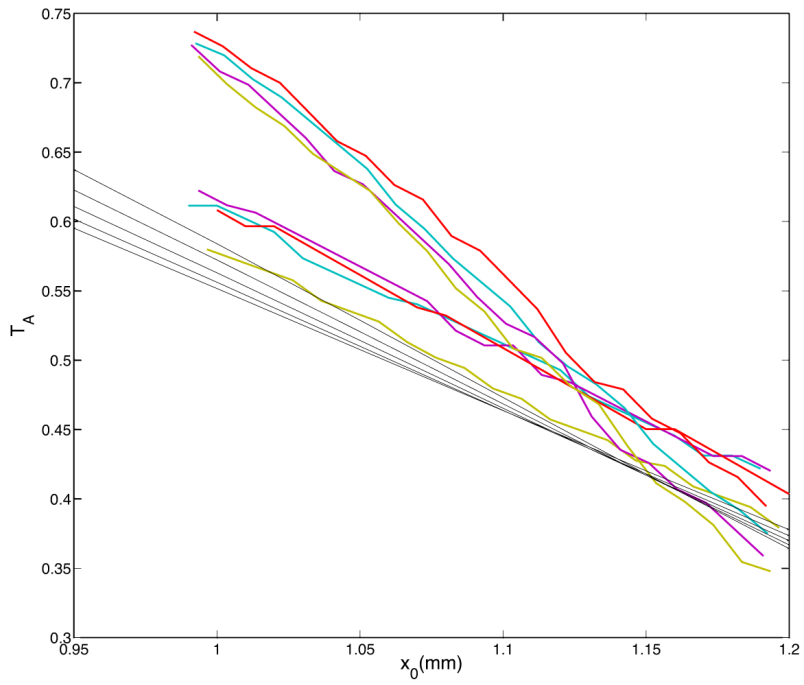
Sensor	$P_E(\text{max})$ μW	$P_E(\text{mean})$ μW	$P_E(\text{min})$ μW	Error ($\pm\text{frac}$)
1	82.91	79.08	75.25	0.0484
2	76.53	73.10	69.67	0.0469
3	59.05	56.07	53.09	0.0531
4	69.19	65.98	62.77	0.0486
5	68.61	65.16	61.72	0.0529
6	59.48	56.72	53.95	0.0488
7	74.65	71.30	67.95	0.0470
8	84.89	81.14	77.39	0.0462
9	52.83	50.09	47.35	0.0547
10	20.82	19.45	18.08	0.0705
11	28.50	26.60	24.69	0.0715
12	36.47	34.64	32.81	0.0528
13	33.14	31.31	29.48	0.0585
14	32.61	30.95	29.30	0.0535
15	26.22	24.99	23.76	0.0491
16	67.15	64.10	61.04	0.0476

In order to find the heat flux to the photodetector during the experiment, the values from Table A.3 are divided by the values of “ A ” from Table A.1, which garners a new range of possible heat fluxes. The additional uncertainty introduced by the area prediction increases the uncertainty to a range of ± 6 % to ± 9 %. The main value of interest is the unfiltered heat flux to the wall with the ambient measurements subtracted, resulting in the net heat radiative heat flux from the flame to the wall, as defined by Eq. A.9. When the response values in Table A.2 along with maximum associated gain functions are placed into Eq. A.9, and the maximum values of “ T_S ” and “ A ” are used from Table A.1, the minimum possible heat flux from the flowfield to the wall is given. Conversely, when the minimum associated gain functions from Table A.2 are use along with the minimum values of “ T_S ” and “ A ” from Table A.1, the maximum possible heat flux from the flowfield to the wall is given. The resulting

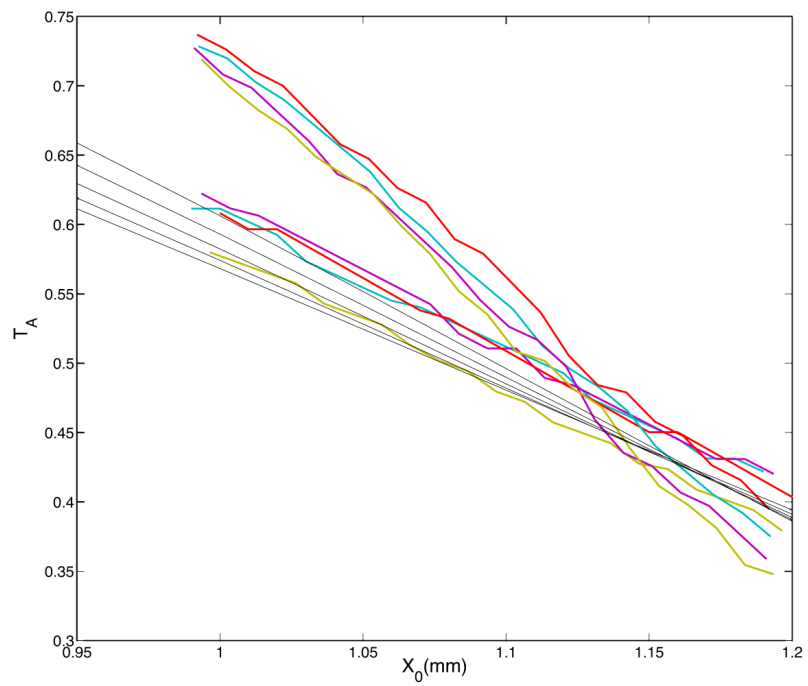
range of heat fluxes along with a mean value and a relative deviation are given in Table A.4.

Table A.4: Radiative Heat Flux Predictions to the wall during experiments.

Sensor	$F_C(\text{max})$ W/m^2	$F_C(\text{mean})$ W/m^2	$F_C(\text{min})$ W/m^2	Error ($\pm\text{frac}$)
1	9.50	8.47	7.44	0.121
2	8.74	7.81	6.87	0.120
3	6.93	6.16	5.38	0.126
4	8.22	7.33	6.44	0.121
5	8.07	7.17	6.27	0.126
6	6.94	6.19	5.44	0.122
7	8.57	7.66	6.74	0.120
8	9.63	8.61	7.58	0.119
9	4.22	3.74	3.26	0.137
10	1.27	1.11	0.95	0.143
11	1.85	1.62	1.38	0.144
12	2.66	2.37	2.07	0.126
13	2.51	2.22	1.93	0.131
14	2.31	2.05	1.79	0.126
15	1.66	1.48	1.30	0.122
16	5.06	4.51	3.97	0.120

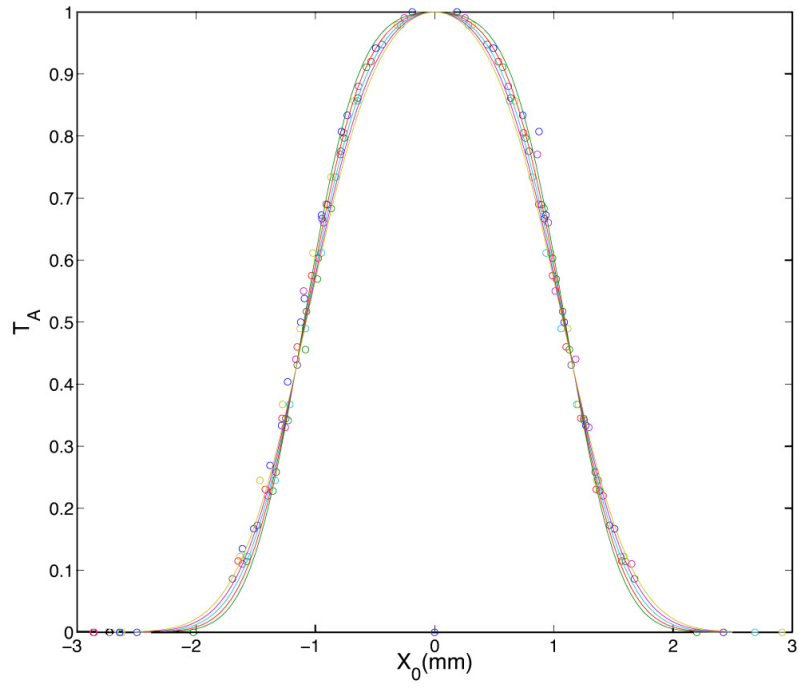


(a)

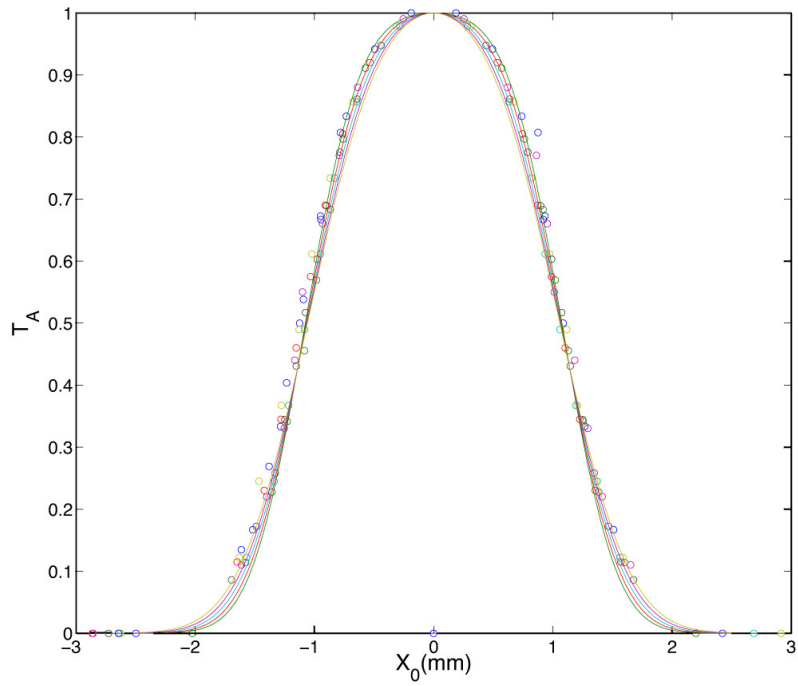


(b)

Figure A.3: Normalized incident power on a photodetectors vs. beam position for multiple beam widths for numerical data (black/thin) and experimental data (colored/thick). Numerical predictions correspond to a radius of a) 1.13 mm and b) 1.15 mm



a)



b)

Figure A.4: Normalized incident power on a photodetectors vs. beam position. Experimental data for multiple detectors given by symbols. Numerical predictions for multiple beam widths given by curves for a photodetector radius of (a) 1.13 mm and (b) 1.15 mm

APPENDIX B

Spectral Model Error Statistics

This appendix gives statistics on the error estimators for the two-point low-spectral-fidelity narrow-band spectral model developed in Section 4.2. The values for water vapor, carbon dioxide, the hydroxyl radical, carbon monoxide, and methane are given in Tables B.1, B.2, B.3, B.4, and B.5, respectively.

B.1 Spectral Model Statistics Error Tables

Table B.1: Statistics of error predictor E_{ν_2} for water vapor at a partial pressure 1 atm (101.325 kPa) for various path lengths and temperatures.

Temperature (K)	Path Length (m)	Max	Mean	Standard Deviation
500	0.001	0.25	6.35×10^{-3}	0.02
500	0.01	0.23	1.02×10^{-2}	0.03
500	0.1	0.81	2.70×10^{-2}	0.07
500	1	0.99	6.76×10^{-2}	0.13
1000	0.001	0.16	2.72×10^{-3}	0.01
1000	0.01	0.15	5.69×10^{-3}	0.02
1000	0.1	0.40	1.78×10^{-2}	0.05
1000	1	0.94	5.46×10^{-2}	0.12
1500	0.001	0.17	1.58×10^{-3}	0.01
1500	0.01	0.17	2.98×10^{-3}	0.01
1500	0.1	0.29	1.30×10^{-2}	0.04
1500	1	0.98	3.82×10^{-2}	0.08
2000	0.001	0.17	1.22×10^{-3}	0.01
2000	0.01	0.17	1.79×10^{-3}	0.01
2000	0.1	0.21	7.96×10^{-3}	0.03
2000	1	0.64	2.62×10^{-2}	0.06
2500	0.001	0.17	1.07×10^{-3}	0.01
2500	0.01	0.17	1.29×10^{-3}	0.01
2500	0.1	0.17	4.41×10^{-3}	0.02
2500	1	0.43	1.71×10^{-2}	0.04
3000	0.001	0.17	1.00×10^{-3}	0.01
3000	0.01	0.17	1.07×10^{-3}	0.01
3000	0.1	0.16	2.79×10^{-3}	0.01
3000	1	0.26	1.12×10^{-2}	0.03

Table B.2: Statistics of error predictor E_{ν_2} for carbon dioxide at a partial pressure 1 atm (101.325 kPa) for various path lengths and temperatures.

Temperature (K)	Path Length (m)	Max	Mean	Standard Deviation
500	0.001	0.84	1.07×10^{-2}	0.05
500	0.01	0.74	1.77×10^{-2}	0.06
500	0.1	2.52	2.43×10^{-2}	0.14
500	1	2.52	3.82×10^{-2}	0.15
1000	0.001	0.66	5.77×10^{-3}	0.04
1000	0.01	0.81	1.03×10^{-2}	0.06
1000	0.1	0.84	1.27×10^{-2}	0.06
1000	1	8.16	4.66×10^{-2}	0.42
1500	0.001	0.37	3.69×10^{-3}	0.03
1500	0.01	1.01	7.25×10^{-3}	0.06
1500	0.1	0.56	7.88×10^{-3}	0.04
1500	1	3.37	2.79×10^{-2}	0.18
2000	0.001	0.30	2.81×10^{-3}	0.02
2000	0.01	0.91	5.68×10^{-3}	0.05
2000	0.1	0.68	6.40×10^{-3}	0.04
2000	1	1.77	1.88×10^{-2}	0.11
2500	0.001	0.30	2.46×10^{-3}	0.02
2500	0.01	0.64	4.57×10^{-3}	0.04
2500	0.1	0.99	6.35×10^{-3}	0.05
2500	1	1.63	1.71×10^{-2}	0.11
3000	0.001	0.30	2.31×10^{-3}	0.02
3000	0.01	0.41	3.72×10^{-3}	0.03
3000	0.1	1.22	6.22×10^{-3}	0.06
3000	1	1.22	1.38×10^{-2}	0.09

Table B.3: Statistics of error predictor E_{ν_2} for the hydroxyl radical at a partial pressure 1 atm (101.325 kPa) for various path lengths and temperatures.

Temperature (K)	Path Length (m)	Max	Mean	Standard Deviation
500	0.001	1.00	1.44×10^{-2}	0.06
500	0.01	1.00	1.38×10^{-2}	0.06
500	0.1	1.00	1.72×10^{-2}	0.08
500	1	1.02	2.82×10^{-2}	0.12
1000	0.001	0.22	8.89×10^{-3}	0.03
1000	0.01	0.22	6.27×10^{-3}	0.02
1000	0.1	0.22	6.77×10^{-3}	0.02
1000	1	1.02	2.43×10^{-2}	0.11
1500	0.001	0.27	4.59×10^{-3}	0.02
1500	0.01	0.27	4.22×10^{-3}	0.02
1500	0.1	0.27	5.28×10^{-3}	0.02
1500	1	0.93	2.39×10^{-2}	0.11
2000	0.001	0.28	4.12×10^{-3}	0.02
2000	0.01	0.28	3.91×10^{-3}	0.02
2000	0.1	0.28	4.89×10^{-3}	0.02
2000	1	0.75	2.39×10^{-2}	0.10
2500	0.001	0.29	3.67×10^{-3}	0.02
2500	0.01	0.29	3.58×10^{-3}	0.02
2500	0.1	0.29	4.47×10^{-3}	0.02
2500	1	0.60	2.23×10^{-2}	0.09
3000	0.001	0.29	3.67×10^{-3}	0.02
3000	0.01	0.29	3.44×10^{-3}	0.02
3000	0.1	0.33	5.02×10^{-3}	0.02
3000	1	0.51	1.99×10^{-2}	0.07

Table B.4: Statistics of error predictor E_{ν_2} for carbon monoxide at a partial pressure 1 atm (101.325 kPa) for various path lengths and temperatures.

Temperature (K)	Path Length (m)	Max	Mean	Standard Deviation
500	0.001	0.93	1.57×10^{-2}	0.09
500	0.01	2.16	4.25×10^{-2}	0.25
500	0.1	1.82	3.60×10^{-2}	0.18
500	1	2.18	8.41×10^{-2}	0.33
1000	0.001	1.00	1.93×10^{-2}	0.10
1000	0.01	2.78	6.72×10^{-2}	0.36
1000	0.1	3.38	8.79×10^{-2}	0.38
1000	1	3.29	1.16×10^{-1}	0.43
1500	0.001	0.57	1.47×10^{-2}	0.07
1500	0.01	2.43	6.70×10^{-2}	0.33
1500	0.1	3.79	1.26×10^{-1}	0.52
1500	1	2.96	1.36×10^{-1}	0.46
2000	0.001	0.42	1.40×10^{-2}	0.06
2000	0.01	2.14	6.21×10^{-2}	0.30
2000	0.1	3.96	1.48×10^{-1}	0.61
2000	1	4.16	1.60×10^{-1}	0.50
2500	0.001	1.00	1.38×10^{-2}	0.07
2500	0.01	1.89	5.74×10^{-2}	0.26
2500	0.1	3.96	1.63×10^{-1}	0.65
2500	1	4.50	1.83×10^{-1}	0.54
3000	0.001	0.30	9.14×10^{-3}	0.04
3000	0.01	1.68	5.23×10^{-2}	0.23
3000	0.1	3.89	1.69×10^{-1}	0.66
3000	1	4.70	2.09×10^{-1}	0.58

Table B.5: Statistics of error predictor E_{ν_2} for methane at a partial pressure of 1 atm (101.325 kPa) for various path lengths and temperatures.

Temperature (K)	Path Length (m)	Max	Mean	Standard Deviation
500	0.001	0.51	1.22×10^{-2}	0.05
500	0.01	1.99	4.91×10^{-2}	0.22
500	0.1	2.05	6.42×10^{-2}	0.21
500	1	5.46	1.31×10^{-1}	0.42
1000	0.001	0.21	4.43×10^{-3}	0.01
1000	0.01	0.80	1.97×10^{-2}	0.08
1000	0.1	3.17	6.01×10^{-2}	0.25
1000	1	3.68	1.01×10^{-1}	0.29
1500	0.001	0.23	2.48×10^{-3}	0.01
1500	0.01	0.33	7.75×10^{-3}	0.03
1500	0.1	2.31	4.18×10^{-2}	0.18
1500	1	3.75	8.92×10^{-2}	0.29
2000	0.001	0.24	1.93×10^{-3}	0.01
2000	0.01	0.24	3.50×10^{-3}	0.01
2000	0.1	0.92	1.79×10^{-2}	0.07
2000	1	4.08	8.03×10^{-2}	0.32
2500	0.001	0.25	2.32×10^{-3}	0.02
2500	0.01	0.25	2.30×10^{-3}	0.01
2500	0.1	0.29	7.08×10^{-3}	0.03
2500	1	2.21	4.36×10^{-2}	0.17
3000	0.001	0.25	1.81×10^{-3}	0.01
3000	0.01	0.25	1.91×10^{-3}	0.01
3000	0.1	0.25	3.50×10^{-3}	0.01
3000	1	0.86	1.83×10^{-2}	0.07

BIBLIOGRAPHY

BIBLIOGRAPHY

- [1] Douglas Adams. *Life, The Universe, and Everything*. 1982.
- [2] Air Force Research Laboratory. X-51a flight ends prematurely, <http://www.af.mil/news/story.asp?id=123314425>, August 2012.
- [3] John D. Anderson. *Modern Compressible Flow: With Historical Perspective*. McGraw Hill, New York, 3rd edition, 2002.
- [4] Gal Berkooz, Philip Holmes, and John L. Lumley. The proper orthogonal decomposition in the analysis of turbulent flows. *Annual Review of Fluid Mechanics*, 25:539–575, 1993.
- [5] Russell R. Boyce, Sullivan Gerard, and Allan Paull. The HyShot scramjet flight experiment- flight data and CFD calculations compared. Number 2003-7029 in 12th AIAA International Space Planes and Hypersonic Systems and Technologies, Norfolk, VA, 2003. AIAA.
- [6] Russell R. Boyce and Allan Paull. Scramjet intake and exhaust CFD studies for the HyShot scramjet flight experiment. Number 2001-1891 in 10th international Space Planes and Hypersonic Systems and Technologies Conference, Kyoto, Japan, April 2001. AIAA.
- [7] Michael S. Brown. Private communication. February 2013.
- [8] Michael S. Brown, Gregory C. Herring, Karen Cabell, Neal Hass, Todd F. Barhorst, and Mark R. Gruber. Optical measurements at the combustor exit of the HIFiRE 2 ground test engine. Number 2012-0857 in 50th AIAA Aerospace Sciences Meeting including the New Horizons Forum and Aerospace Exposition, Nashville, Tennessee, January 2012. AIAA.
- [9] Jonathan M. Burt, Evgeny Titov, and Eswar Josyula. Sensitivity analysis and uncertainty quantification for a set of hypersonic shock interaction flows. Number 2012-3100 in 43rd AIAA Thermophysics Conference, New Orleans, LA, June 2012. AIAA.
- [10] Michael D. Bynum and Robert A. Baurle. A design of experiments study for the HIFiRE flight 2 ground test computational fluid dynamics results. Number 2011-2203 in 17th AIAA International Space Planes and Hypersonic Systems and Technologies Conference, San Francisco, CA, April 2011. AIAA.

- [11] Karen Cabell, Neal E. Hass, Andrea M. Storch, and Mark R. Gruber. Hi-FiRE direct-connect rig (HDCR) phase 1 scramjet test results from the NASA Langley arc-heated scramjet test facility. Number 2011-2248 in 17th AIAA International Space Planes and Hypersonic Systems and Technologies Conference, San Francisco, CA, April 2011. AIAA.
- [12] Yunus A. Çengel and Michael A. Boles. *Thermodynamics an Engineering Approach*. McGraw Hill, New York, 4th edition, 2002.
- [13] S. Chandrasekhar. *Radiative Transfer*. Dover Publications Inc, New York, 1960.
- [14] M. Cherkaoui, J. L. Dufresne, Richard Fournier, J. Y. Grandpeix, and A. Lallec. Monte Carlo simulation of radiation in gases with a narrow-band model and a net-exchange formulation. *Journal of Heat Transfer*, 118:401–407, May 1996.
- [15] Pedro J. Coelho. Numerical simulation of the interaction between turbulence and radiation in reactive flows. *Progress in Energy and Combustion Science*, 33:311–383, January 2007.
- [16] Pedro J. Coelho. Turbulence–radiation interaction: From theory to application in numerical simulations. *Journal of Heat Transfer*, 134, March 2012.
- [17] Pedro J. Coelho, P. Perez, and Mouna El Hafi. Benchmark numerical solutions for radiative heat transfer in two-dimensional axisymmetric enclosures with nongray sooting media. *Numerical Heat Transfer, Part B*, 43(5):425–444, 2003.
- [18] Meredith B. Colket and Louise J. Spadaccini. Scramjet fuels autoignition study. *Journal of Propulsion and Power*, 17(2):315–327, 2001.
- [19] Andrew J. Crow. Eyes of solace, www.mildlymiffed.com, April 2012.
- [20] Andrew J. Crow, Iain D. Boyd, Michael S. Brown, and Jiwen Liu. Thermal radiative analysis of the HiFiRE-2 scramjet engine. Number 2012-2751 in 43rd AIAA Thermophysics Conference, New Orleans, LA, June 2012. AIAA.
- [21] Andrew J. Crow, Iain D. Boyd, and Vincent E. Terrapon. Radiation modeling of a hydrogen-fueled scramjet. Number 2011-3769 in 42nd AIAA Thermophysics Conference, Honolulu, HI, June 2011. AIAA.
- [22] Andrew J. Crow, Iain D. Boyd, and Vincent E. Terrapon. Radiation modeling of a hydrogen fueled scramjet. *Journal of Thermophysics and Heat Transfer*, 27(1):11–21, January 2013.
- [23] Albert Einstein. Über einen die erzeugung und verwandlung des lichtet betreffenden heuristischen gesichtspunkt (Concerning an heuristic point of view toward the emission and transformation of light). *Annalen der Physik*, 322(6):132–148, 1905.

- [24] M . S. Eldred, L. P. Swiller, and G. Tang. Mixed aleatory-epistemic uncertainty quantification with stochastic expansions and optimization based interval estimation. *Reliability Engineering and System Safety*, 96:1092–1113, 2011.
- [25] Shelly M. Ferlemann, Charles R. McClinton, Ken E. Rock, and Randy T. Voland. Hyper-X Mach 7 scramjet design, ground test and flight results. Number 2005-3322 in 13th International Space Plane and Hypersonics Systems and Technologies, Capua, Italy, May 2005. AIAA.
- [26] Krzysztof J. Fidkowski and David L. Darmofal. Output-based error estimation and mesh adaptation in computational fluid dynamics: Overview and recent results. Number 2009-1303 in 47th AIAA Aerospace Sciences Meeting Including The New Horizons Forum and Aerospace Exposition, Orlando, FL, January, 2009. AIAA.
- [27] Krzysztof J. Fidkowski, Marco A. Ceze, and Philip L. Roe. Entropy-based drag-error estimation and mesh adaptation in two dimensions. *Journal of Aircraft*, 49(5):1485–1496, 2012.
- [28] W. A. Fiveland. Discrete ordinate methods for radiative heat transfer in isotropically and anisotropically scattering media. *Journal of Heat Transfer*, 109(3):809–812, August, 1987.
- [29] W. A. Fiveland. Three-dimensional radiative heat-transfer solutions three-dimensional radiative heat-transfer solutions by the discrete-ordinates method. *Journal of Thermophysics and Heat Transfer*, 2(4):309–316, October, 1988.
- [30] J. A. Fleck and J. D. Cummings. An implicate Monte Carlo scheme for calculating time and frequency dependent nonlinear radiation transport. *Journal of Computational Physics*, 8:313–342, 1971.
- [31] Grant. R Fowles. *Introduction to Modern Optics*. Dover Publications Inc, New York, 2nd edition, 1975.
- [32] Ronald S. Fry. A century of propulsion technology evolution. *Journal of Propulsion and Power*, 20(1):27–58, 2004.
- [33] A. D. Gardner, Klaus Hannemann, and Johan Steelant. Post flight analysis of the HyShot supersonic combustion flight experiment in HEG. Number 2005ESASP.563..563G in Fifth European Symposium on Aerothermodynamics for Space Vehicles, Cologne, Germany, November 2005. European Space Agency.
- [34] S. Ghosh, R. Friedrich, M. Pfitzner, Chr. Stemmer, B. Cuenot, and Mouna El Hafi. Effects of radiative heat transfer on the structure of turbulent supersonic channel flow. *Journal of Fluid Mechanics*, 677:417–444, 2011.
- [35] R. Gonçaves, M. Lecanu, S. Ducruix, O. Gicquel, E. Iacona, and D. Veynante. Coupled large eddy simulations of turbulent combustion and radiative heat transfer. *Combustion and Flame*, 152(3):387–400, 2008.

- [36] Richard M. Goody and Yuk L. Yung. *Atmospheric Radiation Theoretical Basis*. Oxford University Press, New York, 2nd edition, 1989.
- [37] Vincent Goutiere, Fengshan Liu, and Andre Charette. An assessment of real-gas modeling in 2D enclosures. *Journal of Quantitative Spectroscopy and Radiative Transfer*, 64:299–326, 2000.
- [38] William L. Grosshandler. Radiative heat transfer in nonhomogeneous gases: A simplified approach. *International Journal of Heat and Mass Transfer*, 23:1447–1459, 1980.
- [39] Mark R. Gruber, Stephen Smith, and Turun Mathur. Experimental characterization of hydrocarbon-fueled, axisymmetric, scramjet combustor flowpaths. Number 2011-2311 in 17th AIAA International Space Planes and Hypersonic Systems and Technologies Conference, San Francisco, CA, April 2011. AIAA.
- [40] Joseph M. Hank, James S. Murphy, and Richard C. Mutzman. The X-51a scramjet engine flight demonstration program. Number 2008-2540 in 15th AIAA International Space Planes and Hypersonic Systems and Technologies Conference, Dayton, OH, April 2008. AIAA.
- [41] J. M. Hartmann, R. Levi Di Leon, and Jean Taine. Line-by-line and narrow-band statistical model calculations for H₂O. *Journal of Quantitative Spectroscopy and Radiative Transfer*, 32(2):119–127, 1984.
- [42] D. B. Helmer, L. M. Campo, and J. K. Eaton. Three-dimensional features of a Mach 2.1 shock/boundary layer interaction. *Experimental Fluids*, 53:1347–1368, 2012.
- [43] Robert W. Higgins and Constantine C. Pappas. An experimental investigation of the effects of surface heating on boundary-layer transition on a flat plate in supersonic flow. Technical Note NACA TN 2351, National Advisory Committee for Aeronautics, Moffett Field, CA, April 1951.
- [44] Charles Hirsch. *Numerical Computation of Internal & External Flows*. Butterworth-Heinemann, Oxford, UK, 2nd edition, 2007.
- [45] H. B. Hopkins, W. Konopka, and J. Leng. Validation of scramjet exhaust simulation technique. Technical Report CR-2688, NASA Langley Research Center, June 1976.
- [46] Xianglei Huang, John Farrara, Stephen S. Leroy, Yuk L. Yung, and Richard M. Goody. Cloud variability as revealed in outgoing infrared spectra: Comparing model to observation with spectral eof analysis. *Geophysical Research Letters*, 29(8), 2002.
- [47] Ronald L. Iman and Jon C. Helton. An investigation of uncertainty and sensitivity analysis techniques for computer models. *Risk Analysis*, 8(1):71–90, 1988.

- [48] Frank P. Incropera and David P. Dewitt. *Fundamentals of Heat and Mass Transfer*. John Wiley & Sons, Hoboken, NJ, 5th edition, 2002.
- [49] A. Ingenito, C. Bruno, and D. Cecere. LES of the HyShot scramjet combustor. Number 2010-758 in 48th AIAA Aerospace Sciences Meeting Including the New Horizons Forum and Aerospace Exposition, Orlando, FL, January 2010. AIAA.
- [50] Adam Irvine. *High Fidelity Radiative Thermal Transport Simulations of a Scramjet Propulsion System*. PhD thesis, University of Michigan, Ann Arbor, MI, 2013.
- [51] Kevin R. Jackson, Mark R. Gruber, and Todd Barhorst. The HIFiRE flight 2 experiment: An overview and status update. Number 2009-5029. AIAA, 2009.
- [52] Kevin R. Jackson, Mark R. Gruber, and Salvatore Buccellato. HIFiRE flight 2 overview and status update 2011. Number 2011-2202 in 17th AIAA International Space Planes and Hypersonic Systems and Technologies Conference, San Francisco, CA, April 2011. AIAA.
- [53] Kirk A. Jensen, Jean-Francois Ripoll, Alan A. Wray, David Joseph, and Mouna El Hafi. On various modeling approaches to radiative heat transfer in pool fires. *Combustion and Flame*, 148:263–279, January 2007.
- [54] David Joseph, Mouna El Hafi, Richard Fournier, and Bénédicte Cuenot. Comparison of three spatial differencing schemes in discrete ordinates methods using three-dimensional unstructured meshes. *International Journal of Thermal Sciences*, 44:851–864, April, 2005.
- [55] David Joseph, Patrice Perez, Mouna El Hafi, and Bénédicte Cuenot. Discrete ordinates and Monte Carlo methods for radiative transfer simulation allied to computational fluid dynamics combustion modeling. *Journal of Heat Transfer*, 131(052701):052701–1 052701–9, May 2009.
- [56] Sebastian Karl, Klaus Hannemann, Andreas Mack, and Johan Steelant. CFD analysis of the HyShot II scramjet experiment in the HEG shock tunnel. Number 2008-2548 in 15th AIAA International Space Planes and Hypersonic Systems and Technologies Conference, Dayton, OH, January, 2008. AIAA.
- [57] Nuray Kayakol, Nevin Selçuk, Ian Cambell, and Ömer L. Gülder. Performance of discrete ordinates method in a gas turbine combustor simulator. *Experimental Thermal and Fluid Science*, 21:134–141, 2000.
- [58] Yaser Khalighi, Joseph W. Nicholes, Snjiva K. Lele, Frank Ham, and Parviz Moin. Unstructured large eddy simulation for prediction of noise issued from turbulent jets in various configurations. Number 2011-2886 in 17th AIAA/CEAS Aeroacoustics Conference (32nd AIAA Aeroacoustics Conference), Portland, OR, June 2011. AIAA.

- [59] Andrew A. Lacis and Valdar Oinas. A description of the correlated k distribution method for modeling nongray gaseous absorption, thermal emission, and multiple scattering in vertically inhomogeneous atmospheres. *Journal of Geophysical Research*, 96(D5):9027–9063, May 1991.
- [60] Edward W. Larsen. Analysis of a Monte Carlo method for nonlinear radiative transfer. *Journal of Computational Physics*, 71:50–64, 1987.
- [61] Johan Larsson. Large eddy simulation of the HyShot II scramjet combustor using a supersonic flamelet model. Number 2012-4261 in 48th AIAA/ASME/SAE/ASEE Joint Propulsion Conference & Exhibit, Atlanta, GA, July 2012. AIAA.
- [62] Chung K Law. *Combustion Physics*. Cambridge University Press, New York, 2006.
- [63] Arthur H Lefebvre. Flame radiation in gas turbine combustion chambers. *International Journal of Heat and Mass Transfer*, 27(9):493–1510, 1984.
- [64] George H. Lindquist and F. S. Simmons. A band model formulation for very nonuniform paths. *Journal of Quantitative Spectroscopy and Radiative Transfer*, 12:807–820, 1972.
- [65] K. N. Liou. *An Introduction to Atmospheric Radiation*. Academic Press, San Diego, 2nd edition, 2002.
- [66] Fengshan Liu, Gregory J. Smallwood, and Ömer L. Gülder. Application of the statistical narrow-band correlated-k method to low-resolution spectral intensity and radiative heat transfer calculations - effects of the quadrature scheme. *International Journal of Heat and Mass Transfer*, 43:3119–3135, 2000.
- [67] Fengshan Liu, Gregory J. Smallwood, and Ömer L. Gülder. Application of the statistical narrow-band correlated-k method to non-grey gas radiation in CO₂-H₂O mixtures: Approximate treatments of overlapping bands. *Journal of Quantitative Spectroscopy and Radiative Transfer*, 68:401–417, 2001.
- [68] Jiwen Liu. *GRASP: A General Radiation Simulation Program User's Manual*. Engineering Sciences Inc., WPAFB, OH 45433-0630, 2nd (2.0) edition, December, 1997.
- [69] Jiwen Liu and Michael S. Brown. Radiative heating in hydrocarbon-fueled scramjet engines. Number 2012-3775 in 48th AIAA/ASME/SAE/ASEE Joint Propulsion Conference & Exhibit, Atlanta, GA, July 2012. AIAA.
- [70] Jiwen Liu and Mark R. Gruber. Preliminary preflight CFD study on the HI-FiRE flight 2 experiment. Number 2011-2204 in 17th AIAA International Space Planes and Hypersonic Systems and Technologies Conference, San Francisco, CA, April 2011. AIAA.

- [71] Jiwen Liu and S. N. Tiwari. Investigation of radiative transfer in nongray gases using a narrow band model and Monte Carlo simulation. *Transactions of the ASME*, 116:160–166, February 1994.
- [72] Jiwen Liu and S. N. Tiwari. Radiative heat transfer effects in chemically reacting nozzle flow. *Journal of Thermophysics and Heat Transfers*, 10(3):436–444, 1996.
- [73] LinHua Liu, HePing Tan, and ZhiHong He. Inverse radiation problem of source term in three-dimensional complicated geometric semitransparent media. *International Journal of Thermal Sciences*, 40(6):528–538, 2001.
- [74] C. B. Ludwig, W. Malkmus, J. E. Reardon, and J. A. L. Thomson. Handbook of infrared radiation from combustion gases. Technical Report SP-3080, NASA, 1973.
- [75] Michael F. Modest. *Radiative Heat Transfer*. Academic Press, San Diego, 2nd edition, 2003.
- [76] Michael F. Modest and Robert J. Riazzi. Assembly of full-spectrum k-distributions from a narrow-band database; effects of mixing gases, gases and nongray absorbing particles, and mixtures with nongray scatterers in nongray enclosures. *Journal of Quantitative Spectroscopy and Radiative Transfer*, 90:169–189, 2005.
- [77] H. F. Nelson. Radiative heating in scramjet combustors. *Journal of Thermophysics and Heat Transfer*, 11(1):59–64, 1997.
- [78] Gopalendu Pal and Michael F. Modest. A narrow band-based multiscale multi-group full-spectrum k-distribution method for radiative transfer in nonhomogeneous gas-soot mixtures. *Journal of Heat Transfer*, 132, February 2010.
- [79] Gopalendu Pal, Michael F. Modest, and Liangyu Wang. Hybrid full-spectrum correlated k-distribution method for radiative transfer in nonhomogeneous gas mixtures. *Journal of Heat Transfer*, 130, August 2008.
- [80] Gerald L. Pellett, Sarah N. Vaden, and Lloyd G. Wilson. Opposed jet burner extinction limits: Simple mixed hydrocarbon scramjet fuels vs air. Number 2007-5664 in 43rd AIAA/ASME.SAE/ASEE Joint Propulsion Conference and Exhibit, Cincinnati, OH, July 2007. AIAA.
- [81] René Pečnik, Vincent E. Terrapon, Frank Ham, Gianluca Iaccarino, and Heinz Pitsch. Reynolds-averaged navier-stokes simulations of the HyShot II scramjet. *AIAA Journal*, 50(8):1717–1732, August 2012.
- [82] Charles D. Pierce and Parviz Moin. Progress-variable approach for large-eddy simulation of non-premixed turbulent combustion. *Journal of Fluid Mechanics*, 504:73–97, 2004.

- [83] Laurent Pierrot, Anouar Soufaiani, and Jean Taine. Accuracy of narrow-band and global models for radiative transfer in H₂O, CO₂, and H₂O-CO₂ mixtures at high temperature. *Journal of Quantitative Spectroscopy and Radiative Transfer*, 62:523–548, 1999.
- [84] Max Planck. *The Theory of Heat Radiation*. Dover Publications Inc, New York, 2nd edition, 1991.
- [85] Stephen B. Pope. *Turbulent Flows*. Cambridge University Press, New York, 2000.
- [86] R. Porter, F Liu, M. Pourkashanian, A. Williams, and D. Smith. Evaluation of solution methods for radiative heat transfer in gaseous oxy-fuel combustion environments. *Journal of Quantitative Spectroscopy and Radiative Transfer*, 111:2084–2094, 2010.
- [87] G. D. Raithby and E. H. Chui. A finite-volume method for predicting a radiant heat transfer in enclosures with participating media. *Journal of Heat Transfer*, 112:415–423, May 1990.
- [88] R. A Reed and M. W. Slack. Infrared measurements of a scramjet exhaust. Technical Report CR-3242, NASA Langley Research Center, January 1980.
- [89] P. H. Rivière, S. Langlois, Anouar Soufaiani, and Jean Taine. An approximate data base of H₂O infrared lines for high temperature applications at low resolution statistical narrow-band model parameters. *Journal of Quantitative Spectroscopy and Radiative Transfer*, 53(2):221–234, 1995.
- [90] P. J. Roache. Quantification of uncertainty in computational fluid dynamics. *Annual Review of Fluid Mechanics*, 29:123–160, 1997.
- [91] L. S. Rothman. The HITRAN 2004 molecular spectroscopic database. *Journal of Quantitative Spectroscopy and Radiative Transfer*, 96:139–204, 2005.
- [92] L. S. Rothman, I. E. Gordon, R. J. Barberand H. Dothe, R. R. Gamache, A. Goldman, V. I. Perevalov, S. A. Tashkun, and J. Tennyson. HiTemp, the high-temperature molecular spectroscopic database. *Journal of Quantitative Spectroscopy and Radiative Transfer*, 111:2139–2150, 2010.
- [93] Christopher J. Roy and William L. Oberkampf. A complete framework for verification, validation, and uncertainty quantification in scientific computing. Number 2010-124 in 48th AIAA Aerospace Sciences Meeting Including the New Horizons Forum and Aerospace Exposition, Orlando, FL, January 2010. AIAA.
- [94] Vladimir V. Rozanov and Alexei V. Rozanaov. Generalized form of the direct and adjoint radiative transfer equations. *Journal of Quantitative Spectroscopy and Radiative Transfer*, 104:155–170, 2007.

- [95] Carlos T. Salinas. Inverse radiation analysis in two-dimensional gray media using discrete ordinates method with a multidimensional scheme. *International Journal of Thermal Sciences*, 49(2):302–310, 2010.
- [96] Jan Martinez Schramm, Sebastian Karl, and Johan Steelant. Ground testing of the HyShot II scramjet configuration in HEG. Number 2008-2547 in 15th AIAA International Space Planes and Hypersonic Systems and Technologies Conference, Dayton, OH, May 2008. AIAA.
- [97] Yohann Scribano, Nir Goldman, R. J. Saykally, and Claude Leforestier. Water dimers in the atmosphere III: Equilibrium constant from a flexible potential. *Journal of Physical Chemistry*, 110:5411–5419, 2006.
- [98] L. Sirovich. Chaotic dynamics of coherent structures. *Physica D*, 37:126–145, 1989.
- [99] Michael K. Smart. Scramjets. In *Papers Presented During the AVT-150 RTO AVT/VKI Lecture Series*, RTO-EN-AVT-150 - Advances on Propulsion Technology for High-Speed Aircraft, pages 9–1–9–38, Genèse, Belgium, March 2007. NATO Science and Technology Organization.
- [100] Michael K. Smart, Neal E. Hass, and Allan Paull. Flight data analysis of the HyShot 2 scramjet flight experiment. *AIAA Journal*, 44(10):2366–2375, October 2006.
- [101] Anouar Soufaini and E. Djavdan. A comparison between weighted sum of gray gases and statistical narrow-band radiation models for combustion applications. *Combustion and Flame*, 97:240–2540, 1994.
- [102] Anouar Soufaini, J. M. Hartmann, and Jean Taine. Validity of band-model calculations for CO₂ and H₂O applied to radiative properties and conducting-radiative transfer. *Journal of Quantitative Spectroscopy and Radiative Transfer*, 32(2):243–257, 1985.
- [103] Anouar Soufaini and Jean Taine. High temperature gas radiative property parameters of statistical narrow-band model for H₂O, CO₂, and CO, and correlated-k model for H₂O and CO₂. *International Journal of Heat and Mass Transfer*, 40(4):987–991, 1997.
- [104] Andrea M. Storch, Michael Bynum, Jiwen Liu, and Mark R. Gruber. Combustor operability and performance verification for HIFiRE flight 2. Number 2011-2249 in 17th AIAA International Space Planes and Hypersonic Systems and Technologies Conference, San Francisco, CA, April 2011. AIAA.
- [105] Jochen Ströhle and Pedro J. Coelho. On the application of the exponential wide band model to the calculation of radiative heat transfer in one- and two-dimensional enclosures. *International Journal of Heat and Mass Transfer*, 45:2129–2139, 2002.

- [106] L. P. Swiller and A. A. Giunta. Aleatory and epistemic uncertainty quantification for engineering applications. Technical Report SAND2007-2670C, Sandia National Laboratory, Albuquerque, NM, July 2007.
- [107] Arthur C. Taylor III, Gene W. Hou, and Vamishi Mohan Korivi. Methodology for calculating aerodynamic sensitivity derivatives. *AIAA Journal*, 30(10):2411–2419, October 1992.
- [108] S. N. Tiwari, S. B. Pidugu, and T. O. Mohieldin. Radiative interaction in supersonic flows of premixed hydrogen in expanding nozzles. Number 99-1052 in 37th AIAA Aerospace Sciences Meeting and Exhibit, Reno, NV, January, 1999. AIAA.
- [109] Walter G. Vincenti and Charles H. Kruger. *Introduction to Physical Gas Dynamics*. Robert E. Krieger Publishing Company, Malabar, Florida, 2nd edition, 1965.
- [110] Anquan Wang and Michael F. Modest. High-accuracy, compact database of narrow-band k-distributions for water vapor and carbon dioxide. *Journal of Quantitative Spectroscopy and Radiative Transfer*, 93:245–261, 2005.
- [111] Anquan Wang and Michael F. Modest. Spectral Monte Carlo models for nongray radiation analyses in inhomogeneous participating media. *International Journal of Heat and Mass Transfer*, 50:3877–3889, 2007.
- [112] Liangyu Wang and Michael F. Modest. Treatment of wall emission in the narrow-band based multiscale full-spectrum k-distribution method. *Journal of Heat Transfer*, 129:743–748, June 2007.
- [113] Qiqi Wang, Karthik Duraisamy, Juan J. Alonso, and Gianluca Iaccarino. Risk assessment of scramjet unstart using adjoint-based sampling methods. *AIAA Journal*, 50(3):581–592, March 2012.
- [114] B. Window and G. Harding. Thermal emissivity of copper. *Journal of the Optical Society of America*, 71(3):354–357, March, 1981.
- [115] Hongmei Zhang and Michael F. Modest. Evaluation of the Planck-mean absorption coefficients from HITRAN and HiTemp databases. *Journal of Quantitative Spectroscopy and Radiative Transfer*, 73:649–653, 2002.